ANDREIA MELISSA GUEDES DA SILVA AFONSO

NON-INVASIVE MONITORING OF KIWIFRUIT RIPENING

UALg FCT

UNIVERSIDADE DO ALGARVE

FACULDADE DE CIÊNCIAS E TECNOLOGIA

2023

ANDREIA MELISSA GUEDES DA SILVA AFONSO

NON-INVASIVE MONITORING OF KIWIFRUIT RIPENING

Doutoramento em Ciências Agrárias e Ambientais

Trabalho efetuado sob a orientação de:

Professor Doutor Rui Manuel Neves Guerra

Professora Doutora Maria Dulce Carlos Antunes

UNIVERSIDADE DO ALGARVE
FACULDADE DE CIÊNCIAS E TECNOLOGIA

2023

Non-invasive monitoring of kiwifruit ripening

Declaração de autoria do trabalho:

Declaro ser a autora deste trabalho, que é original e inédito. Autores e trabalhos consultados estão devidamente citados no texto e constam da listagem de referências incluída.

(Andreia Melissa Guedes da Silva Afonso)

“Aqueles que amamos nunca morrem,
apenas partem antes de nós”

- Amado Nervo -

Acknowledgments

In the first place, I would like to thank my excellent supervisors for their effort and support in this entire journey. I don’t have enough words for thank both. Professor Dulce Antunes for accepting me as her PhD student and for believe in me, despite, we had never crossed along my academic path. Professor Rui Guerra for encourage me to pursuit a PhD degree and for guiding me, since I started, years ago, my master dissertation. It has been eight years working together! Whenever I needed his help, in all these years, he was present for me.

From Universidade do Algarve, I want also thank Adriana Guerreiro for being one of my orchards adventure companions, Ana M. Cavaco for her empathy and sympathy in some difficult moments that I had been through, Sandra Cruz for always be willing to help and Custódia Gago for her care and friendship. I also thank all my other colleagues with whom I shared the laboratory and that provided me support when needed.

Special thanks to all my family and friends who stood by me. To those who have been with me since the beginning, to those I met in the meantime and to those who left us during this phase.

At last, I would like to thank Frutas Douro ao Minho for providing the access to the orchards assessed in this work, namely to Eng. Fernão Veloso and to Luísa Freitas for the technical assistance, and everyone who, although not mentioned, helped me to achieve this goal.

The author acknowledges the Portuguese Foundation for Science and Technology – FCT for funding the PhD scholarship SFRH/BD/131462/ 2017 and for supporting CEOT through the contracts UID/Multi/00631/2019, UIDB/00631/2020 CEOT BASE and UIDP/00631/2020 CEOT PROGRAMÁTICO.

Abstract

This thesis aims to explore the use of Visible and Near-Infrared Diffuse Reflectance Spectroscopy (VisNIR-DRS) in monitoring the ripening of two kiwifruit species, a yellow- (*Actinidia chinensis* Planch 'Jintao') and a green-fleshed (*Actinidia deliciosa* Liang et Ferguson 'Hayward').

The technique used in this study relies on correlating spectra with fruit internal quality attributes (IQA). However, low correlations in VisNIR-DRS causes problems in generalizing calibration models to new data. Therefore, the study was designed to test VisNIR-DRS in difficult real field conditions. Two orchards were monitored for each cultivar over two years, enabling internal (IV) and external validation (EV) on four independent datasets.

The first part of the study focused on characterizing the time evolution of IQA during ripening.

The second part involved developing calibration models for each IQA, based on the data from the first year. The results showed that it is possible to obtain high-quality predictions for the IQA's daily averages from medium-quality models.

The third part involved the two years' data. Variable selection and orthogonal signal correction were employed to improve the performance of the models, although only the IV performance improved, indicating that these widely recommended techniques are of little value in the context of stringent EV. Usual calibration transfer between the spectrometers used in each year was impossible in the absence of common samples. Therefore, a normalization approach based on daily average spectra was used, resulting in improved model performance.

Lastly, the fourth part addressed the time variation of IQA in cold-stored kiwifruit, along with sensory data and their correlation with the spectra.

According to the results of this study, VisNIR-DRS is a promising and important tool for kiwifruit industry since can be used to follow non-destructively the kiwifruit ripening, either on-tree or during storage, in a higher number of fruit samples and in less time.

Keywords: Spectroscopy; Orchard; Quality; PLS; SSC; ‘Jintao’

Resumo

Esta tese debruça-se sobre a aplicação de Espetroscopia de Refletância Difusa no Visível e Infravermelho Próximo (ERD-VIP) na monitorização do amadurecimento de dois cultivares de kiwi, um de polpa amarela (*Actinidia chinensis* Planch ‘Jintao’) e outro de polpa verde' [*Actinidia deliciosa* (A. Chev.) C.F. Liang et A.R. Ferguson ‘Hayward’]. O estudo realizado enquadra-se, muito genericamente, no âmbito de um esforço global de promover a ERD-VIP como uma ferramenta prática e fiável para monitorizar a qualidade interna dos frutos. Com efeito, o controlo de qualidade dos frutos faz-se, em geral, através de processos destrutivos e demorados e que, pela própria limitação de desperdício na amostragem, conduz a caracterizações estatisticamente incorretas.

Os métodos não invasivos, e a ERD-VIP em particular, permitem amostragens rápidas e uma caracterização estatística da população mais rigorosa. No entanto, a aplicação da ERD-VIP apresenta, ainda, alguns problemas, que têm impedido esta técnica de ser amplamente adaptada pelos produtores.

A ERD-VIP baseia-se na correlação entre os espetros de refletância e os Parâmetros de Qualidade Interna (PQI) a determinar, como por exemplo, o Teor de Sólidos Solúveis (TSS). Com base nesta relação e em técnicas de análise multivariada, como por exemplo o Partial Least Squares (PLS), constroem-se modelos de calibração entre os espetros e os PQI. No entanto, na gama espetral do visível e infravermelho próximo, as bandas espetrais são muito largas e o efeito de interferentes é muito elevado, de onde resulta que os modelos de calibração para os PQI podem apresentar problemas de generalização a novos dados. Isto quer dizer que os modelos de calibração construídos com os frutos de um dado pomar podem realizar previsões de baixa qualidade quando aplicados a um pomar diferente; ou que os modelos construídos num dado ano, com certas características edafo-climáticas, podem falhar quando aplicados aos espetros do ano seguinte. A solução principal para este problema é recolher dados de proveniências o mais abrangentes possível, incluindo vários pomares, anos e condições de produção. No entanto, a abrangência das condições de calibração pode resultar numa perda de precisão

relativamente a modelos mais localizados, no tempo e no espaço. Por exemplo, pode ser vantajoso desenvolver um modelo multi-anual para o mesmo pomar, garantindo maior especificidade. A análise da relação entre os dados de partida de um modelo e as suas características algébricas (vetor de regressão, loadings, scores, etc.), a que poderíamos chamar de meta-modelação, é uma área de investigação ainda com pouca expressão, mas que será crucial para resolver os problemas de generalização dos modelos de calibração. O objetivo mais lato desta tese é contribuir para este esforço de meta-modelação.

A vasta maioria dos trabalhos realizados em ERD-VIP aplicada à determinação dos PQI processa-se na pós-colheita, o que significa que os frutos têm todos o mesmo estado de maturação e apresentam, por isso, bastante homogeneidade. Os resultados destes trabalhos são importantes para mostrar que a ERD-VIP pode ser utilizada, imediatamente antes da aquisição pelo consumidor, para classificar ou categorizar os frutos em escalões de qualidade. Existem muito menos trabalhos a aplicar a ERD-VIP durante a pré-colheita, em particular com o objetivo de poder prever a data ótima de colheita. Contudo, esta aplicação é tão ou mais importante que a anterior, pois permite monitorizar os pomares durante o amadurecimento da fruta e contribuir para a sua gestão adequada. A monitorização na pré-colheita tem, no entanto, algumas características que a tornam potencialmente mais complicada do que a que é feita apenas na pós-colheita. A principal diferença é que os frutos avaliados englobam um conjunto de estados de maturação muito heterogéneo, o que levanta problemas adicionais à modelação espetral. Com efeito, a estrutura e a constituição química dos frutos alteram-se durante o processo de maturação, o que tem consequências ao nível da propagação da luz e das relações espetrais entre os vários componentes. Assim, os estudos pré-colheita têm de se adaptar a uma estrutura física e química dos frutos que é mais dinâmica do que a encontrada na pós-colheita, o que dificulta o estabelecimento de padrões entre características espetrais e os PQI. Por outro lado, representa um campo de estudo mais desafiante e útil ao desenvolvimento da meta-modelação e permite ter uma perspetiva abrangente sobre os processos fisiológicos e a sua manifestação ao nível espetral.

Procurando um enquadramento nos problemas descritos acima, optou-se, neste trabalho, por um desenho experimental que pudesse contribuir para as esclarecer as questões associadas à generalização dos modelos, num contexto de monitorização pré-colheita. Com este intuito, foram escolhidos dois pomares para cada cultivar (dois de kiwi polpa amarela e dois de kiwi de polpa verde) e as medidas de campo foram realizadas durante dois anos. Desta forma foi possível realizar validação externa dos modelos, dado que, para cada cultivar, obtiveram-se quatro conjuntos de dados independentes entre si: pomar 1/ano 1, pomar 2/ano 1, pomar 1/ano 2 e pomar 2/ano 2. Na validação externa usam-se três destes conjuntos independentes para fazer a calibração e o quarto para fazer a validação. A validação externa é, com efeito, um dos pilares essenciais para avaliar a capacidade de generalização dos modelos de calibração. No entanto, a maior parte dos estudos apresentados na literatura apresenta apenas uma calibração interna, em que os espetros de fontes diferentes (diferentes pomares, produtores ou anos) são distribuídos igualmente pelos conjuntos de calibração e validação. Deste modo não há verdadeira heterogeneidade entre calibração e validação, eliminando, em grande parte, o aparecimento de problemas relacionados com a generalização dos modelos a novos dados. Neste trabalho faz-se um paralelo entre os resultados obtidos em validação interna e externa, mostrando como os primeiros são sempre excessivamente otimistas.

Na primeira parte do trabalho faz-se uma descrição da evolução dos PQI ao longo do processo de amadurecimento. Foram medidos dez PQI: os parâmetros de colorimetria L*, a*, b*, Hue e chroma, mais os parâmetros físico-químicos de firmeza, massa seca, TSS, pH e acidez titulável. O conhecimento da fisiologia dos kiwis e a interpretação da evolução dos PQI à luz dessa fisiologia são muito importantes para que se possa entender melhor as diferenças nos modelos de calibração obtidos em condições diferentes.

Na segunda parte do trabalho faz-se um estudo inicial dos modelos de calibração com apenas um ano de medidas. Para cada cultivar havia apenas, nessa altura, dois conjuntos de dados independentes. A validação externa, que consiste em modelar com um desses conjuntos e prever o outro, conduziu a resultados muito pobres, pelo que se adotou uma abordagem híbrida, em que cada conjunto de dados era dividido em dois subconjuntos de árvores diferentes. Fez-se então o estudo com quatro conjuntos independentes de árvores. A qualidade das previsões depende muito do PQI. Os melhores resultados são obtidos para TSS, Hue e a* (Standard Deviation Ratio - SDR > 2). A firmeza e a percentagem de massa seca podem ser previstas de forma grosseira (SDR ~ 1.5), mas os restantes parâmetros não podem ser previstos de forma minimamente aceitável. Mostrou-se ainda que, mesmo partindo de modelos de calibração medianos, é possível obter previsões de grande qualidade da média diária dos PQI (SDR > 6), o que é, no fundo, o objeto de interesse para os produtores.

Na terceira parte da tese faz-se um estudo detalhado da validação externa e interna em dois anos. Além disso, houve um problema adicional, relacionado com a perda do espetrómetro no início do segundo ano. Isto tornou o processo de validação ainda mais complicado, pois passou a incorporar uma componente de transferência de calibração entre os dois instrumentos. Tratou-se, portanto, de um problema de validação em dois pomares, dois anos e dois espetrómetros, o que corresponde ao caso real mais difícil de tratar. Perante este programa complexo, optou-se por concentrar os esforços na modelação do TSS, um dos PQI mais importante, tanto na determinação da data ótima de colheita, como na determinação do estado ótimo para consumo. Começou-se por comparar os resultados de validação interna com os de validação externa. Os resultados mostraram que a validação interna dá conta de todas as fontes de variabilidade (incluindo formas espetrais globalmente diferentes, fornecidas por cada um dos espetrómetros) e consegue fazer boas previsões (SDR = 2). Já os resultados de validação externa são bastante fracos, com um valor global de SDR = 1.4 (considerando em conjunto as previsões feitas para cada pomar), mas com valores individuais (SDR calculado apenas no conjunto de previsões de cada pomar) de 1 nos piores casos, ou seja, sem qualquer capacidade de previsão. Procurou-se então melhorar a performance do modelo utilizando duas técnicas muito usadas na literatura: a seleção de variáveis (SV) e correção de sinal ortogonal (Orthogonal Signal Correction - OSC). A ideia subjacente à aplicação destas técnicas é a mesma: eliminar a influência de componentes espectrais pouco informativas e que possam ser contraproducentes na validação. Em ambos os casos se verificou que a validação interna pode beneficiar da aplicação destes métodos, mas não a validação externa. Isto está de acordo com a ideia de que SV e OSC otimizam o espaço associado a três dos conjuntos de dados, mas que essa otimização não generaliza necessariamente ao quarto conjunto de dados.

SV e OSC são duas das técnicas mais amplamente recomendadas para melhorar a robustez dos modelos. Neste trabalho mostra-se, portanto, que estas técnicas valem de pouco no contexto de uma validação externa difícil. Tentou-se uma transferência de calibração, mas na ausência de amostras comuns, as técnicas habituais não funcionam. Foi então tentada uma abordagem baseada na normalização aos espetros médios diários. Selecionou-se o conjunto com mais dias de medição como "master" e os restantes como "slaves". Em cada dia de medição, os espetros "slave" são multiplicados pela razão entre as médias “master” e “slave” desse dia. Isto permitiu compensar, em grande parte, as variações espetrais induzidas pelos espetrómetros e também variações de fundo espetral causadas por texturas diferentes. Foi assim possível aumentar bastante a performance do modelo em validação externa, passando o SDR de 1.4 para 1.8. Este valor permite realizar previsões médias diárias de TSS de elevada qualidade (SDR = 2.8). Demonstrou-se que mesmo numa conjuntura adversa de troca de espetrómetro, sem possibilidade de haver amostras comuns, é possível usar o modelo de calibração calculado num dado conjunto de frutos para prever o SSC de um conjunto de frutos independente (outro pomar e/ou ano).

Na quarta parte da tese estuda-se a etapa de pós-colheita e armazenamento dos kiwis. Fez-se o estudo da variação dos PQI em função do tempo e realizou-se a análise dos dados sensoriais adquiridos a partir de painéis de provadores. A partir destes dados foi possível perceber quais são as características organoléticas mais valorizadas pelos consumidores. Por fim, procurou-se identificar algum tipo de padrão espetral que pudesse ser usado para correlacionar/antecipar a resposta sensorial, tendo se verificado uma boa correlação entre SSC e a refletância dos espectros dos kiwis nos comprimentos de onda entre 635 – 780 nm.

De acordo com os resultados deste estudo, VisNIR-DRS é uma ferramenta promissora que pode ser usada para monitorizar o amadurecimento de kiwis na

árvore, ou durante o armazenamento em pós-colheita. Isto é de grande importância para a indústria de kiwis, uma vez que permite que a monitorização do amadurecimento, seja feita de forma não destrutiva e num maior número de frutos, em menos tempo.

Palavras-chave: Espectroscopia; Pomares; Qualidade; PLS; TSS; ‘Jintao’

Contents

Abbreviations

Abs	Absorbance
ANN	Artificial neural networks
C	Celsius
Ca	Calcium
Chl a	Chlorophyll a
Chl b	Chlorophyll b
CO_2	Carbon dioxide
CR	Continuum Removal
CT	Calibration transfer
CV	Cross-validation
DAFB	Days after full bloom
DM	Dry matter
EV	External Validation
FT - NIR	Fourier transform-near infrared spectroscopy
g	Gram
GF	Gaussian filter
IQA	Internal quality attribute
IR	Infrared
IV	Internal Validation
K	Potassium
KM	Kubelka-Munk
KS	Kennard-Stone
LSNV	Local SNV
LVs	Latent variables
m	Meter
mm	Millimeter
max	Maximum
MDS	Multidimensional scaling
min	Minimum
mg	Milligram

Mg	Magnesium
MLR	Multiple linear regression
MSC	Multiplicative scatter correction
N	Newton
NaOH	Sodium hydroxide
NIR	Near infrared
nm	Nanometer
O_2	Oxigen
OSC	Orthogonal signal correction
P	Phosphorus
PLS	Partial least squares
PCA	Principal component analysis
R^2	Coefficient of determination
RH	Relative humidity
RMSECV	Root-mean-square of error of cross-validation
RMSEP	Root-mean-square of error prediction
RMSET	Root-mean-square of error in tuning
ROC	Receiver operating characteristic analysis
SDR	Standard deviation ratio
SDRcv	Standard deviation ratio of cross-validation
SDRt	Standard deviation ratio of tuning
SNR	Signal to noise ratio
SNV	Standard normal variate
SG	Savitzky-Golay
SSC	Soluble solids content
SVM	Support vector machine regression
TA	Titrable acidity
Tol	Tolerance
VarSel	Variable selection
VisNIR-DRS	Visible and Near-Infrared Diffuse Reflectance Spectroscopy
µg	Microgram

Chapter 1

General Introduction

1.1 Kiwifruit characterization

Consumers are very much aware of food quality and nutritional value along with their impact on our health, especially since COVID-19 pandemic (Si et al., 2022). Nowadays, fruit quality refers to both external and internal attributes (Tian et al., 2020).

Kiwifruit (*Actinidia spp*.) is an important economic crop worldwide (Xiao & Li, 2022), because of its delicious taste, high nutritional value (Wang et al., 2022a), and for being helpful to digestion and gut function (Gao et al., 2021).

Its content of vitamin C, one of the most well-known antioxidant compounds (Kumarihami et al., 2022), higher than in other fruit, including orange, lemon, and apple (Roberts & Gordon, 2003; Liang et al., 2021) (Table 1.1), vitamins A, E and K, polyphenols (Iwasawa et al., 2011), potassium, magnesium and folic acid (Garcia et al., 2012), are some of the reasons why kiwifruit is widely appreciated. Moreover, this fruit has been associated to lowering blood lipid levels and alleviating skin disorders (Sanz et al., 2021), exhibiting antioxidant and anti-inflammatory actions which might help prevent cancer, diabetes, cardiovascular and degenerative diseases (Sanz et al., 2021).

Table 1.1: Nutritional composition of kiwifruit and other fruit. The amounts are specified per 100 g of the fruit. Values presented for kiwifruit relate to *Actinidia deliciosa* (Source: U.S. Department Agriculture, 2019).

	Sugars (g)	**Fiber (g)**	**Vitamin C (mg)**	**Vitamin E (mg)**	**Vitamin K (µg)**	**Folate (µg)**	**Mg (mg)**	**Ca (mg)**	**K (mg)**	**P (mg)**
Kiwifruit	8.99	3	92.7	1.46	40.3	25	17	34	312	34
Apple	10.39	2.4	4.6	0.18	2.2	3	5	6	107	11
Orange	9.35	2.4	53.2	0.18	0	30	10	40	181	14
Pomegranate	13.67	4	10.2	0.6	16.4	38	12	10	236	36
Pear	9.75	3.1	4.3	0.12	4.4	7	7	9	116	12
Melon	5.69	0.9	21.8	0.05	2.5	8	11	11	182	5
Mango	13.66	1.6	36.4	0.9	4.2	43	10	11	168	14
Blueberry	9.96	2.4	9.7	0.57	19.3	6	6	6	77	12
Grape	16.25	0.9	4	0.19	14.6	4	5	14	191	10
Banana	12.23	2.6	8.7	0.1	0.5	20	27	5	358	22
Pineapple	9.85	1.4	47.8	0.02	0.7	18	12	13	109	8
Peach	8.39	1.5	6.6	0.73	2.6	4	9	6	190	20

The genus *Actinidia* includes 76 species, with *Actinidia chinensis* (Planch.) and *Actinidia deliciosa* (A. Chev.) C. F. Liang & A. R. Ferguson, being the most commercially dominant (Ramstad et al., 2016; Liang et al., 2021).

In general, kiwifruit is composed of four main tissues: a central core, an inner pericarp containing locules and seed, an outer pericarp, and the skin (Richardson et al., 2011) (Figure 1.1). These tissues differ in minerals (Ferguson, 1980), cell wall composition (Redgwell et al., 1990) and cell characteristics (Hallett et al., 1992; Harker & Hallet, 1994).

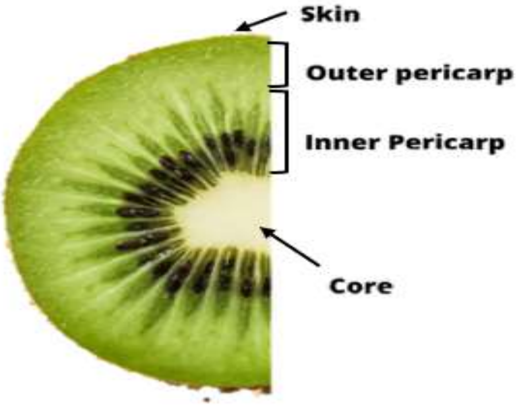

Figure 1.1: Tissue zones of kiwifruit (adapted from Richardson et al., 2011).

The appearance, weight, flavour, texture, aroma, and nutritional quality vary significantly among, and within kiwifruit species and cultivars if climatic conditions differ during growth (Guo et al., 2017; Xie et al., 2019; Liang et al., 2021).

The green fleshed ‘Hayward’ belongs to *Actinidia deliciosa* and is the most commercialized variety on the international market, because of its size, taste, and long storage life (Testolin & Ferguson, 2009; Chai et al., 2021), maintaining good quality in terms of texture, flavour and the absence of disorders (Burdon et al., 2014a).

In fact, approximately 90 % of the kiwifruit commercialized is ‘Hayward’ (Ma et al., 2017). However, in recent years, yellow-fleshed *A. chinensis* var. *chinensis* cultivars ‘Hort16A’, ‘Jintao’, ‘Zesy002’, ‘Zesy003’, ‘Soreli’ and ‘Dori’ (Gambi et al., 2018), which are sweeter and have a higher commercial value than the green fleshed ones (Testolin & Ferguson, 2009), are gaining more attention.

The kiwifruit grows naturally at altitudes of 600 - 2000 m, relative humidity of 76 – 78 % and soil pH 5.0 - 6.5 in areas with frequent irrigation or rainfall (Torkashvand et al., 2016; Torkashvand et al., 2017).

China, New Zealand, Italy, Iran and Chile are the main kiwifruit producers worldwide (Statista, 2022) (Figure 1.2). In Portugal, kiwifruit production has been growing and are located mainly in the coastal regions of the north (70 %) and centre (29 %) (Castro et al., 2021).

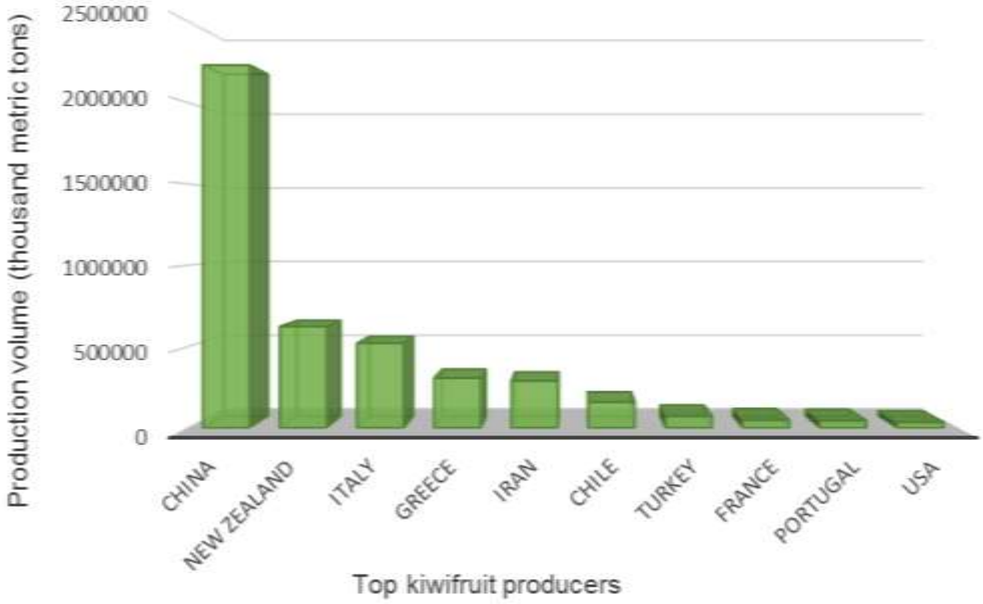

Figure 1.2: Production volume of kiwifruit worldwide in 2020 (Source: Statista, 2022).

Kiwifruit is a typical climacteric fruit that is harvested mature but unripe (Burdon et al., 2013; Tian et al., 2022a). Climacteric fruit, if harvested after physiological maturity, will ripe until they reach consumer maturity, while for non-climacteric fruit, harvest maturity and consumer maturity are the same (Shah 2020).

Kiwifruit is harvested when the soluble solid content (SSC) reaches approximately 6.2 ºBrix (Burdon et al., 2016; Yi et al., 2016; Wang et al., 2021; Wang et al., 2022b), flesh firmness is equal or greater than 62 N (Benelli et al., 2022) and dry matter (DM) is in the range 12 - 20% (Burdon et al., 2004), in the case of green fleshed kiwifruit. For the yellow fleshed cultivars, additionally, the hue angle must reach the minimum of 103 º, which indicates the pulp colour change from green to yellow (Costa et al., 2010; Afonso et al., 2022).

Kiwifruit ripening is affected by environmental conditions, management and other factors and, since its appearance barely gives any information about it (Liu et al., 2019), the choice when to harvest depends on internal attributes, which are the key to kiwifruit productivity and quality. The establishment of the optimal harvest date is a critical step in the fruit ripening process up to an acceptable eating quality, retaining adequate firmness and avoiding physiological disorders (Burdon et al., 2021). Overall, once the ripening process on climacteric fruit, continues after harvest (Antunes et al., 2000; Ma et al., 2022), there is either the risk that if kiwifruit are harvested too early, they will not reach full flavour and aroma (Bertone et al., 2012; Berardinelli et al., 2019), or if they are harvested too late, their storage life will be shorted (Burdon et al., 2014a).

In fact, quality deterioration and texture softening are the cause of 28 – 36 % postharvest loss of fruit and vegetables (Shafiee-Jood & Cai, 2016; Wang et al., 2021). Firmness retention during storage is very difficult, since orchard practices and storage conditions affect the rate of softening and, furthermore, the time each fruit needs to soften can be very different (Xiao & Li, 2022). Reducing postharvest loss is still one of the main challenges for the horticultural industry (Kader, 2005; Jabbar et al., 2014).

In order to satisfy consumers' expectation, SSC should exceed 12.5 ºBrix and firmness be in the range 9 – 13 N (Crisosto & Kader, 1999; Benelli et al., 2022). Considering those values, 'Hayward' kiwifruit can be stored for about six months at 0 ºC and 90 – 95 % relative humidity (Boquete et al., 2004; Hu et al., 2017), while *A.*

chinensis for four months or less (Asiche et al., 2017; Chai et al., 2021). However, kiwifruit can exhibit chilling-injury disorders during this period, including pulp browning and increased electrolyte leakage (Lee & Kader, 2000; Gerasopoulos et al., 2006), due to the low storage temperatures (Chai et al., 2021). Besides that, at the end of the kiwifruit shelf life, the ethylene production and respiration rate increase (Antunes et al., 2000; Chai et al., 2021), what accelerates metabolite consumption and senescence (Li et al., 2016; Chai et al., 2022), leading to a very short edible window, approximately 3 - 4 days (Antunes et al., 2000; Chai et al., 2021). On the other hand, repacking or removing not edible kiwifruit incurs significant labour cost (Xiao & Li, 2022).

1.2 Kiwifruit ripening

The rate of kiwifruit softening varies enormously, between and within batches (Jabbar et al., 2014; Goldberg et al., 2019), and is influenced by orchard practices, maturity at harvest, duration and postharvest storage conditions (Xiao & Li, 2022).

Softening of kiwifruit occurs in two or, if harvested at early maturity, three phases (Lallu et al., 1989; Burdon et al., 2013).In the initial lag phase, fruit maintain firmness and soften slowly; in the second phase there is a rapid softening to about 20 % of their firmness at harvest; and the final phase is marked by a slow pace, marked by the start of internal ethylene production (Paterson et al., 1991; Antunes & Sfakiotakis, 2002; Xiao & Li, 2022). For late harvested fruit there is no initial lag phase (Li et al., 2022; Xiao & Li, 2022).

The gradually decreased firmness is caused by cell wall degradation, dissolution of the middle lamella and weakened cell adhesion (Schroeder et al., 2006; Wood et al., 2009; Cheng et al., 2022). Fruit firmness is also affected by cell turgor and the number, size and shape of intercellular spaces (Cen et al., 2013).

Pectin degradation, a component of primary cell walls and middle lamella (Benítez et al., 2013; Tilahun et al., 2020), leads to thinner cell walls, cells split and a reduction of cell turgor pressure (Tian & Xu, 2022). The cell turgor pressure declines due to water loss, which affects the connection between the cells and increase intercellular space (Tian & Xu, 2022) as adhesion between cell walls weakens (Rowe et al., 2014).

Kiwifruit with higher DM at harvest is associated with better firmness retention and less transpiration during storage (Tombesi et al., 1993; Famiani et al., 2012), suggesting that fruit with a higher initial water content soften more quickly (Li et al., 2022). Also, during kiwifruit ripening, the metabolism of carbohydrates, acids, pigments and volatile organic compounds go through various and significant changes (Chai et al., 2022).

At harvest, most of the kiwifruit carbohydrates comprise starch (Jordan et al., 2000; Wang et al., 2021), unlike other fruit, such as peach, strawberry, grape and melon, that primarily accumulate soluble sugars (Choi et al., 2022).

As kiwifruit ripe, the starch is hydrolysed into soluble sugars, glucose and fructose, and the water is consumed under respiration (Liu et al., 2019), causing a gradual SSC increase, while moisture content decrease along storage (Cheng et al., 2022). The starch conversion is visible on the juice, as it changes from a milky pale green, containing starch, to a clear darker green (Burdon et al., 2004).

The chlorophyll and carotenoid contents are responsible for green- and yellow- fleshed colour kiwifruit, respectively, during development (McGhie & Ainge, 2002; Xia et al., 2021). In fact, the class, amount and ratio of the pigments determine the fruit pulp colour and its intensity (Luan et al., 2019; Xia et al., 2021).

The chlorophyll content generally decreases, as ripening progresses, whereas other pigments are usually biosynthesised and accumulated (Benelli et al., 2022). In the case of yellow-fleshed kiwifruit, the decay in chlorophyll pigments no longer masks the carotenoids, such as lutein and β-carotene, leading to yellow colour in kiwifruit (Ampomah-Dwamena et al., 2009; Montefiori et al., 2009; Pilkington et al., 2012; Gambi et al., 2018). This process is mediated by the chloroplast-located protein stay-green that dismantles chlorophyll-protein complexes (Borovsky & Paran, 2008; Gambi et al., 2018).

Relatively to a* and b* values, both increase significantly, indicating the greenness decreased and yellowness increased, respectively, which is also confirmed by the changes in Hue. Meanwhile L* decreases as kiwifruit turn darker (Yi et al., 2016; Chai et al., 2021) and chroma, that reflects saturation, remains stable during late ripening (Yi et al., 2016).

Respiration consumes organic acids as substrates, leading to a decrease in titrable acidity (TA) during storage (Kumarihami et al., 2022). The main organic acids in kiwifruit are citric acid, quinic acid and malic acid in much smaller amounts (Marsh et al., 2009; Yi et al., 2016; Wang et al., 2021), while the most abundant fatty acids are α-linoleic acid, oleic acid, palmitic acid, and linoleic acid (Antunes & Sfakiotakis, 2008; Choi et al., 2022), although acid percentage composition shown a wide variability among cultivars (Choi et al., 2022). The ascorbic acid (vitamin C) content in kiwifruit decreases gradually during kiwifruit ripening due physical dissolution and oxidative decomposition (Zhang et al., 2021).

Volatile organic compounds are released during kiwifruit ripening and are the main responsible for kiwifruit flavour and aroma (Yi et al., 2016; Chai et al., 2022). In fact, kiwifruit aroma is the result of a MIXture of volatile compounds, and together with sweetness and acidity, are critical to consumer acceptance and commercial success (Marsh et al., 2006; Garcia et al., 2012; Wang et al., 2021). Thus, as sugars and flavour content increase, while total acids decrease, sensory properties improve along ripening process (Song & Bangerth, 1996; Kader, 2008; Bertone et al., 2012).

Kiwifruit respiration does not change significantly until autocatalysis of ethylene production and, in fact, in the absence of external ethylene, its rise takes place simultaneously with the rise of ethylene production (Antunes, 2007) (Figure 1.3).

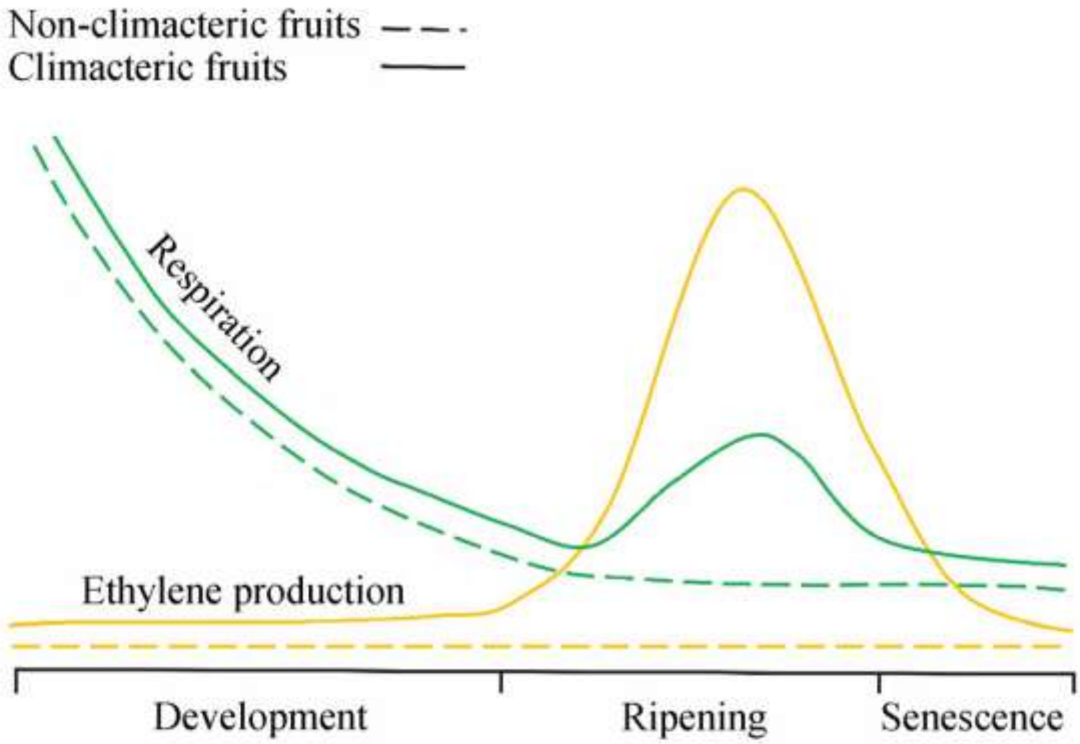

Figure 1.3: Changes in respiration rate and ethylene production between non-climacteric and climacteric fruit (Source: Ji et al. 2021).

Autocatalysis of ethylene occurs when kiwifruit reaches eating softness (Antunes et al., 2000; Chai et al., 2021). In unripe kiwifruit, ethylene production only occurs due physical, physiological or pathological damage (Feng et al., 2003; Huang et al., 2021). Kiwifruit is highly sensitive to exogeneous ethylene and an exposure to even a small concentration (Xiao & Li, 2022) can accelerate senescence and cause fruit loss (Jabbar & East, 2016; Xiao & Li, 2022). To trigger and also accelerate fruit ripening, ethylene (Paul et al., 2012) or modulated temperature treatments can be performed (Mitalo et al., 2019; Ozturk et al., 2019; Chai et al., 2022), while to delay fruit senescence ozone and oxalic acid are usually applied (Tian et al., 2002; Wang et al., 2009; Minas et al., 2012; Xia et al., 2016).

Modified atmosphere is commonly used to extend kiwifruit storage life, as for many other climacteric fruit (Wang et al., 2005; Liu et al., 2013; Xia et al., 2016), through the increase of CO_2 and decreased of O_2 concentrations (Harman & McDonald, 1982; Manolopoulou et al., 1997; Antunes & Sfakiotakis, 2002; Hertog et al., 2004). Commercially, to avoid water loss, fruit can be marketed in packs with polylimers or bags to create a high humidity environment (Burdon et al., 2014b), while storage cold chambers should be at 95 – 98 % relative humidity.

1.3 Kiwifruit quality attributes

Unlike other fruit, is not possible to visually assess kiwifruit ripening, due to the lack of any external colour changes (Sneddon et al., 2022). The major internal quality attributes to determine kiwifruit optimal harvest date are the SSC, firmness, and DM (Afonso et al., 2022).

For the yellow-fleshed kiwifruit cultivars which are more aromatic and sweeter than the green ones, and present a higher commercial value (Testolin & Ferguson, 2009), their flesh colour has a major impact on the consumer (Schaare & Fraser, 2000) and it is also a parameter consider. Chlorophyll must be fully degraded (Pilkington et al., 2012, Gambi et al., 2018; Burdon et al., 2021), with total conversion from green to yellow (Burdon et al., 2014a), when consumers eat the fruit.

While firmness is directly related to texture and consumer acceptance, SSC and acidity are related to kiwifruit flavour, more precisely to sweetness and sourness respectively (Zhu et al., 2017; Ma et al., 2021).

The Magness-Taylor penetration is currently the standard method for determining fruit firmness. However, to ensure the same force, testing speed and puncture distance must also be similar, to ensure the repeatability of the measurements, leading to the general use of the Texture Analyzer (Tian & Hu, 2022). This device can be used either for puncture, that damages fruit, either for compression tests that can cause bruises even though wounds are not visible (Sirisomboon et al., 2012; Tian & Hu, 2022). Both puncture and compression tests cannot be implemented as online measuring method for fruit firmness grading (Tian et al., 2022a).

SSC and pH are usually determined using a Brix refractometer (Magwaza & Opara, 2015; Ma et al., 2021) and a titrator, pH meter or acid meter, respectively (Wati et al., 2021). These methods require the sample conversion to liquid thus involve destructive and time-consuming analysis (Wati et al., 2021). Otherwise, dry matter is measured by cutting and drying equatorial slices of kiwifruit until constant weigh.

Overall, conventional measurement methods are destructive, time-consuming, do not allow neither monitoring the same fruit over time neither be statistically representative of the biological variability (Bertone et al., 2012), since to reduce fruit loss and time, only a small number of fruit is destroyed, which leads to a deficient orchard management (Cavaco et al., 2018; Afonso et al., 2022; Li et al., 2022a).

Therefore, the development of fast and non-destructive methods for assessing kiwifruit internal quality is fundamental (Zhu et al., 2017) for suitable postharvest storage and to comply with consumers´ demands (Asiche et al., 2017; Goldberg et al., 2019; Ma et al., 2022).

1.4 Non-invasive methods

According to Nicolaï et al. (2014), the non-destructive methods used to assess fruit quality attributes can be classified in optical-, mechanical-, x-ray radiography and tomography-, magnetic resonance imaging-, mass spectrometry- and gas sensors and electronic noses-based techniques.

Mechanical techniques can be classified into two categories: 1) application of an external force to measure local force deformation curve; 2) measuring whole fruit response after it has been excited (Nicolaï et al., 2014). Mechanical-based methods, generally used for texture evaluation, include micro-deformation, vibration measurements, acoustic impulse response, falling or impact, forced or hammer impact, and ultrasonic methods (Phourkhark et al., 2017; Tian & Xu, 2022). Vibrational analysis has been used to derive fruit firmness (Sugiyama et al., 2005), since, for fruits of the same size and shape, the greater the resonant frequency, the firmer the flesh (Abbott, 1999). Acoustic impulse response to was used to assess internal quality by recording the sound which is produced when hit the fruit and performed a fourier transform on the signal (Lakshimi et al., 2017).

X-ray radiography was used to investigate internal disorders in fruit and vegetables (Haff & Toyofuku, 2008), since absorption properties differences between surrounding materials will become visible; magnetic resonance imaging to detect internal defects and measure physical properties (Nicolaï et al., 2014).

Gas sensors and electronic noises are able to recognize simple and complex odours (Garner & Bartlett, 1994; Zerbini et al., 2006). This way, volatile compounds interact with these sensors and the response given by them to each sample is a “fingerprint” of the compound or MIXture (Zerbini et al., 2006; Lakshimi et al., 2017).

Optical based techniques will be the focus of the next section.

1.4.1 Optical methods

Light propagation in turbid medium, such as fruit, is a complex process (Gao et al., 2021). When the light penetrates a sample, it may be reflected, absorbed, or transmitted (Nicolaï et al., 2007; Cavaco et al., 2022), since the light can penetrate deeper than the thickness of the peel reaching the pulp tissue (Alexandrakis et al., 1998; Si et al., 2022).

Reflection can occur through specular reflection when light illuminates smooth surface and causes gloss, external diffuse reflection induced by rough surfaces or scattering effect (Nicolaï et al., 2007). The first two only provide information about the surface sample, while, for the latter, the light penetrates the sample and emerges again at the surface after partial absorption and multiple scattering inside the inner tissues (Nicolaï et al., 2007; Cavaco et al., 2022).

There are three basic modes to collect fruit spectra, interactance, reflectance and transmittance (Nicolaï et al., 2007), according to the position of the light source and the detector (Hong & Chia, 2021) (Figure 1.4).

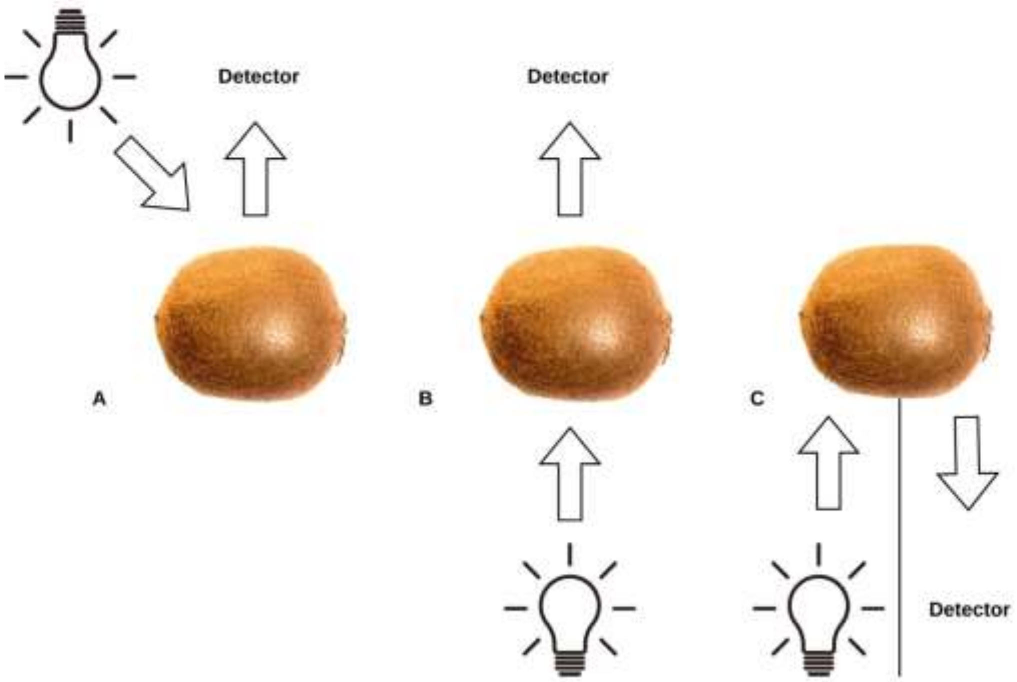

Figure 1.4: Schematic of the tree acquisition modes: A) Reflectance; B) Transmittance; C) Interactance (adapted from Nicolaï et al., 2007).

In the interactance mode the light source and the spectrometer are positioned parallel to each other and in contact with the fruit (Nicolaï et al., 2007). Reflectance mode require no contact with the fruit (Schaare & Fraser, 2000), the light and detector are positioned on the same side of the fruit but mounted under a 45º angle (Nicolaï et al., 2007). Interactance and reflectance are the most used in fruit (Tian & Xu, 2022), and both aim to acquire diffuse reflectance and to avoid specular reflectance (Hong & Chia, 2021). In the transmittance mode the light travel through the fruit (Hong & Chia, 2021) since the light source is positioned opposite to the detector (Nicolaï et al., 2007).

Biological tissues are composed by nucleus, cytoplasm, and various organelles (Rojas-Candelas et al., 2021), with different physical structures and chemical components and, consequently, with different optical properties (Si et al., 2022). When photons enter the biological tissues, they will move straightforward until hitting an absorbing particle (Lu et al., 2020), and then transformed into thermal or other form of energy (Lu, 2016; Si et al., 2022), or into a scattering element, changing the travel direction (Lu et al., 2020).

The main absorption components in plant and fruit tissues, are pigments, water and carbohydrates (Si et al., 2022), while the main scattering elements are the cell wall interfaces (McGlone et al., 1997). For this reason, it is reported that scattering process is related to physical structures, such as density, texture, cell size, while the light absorption depends on the chemical composition (Qin & Lu, 2009; Rizzolo et al., 2014; Zhu et al., 2016; Gao et al., 2021).

However suspended particles, such as starch granules, chloroplasts, and mitochondria, but also pores and other heterogeneities may also induce scattering caused by a different refractive index between the particle surface and the surroundings (Il'yasov & Krasnikov, 1991; Nicolaï et al., 2007). Scattering also depends on particles' size, shape and microstructure (Nicolaï et al., 2007), complicating the relation between the light collected and the internal quality of the fruit (Saeys et al., 2019).

Absorption and scattering processes are characterized by the absorption coefficient (*μa*) and reduced scattering coefficient (*μs'*) (Tuchin, 2000; Cen et al., 2013), although different cultivars, due to different flavours and textures, may have different absorption and scattering properties (Cheng et al., 2022). This way, spectroscopic methods provide a fingerprint of the sample analysed (Zhu et al., 2017).

The absorption and scattering coefficients of light refer to the probability of light being absorbed or scattered per unit length in a sample (Welch & Gemert, 2010; Tian & Xu, 2022).

Besides those, on the scattering process, also a scattering angle, which represents the direction taken by a photon when hits a scattering particle, and the proportion of photons that would be scattered in a particular direction, named anisotropic coefficient (g) (Tian & Xu, 2022), can be defined. Values of g range between -1 (total backward scattering) and 1 (total forward scattering) (Lu et al., 2020). In fruit the light usually scatters forward and the g value is between 0.7 - 0.9 (Lu, 2016; Lu et al., 2020; Tian & Xu, 2022).

1.4.1.1 VisNIR-DRS spectroscopy

VisNIR-DRS spectroscopy, which have become one of the most successful non-destructive methods for quality assessment of fruits (Walsh et al., 2020a, b; Cavaco et al., 2021a; Tian et al., 2022b), analyse multiple attributes simultaneously, besides being a low-cost, reliable (Nicolai et al., 2007; Cruz et al., 2021; Afonso et al., 2022) and chemical-free method (Shah et al., 2020).

According to the Lambert-Beer law, the light absorbance is linearly proportional to the concentration of an absorbing composition (Yadav et al., 2015; Lin et al., 2018; Suzuki et al., 2018; Hong & Chia, 2021). This law is limited to clear liquids and although fruit are considered a turbid medium, meaning that the light that interacts with the fruit tissue is not only absorbed but also scattered, it is based on this law that VisNIR-DRS spectroscopy spectra has been related to the quality attributes of fruit (Liu et al., 2019).

On the Vis region of the spectrum (400 – 750 nm) (Figure 1.5), anthocyanins, carotenoids and chlorophyll a are responsible by light absorption (Abbot, 1999), each one, at different specific wavelengths (Zude, 2008).

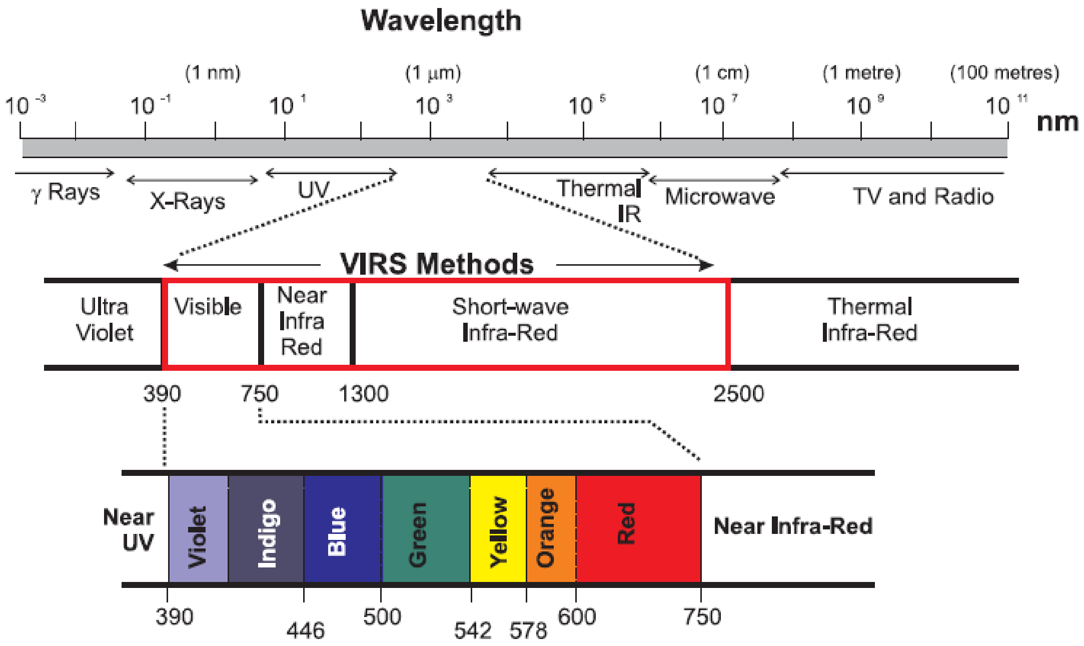

Figure 1.5: The electromagnetic spectrum showing the different regions of interest when using VisNIR-DRS spectroscopy (Source: Kerr et al., 2011).

Chlorophyll a absorption spectrum presents two dominant absorption bands, one at the blue (420 nm) and another at the red (680 nm) (Liew et al., 2008); carotenoids absorb around 500 nm; and anthocyanins at 550 - 600 nm (Beers et al., 2017).

The NIR (750 –1300 nm) is associated with the macro constituents (Walsh et al., 2020), water (Nicolai et al., 2007) and sugars (Pu et al., 2016; Benelli et al., 2022), showing a strong absorption peak around 970 nm, which corresponds to a combination of O-H in water and second overtone of C-H stretching in carbohydrates (Kamruzzamanet al., 2011; Shinzawa et al., 2011; Liu et al., 2019). There are also two another absorption peaks at 750 nm and 840 nm caused by O-H and C-H associated with water (Huang et al., 2018; Tian et al., 2022b).

The use of Fourier transform-near infrared spectroscopy (FT-NIR) to evaluate freshness, safety and shelf-life has increasing, since it provides a faster spectral acquisition, require limited sample pre-treatment (Wang et al., 2022a), increases the sensitivity of various vibrational spectroscopy techniques (Ropodi et al., 2018; Tirado-Kulieva et al., 2022), and its reproducibility and precision are higher than NIR

(Cicorritti et al., 2019). However, it requires a time-consuming calibration (Wang et al., 2022a).

1.4.1.2 Time and spatially resolved techniques

Conventional VisNIR-DRS spectroscopy provides information about the combined effect of light absorption and scattering (Tian & Xu, 2022), but not the individual information of each process (Tian et al., 2022b). New technologies, such as time-resolved, frequency domain, spatially resolved and integrating sphere measurements (Aernouts et al., 2015; Hu et al., 2020; Milej et al., 2016; Beers et al., 2017; Tian et al., 2022b), have been studied to evaluate absorption and scattering of the tissues separately (Si et al., 2022).

Time-resolved injects a monochromatic pulse into the fruit to measure, with an appropriate model, the light temporal distribution to estimate the optical properties of the fruit (Torricelli et al., 2015; Rizzolo & Vanoli, 2016; Lu et al., 2020; Cavaco et al., 2022). With this technique, the spectra acquired for the whole fruit is very similar to the spectra of the same peeled fruit (Vanoli et al., 2020; Ma et al., 2022). Yet, time-resolved and frequency domain are expensive, signal conversion is still a complex process (Tian et al., 2022b), measurements are time-consuming, and the need of a good contact between the fruit and the detector prevents this technique to be used for on-line grading (Tian & Xu, 2022). On the other hand, spatially resolved method is gaining interest due to its low instrument cost, easy implementation and fast measurement (Tian et al., 2022b; Ma et al., 2022). This method illuminates the fruit surface with constant intensity and measures the reemitted light at different distances from the light source (Lu et al., 2020; Cavaco et al., 2022), giving us information about the different depths of the fruit (Si et al., 2022).

1.4.1.3 Spectral imaging

Spectral imaging can be divided into hyperspectral and multispectral imaging (Cozzolino & Roberts, 2016). Hyperspectral imaging technique combines image analysis and spectroscopy (Benelli et al., 2022), obtaining both spectral and spatial information over a wide spectral range (300 to 2600 nm) (Gowen et al., 2007; Chandrasekaran et al., 2019) at spatial resolutions varying from the level of single cells up to the macroscopic objects (Liu et al., 2014; Gowen et al., 2015; Zhu et al., 2017). The spectral and spatial information of fruit are obtained by a high-performance CCD camera and an imaging spectrometer (Tian & Xu, 2022), which allows acquire data as image at each wavelength and as spectra for each pixel (Chandrasekaran et al., 2019).

Multispectral is a form of hyperspectral imaging but differs from it by using a set of filters and a common digital camera (Cavaco et al., 2022) to obtain the imaging spectral information at a few discrete wavebands (Cozzolino & Roberts, 2016),

These technologies are gaining importance to evaluate crops and other commodities with characteristics and properties that may vary spatially (Kim et al., 2001; Gowen et al., 2007; Gowen et al., 2010; Cozzolino & Roberts, 2016; Cavaco et al., 2022).

1.4.1.4 Portable devices

In the last years, the demand for handheld and/or portable devices for non-destructive fruit quality assessment has gain importance (Shaha et al., 2020), also for kiwifruit. Rocchi et al. (2016) used a device based on the VisNIR-DRS (Kiwi meter) to monitor fruit flesh colour evolution non-destructively by means of the DAindex^{TM}; Guo et al. (2019) used a handheld VisNIR-DRS micro-spectrometer, which was just about 550 g in weight, to assay SSC; Sarkar et al. (2020) used a low precision portable near-infrared spectrophotometer F-750 Produce Quality Meter (Felix Instruments Inc., USA) to determine the soluble solids content of hardy kiwifruit; Singh et al. (2020) used a low-cost VisNIR-DRS multispectral detector on kiwifruit to measure SCC and DM non-destructively. Even the use of low-cost portable spectrometers with smartphone connectivity, like the SCiO (Consumer Physics Inc., Tel Aviv, Israel), that was used by Li et al. (2018) to predict kiwifruit quality, has gain considerable interest.

Although their accuracy and cost-effective, only a few portable devices have been used on-tree, despite the fruit we may be referring to, since in orchards many external factors, such as light and temperature, can affect models’ prediction performance (Cavaco et al., 2018, 2021b, 2022).

1.4.2 Chemometrics

In VisNIR-DRS spectroscopy, most absorption bands are overtone or combination bands, resulting in broad and overlapping peaks (Nicolaï et al., 2007). Moreover, the fruit high content of water, approximately 85 %, turn them sensitivity to temperature variations with a wavelength shift in the O-H absorption region (Anderson & Walsh, 2022). Furthermore, spectra may be complicated by the complexity of the fruit’s tissues heterogeneities and microstructure, which have many spectrally active components (Saeys et al., 2019), by instrumental noise as well as other sources of variability (Nicolaï et al., 2007). It is fundamental to minimize environment interference, such as light and temperature, or taking them into account when processing data (Nicolaï et al., 2007).

To overcome all these problems and the high volume of data, considered one of the main spectroscopic difficulties (Lorent et al., 2015), the relevant information about fruit quality attributes must be extracted and combined through multivariate data analyses techniques (Sayes et al., 2019), also called chemometrics.

For this purpose, a variety of chemometric methods and machine learning algorithms can be applied, such as multiple linear regression (MLR), principal component analysis (PCA), partial least squares regression (PLS), support vector machine regression (SVM), artificial neural networks (ANN), orthogonal signal correction (OSC), Gaussian filter (GF), standard normal variate (SNV), Savitzky-Golay filter (SG) and multiplicative scatter correction (MSC) (Wu & Sun, 2013; Hu et al., 2017) (Tirado-Kulieva et al., 2022). These methodologies can be divided into exploratory data analysis, classification techniques and regression techniques (Shah et al., 2020).

Chemometrics flow comprises two main steps: spectral pre-treatments or pre-processing, and regression methods (Wang et al., 2015).

The pre-processing method selected can take into consideration quality attribute intended, for example, if it is chemical, could be useful remove the effect of scattering through multiplicative scatter correction (Anderson & Walsh, 2022). Many combinations of spectral pre-treatments and their parameters (interval width, polynomial order, etc.) can be applied to determine the optimum result (Anderson & Walsh, 2022). The parameters must be selected carefully to avoid spectral noise amplification and to not remove information that might be useful (Nicolaï et al., 2007).

The usual pre-processing procedures are mean centering of spectra, derivatives, standard normal variate (SNV) and multiplicative scatter correction (MSC) (Anderson & Walsh, 2022). Mean centering reduces instrumental noise, optical distance, and environment contribution, while first and second derivatives reduce the effect of specular reflection (Li et al., 2018), help to distinguish superposed peaks, rise sensitivity and spectral resolution (Wang et al., 2015). Savitzky-Golay (SG) is the most used for smoothing data (Li et al., 2018). SNV substrates the average value of a spectrum from the original one and then divide it by the standard deviation, eliminating particle size and scattering effects (Barnes et al., 1989; Wang et al., 2015). MSC adapts each spectrum to a reference one through least squares regression method (Lorent et al., 2015), correcting additive and multiplicative effects caused by the fact that light does not travel the same distance in the fruit (Shao et al., 2007). The greater the distance travelled by light, the lower is the reflectance value, since less light is detected (Martens & Naes, 1987; Shao et al., 2007). Wavelength selection can also be evaluated to improve the model performance (Ma et al., 2021) and is considered a form of data pre-treatment (Anderson & Walsh, 2022).

Regression is a statistical procedure used to establish a relation between the dependent and the independent variables, that is, to produce a calibration model (Chandrasekaran et al., 2019). When using VisNIR-DRS spectroscopy, calibration refers to establish a mathematical relationship between the transformed spectra and the fruit traditional measurement (Zeaiter et al., 2005; Li et al., 2022a).

Partial least squares regression (PLS) is the most used regression model to predict fruit quality (Li et al., 2018). PLS is a dimension reduction technique based on the scores of latent variables (LVs) (Anderson & Walsh, 2022) that are selected by their relevance for predicting the dependent variables (Wang et al., 2015). It is the most common multivariate linear regression method (Walsh et al., 2020a; Li et al., 2022a) and is very used to predict dependent variables from a large set of independent ones (Yang et al., 2017; Ma et al., 2022).

Internal validation uses a dataset related to calibration set through techniques as leave-one-out, while external validation uses a dataset independent from the calibration one, giving a more realistic vision about model robustness (Li et al., 2022a). However, approximately, 90 % of publications still use adapted cross-validation methods or select sets very similar to the calibration set (Walsh et al. 2020a; Li et al., 2022a).

Models are considered robust when their prediction accuracy is not affected by external factors (Wang et al., 1991; Kaur et al., 2022). In fact, models fail due to two main reasons, which are lack of interest attribute variability or due to external variability that hides the attribute variability (Mishra & Nikzad-Langerodi, 2020; Mishra et al., 2020; Mishra & Woltering, 2021). To improve prediction accuracy and model robustness, a big volume of data, a wide range of reference values (Magwaza et al., 2014; Hu et al., 2017), and data from different cultivars, seasons, geographic location, or ripeness level should be use in calibration (Cavaco et al., 2018; Pires et al., 2022; Anderson et al., 2020; Anderson et al., 2021; Mishra & Woltering, 2021).

Models' robustness can be evaluated through coefficient of determination (R^2), root-mean-square of error prediction in validation (RMSEP) and standard deviation ratio (SDR) (Afonso et al., 2022) that must be greater than 2.5, for industrial purposes (Cortés et la., 2010; Tirado-Kulieva et al., 2022).

1.4.3 Non-invasive methods for kiwifruit quality assessment

Kiwifruit quality assessment based on non-destructive methods has been used to construct calibration models to predict various attributes: i) SSC through imaging spectroscopy (Martinsen & Schaare, 1998), dielectric spectroscopy (Ragni et al., 2012; Fazayeli et al., 2019), Vis-IR (Lee et al., 2012; Shibang, 2021), FT-IR (Chen & Han, 2012; Santagapita et al., 2016; Ciccoritti et al., 2019), IR (Arazuri et al., 2005), VisNIR-DRS (Schaare & Fraser, 2000; Mcglone et al., 2007; Moghimi et al., 2010; Li et al., 2017; Vieira et al., 2017; Afonso et al., 2022), NIR (Mcglone & Kawano, 1998; Mcglone et al., 2002a; Clark et al., 2004; Kim et al., 2018; Li et al., 2018; Lee et al., 2019), hyperspectral imaging (Guo et al., 2016; Zhu et al., 2017, Benelli et al., 2022; Ma et al., 2021), time and/or spatially resolved spectroscopy (Ma et al., 2022), integrating sphere measurements (Cheng et al., 2022; Tian et al., 2022b), color and fluorescence imaging (Nie et al., 2020); ii) firmness by a non-contact laser air-puff method (Mcglone & Jordan, 2000, mechanical measurements (Ragni et al., 2010; Blanke, 2013; Pourkhak et al., 2017; Goldberg et al., 2019), acoustic method (Javadi & Nassari, 2017; Tian et al., 2022b), dielectric spectroscopy (Ragni et al., 2012; Fazayeli et al., 2019), NIR (Mcglone & Kawano, 1998; Li et al., 2018), Vis-IR (Lee et al., 2012; Xiao & Li, 2022), FT-IR (Fu et al., 2007; Santagapita et al., 2016; Wang et al., 2022a), hyperspectral imaging (Zhu et al., 2017; Benelli et al., 2022), VisNIR-DRS (Vieira et al, 2017; Li et al., 2017; Afonso et al., 2022) and integrating sphere measurements (Cheng et al., 2022, Tian et al., 2022b); iii) dry-matter (DM) by NIR (Mcglone & Kawano, 1998; Clark et al., 2004; Kim et al., 2018), VisNIR-DRS (Mcglone et al., 2002b; Mcglone et al., 2007; Vieira et al., 2017; Afonso et al., 2022), FT-IR (Tang et al., 2010; Qiang et al., 2010; Santagapita et al., 2016; Ciccoritti et al., 2019) and integrated sphere measurements (Cheng et al., 2022); iv) juice pH, by dielectric spectroscopy (Fazayeli et al, 2019), VisNIR-DRS (Moghimi et al., 2010; Afonso et al., 2022) , hyperspectral imaging (Zhu et al., 2017; Ma et al., 2021) and hyperspectral fluorescence imaging (Wang et al., 2022c); v) titrable acidity (TA), by Vis-IR (Lee et al., 2012), VisNIR-DRS (Vieira et al., 2017; Afonso et al., 2022) and FT-IR (Ciccoritti et al., 2019); and vi) flesh colour, by VisNIR-DRS (Schaare & Fraser, 2000; Clark et al., 2004; Mcglone et al., 2007; Afonso et al., 2022).

1.5 Aims and chapters

The global aim of this thesis was to assess non-destructively whole fruit ripening of two different cultivars of kiwifruit, namely, the green-fleshed ‘Hayward’ and the yellow-fleshed ‘Jintao’, from on-tree, through storage and up to the eating-ripe phase, using VisNIR-DRS spectroscopy. The main focus was on the construction of calibration models to predict several internal quality attributes, such as pulp CIE Lab parameters L*, a* and b*, hue angle, chroma, firmness, dry matter, SSC, pH and titrable acidity, for ‘Jintao’ kiwifruit, a cultivar much less studied, sweeter, with a higher commercial value than ‘Hayward’, and which growth area is extending in Portugal.

To achieve this goal, the following questions needed to be answered:

- Which are the best IQA to assess ‘Jintao’ kiwifruit ripening?
- What pre-processes and wavelengths can ensure better performance models for each IQA?
- Can the use of average values instead of individual ones be a new approach to improve performance models?
- Are the models robust?
- Which variables have more impact in consumers’ perception to score general flavour?
- During storage, which IQA have a good correlation with reflectance spectra and at which wavelength?

These questions were answered along the following seven chapters comprised by this thesis:

Chapter 2 - Material and methods

Description of the fruit, orchards, equipment and methods applied throughout this work plan.

Chapter 3 - Ripening evolution of kiwifruit on-tree

The aim of this chapter was to assess the ripening progress of the yellow-fleshed kiwifruit 'Jintao' at two different orchards in a real-life situation of orchard monitoring, starting the measurement period as two months before harvest to late-harvest.

The data of this chapter would be the first step for the development of a non-destructive portable equipment, based on VisNIR-DRS, which can be further used in the field on-tree to determine harvest date, in an accurate and fast way, benefiting the kiwifruit chain production and marketing.

Chapter 4 - Non-destructive prediction models of ‘Jintao’ internal quality

The goal for this chapter was the construction of calibration models for ‘Jintao’ kiwifruit quality attributes, using data from two different orchards and a very complete set of IQA (L*, a* and b* from the CIELAB colour space, hue angle, chroma, firmness, DM, SSC, juice pH and TA) using, first, individual kiwifruit values and, then, a new approach, testing if average predictions could represent an improvement over individual ones and allow for an efficient follow-up of ripening. The reason for this is that individual fruit IQA are not relevant for the management of an orchard, particularly to make the decision of harvesting, which is done by considering average values. Consequently, average predictions could be of more interest than individual fruit predictions.

Besides these, since the literature about ‘Jintao’ kiwifruit is limited, the aim was also to select the quality parameters that better characterize this cultivar ripening, considering the models’ performance and their IQA evolution along time.

Chapter 5 – Validation of spectroscopic models

This chapter addresses the question of a truly external validation of ‘Jintao’ kiwifruit spectroscopic models with data acquired in the two orchards, along two years (2018 and 2019) and with two different spectrometers. The aim was to compare this method performance for predict SSC of ‘Jintao’ kiwifruit with the standard internal validation, using variable selection and orthogonal signal correction to improve the performance of the models, and do a calibration transfer.

This chapter will put to test the models' robustness.

Chapter 6 - Kiwifruit storage ripening follow-up

The aim of this chapter was to monitor the ripening in storage of the yellow-fleshed 'Jintao' and green-fleshed 'Hayward' kiwifruit, through organoleptic evaluations, destructive measurements and spectra acquisitions. This way, whole ripening process, since on-tree till eating-ripe phase, is followed.

This chapter intend to test the use of VisNIR-DRS spectroscopy to distinguish the chemical and physical changes that occur during kiwifruit ripening in cold storage and if there are good correlation values between their internal quality attributes and reflectance spectra and at which wavelength.

Chapter 7 – General conclusions and future perspectives

This chapter presents a synthesis of the results obtained in the previous chapters and also mention future perspectives.

Chapter 8 – References

The last chapter contains all the reports and sources cited in the thesis.

Chapter 2

Materials and methods

2.1 Orchards

2.1.1 ‘Jintao’ kiwifruit

Yellow-fleshed kiwifruit (*Actinidia chinensis* Planch ‘Jintao’) were harvested in two commercial orchards (Figure 2.1), namely, orchard 1 (41º39′ 23.6" N, 8º18′ 21.6" W) (Figure 2.2) and orchard 2 (41º38′ 58.2" N, 8º18′ 26.0" W) (Figure 2.3) located in Goães – Amares, Braga, Portugal.

Usually, yellow kiwifruit is harvested after reaching, in average, a flesh hue angle around 103 º (Costa et al., 2010). In Portugal that threshold is usually attained between the end of October and the beginning of November.

Figure 2.1: Aerial photographs of the two orchards of ’Jintao’ kiwifruit marketed by Frutas Douro ao Minho in Goães (Amares), Braga, Portugal. In the left: orchard 1. In the right: orchard 2. The yellow lines represent the borders of the orchards.

Figure 2.2: ‘Jintao’ kiwifruit orchard 1 located in Goães – Amares.

Figure 2.3: ‘Jintao’ kiwifruit orchard 2 located in Goães – Amares.

2.1.2 ‘Hayward’ kiwifruit

Green-fleshed kiwifruit (*Actinidia deliciosa* (A. Chev.) C.F. Liang et A.R. Ferguson) ‘Hayward’) were harvested also from two orchards (Figure 2.4), namely Carrazedo (41°37’46.9”N, 8°23’16.5”W) and Figueiredo (41°37’29.9”N, 8°19’47.5”W), located in Braga, Portugal.

Figure 2.4: Aerial photographs of the two orchards of ’Hayward’ kiwifruit marketed by Frutas Douro ao Minho in Braga, Portugal. In the left: Figueiredo. In the right: Carrazedo. The yellow lines represent the borders of the orchards.

2.2 Fruit orchard sampling

In 2018, fruit sampling started two months before the commercial harvest season and ended one week after it. For ‘Jintao’ kiwifruit, 7 and 8 samplings took place in August 2018 – November 2018 (Table 2.1) inn orchard 1 and in orchard 2, respectively. For ‘Hayward, 7 samplings took place in September 2018 – November 2018 (Table 2.2) in both orchards. In total, 375 ‘Jintao’ kiwifruit (200 in orchard 1 + 175 in orchard 2) and 350 ‘Hayward’ (175 in Carrazedo + 175 in Figueiredo) were collected and evaluated.

Table 2.1: Sampling dates in 2018 and respective days after full bloom (DAFB) of ‘Jintao’ kiwifruit orchards.

Orchard	Sampling date	DAFB
1	07/08/2018	91
2		
1	20/08/2018	104
2		
1	03/09/2018	118
2		
1	17/09/2018	132
2		
1	01/10/2018	146
2		
1	15/10/2018	160
2		
1	29/10/2018	174
2		
1	13/11/2018	189

Table 2.2: Sampling dates in 2018 and respective days after full bloom (DAFB) of 'Hayward' kiwifruit orchards.

Orchard	Sampling date	DAFB
Carrazedo **Figueiredo**	03/09/2018	90
Carrazedo **Figueiredo**	17/09/2018	104
Carrazedo **Figueiredo**	01/10/2018	118
Carrazedo **Figueiredo**	15/10/2018	132
Carrazedo **Figueiredo**	29/10/2018	146
Carrazedo **Figueiredo**	13/11/2018	161
Carrazedo **Figueiredo**	27/11/2018	175

In 2019, due to the “loss” of the spectroscopic equipment and consequent delay for its replacement, it was not possible to performed spectroscopic measurements during September. To compensate this unforeseen event, samplings were carried out weekly during October. 7 samplings were taken for 'Jintao' (Table 2.3) and 8 for 'Hayward' kiwifruit in September 2019 – November 2019 (Table 2.4). In total, 350 'Jintao' kiwifruit (175 in orchard 1 + 175 in orchard 2) and 400 'Hayward' (200 in Carrazedo + 200 in Figueiredo) were collected and evaluated, however, as explained above, only 250 'Jintao' and 300 'Hayward' kiwifruit spectra were acquired.

Table 2.3: Sampling dates in 2019 and respective days after full bloom (DAFB) of ‘Jintao’ kiwifruit orchards. * No spectroscopic measurements were performed.

Orchard	Sampling date	DAFB
1	03/09/2019*	112
2		
1	17/09/2019*	126
2		
1	09/10/2019	148
2		
1	15/10/2019	154
2		
1	23/10/2019	162
2		
1	29/10/2019	168
2		
1	12/11/2019	182
2		

Table 2.4: Sampling dates in 2019 and respective days after full bloom (DAFB) of 'Hayward' kiwifruit orchards. * No spectroscopic measurements were performed.

Orchard	Sampling date	DAFB
Carrazedo **Figueiredo**	03/09/2019*	101
Carrazedo **Figueiredo**	17/09/2019*	115
Carrazedo **Figueiredo**	09/10/2019	137
Carrazedo **Figueiredo**	15/10/2019	143
Carrazedo **Figueiredo**	23/10/2019	151
Carrazedo **Figueiredo**	29/10/2019	157
Carrazedo **Figueiredo**	12/11/2019	171
Carrazedo **Figueiredo**	27/11/2019	186

After harvest, kiwifruit temperature was determined with an infrared handheld digital thermometer EEM100 (Perel, Velleman, Belgium) and the VisNIR-DRS spectra acquired from each fruit. Then, all fruit were shipped to the laboratory, where complementary standard destructive measurements were made in the next day.

The flowchart for sampling and measurement procedures is described in the Figure 2.5.

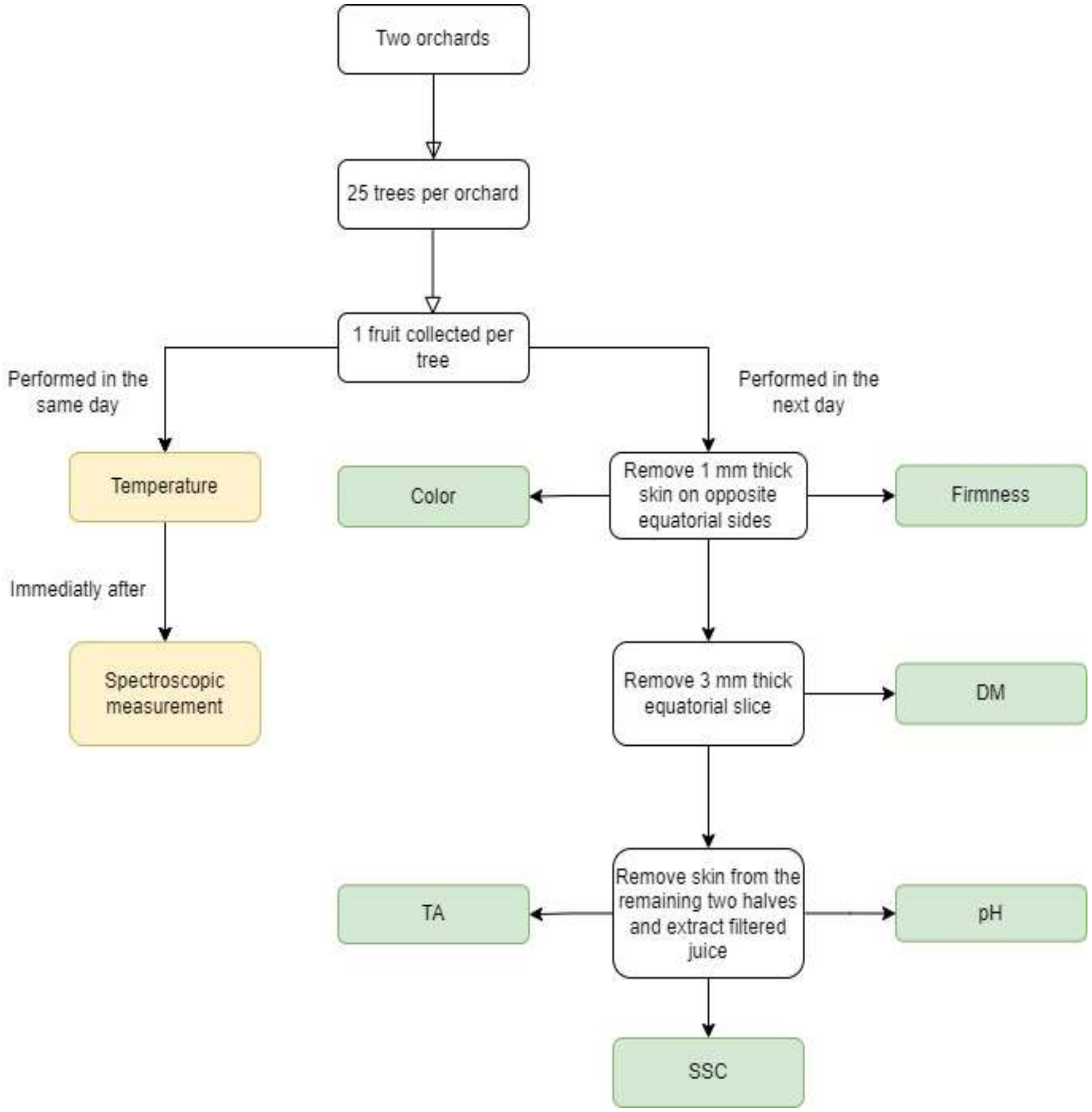

Figure 2.5: Flowchart for orchard sampling and measurements. These procedures were repeated for each orchard and for each sampling date.

2.3 Spectroscopy

The spectroscopy setup consisted of a VisNIR-DRS spectrometer USB4000 (Ocean Optics, USA), working in the range 345 – 1037 nm, a light source LS-1-LL (Ocean Optics, USA) and a bifurcated fiber with an interactance probe FCR-7UVIR400–2-BX/ME (Avantes, Netherlands). The probe works by sending light from the source to the sample through six illumination fibers and collecting the sample's reflection by a 7th fiber, in the center of the reflection probe, that is coupled to the spectrometer. The absolute reference material was a disk of Spectralon white surface (WS-1, Ocean Optics, USA), held at a constant height (0.47 mm) below the probe. The fruit to measure were introduced into a cup. The lid of the cup had a hole for the insertion of the probe and insured blocking of the sunlight during the spectroscopic measurements in a setup similar to the one described by Cavaco et al. (2018). The main difference was that three spectra were acquired, along the equatorial area of each kiwifruit, to improve the measurements' statistics.

Since October 2019, the spectrometer was replaced by an AvaSpec-Mini2048CL (Avantes, Netherlands), the light source by an AvaLight-HAL-S-Mini (Avantes, Netherlands) and the reference material by the WS-2 reference tile (Avantes, Netherlands).

2.4 Fruit quality attributes

The several quality attributes were measured following the sequence described in Figure 2.5.

First, a 1 mm thick skin was removed at both opposite equatorial sides of kiwifruit for measurements of pulp colour with a Minolta Chroma Meter CR-300 (Minolta, Japan) using the CIE L*a*b* space. The hue angle colour and chroma were calculated by the following equations (McGuire, 1992):

$$h^{o} = \arctan\left(\frac{b^*}{a^*}\right) \qquad (2.1)$$

$$C^* = \sqrt{a^{*2} + b^{*2}} \qquad (2.2)$$

Pulp firmness was determined by puncture with a texturometer (Chatillon TCD200, Digital Force Gauge DFIS 50, John Chatillon & Sons, Inc., USA) using a cylinder probe of 8 mm at a depth of 7 mm.

Then, 3 mm thick kiwifruit equatorial slices (1 per fruit) were cut, weighed and dried at 105 ºC until constant weight for determination of DM, expressed as percentage of dry weight relatively to fresh weight (%). The remaining of the kiwifruit were peeled and squeezed. The juice filtered by a cotton cloth was used for the measurements of SSC, pH and titratable acidity. SSC was determined by using a digital refractometer HI 96801 (Hanna Instruments, USA) and expressed as %. With a TitroLine 6000 (SI Analytics, Germany), juice pH and Total TA, expressed as mass percentage of citric acid per 100 mL juice (%), were determined using 2 mL kiwifruit juice diluted with 8 mL distilled water, and titrated with 0.1N NaOH until a pH of 8.2.

2.5 Fruit storage sampling

After the commercial harvest season, fruit were shipped to the University of Algarve, and stored therein at 0 ºC, normal atmosphere and relative humidity of 90 – 95 %.

To evaluate ripening during storage, sixteen fruit of each cultivar, were drawn every 15 days (Table 2.5 to Table 2.**10**). After being removed from the refrigerated chamber, their temperature was registered with an infrared handheld digital thermometer EEM100 (Perel, Velleman, Belgium) and the VisNIR-DRS spectra acquired from each fruit. Then, complementary standard destructive measurements were made in 8 fruit, of each cultivar. The remaining eight fruit were kept one week at room temperature to simulate commercial shelf-life. After this time, the VisNIR-DRS spectra were acquired again from each fruit and destructive measurements were performed.

The flowchart for storage sampling and measurement procedures is described in Figure 2.6.

Table 2.5: Storage sampling dates in 2018/2019 and respective storage days for ‘Jintao’ kiwifruit.

Sampling date	Storage Days
26/11/2018	25
10/12/2018	39
26/12/2018	55
14/01/2019	74
29/01/2019	89
12/02/2019	103
13/03/2019	132
27/03/2019	146

Table 2.6: Storage sampling dates in 2018/2019 and respective storage days for ‘Hayward’ kiwifruit.

Sampling date	Storage Days
10/12/2018	10
26/12/2018	26
14/01/2019	45
29/01/2019	60
12/02/2019	74
13/03/2019	103
27/03/2019	117
10/04/2019	131
23/04/2019	144
07/05/2019	158
21/05/2019	172

Table 2.7: Sampling storage dates in 2019/2020 and respective storage days for 'Jintao' kiwifruit.

Sampling date	Storage Days
04/12/2019	33
19/12/2019	48
02/01/2020	62
15/01/2020	75
29/01/2020	89
12/02/2020	103
26/02/2020	117
11/03/2020	131

Table 2.8: Sampling storage dates in 2019/2020 and respective storage days for 'Hayward' kiwifruit.

Sampling date	Storage Days
04/12/2019	19
19/12/2019	34
02/01/2020	48
15/01/2020	61
29/01/2020	75
12/02/2020	89
26/02/2020	103
11/03/2020	117

Table 2.9: Sampling storage dates in 2020/2021 and respective storage days for ‘Jintao’ kiwifruit.

Sampling date	Storage Days
26/10/2020	0
12/11/2020	17
26/11/2020	31
09/12/2020	44
22/12/2020	57
04/01/2021	70
18/01/2021	84
02/02/2021	99
15/02/2021	112
02/03/2021	127
13/04/2021	140

Table 2.10: Sampling storage dates in 2020/2021 and respective storage days for ‘Hayward’ kiwifruit.

Sampling date	Storage Days
12/11/2020	0
26/11/2020	14
09/12/2020	27
22/12/2020	40
04/01/2021	53
18/01/2021	67
02/02/2021	82
15/02/2021	95
02/03/2021	110
29/03/2021	137
13/04/2021	152

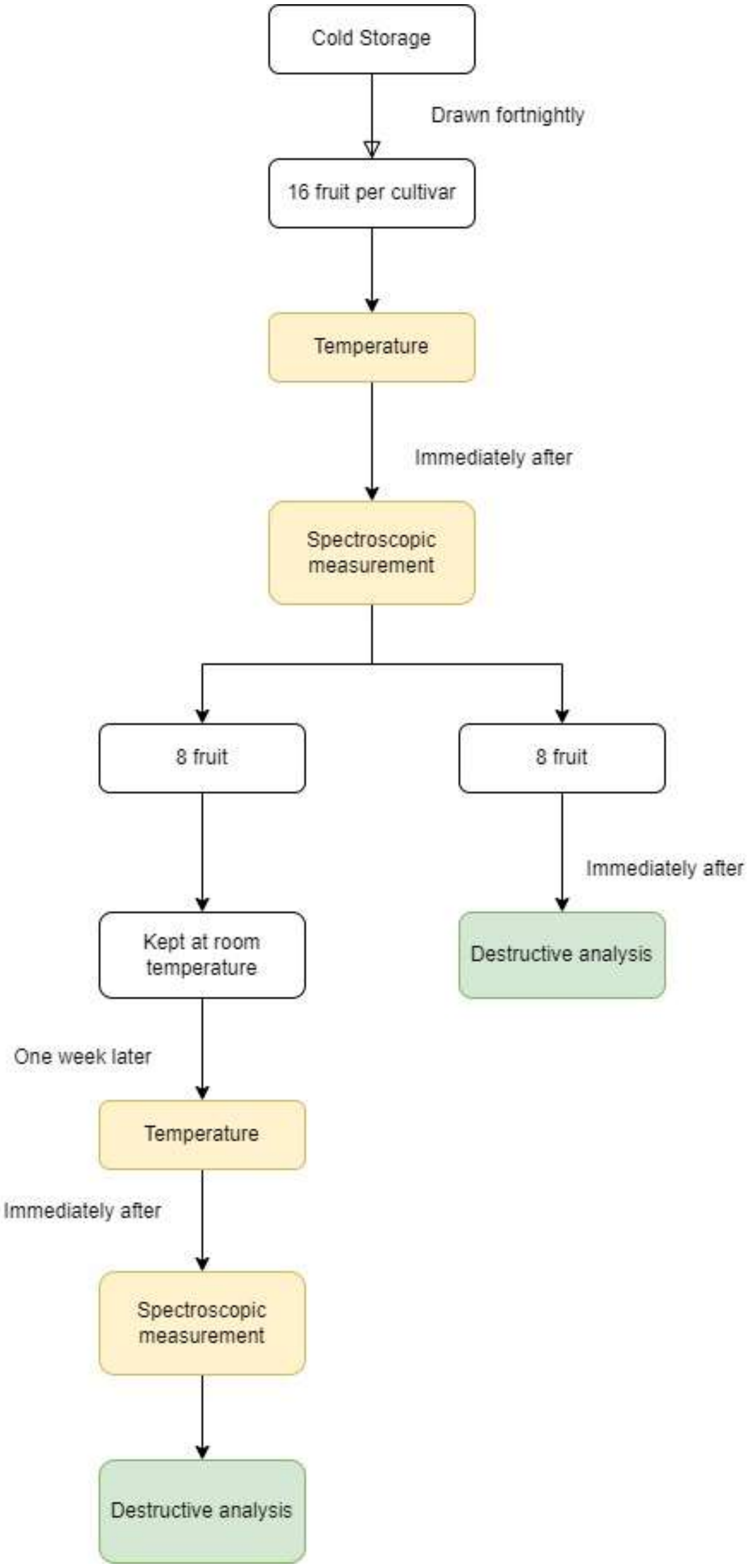

Figure 2.6: Flowchart for storage sampling and measurements. These procedures were repeated for each orchard and for each sampling date.

2.6 Sensory evaluation

A semi-trained panel, recruited from faculty staff and students, with 15 to 32 elements, did sensory evaluations based on a 7-point hedonic scale (1 = dislike extremely, 2 = dislike; 3= slightly dislike, 4 = neither like nor dislike, 5 = slightly like, 6 = like, 7 = like very much) (Gol et al., 2013), for the following parameters: fruit appearance, pulp appearance, aroma, texture, sweetness, acidity, and general taste. In general, all parameters were evaluated after 2.5 and 4.5 months of storage for 'Jintao' kiwifruit (Table 2.11) and after 2 and 4 months for 'Hayward' kiwifruit (Table 2.12). In 2020, 'Hayward' kiwifruit parameters were only evaluated once due to COVID-19 pandemic.

All fruit presented to sensory panellists were at room temperature.

Table 2.11: Dates and respective storage days at sensory evaluations of 'Jintao' kiwifruit.

	Date	Storage Days
2019	14/01/2019	74
	13/03/2019	132
2020	10/01/2020	75
	03/03/2020	131
2021	05/01/2021	70
	02/03/2021	127

Table 2.12: Dates and respective storage days at sensory evaluations of 'Hayward' kiwifruit.

	Date	Storage Days
2019	15/02/2019	74
	16/04/2019	131
	22/05/2019	172
2020	14/01/2020	61
2021	08/01/2021	53
	10/03/2021	123
	14/04/2021	152

2.7 Data analysis

2.7.1 Software

The descriptive statistical analysis of the quality attributes and sensory evaluation were performed in IBM SPSS Statistics 27 (IBM Corp., Armonk, NY, USA).

The multivariate data analysis was performed in MATLAB R2019a, version 9.6 (The MathWorks, Inc., Natick, MA, USA). Most of the functions and scripts were implemented in-house, including the PLS regression through the NIPALS algorithm, available in Andersson (2009), the calculation of the VIP scores, according to Farres et al. (2015) and the pre-processing and variable selection procedures (used in chapter 5). PLS Toolbox (PLS Toolbox, version 8.7, Eigenvector Research, Inc., Manson, WA, USA) was used to supply specific functions: the Savitzky-Golay filter (Savitzky & Golay, 1964) function savgol, the Orthogonal Signal Correction, implemented through the functions osccalc and oscapp, and the Kennard-Stone algorithm.

2.7.2 Data analysis in chapter 3

The nonparametric multivariate Kruskal-Wallis (MKW) test was used to compare the dependent variables in each orchard. The effects of orchard and date on each of the quality parameters were tested by a full factorial MANOVA (type III) and further multi-comparisons among variables were performed by the Bonferroni test for a significance level of $p < 0.05$ (Oja, 2010).

2.7.3 Data analysis in chapter 4

Calibration models were obtained for the following quality attributes: L*, a* and b* from the CIELAB colour space, hue angle, chroma, firmness (N), dry matter % (W/W), soluble solids content (%), juice pH and titratable acidity (%).

The analysis performed in chapter 4 is based on the first year only. Therefore, there are only two independent datasets for ‘Jintao’, one for each orchard. They were divided into two subsets of different trees (trees 1 to 12 in the first subset and trees 13 to 25 in the second subset).

Data modelling was performed in two ways. The first approach was the usual development of calibration models for the various quality attributes and subsequent validation on independent individual fruit. The second approach was to use those models to perform the prediction of average quality attributes for each orchard and each day. PLS models were obtained using all data from both orchards and from all measurement days.

2.7.3.1 Spectroscopic signal to noise ratio

The signal-to-noise ratio (SNR) calculation was performed on R, the reflectance matrix. Each line of R is a spectrum $R_i(\lambda)$ ($i = 1, \ldots, M$ = number of fruit). The following steps were taken:

1) Smoothing of each line of R by a Savitzky-Golay filter (denoted SG (width, order)) of 81 points and second polynomial order, $S_i(\lambda) = SG(R_i(\lambda), 81, 2)$.

2) Calculation of the squared fluctuations (around the baseline) for each spectrum: $F_i^2(\lambda) = (R_i(\lambda) - S_i(\lambda))^2$.

3) The noise level at each wavelength was calculated by assuming that the fluctuations on the 40 closest neighbours are equivalent to those that would be observed in 40 repetitions at the same wavelength (time fluctuations) as $n_i(\lambda) = \sqrt{SG\ (F_i^2(\lambda), 41, 0)}$.

4) SNR for each spectrum was calculated by $SNR_i(\lambda) = S_i(\lambda) / n_i(\lambda)$.

5) The final noise figure was calculated from the average of all fruit: $SNR(\lambda) = \Sigma_i\, SNR_i(\lambda) / M$.

2.7.3.2 Pre-processing

The pre-processing step included three different procedures: elimination of hot pixels, transformations and elimination of outliers. Hot pixels were identified visually, and their counts substituted by the mean value of the two adjacent pixels. The transformations of spectra used were absorbance (log (1/R)), standard normal variate transformation (SNV) (Barnes et al., 1989) and the Savitzky-Golay filter (Savitzky and Golay, 1964), either for smoothing or derivation (first and second derivatives). Combinations of these transformations were also performed. The spectral range was also tested, from the full spectrometer range, 345 – 1037 nm, to subranges obtained by varying systematically the upper and lower limits. Outlier samples were detected and rejected. Three types of outliers were considered: i) when the norm of the transformed spectra diverges from the average norm more than 3 standard deviations (3σ outliers); ii) 3σ outliers in the PLS scores of the calibration samples; iii) 3σ outliers in the PLS projected scores of the validation samples.

2.7.3.3 Cross-validation

In chapter 4, data from each orchard was divided in two subsets according to the number of the tagged tree (trees 1 – 12 assigned to the first subset and trees 13 – 25 to the second subset). The whole data was subjected to a 4 × 5-fold double (or nested) cross-validation (CV) as shown in Figure 2.7.

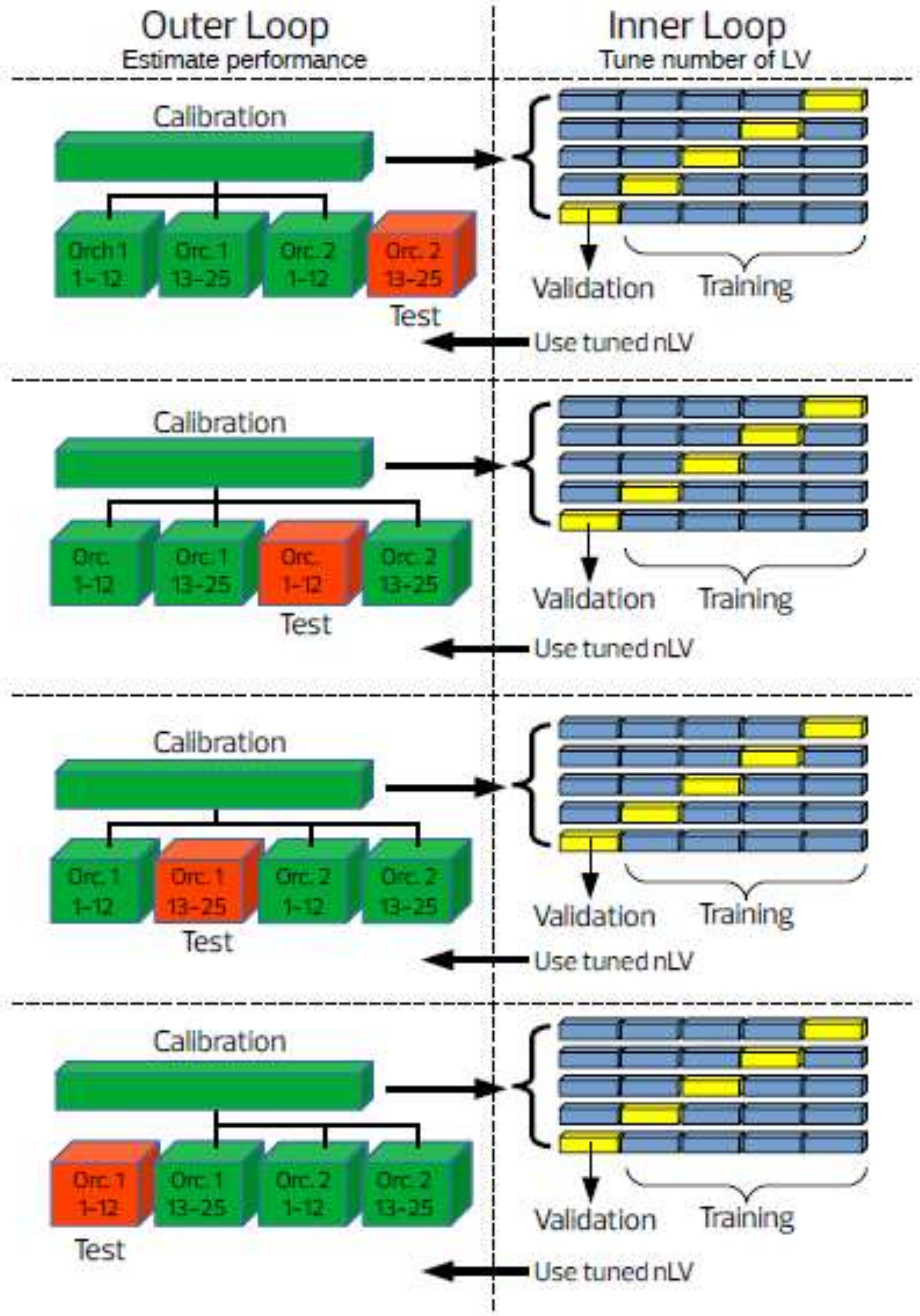

Figure 2.7: Illustration of the 4 x 5-fold double (or nested) cross-validation (CV) performed in chapter 4. The process consists of an outer loop of 4 segments (corresponding to the 2 orchards x 2 subsets) and an inner loop of 5 splits. (Source: Afonso et al., 2022).

The nomenclature and the pseudo-code are described in Filzmoser et al. (2009), except that there was no repetition (a single run was performed):

- Each segment (i = 1, 2, 3, 4) is taken at a time as test set, and the remaining three aggregated as calibration set (outer loop).
- CV is performed in each calibration set i. First, it is divided in 5 splits (Venetian blinds, in this work). Then, each split (j = 1, 2, 3, 4, 5) is taken at a time as validation set and the remaining four are aggregated as training set (inner loop). The optimal number of latent variables, $nLV_{opt}\ (i)$ is obtained and the corresponding PLS model built from the entire calibration set i.
- The i-th PLS model is applied to the i-th test set.
- A global statistic is calculated from the four test sets.

2.7.3.4 Statistical parameters characterizing model's performance

The performance of the models was characterized by the parameters (Nicolaï et al., 2007):

1. The squared correlation coefficient (R^2);
2. Root mean square of error in prediction (RMSEP) that is given by

$$\text{RMSEP} = \sqrt{\frac{1}{n_{val}} \sum_{i=1}^{n_{val}} \left(y_{val,i} - \hat{y}_{val,i} \right)^2}\ , \qquad (2.3)$$

where $y_{val,i}$ stands for the validation true values (reference destructive data), $\hat{y}_{val,i}$ for the corresponding predictions and n_{val} is the number of validation samples;

3. Standard deviation ratio (SDR)

$$\text{SDR} = \frac{\sigma\ (y_{val})}{RMSEP} = \frac{RMSEP\ if\ all\ predictions = < y_{val} >}{RMSEP}\ , \qquad (2.4)$$

where σ (y_{val}) is the standard deviation of the validation true values. The first equality is the usual definition. The second equality was inserted deliberately to compare SDR with PG (below).

4. The bias represents the average prediction offset and is given by

$$\text{Bias} = < \hat{y}_{val} > - < y_{val} > , \tag{2.5}$$

where $< \hat{y}_{val} >$ represents the average of the predictions for the validation set.

5. Slope is the slope of the linear regression $\hat{y}_{val}$ vs. y_{val}

The same parameters in the steps of cross-validation and calibration are represented with a different ending:

- Cross-validation (cv): R^2_{cv}, RMSECV, SDR_{cv}, $bias_{cv}$ and $slope_{cv}$;
- Calibration (c): R^2_c, RMSEC, SDR_c, $bias_c$ and $slope_c$.

2.7.3.5 Statistical parameters characterizing model's performance for daily average predictions

The average and standard deviation of the reference quality attributes values and their corresponding predictions were calculated for each day and orchard, resulting in a dataset of 8 or 7 pairs of values (average prediction, average reference value) for both orchards. The prediction statistics were calculated from these pairs of values, specifically, RMSEP, R^2, bias and SDR. Furthermore, the average predictions were compared with the average reference measurements through a t-test.

2.7.4 Data analysis in chapter 5

In chapter 5, a detailed study of the external and internal validation in two years is made. As already mentioned, there was an additional problem related to the loss of the spectrometer at the beginning of the second year. This made the validation process even more complicated, as it implied also a calibration transfer between the two instruments. It was, therefore, a problem of validation in two orchards, two years and two spectrometers, which corresponds to the most difficult real case to deal with.

2.7.4.1 The design of internal and external validations

In chapter 5, there was the inclusion of another year and the total of datasets was four. This allowed to perform strict external validation:

1) Calibrate with datasets 1, 2 and 3; validate with dataset 4;
2) Calibrate with datasets 1, 2 and 4; validate with dataset 3;
3) Calibrate with datasets 1, 3 and 4; validate with dataset 2;
4) Calibrate with datasets 2, 3 and 4; validate with dataset 1.

The statistical parameters presented in context of external validation represent averages of the four results, obtained for each one of the branch validations: p = (p1 +p2 +p3 +p4) =4, where p represents any statistical parameter, such as RMSEP, SDR or R^2 (see Section 2.7.3.4).

The standard internal validation was also performed in order to compare the performance of both methods and highlight the true difficulty of applying the calibration models to new, independent, datasets. In chapter 5, standard validation joins the four original datasets into a single one. Then, the data split is performed in such a way that calibration and validation subsets have the same statistical properties in terms of average and standard deviation. This is often done in an optimal way through the Kennard-Stone (KS) algorithm (Kennard, 1969), or simply by sub sampling the full dataset at equal steps. The last method, however, generally delivers sub optimal results. Therefore, the KS method was the preferred one to perform internal validation.

Standard internal validation tends to give much better results than external validation for obvious reasons. In the latter, spectral characteristics of the validation set may not be well represented in the calibration set, while in the former, homogeneity of the two sets usually insures a much better performance of the calibration model in the validation set.

The internal and external validation schemes used in chapter 5 are represented in Figure 2.8.

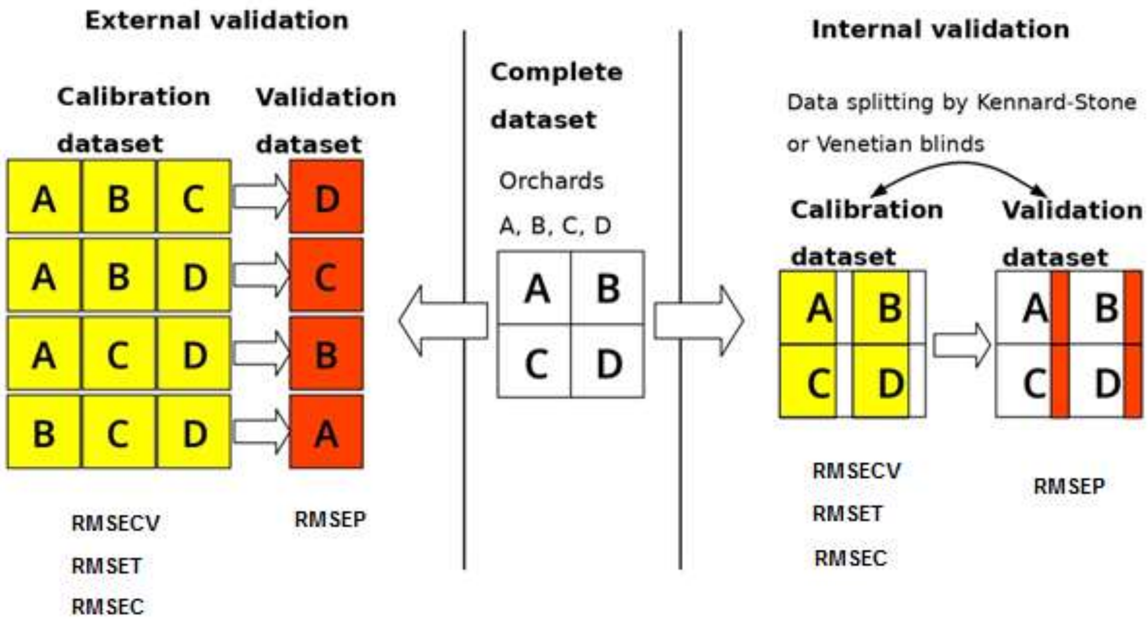

Figure 2.8: The two validation schemes used in this chapter. On the left: external validation. On the right: standard internal validation. The four datasets available are represented as A, B, C and D. In external validation, three datasets are used for model calibration (in yellow) and the remaining one is left for validation (in red). In the standard internal procedure, a specific percentage of the samples (usually 70 % - 80 %) is used for calibration (the fraction of A, B, C and D assigned to yellow) and the remaining are used for validation (the fraction of the datasets in red).

2.7.4.2 Selection of the best pre-processing

Selection of the best pre-processing method is essential to insure optimal results. It is often unclear in the literature if the optimization process uses the correct cost function. Choosing the pre-process in order to minimize RMSEP is a wrong procedure that could be described in ordinary terms as "cheating". In real situations the validation dataset is unknown *a priori*. Therefore, a realistic optimization procedure cannot be based on the knowledge of RMSEP, which is equivalent to tune a model to the desired result. Instead, the optimization process must be based on Root-mean-square of error of cross-validation (RMSECV), which is the correct measure of the available information. The pre-processing yielding the lowest value of RMSECV is also the most plausible choice. It is very common to find that the best RMSECV does not produce the best RMSEP; and that to the best RMSEP corresponds a mediocre value of RMSECV. In the first case, this is a consequence of the fact that the calibration model does not capture the entire variability of the data and may fail, at least partially, upon validation. In the second case, a mediocre RMSECV and a good RMSEP is generally a matter of chance. The calibration model happens to explain well the validation set variability, but in the presence of a new one, it would probably fail. The choice based on RMSECV, on the other side, has more chances to survive new validations against successive validation datasets, although without the optimal results that always happen by chance.

In this work, one more criterion is introduced in order to improve the choice of the best pre-processing. In order to do that, a refinement of the calibration process has been introduced. This is explained in Figure 2.9.

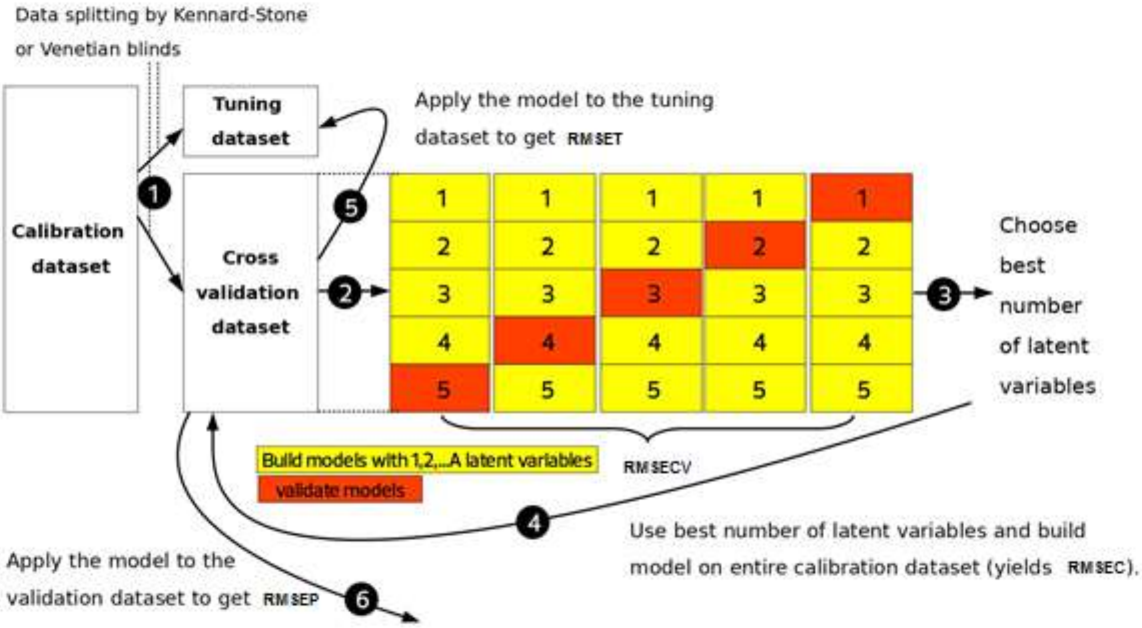

Figure 2.9: The calibration process. The calibration dataset is divided in tuning and cross-validation subsets (step 1) through the KS algorithm. The cross-validation subset is split in 5 subsets (1 to 5, step 2), through the Venetian Blinds method. These subsets are used to determine the best number of latent variables, through the process of 5-fold cross-validation (step 3), which delivers RMSEC. At each step of CV, the models are built with the yellow subsets and the prediction on the red. The selected number of latent variables is then used to build a model in the entire cross-validation subset (step 4) and to calculate RMSEC. This model is then applied to the tuning dataset, to obtain RMSET (step 5) and to the external validation dataset, to get RMSEP (step 6).

The calibration dataset is divided in tuning and cross-validation subsets (step 1, in the figure). Again, KS or Venetian Blinds may be used to split the data, and KS was chosen. The cross-validation subset is split in 5 subsets (1 to 5, step 2), through the Venetian Blinds method. These subsets are used to determine the best number of latent variables, through the process of 5-fold cross-validation (step 3), which delivers RMSECV as a function of the number of latent variables. This is chosen by identifying the point of 95% drop of RMSECV (not its absolute minimum, which is the most common approach). Several tests showed that this criterion is more conservative in terms of the latent variables number and tends to generalize slightly better in validation. The selected number of latent variables is then used to build a model in the entire cross-validation subset (step 4) and to calculate RMSEC. This model is then applied to the tuning dataset, to obtain RMSET (root mean square of error in tuning - step 5) and to the external validation dataset, to get RMSEP (step 6).

The value of RMSET, together with the associated SDR value (SDRt), are used to improve the pre-processing optimization. The basic idea is that RMSET should not exceed RMSECV by a small margin, called here tolerance (tol), whose absolute value depends on the parameter under study. For SSC the tolerance is 0.05%:

$$RMSET < RMSECV + tol \tag{2.6}$$

This condition insures a good consistency between cross-validation and validation in the tuning set. However, the y-ranges of the two datasets may differ and SDR is an auxiliary parameter that allows to perform dimensionless comparison. Accordingly, another condition has been set:

$$|\, SDRcv - SDRt \,| < 0.2, \tag{2.7}$$

where $SDRcv = \frac{std\ (Y_{cv})}{RMSECV}$, $SDRt = \frac{std\ (Y_t)}{RMSET}$ and Y_{cv}, Y_t are the measured values for the quality parameter under study, for the CV and tuning datasets, respectively.

Having these two conditions in mind, the selected pre-processing transformation is the one with lower RMECV among all that satisfy (2.6) and (2.7). The selection algorithm is shown in Table 2.13.

Table 2.13: Algorithm for selecting best pre-processing.

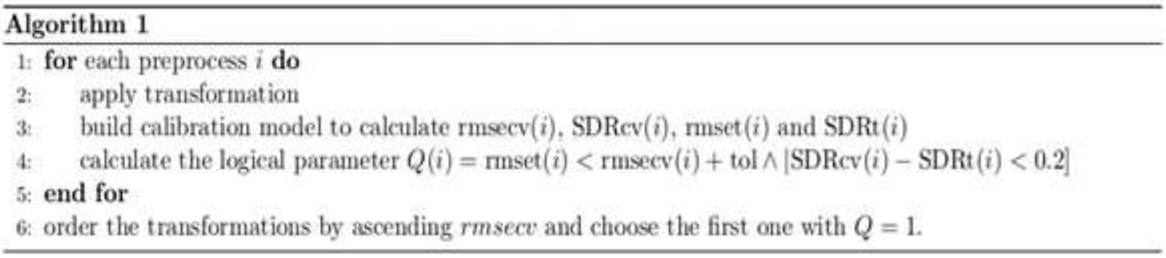

Algorithm 1

```
for each preprocess $i$ do
    apply transformation
    build calibration model to calculate rmsecv($i$), SDRcv($i$), rmset($i$) and SDRt($i$)
    calculate the logical parameter $Q(i) = \mathrm{rmset}(i) < \mathrm{rmsecv}(i) + \mathrm{tol} \wedge |\mathrm{SDRcv}(i) - \mathrm{SDRt}(i) < 0.2]$
end for
order the transformations by ascending $rmsecv$ and choose the first one with $Q = 1$.
```

2.7.4.3 Three optimization schemes for the selection of best pre-processing

It would be impossible top test all the possible transformations. Therefore, three modes of optimization were adopted in parallel, and the choices of each one of these modes were then used in the subsequent calculations. The three modes are as follows:

1) **MIX Mode:** Using different types of transformations in the fixed wavelength range 450 nm to 1010 nm, chosen only based on visual observation of the spectra and the appearance of noise in the lower and upper ends of the range.
2) **SNV Mode**: Using only the absorbance followed by SNV transformation, but on a variable range, being the range what is optimized.
3) **SG Mode**: Using only the absorbance followed by the Savitzky-Golay derivation transformation, with variable range and filter width (repeated twice, one run for polynomial order = 2 and derivative order = 1 and the another for polynomial order = 4 and derivative order = 2). In practice, polynomial order and derivative orders are fixed and the filter width and the spectral range are optimized.

The first scheme (MIX Mode) allows to test the general type of transformation that may work better, while the other two (SNV and SG Modes) use the most used transformations but tuned in wavelength range and filter width. The complete description of transformations used in MIXed Mode is shown in Table 2.14.

Table 2.14: List of transformations used for pre-processing optimization in the MIX Mode. Abbreviations for the parameters tested: d = derivative order, g = gap, s = segment, w = filter width. Notes: [1] CR has been applied within the pigments wavelength range: 550-750 nm. [2] r is the wavelength range, that is, 560 nm. [3] By ”diff” it is meant the subtraction of adjacent points. This operation was applied once (diff) or twice (diff^2). [4] The Kubelka-Munk transformation is given by $z = (1 - R)^2/2R$. [5] LNSV, also known as Piece-wise SNV, is a moving window SNV. [6] The Savitzky-Golay filter is kept fixed, with width = r/16, polynomial order 2 and derivative order 1. [7] Normalization to the area, to the interval [0,1], and to the maximum value. [8] Only first derivative order in SG. [9] The derivative order is also varied between 1 and 2. [10] Raw data is simply the reflectance.

Transformation	Parameters varied	Range of variation	Notes
absorbance (abs)			
Continuum Removal (CR)			[1]
Kubelka-Munk (KM)			[4]
abs + Local SNV (LSNV)	w	$w=r/2^n$, n=1:6	[2,5]
abs + Savitzky-Golay (SG)	w and d	$w=r/2^n$, n=1:6; d=1,2	
SNV			
abs + CR			[1]
abs + SNV			
abs + smooth + diff	w and d	$w=r/2^n$, n=1:6; d = 1:2	[2,3]
abs + smooth + diff + SNV	w	$w=r/2^n$, n=1:6	[2,3]
KM + SNV			
abs + LNSV + SG 1/16	w	$w=r/2^n$, n=1:6	[2,6]
abs + normalizations			[7]
abs + norm01 + smooth + diff	w	$w=r/2^n$, n=1:6	[2]
abs + norm01 + SG	w	$w=r/2^n$, n=1:6	[2,8]
abs + Norris Derivative	g, s and d	$g=r/2^n$, n=4:5; $s = r/2^n$, n=5:7; d =1:2	[9]
raw data			[10]
abs + SG + SNV	w and d	$w=r/2^n$, n=1:6; d=1,2	

2.7.4.4 Variable selection

The variable selection adopted in chapter 5 is a MIXed formulation, using two criteria simultaneously, one for the regression vector, and another for the VIP scores. The basic idea for the regression vector criteria is that uninformative variables will tend to have a regression coefficient close to zero. Suppose the cross-validation step is performed N times, each time with a different subset chosen randomly from the entire dataset. The N cross-validations give N regression vectors. If λ_{un} is a wavelength without any information relevant to the model, then the corresponding regression coefficient, b (λ_{un}), takes N values arbitrarily distributed around zero. The criterion to select a variable was an extreme application of this principle: to select only the variables which have always the same sign of b (λ) for all the N calibration runs. This means that the contribution given by that specific variable to the model is consistent across the N runs, being always positive or always negative. On the contrary, a variable with positive and negative regression coefficients brings some uncertainty to the model, since sometimes it contributes in one direction, and other times it contributes in the opposite direction. The selection based in the VIP scores is yet simpler, since retain only those variables with VIP > 0.8. The VIP threshold is usually 1, but, given the low correlation of the spectra with SSC, imposing this limit would result in an excessive elimination of variables. The process of variable selection, as described, in iterated until no more improvement in RMSECV is observed. The application of variable selection in IV and EV have slight differences, and they are explained in the following two subsections.

2.7.4.4.1 Variable selection in IV

The algorithm for variable selection in internal validation, adopted here, is described in Table 2.15. In the end of the algorithm, the last iteration successful in lowering RMSECV is kept, together with all model parameters and variables, as well as the retained wavelengths. The validation has been performed at the same time (although it had no influence whatsoever in the variable selection). Therefore, the algorithm delivers simultaneously the selected wavelengths and the validation results.

Table 2.15: Algorithm for variable selection in internal validation

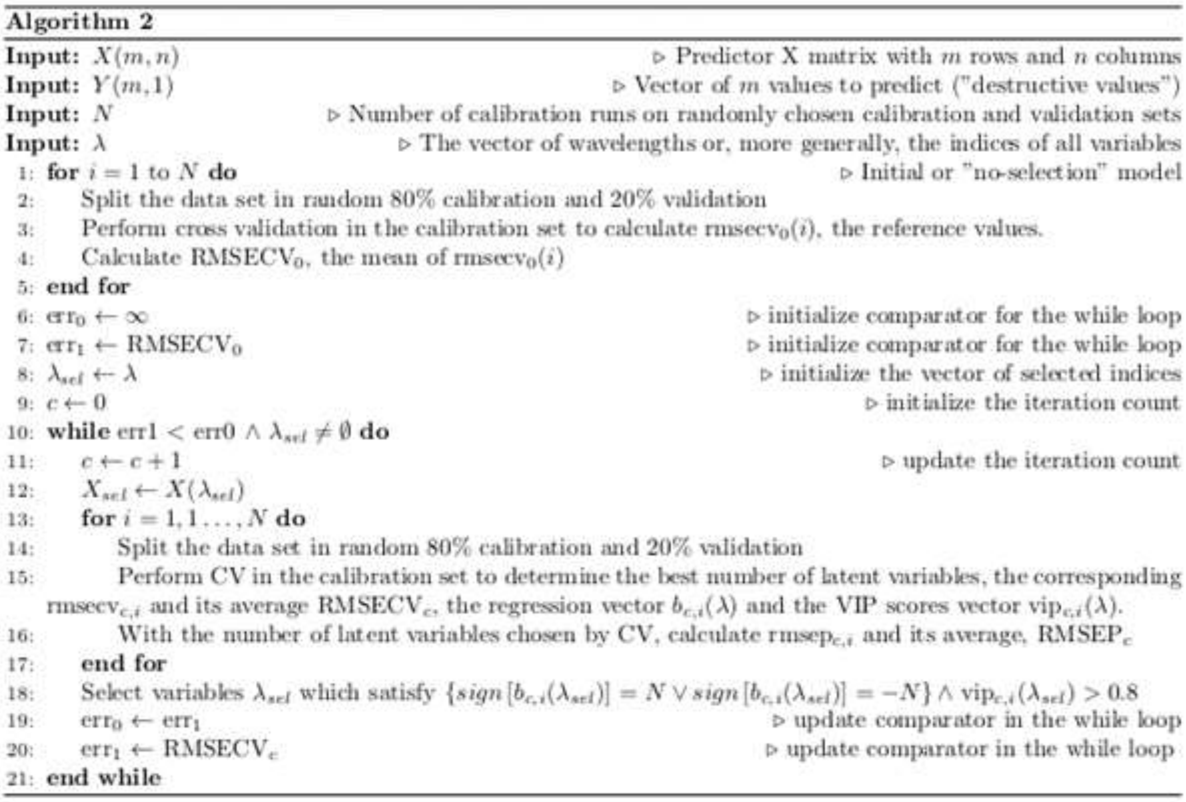

```
Algorithm 2
Input: $X(m,n)$                ▷ Predictor X matrix with $m$ rows and $n$ columns
Input: $Y(m,1)$                ▷ Vector of $m$ values to predict ("destructive values")
Input: $N$                     ▷ Number of calibration runs on randomly chosen calibration and validation sets
Input: $\lambda$               ▷ The vector of wavelengths or, more generally, the indices of all variables
 1: for $i = 1$ to $N$ do                                  ▷ Initial or "no-selection" model
 2:     Split the data set in random 80% calibration and 20% validation
 3:     Perform cross validation in the calibration set to calculate $\mathrm{rmsecv}_0(i)$, the reference values.
 4:     Calculate $\mathrm{RMSECV}_0$, the mean of $\mathrm{rmsecv}_0(i)$
 5: end for
 6: $\mathrm{err}_0 \leftarrow \infty$                     ▷ initialize comparator for the while loop
 7: $\mathrm{err}_1 \leftarrow \mathrm{RMSECV}_0$          ▷ initialize comparator for the while loop
 8: $\lambda_{sel} \leftarrow \lambda$                    ▷ initialize the vector of selected indices
 9: $c \leftarrow 0$                                       ▷ initialize the iteration count
10: while $\mathrm{err1} < \mathrm{err0} \wedge \lambda_{sel} \neq \emptyset$ do
11:     $c \leftarrow c + 1$                               ▷ update the iteration count
12:     $X_{sel} \leftarrow X(\lambda_{sel})$
13:     for $i = 1, 1 \ldots, N$ do
14:         Split the data set in random 80% calibration and 20% validation
15:         Perform CV in the calibration set to determine the best number of latent variables, the corresponding
    $\mathrm{rmsecv}_{c,i}$ and its average $\mathrm{RMSECV}_c$, the regression vector $b_{c,i}(\lambda)$ and the VIP scores vector $\mathrm{vip}_{c,i}(\lambda)$.
16:         With the number of latent variables chosen by CV, calculate $\mathrm{rmsep}_{c,i}$ and its average, $\mathrm{RMSEP}_c$
17:     end for
18:     Select variables $\lambda_{sel}$ which satisfy $\{sign\,[b_{c,i}(\lambda_{sel})] = N \vee sign\,[b_{c,i}(\lambda_{sel})] = -N\} \wedge \mathrm{vip}_{c,i}(\lambda_{sel}) > 0.8$
19:     $\mathrm{err}_0 \leftarrow \mathrm{err}_1$           ▷ update comparator in the while loop
20:     $\mathrm{err}_1 \leftarrow \mathrm{RMSECV}_c$        ▷ update comparator in the while loop
21: end while
```

2.7.4.4.2 Variable selection in EV

Consider the example where calibration is performed in the datasets 1,2 and 3, and validation performed in dataset 4. The algorithm described above is applied only to the aggregate 1+2+3. Therefore, the calibration dataset (1+2+3) is split into cross-validation dataset (= random 80% of 1+2+3) and tuning dataset (= the remaining 20% of 1+2+3). Therefore, the designations “calibration set” and “validation set”, in internal validation, correspond to “CV set” and “tuning set”, in external validation (EV). The process follows as described in Algorithm 2, except that the condition that triggers the WHILE loop is performed on RMSET (corresponding to the predictions on the tuning set). Line 7 becomes

$$\mathrm{err1} \leftarrow \mathrm{RMSET}_0, \qquad (2.8)$$

where RMSET0 is the initial, no variable selection, RMSET value. Also, line 20 becomes

$$\mathrm{err1} \leftarrow \mathrm{RMSET_C}. \qquad (2.9)$$

After the iteration process is finished, the new model is applied to the validation set (in this example, the dataset 4).

2.7.4.5 Orthogonal Signal Correction

Orthogonal Signal Correction (OSC) is a technique developed by Wold and co-workers (Wold et al., 1998) in order to remove from the spectral matrix, X, only the part that is unrelated to Y. This was made by ensuring that the removed part is mathematically orthogonal to the block Y, or as close to orthogonal as possible. Here, by “orthogonal" one should understand “whose variation does not affect Y". The variance in the X block that is orthogonal to Y is identified as some number of factors, described as components. This represents another form of pre-processing. It is calibrated on some dataset and then can be applied to a new one. In that case, the same directions (orthogonal to Y) are removed from the new data prior to applying the model. The idea behind the application of OSC is to remove unwanted - and hence noisy - information in the spectral data relatively to the Y quantity to measure. If successful, this removal should improve the PLS model built on the “deflated" matrix.

Here, the functions osccalc and oscapp of the PLS Toolbox (PLS_Toolbox 9.0, 2021) are used to calculate the OSC in the calibration dataset (osccalc) and to apply it to the validation dataset (oscapp). There are three settings for the OSC pre-processing method: number of components, number of iterations, and tolerance level. The number of components defines how many times the entire process will be performed and is equivalent to the number of components in PCA. In general, two components are sufficient, as prescribed in (Wold et al., 1998). However, we have fixed that number in three, due to the low correlation of the data. The number of iterations defines how many cycles will be used to the orthogonality to Y as good as possible. This was chosen to be 5, to avoid overfit. Finally, the tolerance level defines the percent variance that must be captured by the PLS model(s), developed within the process of orthogonalization. The default for this parameter in PLS toolbox is

99.9 %, but here it was lowered to 80%, by the same reason, the low correlation of the data and the possibility of overfit. The procedure in this section is simple: OSC is applied to the calibration data, X_{cal}, Y_{cal}, and then a PLS model is built between the calibration $X_{cal}^{(1)}$ (the X_{cal} matrix with the orthogonal-to-Y part removed) and Y_{cal}. The correction is then applied to the validation X_{val}, to obtain $X_{val}^{(1)}$and the model is applied to the latter.

2.7.4.6 Calibration transfer procedure

In what follows it will be adopted the terminology "master" for the base instrument and "slave" for the one to which the model is wanted to be transferred.

A approach based on a normalization to daily averages was performed. Extrapolating the concept of calibration transfer between instruments, this procedure effectively does calibration transfer between orchards as well. In this extended view, "master" and "slave" become specific sets of data, acquired for a given spectrometer, in a given year, in a given orchard. Hence, the most comprehensive set of acquisition dates is defined as the master, $M_{ij}(\lambda)$, which in this case is Orchard 1/2018, and the remaining as slave, $S_{ij}^{(k)}(\lambda)$, k = 1; 2; 3:

$M_{ij}(\lambda), i$ = 1, 2, … 8 (days); j = 1, 2, … 25 (fruit), [Orchard 1/ 2018] (2.10)

$S_{ij}^{(1)}(\lambda), i$ = 1, 2, … 7 (days); j = 1, 2, … 25 (fruit), [Orchard 2/ 2018] (2.11)

$S_{ij}^{(2)}(\lambda), i$ = 1, 2, … 5 (days); j = 1, 2, … 25 (fruit), [Orchard 1/ 2019] (2.12)

$S_{ij}^{(3)}(\lambda), i$ = 1, 2, … 5 (days); j = 1, 2, … 25 (fruit), [Orchard 2/ 2019] (2.13)

For both the master and slave data, the average values of the spectra acquired on each day of measurements are calculated (the average of the 25 spectra acquired in each measurement session in an orchard), yielding $\overline{M_\iota}(\lambda)$ and $\overline{S_\iota}\ (\lambda)$.

$\overline{M_\iota}(\lambda),\ i$ = 1, 2, … 8 (days), [Orchard 1/2018] (2.14)

$$\overline{S_i^{(1)}}\,(\lambda),\ \ i = 1, 2, \ldots 7 \text{ (days), [Orchard 2/2018]} \qquad (2.15)$$

$$\overline{S_i^{(2)}}\,(\lambda),\ \ i = 1, 2, \ldots 5 \text{ (days), [Orchard 1/2019]} \qquad (2.16)$$

$$\overline{S_i^{(3)}}\,(\lambda),\ \ i = 1, 2, \ldots 5 \text{ (days), [Orchard 2/2019]} \qquad (2.17)$$

There is a mismatch between the 2018 and the 2019 DAFB. For example, the second acquisition day in 2019 was 154 DAFB, but the closest corresponding days in 2018 are the fifth (146 DAFB) and the sixth (160 DAFB). The master for the 2nd day of 2019 is thus calculated as a linear combination of the 5th and 6th days. Therefore, it corresponds to a “synthetic" master, $\overline{M_i^{(2)}}\,(\lambda)$, calculated for the 2019 slaves. In this example,

$$\overline{M_2^{(2)}}\,(\lambda) = \frac{160-154}{160-146}\,\overline{M_5}(\lambda) + \frac{154-146}{160-146}\,\overline{M_5}\,(\lambda) \qquad (2.18)$$

Similar calculations were performed for the other days in 2019. The day index in the synthetic master corresponds to the day in the slave. Even for G2/2019, the DAFB are the same, except there is no 8th day, as in the master, and therefore a synthetic master is also defined. Generally, it is represented as $\overline{M_i^{(k)}}$, where k = 1, 2, 3 represents the three slave datasets and i represents the days.

The next step is to calculate the ratios and the differences between the averages:

$$R_i^{(k)}\,(\lambda) = \frac{\overline{M_i^{(k)}}\,(\lambda)}{\overline{S_i^{(3)}}\,(\lambda)} \qquad (2.19)$$

$$D_i^{(k)}\,(\lambda) = \overline{M_i^{(k)}}\,(\lambda) - \overline{S_i^{(k)}}\,(\lambda) \qquad (2.20)$$

The idea is that the transformation may be decomposed into a multiplicative and an additive correction. Therefore, the full correction is the average of a fully multiplicative correction a fully additive correction:

$$T_{ij}^{(k)}\,(\lambda) = \frac{R_i^{(k)}\,(\lambda)\ x\ S_{ij}^{(k)}\,(\lambda)}{2} + \frac{S_{ij}^{(k)}\,(\lambda)\ x\ D_i^{(k)}\,(\lambda)}{2}, \qquad (2.21)$$

where $T_{ij}^{(k)}(\lambda)$ is the transformed spectrum, the first term of the right hand side corresponds to the multiplicative correction and the second term corresponds to the additive correction.

2.7.5 Data analysis in chapter 6

Mann-Whitney independent nonparametric test was applied and a Kruskal-Wallis the non-parametric ANOVA was performed to test the significant differences between the mean ranks among the storage time, in different years. Pairwise comparisons to observe the differences and descriptive statistics based on median, minimum, maximum, range and interquartile range were also performed.

A non-metric multidimensional scaling plot method using the ALS call algorithm in a 7-point Likert scale was applied. This method performs multidimensional scaling of proximity or distance-like (Kruskal, 1964) and the results are represented in a cartesian plane, where each axis may be used for representing the overall position in the tasters' mind. Multidimensional scaling refers to models that analyse distances between objects, having been applied Euclidian distances algorithm. Points are arranged in such a way that the geometrical distance between them will reflect empirical relationships in the data.

Receiver operating characteristic (ROC) analysis has become a popular method for assessing the accuracy of medical diagnostic systems. The most desirable property of ROC analysis is that the accuracy indices derived from this technique are not distorted by fluctuations caused by decision criteria. For the application of this procedure, the "*General taste"* variable, evaluated by the panellists' quiz, was considered in binary terms (1 = 7 points attribute the maximum value and 0 = others). A model with a value above 0.5 is considered good, while a value less than 0.5 is no better than random prediction. This classification method is presented only as an accessory and complementary analysis tool.

Chapter 3

Ripening evolution of kiwifruit on-tree

Afonso, A.M.; Guerra, R.; Freitas, L.; Veloso, F.; Cavaco, A.M.; Antunes, M.D. (2022). Ripening evolution of 'Hayward' kiwifruit orchards. *Acta Horticulturae,* 1332: 379-384. http://dx.doi.org/10.17660/actahortic.2022.1332.50.

Afonso, Andreia M.; Guerra, R.; Freitas, L.; Veloso, F.; Cavaco, Ana M.; Antunes, Dulce. (2021). Ripening evolution of 'Hayward' kiwifruit orchards. *X International Symposium on Kiwifruit*, 27-30 september, Yalova, Turkey (poster presentation)

Afonso, Andreia M.; Guerra, Rui; Freitas, L.; Veloso, F.; Cavaco, Ana M; Cruz, S.; Antunes, Dulce. (2019). Ripening of the yellow-fleshed kiwifruit ‘Jintao’ in orchards located in Braga region. *IV PhD Students Meeting in Environment and Agriculture,* 11-12 november, Évora, Portugal (oral communication)

Afonso, Andreia M.; Guerra, Rui; Freitas, L.; Veloso, F.; Cavaco, Ana M; Cruz, S.; Antunes, Dulce. (2019). Monitoring of Actinidia chinensis Planch cv 'Jintao' ripening. *XXIII Meeting of the Spanish Society of Plant Physiology and the XVI Hispano-Portuguese Congress of Plant Physiology*, 26-28 june, Pamplona, Spain (poster presentation)

Afonso, Andreia M.; Guerra, Rui; Freitas, L.; Veloso, F.; Cavaco, Ana M; Cruz, S.; Antunes, Dulce. (2019). Monitoring of Actinidia chinensis Planch cv 'Jintao' ripening. *1st PhD Meeting in Plant Science*, 25 june, Pamplona, Spain (poster presentation)

3.1 Monitoring ripening evolution of ‘Jintao’ kiwifruit orchards

3.1.1 L*, b* and chroma

In 2018, the initial averages of L*, b* and chroma for orchard 1 were, respectively, 59.47, 31.66 and 35.62, while their final values were 59.14, 30.81 and 31.93 (Figure 3.1A, Figure 3.2A and Figure 3.3A). For orchard 2 the corresponding values were 59.62, 31.82 and 35.72 in the beginning, and 66.66, 35.49 and 36.08 in the end.

In 2019, for orchard 1 the initial values were 65.44, 29.04 and 31.69 for the same parameters, while the final values were 61.78, 29.65 and 30.01 (Figures 3.1B, 3.2B and 3.3B).

. For orchard 2, in the beginning, L* was 68.27, b* 29.56 and chroma 32.21. The corresponding values in the end were 64.32, 30.59 and 31.05.

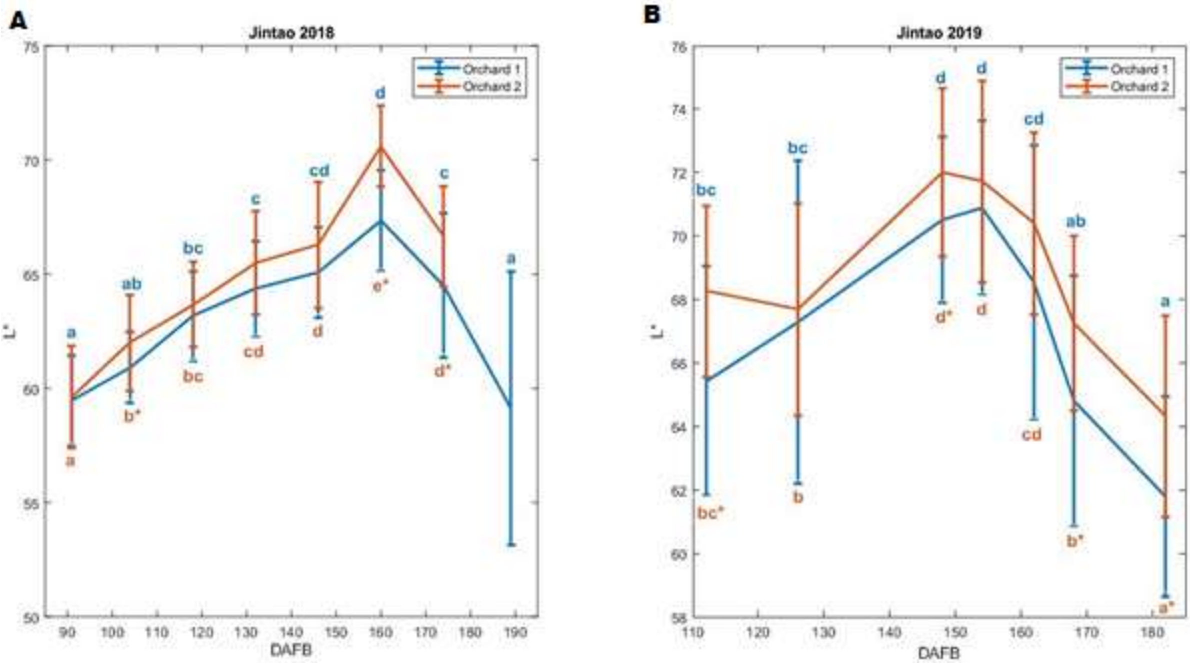

Figure 3.1: ‘Jintao’ kiwifruit temporal evolution of L* along: A) 2018; B) 2019. Data depicted is the Mean ± SE of 25 kiwifruit sampled from 25 different trees tagged across the orchard through time. Statistically different means ($p < 0.05$) between orchards and sampling dates are signalled with an asterisk (*) at higher mean and different letters, respectively. Letters above the error bars are relative to orchard 1 and below them to orchard 2.

For both orchards, in both years, L* shows a similar pattern increasing till, approximately, 160 DAFB, a few days earlier in 2019, and then the values start to decrease. In both years, fruit from orchard 2 show higher L* values.

The b* and chroma values are similar for both orchards in the two years. However, in 2018, b* seems to have a slightly tendency to increase along time, while in 2019 there is no significant differences along time, as chroma in 2018.

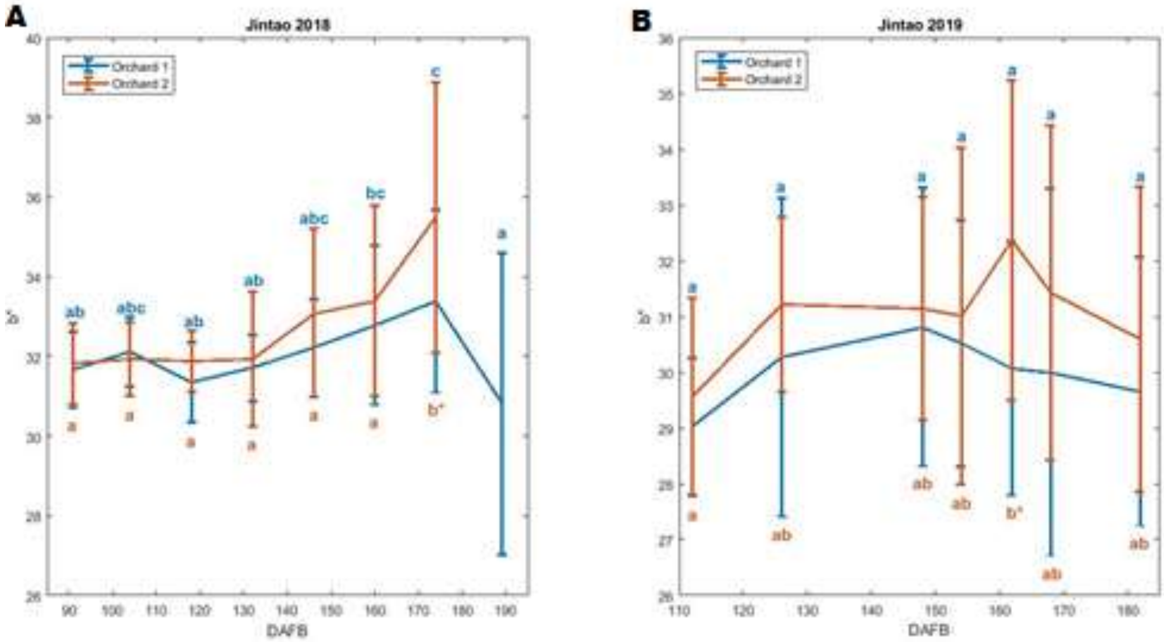

Figure 3.2: ‘Jintao’ kiwifruit temporal evolution of b* along: A) 2018; B) 2019. Data depicted is the Mean ± SE of 25 kiwifruit sampled from 25 different trees tagged across the orchard through time. Statistically different means ($p < 0.05$) between orchards and sampling dates are signalled with an asterisk (*) at higher mean and different letters, respectively. Letters above the error bars are relative to orchard 1 and below them to orchard 2.

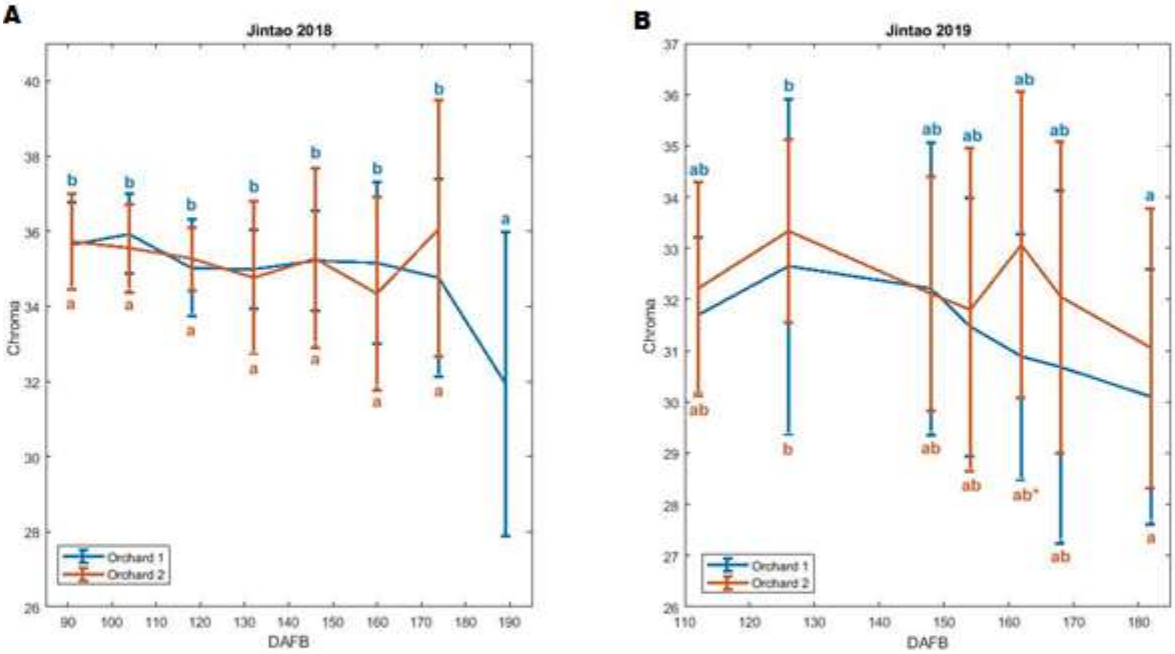

Figure 3.3: 'Jintao' kiwifruit temporal evolution of chroma along: A) 2018; B) 2019. Data depicted is the Mean ± SE of 25 kiwifruit sampled from 25 different trees tagged across the orchard through time. Statistically different means ($p < 0.05$) between orchards and sampling dates are signalled with an asterisk (*) at higher mean and different letters, respectively. Letters above the error bars are relative to orchard 1 and below them to orchard 2.

3.1.2 a* and hue angle

In 2018, the initial averages of a* and hue angle for orchard 1 were -16.33 and 117.3º, while their final values were -8.11 and 104.6 º (Figure 3.4A and Figure 3.5A). For orchard 2, the values started at -16.21 and 117.0 º, respectively, and ended at -6.35 and 100.2º.

As expected, for both orchards in both years, a* increased and hue angle decreased along time, as kiwifruit flesh turn yellow from green colour (Figure 3.4 and Figure 3.5).

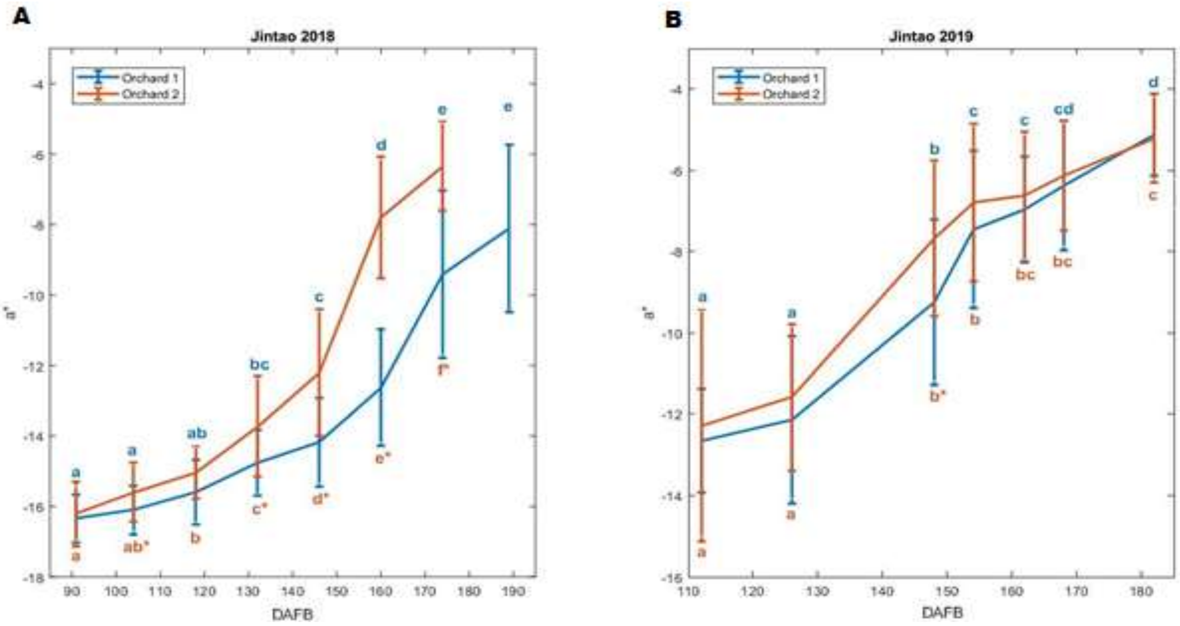

Figure 3.4: 'Jintao' kiwifruit temporal evolution of a* along: A) 2018; B) 2019. Data depicted is the Mean ± SE of 25 kiwifruit sampled from 25 different trees tagged across the orchard through time. Statistically different means ($p < 0.05$) between orchards and sampling dates are signalled with an asterisk (*) at higher mean and different letters, respectively. Letters above the error bars are relative to orchard 1 and below them to orchard 2.

In 2018, the Hue values showed an initial plateau, but they decreased along time, for both orchards (Figure 3.5A). Relatively to the inter-orchard comparison, the values for orchard 2 were always significantly lower than those for orchard 1, except for first date. In fact, the kiwifruit from orchard 2 became yellow-fleshed sooner and reached the colour criteria needed for the harvest (Hue ≥ 103 º) at 160 DAFB (Costa et al., 2010), while kiwifruit from orchard 1 at 190 DAFB was still at ~105 º.

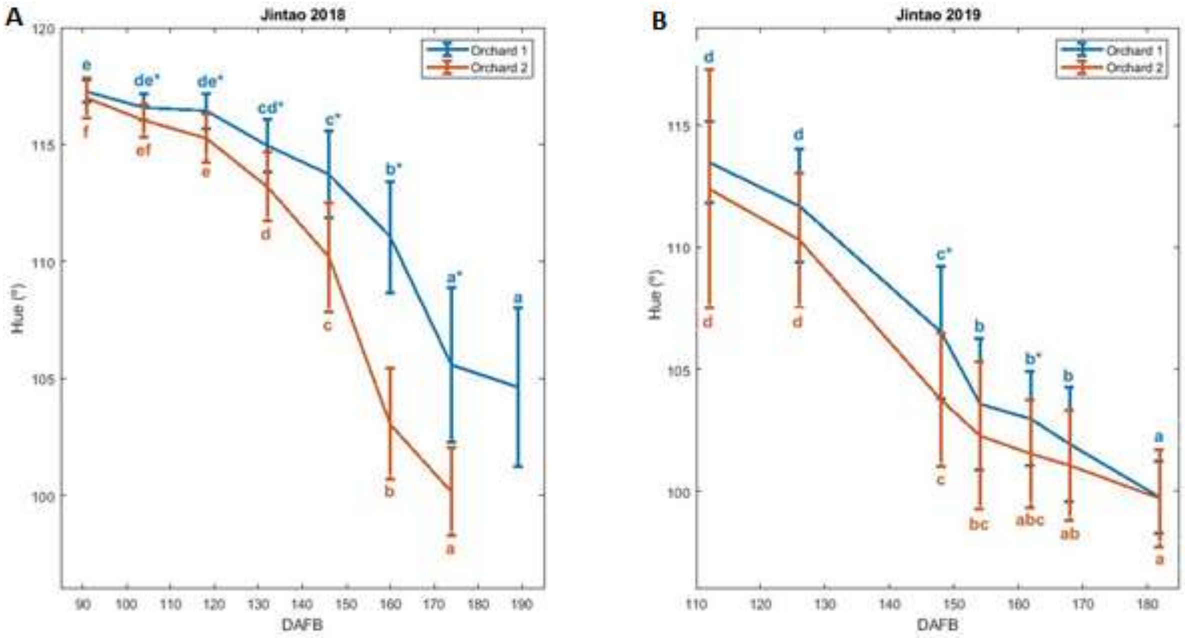

Figure 3.5: 'Jintao' kiwifruit temporal evolution of hue angle along: A) 2018; B) 2019. Data depicted is the Mean ± SE of 25 kiwifruit sampled from 25 different trees tagged across the orchard through time. Statistically different means ($p < 0.05$) between orchards and sampling dates are signalled with an asterisk (*) at higher mean and different letters, respectively. Letters above the error bars are relative to orchard 1 and below them to orchard 2.

In 2019, the initial averages of a* and hue angle for orchard 1 were -12.65 and 113.5º, while the final values were -5.13 and 99.77 º (Figures 3.4B and 3.5B). For orchard 2, in the beginning, a* was -12.28 and Hue 112.4 º. In the end the values were -5.21 and 99.71º.

In 2019, their colour evolution was similar in both orchards, being significantly different only at 148 DAFB, for a* and Hue, and at 163 DAFB for Hue. The colour criteria needed for the harvest was achieved in orchard 2 at 148 DAFB and in orchard 1 at 154 DAFB. So, again, kiwifruit from orchard 2 became yellow-fleshed sooner.

Comparing the values from the two years, in 2019, kiwifruit from both orchards become yellow sooner than the year before and effectively both reach the colour criteria mentioned above (Figure 3.5B).

3.1.3 Firmness, SSC and DM

In 2018, the initial averages of firmness, SSC and dry matter for orchard 1 were 64.5 N, 4.5 % and 10.79 %, while their final values were 35.2 N, 11.4 % and 13.77 % (Figures 3.6A, 3.7A and 3.8A). For orchard 2, the values started at 70.58 N, 4.8 % and 11.00 %, respectively, and ended at 40.25 N, 12.1 % and 16.19 %.

In 2018, firmness (Figure 3.6A) and SSC (Figure 3.7A) also showed an initial plateau. Firmness was higher in orchard 2 in the first four acquisition days (91, 104, 118 and 132 DAFB). Overall, orchard 1 ripened progressively throughout time, while orchard 2 was more irregular. SSC after the plateau, on the fifth acquisition date (146 DAFB), rise very fast, although much more intensely on orchard 2 than in orchard 1. Orchard 2 reached the stipulated SSC to be harvested and stored at 146 DAFB, while orchard 1 at 160 DAFB (Figure 3.7A).

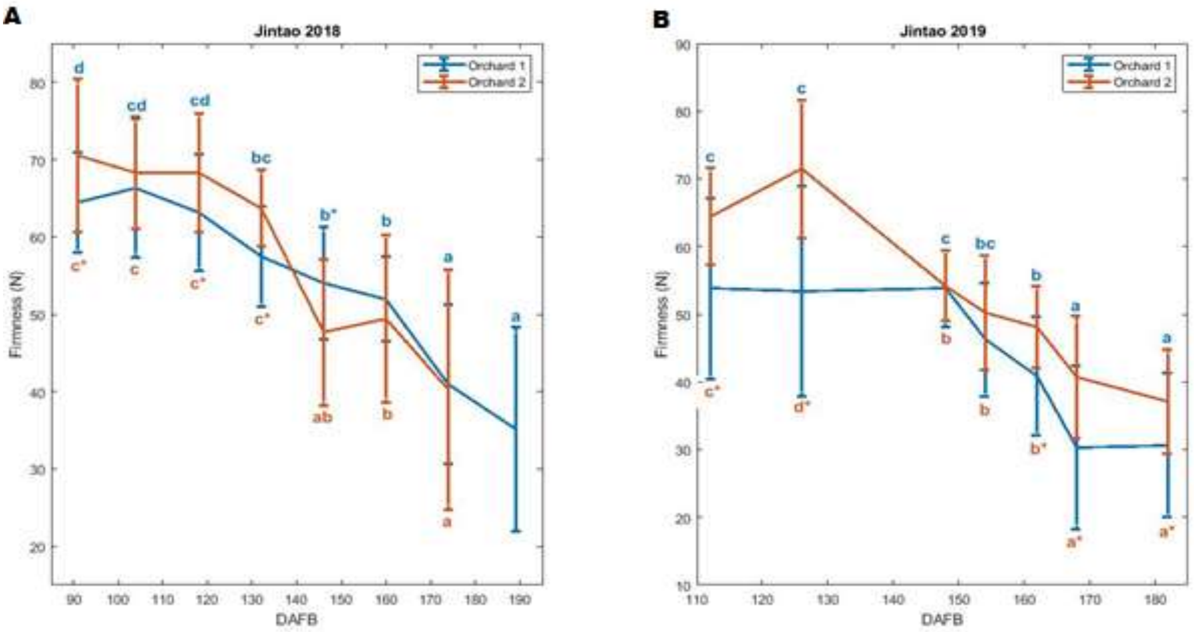

Figure 3.6: ‘Jintao’ kiwifruit temporal evolution of firmness along: A) 2018; B) 2019. Data depicted is the Mean ± SE of 25 kiwifruit sampled from 25 different trees tagged across the orchard through time. Statistically different means ($p < 0.05$) between orchards and sampling dates are signalled with an asterisk (*) at higher mean and different letters, respectively. Letters above the error bars are relative to orchard 1 and below them to orchard 2.

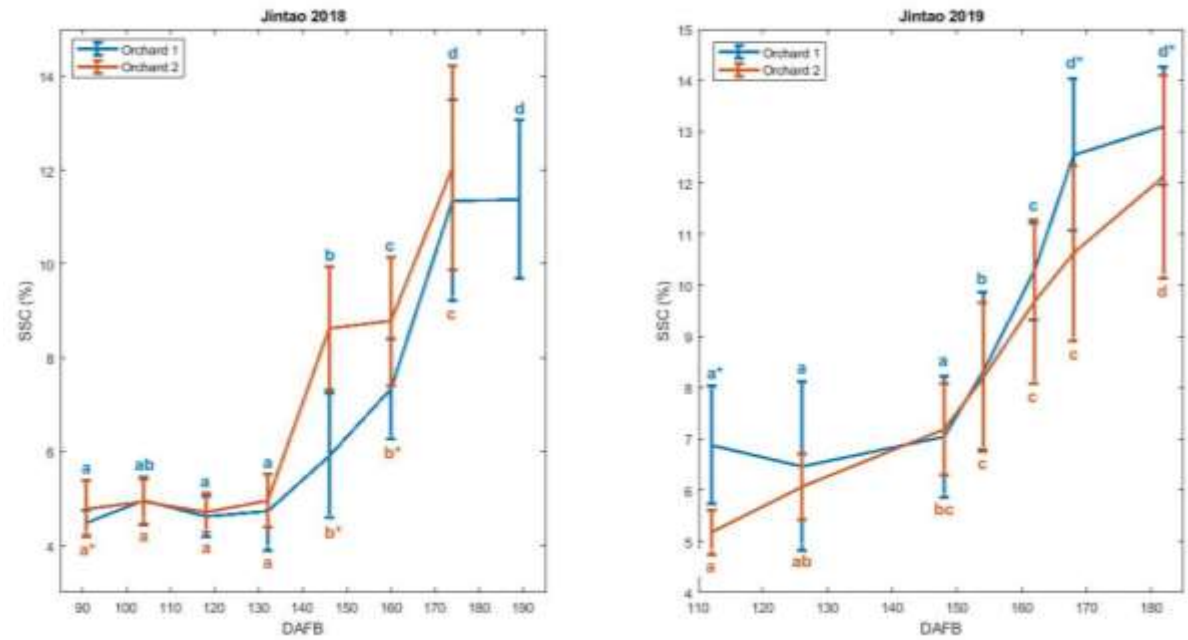

Figure 3.7: 'Jintao' temporal evolution of SSC along: A) 2018; B) 2019. Data depicted is the Mean ± SE of 25 kiwifruit sampled from 25 different trees tagged across the orchard through time. Statistically different means ($p < 0.05$) between orchards and sampling dates are signalled with an asterisk (*) at higher mean and different letters, respectively. Letters above the error bars are relative to orchard 1 and below them to orchard 2.

Despite the two orchards were on the same region with similar cultural practices, their specific location seems to affect the fruit ripening (Cavaco et al., 2021a).

Indeed, since orchard 2 became yellow-fleshed and attained a higher SSC earlier than those from orchard 1, harvest started at 167 DAFB in orchard 2, while in orchard 1 it was initiated one week later at 174 DAFB. The different timings exhibited by them demonstrate the importance of assessing the major ripening attributes of 'Jintao' kiwifruit along time and in each orchard, to establish more precisely the optimal harvest date at each site and therefore provide fruit with better quality to consumers.

In 2019, the initial averages of firmness, SSC and dry matter for orchard 1 were 53.8 N, 6.9 % and 15.01 %, while the final values were 30.6 N, 13.1 % and 15.31 % (Figures 3.6B, 3.7B and 3.8B). For orchard 2, in the beginning, firmness was

64.5 N, SSC 5.2 % and dry matter 15.14 %. In the end the values were 37.1 N, 12.1 % and 14.77 %.

In 2019, kiwifruit firmness from orchard 2 revealed again an irregular pattern with an increase at 126 DAFB, while orchard 1 show a clear plateau between 112 - 148 DAFB (Figure 3.6B). This plateau was also verified for SSC values from orchard 1. Kiwifruit from orchard 1 had significantly higher SSC than orchard 2 only in the first sampling date and in the last two (Figure 3.7B), so, in this year, both orchards started harvested, at the same time, at 167 DAFB. Dry matter increased till 148 DAFB in orchard 1 and till 154 DAFB in orchard 2 (Figure 3.8B). There were no significative differences between them.

Furthermore, comparing the values from the two years, in 2019, besides SSC, also Hue reached the minimum value of 103 º sooner than in 2018 (Costa et al., 2010). This ripening delay led to less sweet, harder and greener kiwifruit in 2018 than in 2019 (Table 3.1 and Table 3.**2**).

Table 3.1: 'Jintao' kiwifruit orchards global descriptive statistics of the Internal Quality Attributes (IQA) in 2018.

IQA	**Orchard 1**					**Orchard 2**				
	mean	±	std	max	min	mean	±	std	max	min
SSC	6.8	±	3.0	17.3	3.5	6.9	±	2.8	16.2	3.7
Firmness	54.5	±	13.4	84.3	18.2	58.6	±	14.7	91.9	6.6
DM	14.11	±	1.99	19.36	9.63	14.49	±	2.04	18.69	10.31
TA	1.18	±	0.12	1.66	0.88	1.07	±	0.12	1.44	0.77
pH	3.22	±	0.18	3.70	2.78	3.13	±	0.14	3.54	2.86
L*	63.00	±	3.95	74.5	50.34	64.87	±	3.95	73.97	53.01
a*	-13.48	±	3.23	-3.77	-17.72	-12.52	±	3.79	-4.69	-17.45
b*	31.99	±	1.98	39.46	24.84	32.74	±	2.25	39.92	26.15
Hue	112.7	±	5.0	118.0	96.8	110.9	±	6.3	118.0	97.9
Chroma	34.84	±	2.33	40.85	25.55	35.27	±	2.14	40.46	27.74

Table 3.2: 'Jintao' kiwifruit orchards global descriptive statistics of the Internal Quality Attributes (IQA) in 2019.

IQA	Orchard 1					Orchard 2				
	mean	±	std	max	min	mean	±	std	max	min
SSC	9.2	±	2.9	15.4	4.2	8.4	±	2.69	15.2	4.3
Firmness	44.3	±	14.6	71.9	3.0	52.3	±	13.8	85.6	19.5
DM	15.58	±	1.25	18.46	10.42	15.63	±	1.44	18.98	12.05
TA	1.21	±	0.15	1.60	0.85	1.09	±	0.14	1.41	0.81
pH	3.43	±	0.13	3.77	3.07	3.25	±	0.17	3.87	2.88
L*	67.06	±	4.77	75.77	45.27	68.81	±	3.87	76.49	58.17
a*	-8.59	±	3.14	-3.80	-15.57	-8.04	±	3.15	-0.34	-15.07
b*	30.05	±	2.48	37.50	20.81	31.04	±	2.57	37.37	23.46
Hue	105.8	±	5.3	116.7	98.0	104.4	±	5.4	116.1	90.2
Chroma	31.39	±	2.78	38.95	22.65	32.23	±	2.68	39.20	23.91

The ripening delay in 2018 could be caused by the weather extremely hot and extremely dry in August and September that year, according to monthly weather report from "Instituto Português do Mar e da Atmosfera" (IPMA, 2018a; IPMA, 2018b). Effectively, the first days of August were the hottest of the XXI century (IPMA, 2018a).

Although the effect of high temperature is well known on higher plants, is not so well-understood in kiwifruit (Li et al., 2022b). In grapes, high temperatures reduce the rate of ripening and delay harvest ripeness (Greer & Weedon, 2013) and in kiwifruit, Snelgar et al. (2005) reported that increasing temperature during summer reduced fruit growth and SSC.

Contrary to the other three IQA, DM did not show an initial plateau (Figure 3.8). DM values increased from the first date onward and stabilized in the end (except for orchard 1, in 2018, in the last sampling date) (Figure 3.8A). This is a direct result of fruit growth and development, which comprise the enlargement of many pulp tissues, such as cell expansion, cell wall thickening and starch accumulation (Schroder & Atkinson, 2006).

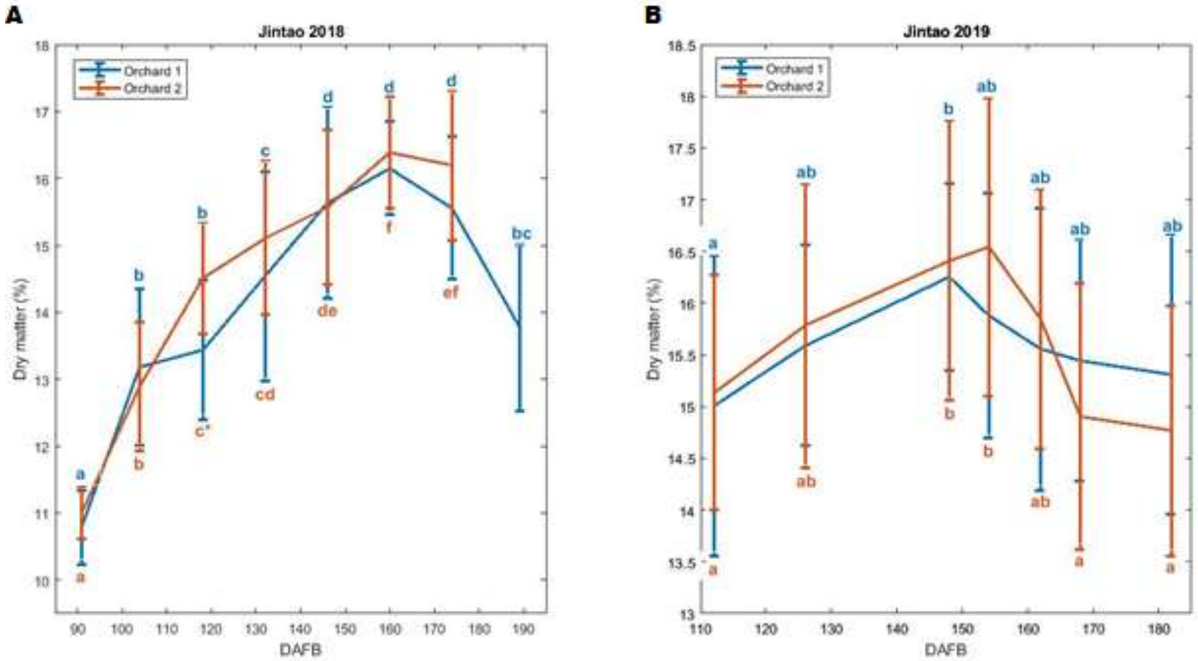

Figure 3.8: ‘Jintao’ kiwifruit temporal evolution of dry matter along: A) 2018; B) 2019. Data depicted is the Mean ± SE of 25 kiwifruit sampled from 25 different trees tagged across the orchard through time. Statistically different means ($p < 0.05$) between orchards and sampling dates are signalled with an asterisk (*) at higher mean and different letters, respectively. Letters above the error bars are relative to orchard 1 and below them to orchard 2.

3.1.4 pH and TA

In 2018, the initial averages of pH and TA for orchard 1 were 3.12 and 1.16 %, while their final values were 3.47 and 1.09 % (Figure 3.9A and Figure 3.10A). For orchard 2, the values started at 3.14 and 1.05 %, respectively, and ended at 3.12 and 1.03 %. pH kiwifruit from orchard 1 slightly increased along time, however from 147 DAFB, both orchards show an irregular pattern since one increase and another decrease (Figure 3.9A).

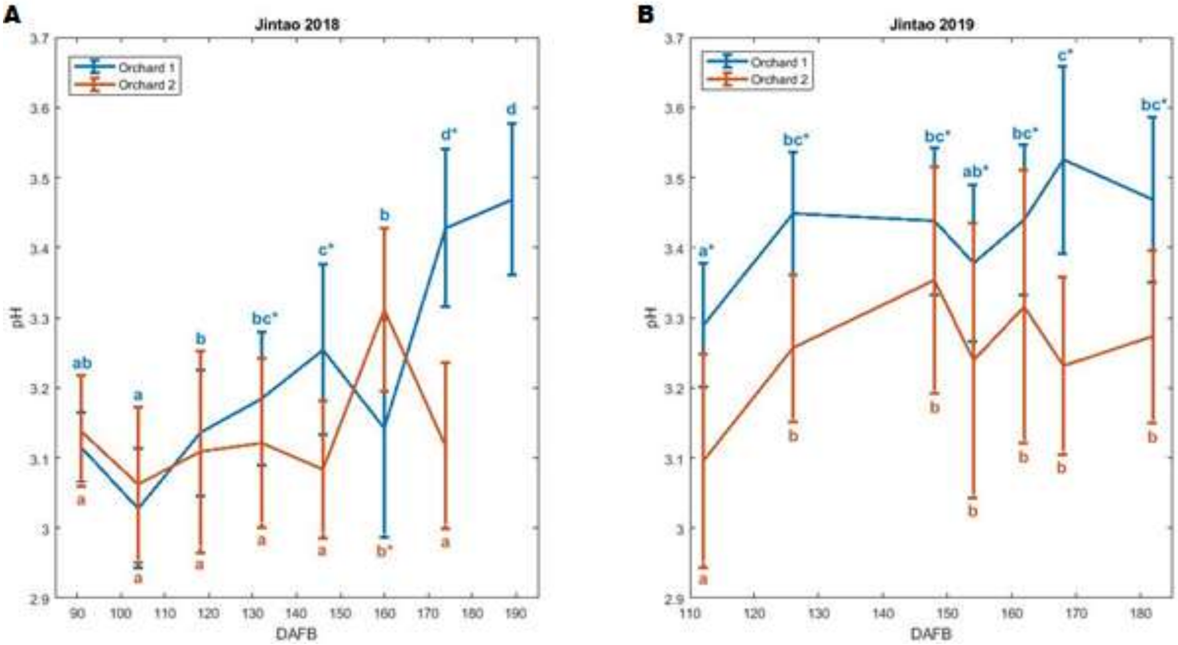

Figure 3.9: 'Jintao' kiwifruit temporal evolution of pH along: A) 2018; B) 2019. Data depicted is the Mean ± SE of 25 kiwifruit sampled from 25 different trees tagged across the orchard through time. Statistically different means ($p < 0.05$) between orchards and sampling dates are signalled with an asterisk (*) at higher mean and different letters, respectively. Letters above the error bars are relative to orchard 1 and below them to orchard 2.

In 2019, for orchard 1 the initial values of pH and TA for orchard 1 were 3.29 and 1.32 %, while the final values were 3.47 and 1.04 % (Figures 3.9B and 3.10B). For orchard 2, in the beginning, pH was 3.10 and TA 1.19 %. In the end the values were 3.27 and 0.97 %. Kiwifruit from both orchards showed a similar evolution pattern, but orchard 1 had always a significant higher pH than those from orchard 2 in both years.

TA showed the same evolution pattern for both orchards and both years with higher TA in kiwifruit from orchard 1 than orchard 2 (Figure 3.10).

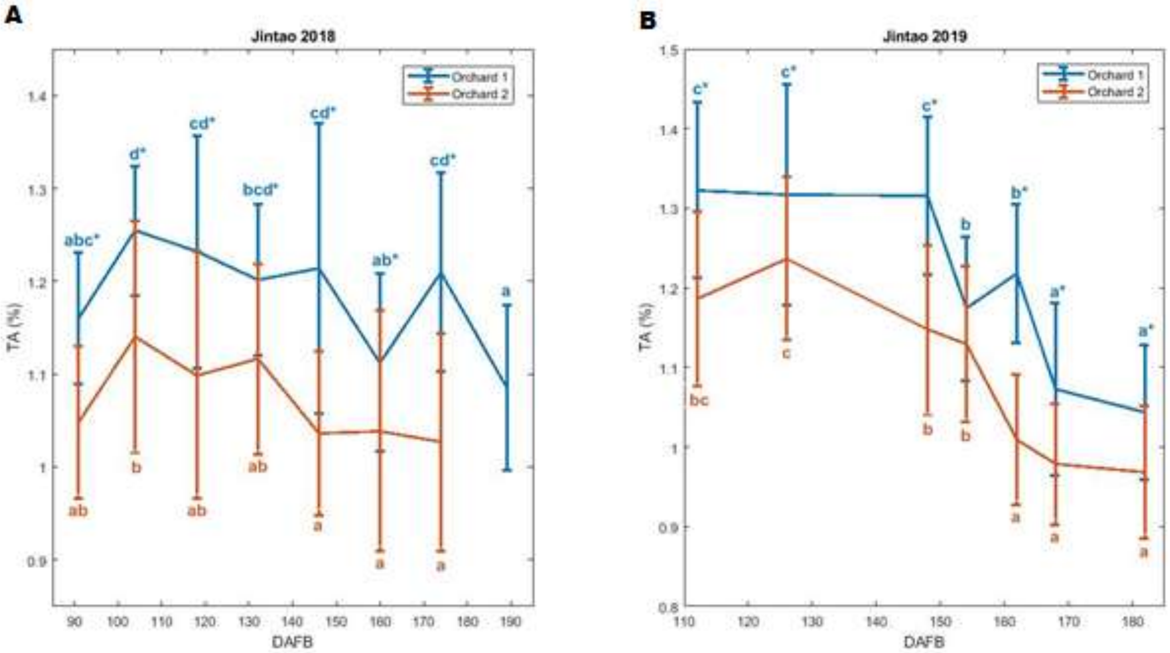

Figure 3.10: 'Jintao' temporal evolution of TA along: A) 2018; B) 2019. Data depicted is the Mean ± SE of 25 kiwifruit sampled from 25 different trees tagged across the orchard through time. Statistically different means ($p < 0.05$) between orchards and sampling dates are signalled with an asterisk (*) at higher mean and different letters, respectively. Letters above the error bars are relative to orchard 1 and below them to orchard 2.

Overall, this section clearly shows the importance to assess the major ripening attributes of 'Jintao' kiwifruit along time and in each orchard, to establish more precisely the optimal harvest date at each site, and therefore provide the best quality fruit to consumers.

3.2 Monitoring ripening evolution of 'Hayward' kiwifruit orchards

3.2.1 L*, b* and chroma

In 2018, the initial averages of L*, b* and chroma for Carrazedo were, respectively, 58.08, 33.25 and 37.35, while their final values were 56.88, 24.91 and 27.73 (Figure 3.11A, Figure 3.12A and Figure 3.13A). For Figueiredo the corresponding values were 59.25, 33.29 and 37.47 in the beginning, and 57.28, 25.30 and 28.17 in the end.

In 2019, for Carrazedo the initial values were 62.70, 32.97 and 37.02 for the same parameters, while the final values were 52.90, 29.61 and 32.86 (Figures 3.11B, 3.12B and 3.13B). For Figueiredo, in the beginning, L* was 61.16, b* 32.52 and chroma 36.24. The corresponding values in the end were 55.90, 30.50 and 33.70.

The L* value was maintained through the fruit ripening process on the tree for both orchards, with the exception at 118 DAFB in 2018 and in the end of 2019. ‘Hayward’ kiwifruit green pulp becomes lighter in the last phases of ripening (Antunes & Sfakiotakis, 2002), as showed in the end of 2019. In 2018, it is possible this situation was not measured since the follow-up ended sooner than in 2019.

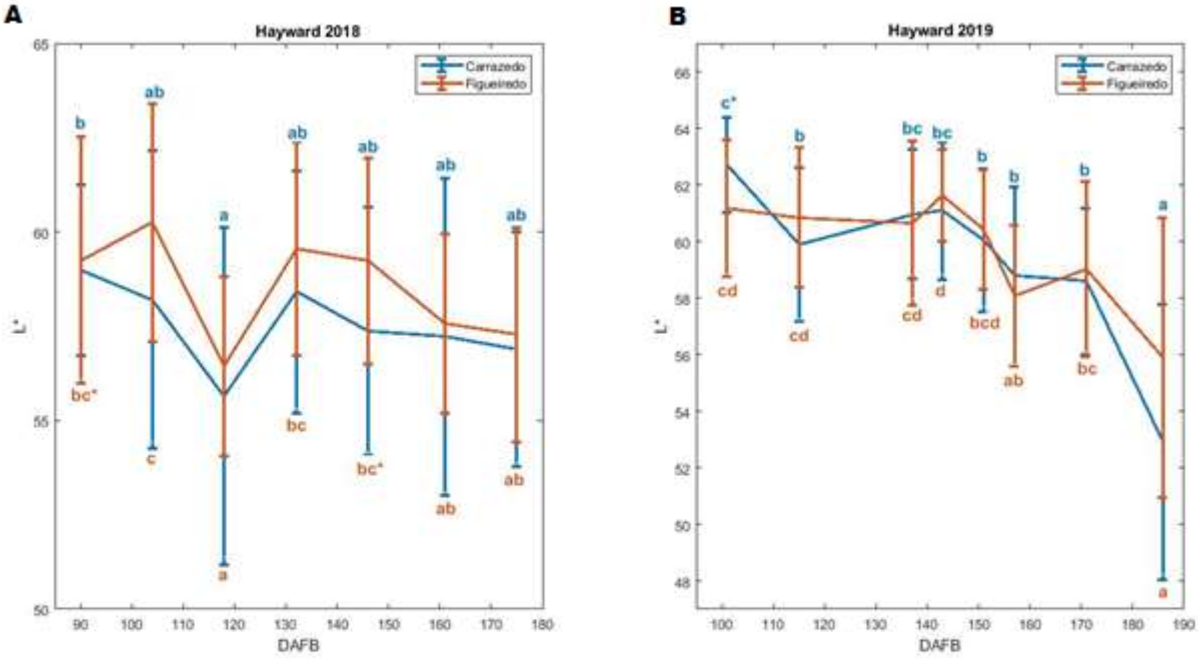

Figure 3.11: ‘Hayward’ kiwifruit temporal evolution of L* along: A) 2018; B) 2019. Data depicted is the Mean ± SE of 25 kiwifruit sampled from 25 different trees tagged across the orchard through time. Statistically different means ($p < 0.05$) between orchards and sampling dates are signalled with an asterisk (*) at higher mean and different letters, respectively. Letters above the error bars are relative to Carrazedo orchard and below them to Figueiredo.

Kiwifruit b* and chroma for both orchards and both years are similar, excepting the last sampling date when a clear decrease is verified (Figure 3.12 and Figure 3.13). In both years, b* and chroma values are higher for Figueiredo than Carrazedo.

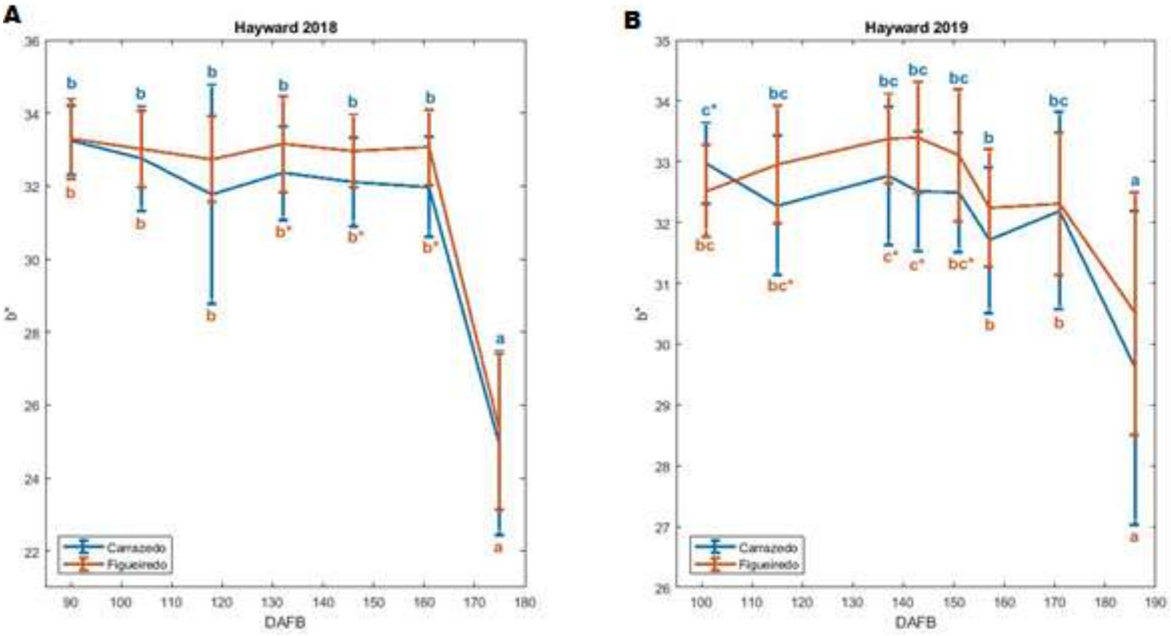

Figure 3.12: 'Hayward' kiwifruit temporal evolution of b* along: A) 2018; B) 2019. Data depicted is the Mean ± SE of 25 kiwifruit sampled from 25 different trees tagged across the orchard through time. Statistically different means ($p < 0.05$) between orchards and sampling dates are signalled with an asterisk (*) at higher mean and different letters, respectively. Letters above the error bars are relative to Carrazedo orchard and below them to Figueiredo.

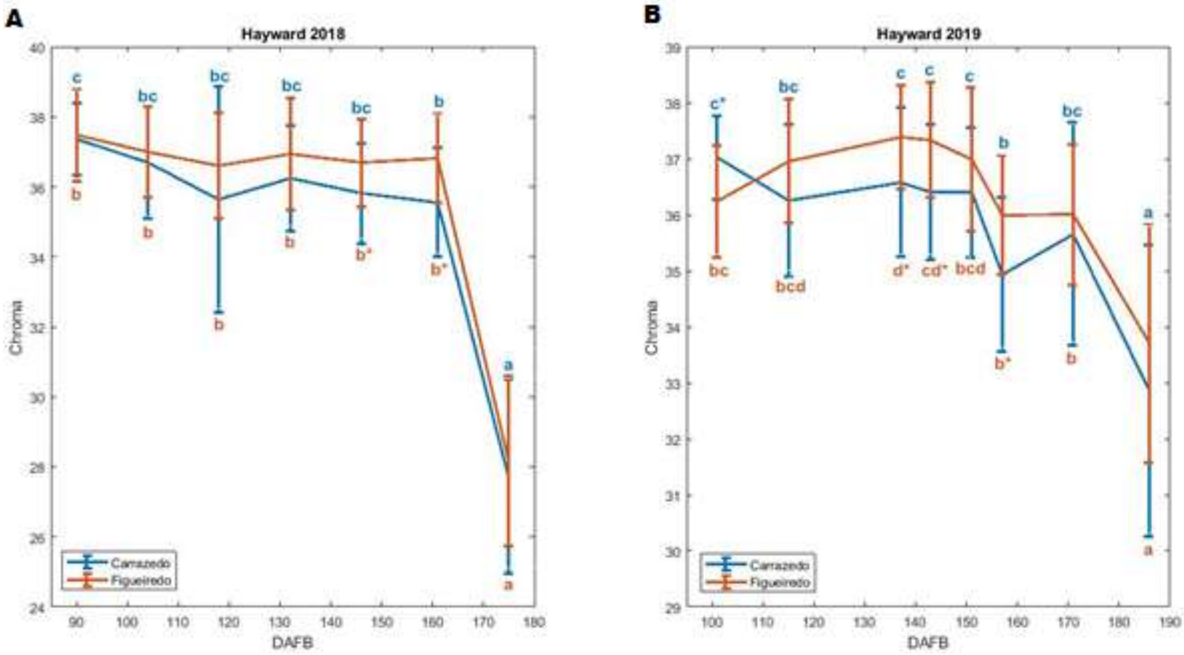

Figure 3.13: 'Hayward' kiwifruit temporal evolution of chroma along: A) 2018; B) 2019. Data depicted is the Mean ± SE of 25 kiwifruit sampled from 25 different trees tagged across the orchard through time. Statistically different means ($p < 0.05$) between orchards and sampling dates are signalled with an asterisk (*) at higher mean and different letters, respectively. Letters above the error bars are relative to Carrazedo orchard and below them to Figueiredo.

3.2.2 a* and hue angle

In 2018, the initial averages of a* and hue angle for Carrazedo were -17.01 and 117.1º, while their final values were -12.16 and 116.0 º (Figure 3.14A and Figure 3.15A). For Figueiredo, the values started at -17.17 and 117.3 º, respectively, and ended at -12.36 and 116.0 º. Kiwifruit a* from both orchards were very similar and follow the same ripening pattern with a significant increase in the final sampling date.

In 2019, the initial averages of a* and hue angle for Carrazedo were -16.83 and 117.0º, while the final values were -14.22 and 115.7 º. For Figueiredo, in the beginning, a* was -15.98 and Hue 116.2 º. In the end the values were -14.32 and 115.2 º. The a* evolution was irregular with also an increase and a peak at 157 DAFB. The clear a* increase (loss of flesh green colour) at the last sampling date, in both years and orchards, can be an indicator of over ripening.

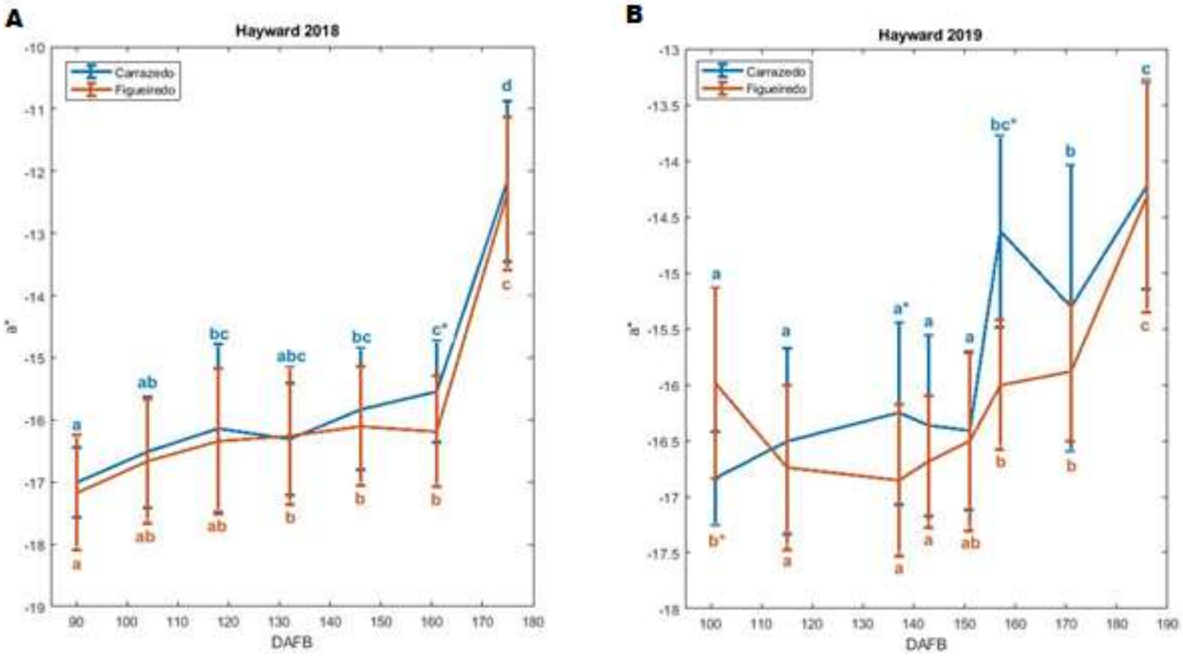

Figure 3.14: ‘Hayward’ kiwifruit temporal evolution of a* along: A) 2018; B) 2019. Data depicted is the Mean ± SE of 25 kiwifruit sampled from 25 different trees tagged across the orchard through time. Statistically different means ($p < 0.05$) between orchards and sampling dates are signalled with an asterisk (*) at higher mean and different letters, respectively. Letters above the error bars are relative to Carrazedo orchard and below them to Figueiredo.

Hue values, in 2018, decreased along time and stabilized in the last sampling dates with no significant differences (Figure 3.15A). In 2019, the Hue evolution was very irregular with a huge decrease peak in Carrazedo at 157 DAFB (Figure 3.15B).

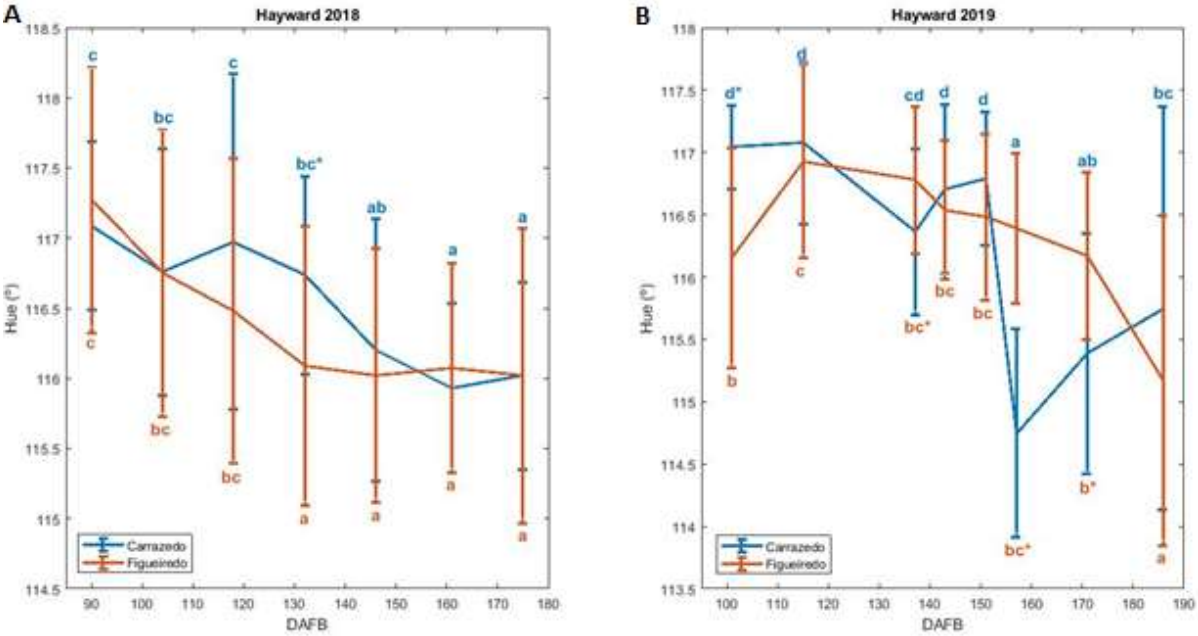

Figure 3.15: 'Hayward' kiwifruit temporal evolution of hue angle along: A) 2018; B) 2019. Data depicted is the Mean ± SE of 25 kiwifruit sampled from 25 different trees tagged across the orchard through time. Statistically different means (p < 0.05) between orchards and sampling dates are signalled with an asterisk (*) at higher mean and different letters, respectively. Letters above the error bars are relative to Carrazedo orchard and below them to Figueiredo.

3.2.3 Firmness, SSC and DM

In 2018, the initial averages of firmness, SSC and dry matter for Carrazedo were 68.8 N, 4.2 % and 12.10 %, while their final values were 36.7 N, 8.2 % and 12.08 % (Figure 3.16A, Figure 3.17A and Figure 3.18A). For Figueiredo, the values started at 77.7 N, 4.3 % and 13.57 %, respectively, and ended at 31.6 N, 9.1 % and 13.17 %. Both Carrazedo and Figueiredo reach a SSC higher than 6.3 % at 161 DAFB.

In 2019, the initial averages of firmness, SSC and dry matter for Carrazedo were 74.3 N, 4.7 % and 14.02 %, while the final values were 37.2 N, 9.1 % and 12.91 % (Figures 3.16B, 3.17B and 3.18B). For Figueiredo, in the beginning, firmness was

73.8 N, SSC 5.4 % and dry matter 14.24 %. In the end the values were 44.7 N, 8.8 % and 13.13 %. At 157 DAFB, Carrazedo and Figueiredo had a SSC higher than 6.3 %.

Firmness and SSC evolved at similar pattern in both orchards in both years. In 2019 the evolution was more irregular, although, in 2018, there is a clear peak in kiwifruit SSC in both orchards (Figures 3.16 and 3.17).

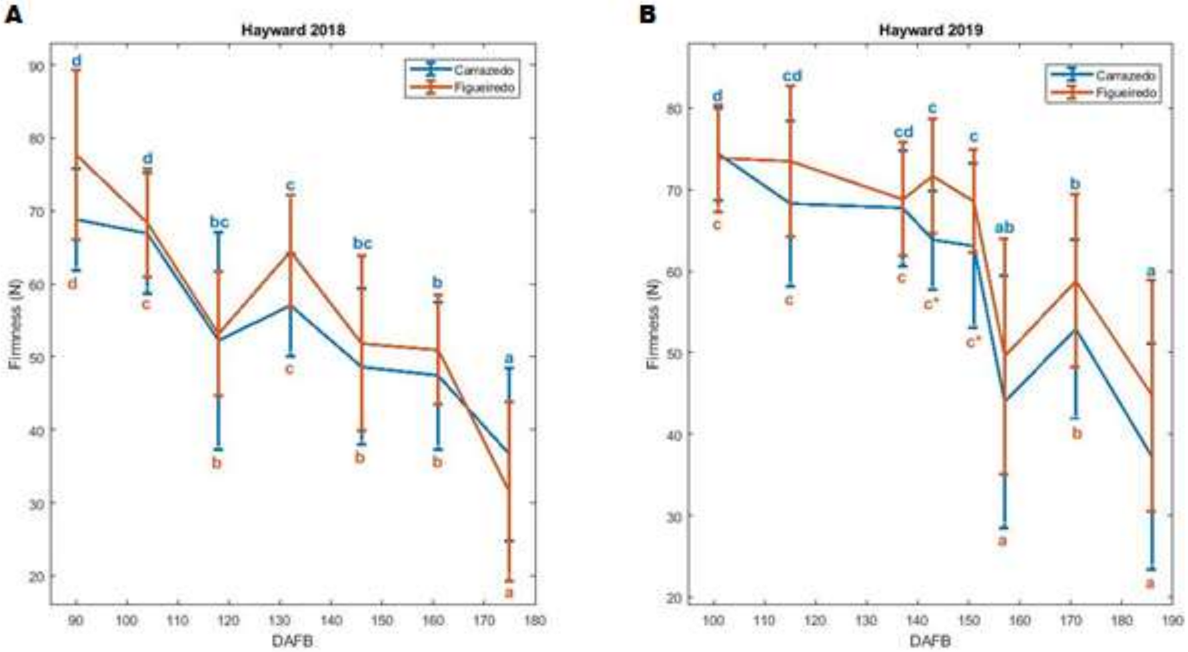

Figure 3.16: 'Hayward' kiwifruit temporal evolution of firmness along: A) 2018; B) 2019. Data depicted is the Mean ± SE of 25 kiwifruit sampled from 25 different trees tagged across the orchard through time. Statistically different means ($p < 0.05$) between orchards and sampling dates are signalled with an asterisk (*) at higher mean and different letters, respectively. Letters above the error bars are relative to Carrazedo orchard and below them to Figueiredo.

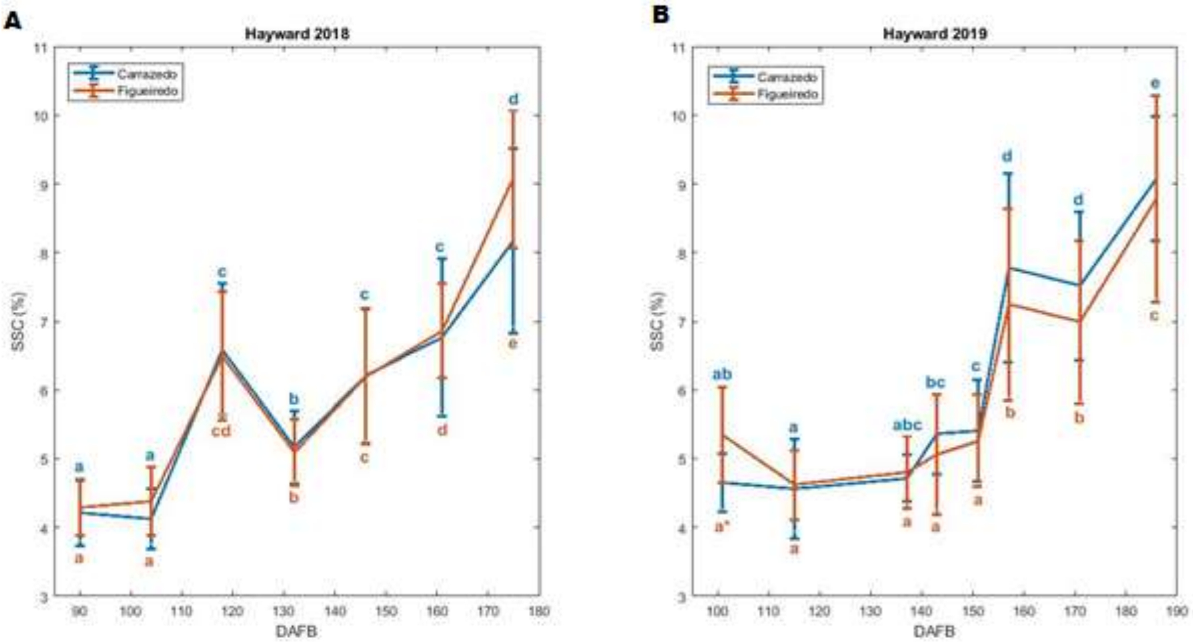

Figure 3.17: ‘Hayward’ kiwifruit temporal evolution of SSC along: A) 2018; B) 2019. Data depicted is the Mean ± SE of 25 kiwifruit sampled from 25 different trees tagged across the orchard through time. Statistically different means ($p < 0.05$) between orchards and sampling dates are signalled with an asterisk (*) at higher mean and different letters, respectively. Letters above the error bars are relative to Carrazedo orchard and below them to Figueiredo.

Comparing the SSC values in the two years, in 2019, at 157 DAFB was higher than 7 %, while in 2018 at 161 DAFB was, approximately, 6.8 %. As ‘Jintao’ kiwifruit, ‘Hayward’ kiwifruit ripened faster in 2019 than in 2018, although the difference was not so big as in the yellow-fleshed kiwifruit. For this reason, the descriptive statistics of ‘Hayward’ are similar in both years (Table 3.3 and Table 3.4).

Table 3.3: ‘Hayward’ orchards global descriptive statistics of the IQAs in 2018.

IQA	Carrazedo					Figueiredo				
	mean	±	std	max	min	mean	±	std	max	min
SSC	5.9	±	1.6	10.7	3.4	6.1	±	1.7	10.8	3.6
Firmness	54.1	±	14.6	88.2	3.7	56.8	±	16.9	103.1	10.4
DM	12.56	±	1.46	16.29	8.10	13.98	±	1.22	17.54	9.93
TA	1.32	±	0.17	1.72	0.76	1.40	±	0.16	1.84	0.91
pH	3.12	±	0.22	3.52	2.57	3.17	±	0.20	3.68	2.70
L*	57.58	±	3.63	64.49	40.68	58.51	±	3.05	66.66	51.44
a*	-15.65	±	1.79	-9.10	-17.88	-15.86	±	1.81	-9.91	-18.61
b*	31.32	±	3.19	34.95	18.45	31.92	±	3.02	36.33	20.85
Hue	116.5	±	0.9	121.36	113.3	116.4	±	1.1	119.3	112.9
Chroma	35.01	±	3.62	39.08	20.58	35.65	±	3.46	40.55	23.17

Table 3.4: ‘Hayward’ orchards global descriptive statistics of the IQAs in 2019.

IQA	Carrazedo					Figueiredo				
	mean	±	std	max	min	mean	±	std	max	min
SSC	6.0	±	1.8	10.8	3.8	6.0	±	1.7	11.9	3.7
Firmness	60.0	±	15.3	90.6	9.4	63.9	±	14.3	87.2	13.6
DM	13.86	±	1.09	16.63	10.36	14.13	±	1.26	17.31	9.31
TA	1.32	±	0.15	1.80	0.96	1.44	±	0.18	2.14	1.01
pH	3.26	±	0.13	3.67	2.94	3.27	±	0.13	3.59	2.92
L*	59.59	±	3.78	65.13	43.06	59.74	±	3.37	66.59	42.61
a*	-15.89	±	1.21	-12.14	-18.1	-16.13	±	1.06	-11.69	-18.38
b*	32.15	±	1.62	34.64	23.30	32.56	±	1.42	35.35	22.86
Hue	116.3	±	1.13	120.7	113.1	116.3	±	0.93	118.1	112.8
Chroma	35.88	±	1.90	38.82	26.97	36.35	±	1.68	39.52	25.89

Dry matter content, in 2018, was always higher in Figueiredo than Carrazedo (Figure 3.18A). In both orchards, dry matter slightly increased through the ripening process till 146 DAFB in Figueiredo and till 132 DAFB in Carrazedo, then decreased. In 2019, as firmness and SSC, dry matter showed an evolution more irregular with also a decreased in the end (Figures 3.16B, 3.17B and 3.18B).

In all sampling dates, average dry matter was higher than 12 %, being an indicator of good fruit quality and good performance through storage (Burdon et al., 2004).

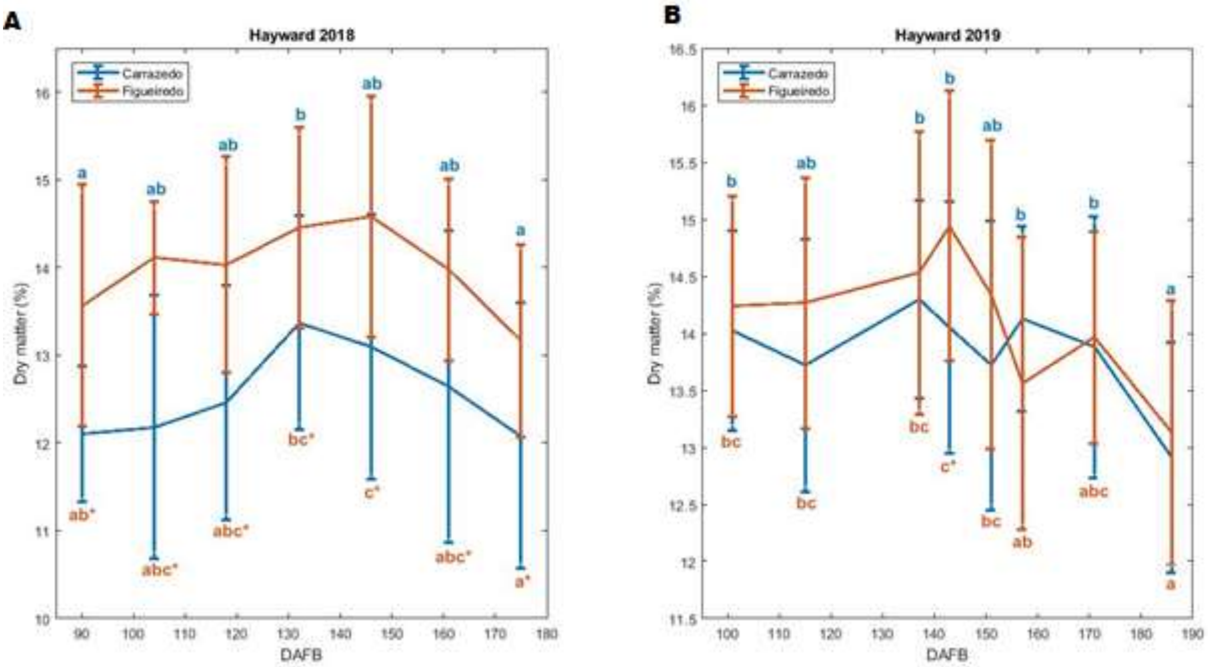

Figure 3.18: 'Hayward' kiwifruit temporal evolution of dry matter along: A) 2018; B) 2019. Data depicted is the Mean ± SE of 25 kiwifruit sampled from 25 different trees tagged across the orchard through time. Statistically different means ($p < 0.05$) between orchards and sampling dates are signalled with an asterisk (*) at higher mean and different letters, respectively. Letters above the error bars are relative to Carrazedo orchard and below them to Figueiredo.

3.2.4 pH and TA

In 2018, the initial averages of pH and TA for Carrazedo were 3.09 and 1.18%, while their final values were 3.38 and 1.34 % (Figure 3.19A and Figure 3.20A). For Figueiredo, the values started at 3.16 and 1.21 %, respectively, and ended at 3.43 and 1.46 %.

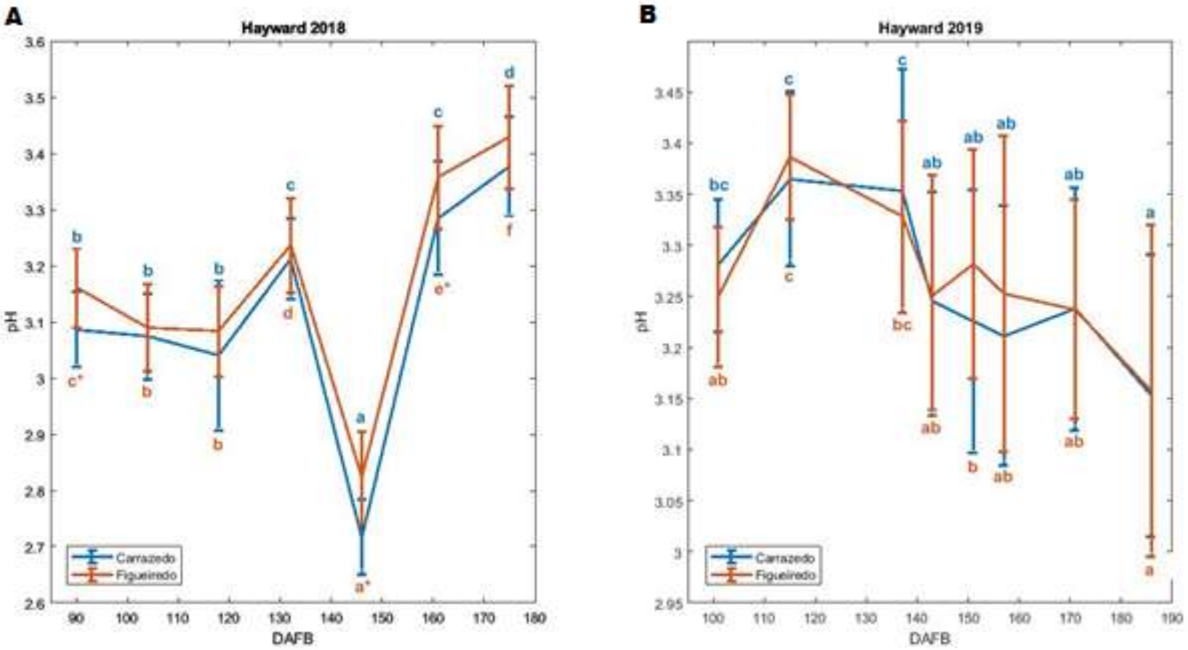

Figure 3.19: ‘Hayward’ kiwifruit temporal evolution of pH along: A) 2018; B) 2019. Data depicted is the Mean ± SE of 25 kiwifruit sampled from 25 different trees tagged across the orchard through time. Statistically different means (p < 0.05) between orchards and sampling dates are signalled with an asterisk (*) at higher mean and different letters, respectively. Letters above the error bars are relative to Carrazedo orchard and below them to Figueiredo.

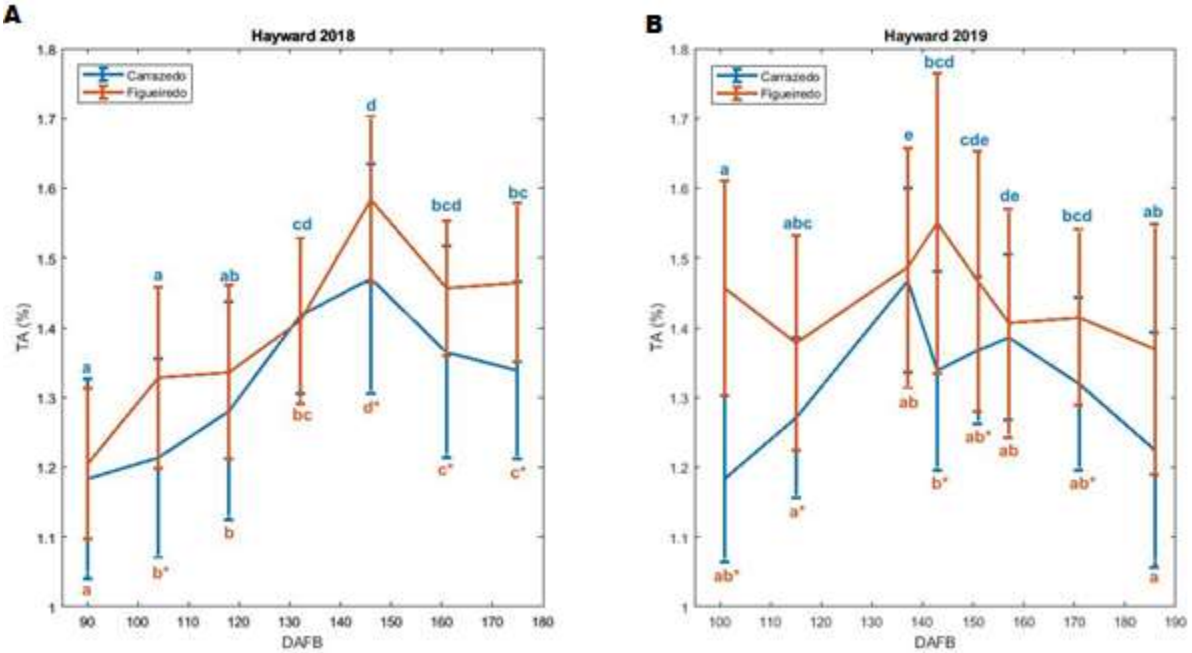

Figure 3.20: ‘Hayward’ kiwifruit temporal evolution of TA along: A) 2018; B) 2019. Data depicted is the Mean ± SE of 25 kiwifruit sampled from 25 different trees tagged across the orchard through time. Statistically different means (p < 0.05) between orchards and sampling dates are signalled with an asterisk (*) at higher mean and different letters, respectively. Letters above the error bars are relative to Carrazedo orchard and below them to Figueiredo.

In 2019, for Carrazedo the initial values of pH and TA were 3.28 and 1.18%, while the final values were 3.15 and 1.23 % (Figures 3.19B and 3.20B). For Figueiredo, in the beginning, pH was 3.25 and TA 1.46 %. In the end the values were 3.16 and 1.37 %.

In 2018, pH kiwifruit of both orchards was stable in the first sampling dates, following then a growing pattern, with exception at 146 DAFB when a sharp decreased was verified. In 2019, the pH evolution was again irregular.

The titrable acidity increased till 146 DAFB and then decreased in both orchards in 2018 (Figure 3.20A). In 2019, although more irregular, TA increased till 137 DAFB in Carrazedo, while till 143 DAFB in Figueiredo (Figure 3.20B). Both decreased after this sampling date. In both years, kiwifruit from Figueiredo had a higher TA than Carrazedo.

Chapter 4

Non-destructive prediction models for ‘Jintao’ kiwifruit internal quality

Afonso, Andreia M.; Antunes, Maria Dulce; Cruz, Sandra; Cavaco, Ana M.; Guerra, Rui. (2022). The use of average calibration model's predictions for the assessment of 'Jintao' kiwifruit quality attributes. *XIII Congreso Nacional y XI Ibérico de Maduración y Postcosecha*, 14-17 june, Zaragoza, Spain (conference paper)

Afonso, Andreia M.; Antunes, Maria Dulce; Cruz, Sandra; Cavaco, Ana M.; Guerra, Rui. (2022). The use of average calibration model's predictions for the assessment of 'Jintao' kiwifruit quality attributes. *XIII Congreso Nacional y XI Ibérico de Maduración y Postcosecha*, 14-17 june, Zaragoza, Spain (poster presentation)

Afonso, A. M., Antunes, M. D., Cruz, S., Cavaco, A. M., & Guerra, R. (2022). Non-destructive follow-up of ‘Jintao’ kiwifruit ripening through VISNIR-DRS spectroscopy–individual vs. average calibration model’s predictions. *Postharvest Biology and Technology*, *188*, 111895.

4.1 Temporal evolution of the average spectra and its relation with tissue structure

The time evolution of the spectra has a similar coarse pattern in both orchards (Figure 4.1A and B). The first three days have higher NIR plateaus, in the range 50–70 %, while the last days have diminished plateaus, in the level 3 5– 50 %. One of the main factors explaining the variation in the plateaus' height is the fruit firmness. It is usually assumed that flesh firmness is directly related with the scattering coefficient and that higher firmness implies more backscattering and a higher level of reflectance. There is indeed a loose relation between the plateau height (measured by the representative wavelength of 842 nm) and the firmness (Figure 4.1D), observed as a global trend of increase in reflectance with firmness, but with a large variability superimposed. This means that there are more factors needed to explain the height of the reflectance plateau than the firmness alone. In the context of ripening follow-up, it is important to understand the causes of the decrease in the NIR plateau since it signals an internal change in fruit. However, the relationship between the reflectance spectra and the fundamental structural and mechanical properties (such as firmness) of plant material (Cen et al., 2013) is not well established, since light interaction with turbid biological materials is a complicated phenomenon, involving both absorption and scattering (Qin & Lu, 2008), whose effects cannot be separated (Cen et al., 2013). Light absorption is related to tissue's chemical composition, while scattering is influenced by the physical and structural properties, such as firmness and cell size (Cen et al., 2013; Cheng et al., 2019). However, the height of the reflectance plateau cannot be taken as a direct measure of firmness, since the scattering effect it represents is always coupled with the absorption effect.

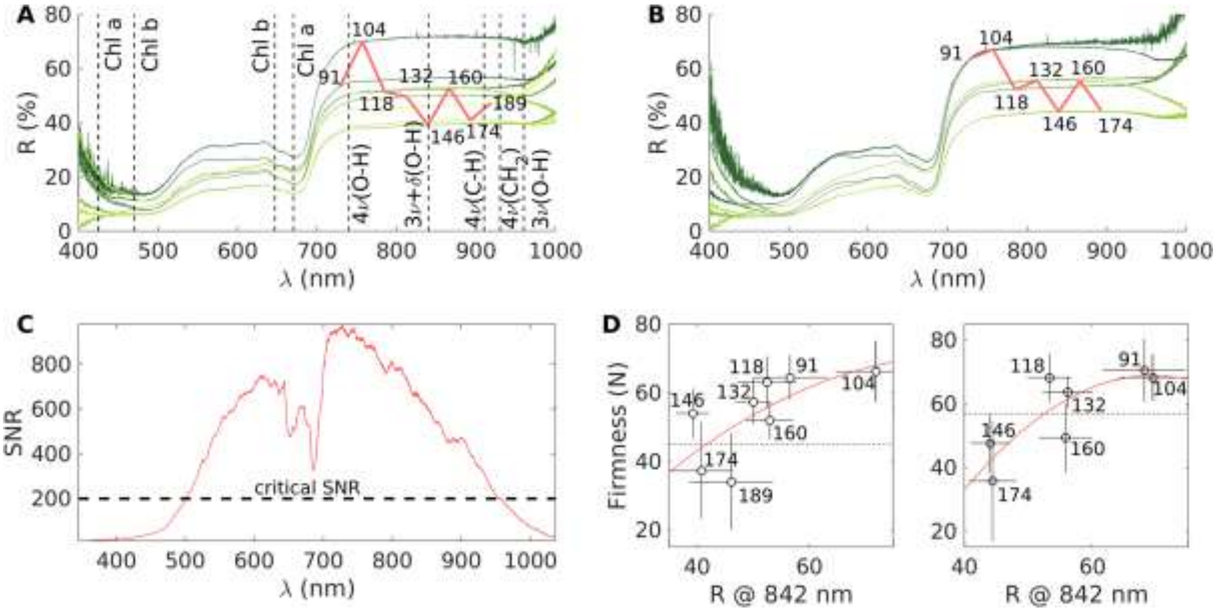

Figure 4.1: A and B) Daily average of VisNIR-DRS 'Jintao' kiwifruit reflectance spectra acquired along time, for orchards 1 and 2, respectively. The numbers above the NIR plateaus indicate the days after full bloom (DAFB). The vertical lines in A represent the nominal positions of the main absorption bands, identified by the overtone (n indicates the (n- 1)-th overtone) and the type of oscillation (*ν* for stretching and *δ* for bending). C) Spectrometer signal-to-noise ratio (SNR) as a function of wavelength. D) Relation between the reflectance at 842 nm, R@842 nm, and the firmness for orchard 1 (left) and orchard 2 (right). The numbers on the spectra represent the measurement day, the horizontal bars represent the standard deviation of R@842 nm and the vertical bars represent the standard deviation of firmness.

Summarizing, *i)* there was an average trend of decrease in the NIR plateau accompanying the ripening process, but *ii)* there was a large variability in that trend, which means that the relationship between firmness and the NIR plateau is not simple.

4.2 Spectroscopic signal to noise ratio

Signal to noise ratio (SNR) drops below 500 nm and above 950 nm (Figure 4.1C). This is due to the quantum efficiency of the detector, but it is further shaped by the absorption of pigments, specifically below 450 nm and around 680 nm. The two valleys at 640 and 680 nm correspond to the red absorption peaks of chlorophyll *b* and *a*, respectively. These valleys are not clearly identified in the reflectance curves, suggesting that SNR analysis may provide a way to increase the spectral resolution.

The water peak around 960 nm falls partly outside the ideal range that should thus be approximately 500 – 950 nm, which compromises its usefulness for model calibration. The construction of calibration models employed the whole spectroscopic available range and the systematic test of sub-ranges. The selection of optimal ranges coincided, in most cases, with the spectral range insuring SNR> 200 (Table 4.1), suggesting that the SNR criteria may even have precedence over the information criteria for the construction of models. The DM model is a clear demonstration of this fact, since it excludes the water band (see Section 4.3.3).

Table 4.1: Summary of principal and best results obtained in the PLS models for 'Jintao' kiwifruit quality attributes.

IQA	RMSEP	R^2	SDR	Bias	Slope	Range	Pre-Process
SSC (%)	1.24	0.80	2.24	-0.16	0.78	675 - 895	SNV
Firmness (N)	8.39	0.61	1.59	0.68	0.63	635 - 870	SNV
Dry matter (%)	1.19	0.66	1.71	0.04	0.68	595 - 931	SNV
TA (%)	0.12	0.12	1.04	0.01	0.18	809 - 883	SNV
pH	0.12	0.43	1.32	0.00	0.48	470 - 948	SNV
L*	2.75	0.50	1.40	0.00	0.55	470 - 840	SNV
a*	1.44	0.82	2.38	-0.02	0.82	660 - 948	SNV
b*	1.60	0.32	1.22	0.10	0.33	470 - 660	SG + SNV
Hue (º)	1.92	0.88	2.91	0.12	0.87	660 - 959	SNV
Chroma	1.69	0.19	1.11	0.13	0.21	486 - 660	SG + SNV

A previous remark valid for all the IQA calibration models is that their wavelength ranges were always shortened relatively to the full range available, either in the lower and in upper values. The main reason to eliminate the upper wavelength region is the noise due to low quantum efficiency of the detector and corresponding low SNR, especially above 950 nm. The main reason for the elimination of lower wavelength regions is that the chlorophyll dominated band is not always useful as a predictor for other attributes.

4.3 ‘Jintao’ kiwifruit calibration model’s predictions

Regarding there are already many published reports, which differ essentially by the coverage of the various sources of IQA variability, some concentrate merely in demonstrating the viability of VisNIR-DRSS to predict IQA. These studies use one homogeneous batch from a single orchard or local market and tend to deliver optimistic results due to the lack of variability in the dataset (Fu et al., 2007; Tang et al., 2010; Quiang et al., 2010; Moghimi et al., 2010; Zhu et al., 2017; Benelli et al., 2022). A second group of publications still uses only one orchard but gathers more variability by measuring fruit in different conditions, either by allowing some delay between the measurements or by using different storage and/or shelf-life conditions. This was done by Arazuri et al. (2005) and Shibang (2021). The work of Ciccoritti et al. (2019) added another layer of variability, by sampling the fruit in two successive years, while Guo et al. (2016) and Vieira et al. (2017) used two different harvesting dates to include fruit in different ripening stages.

Studying multiple orchards allows to include simultaneously several sources of variability (soil, weather conditions, cultural practices). For example, Lee et al. (2012) used data from three orchards and Sarkar et al. (2020) from ten different orchards and four cultivars. More complex datasets were obtained again by combining different orchards/origins and shelf-life conditions (Li et al., 2018) and even cold storage (McGlone et al., 2002b; Lee et al., 2019; Guo et al., 2019). The study of Li et al. (2017) used data from three seasons. Very complete datasets were obtained by combining different orchards/origins and harvest times with different: *i)* shelf-life conditions (Schaare & Fraser, 2000); *ii)* storage conditions (McGlone et al., 2007); *c)* both shelf-life and storage conditions (McGlone & Kawano, 1998; Chen & Han, 2012). A general trend is that the broader is the range of variability included in the model, the lower is its predictive model accuracy.

4.3.1 SSC

The SSC model delivers good performance in the context of VisNIR-DRS in fruit, although a closer inspection reveals that the predictions saturate around 12 % SSC (Figure 4.2A). This does not correspond to the upper range of the SSC values, since the sampling measurements include fruit up to 17 % SSC (Table 3.1), however the model predictions break in the upper SSC range (12 – 16 %) because there is a small number of fruit in this range and a huge peak at 5 % (Figure 4.3).

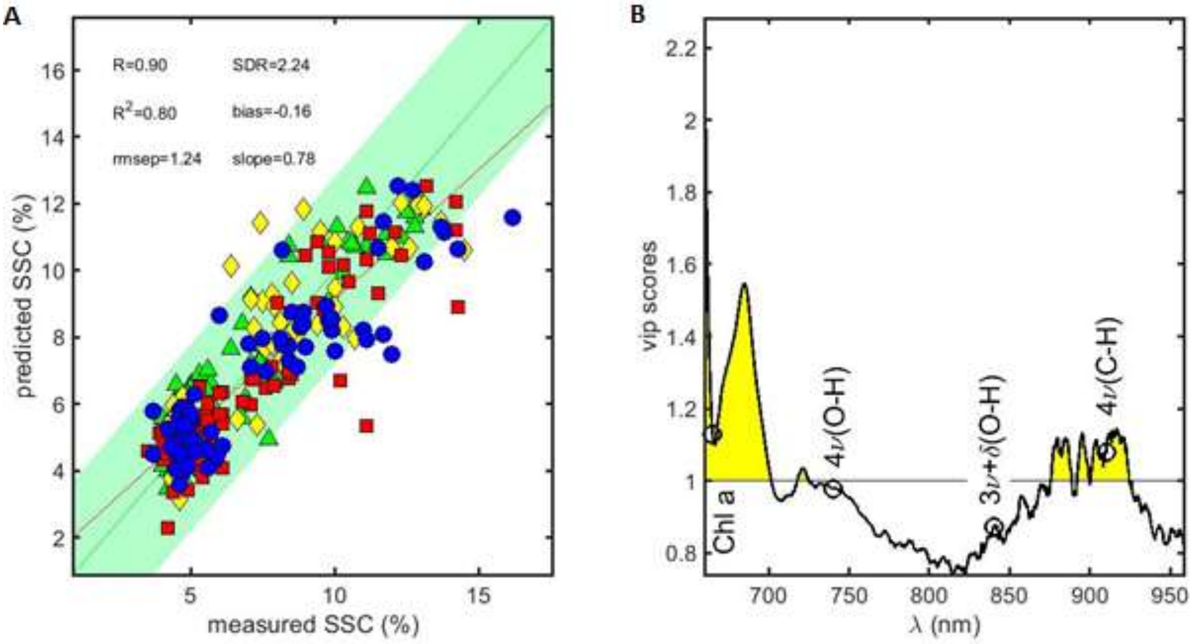

Figure 4.2: A) measured versus predicted values for 'Jintao' kiwifruit SSC. Each symbol corresponds to one test set. The green shadowed band has a half-width equal to the standard deviation of SSC. B) average VIP scores of the four models. The shadowed area corresponds to VIP > 1 and the white circles to the nominal position of the spectroscopic bands indicated.

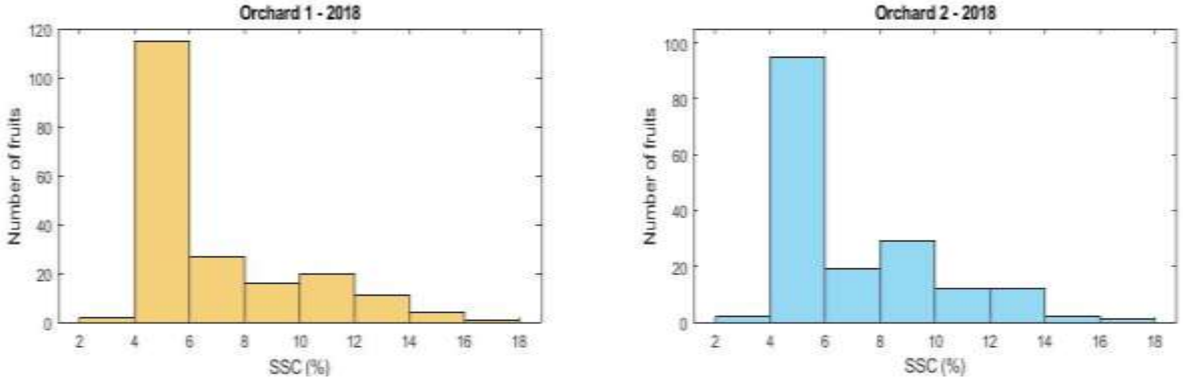

Figure 4.3: Histogram of SSC for 'Jintao' kiwifruit orchard 1 and orchard 2 in 2018.

SSC prediction model with RMSEP = 1.24 % is within the same order of magnitude of those from Benelli et al. (2022) [0.73 – 1.10%], Clark et al. (2004) [0.76 – 0.92 % in IV], Guo et al. (2019) [0.9 %], Lee et al. (2019) [1.38 – 1.58 %], Li et al. (2017) [0.66 –1.02 %], McGlone & Kawano (1998) [0.47 – 0.96 % in EV], Sarkar et al. (2020) [1.0– 2.1 %] and Vieira et al. (2017) [1.0 %].

The VIP scores indicate that the SSC model is relying mostly on the chlorophyll band and on the third overtone of CH and CH_2 stretching, usually assigned to 910 – 930 nm (Figure 4.2B). These three VIP bands illustrate the three main sources of information for the calibration models in VisNIR-DRS. The chlorophyll band around 680 – 690 nm represents an indirect source of information. Indeed, chlorophyll degradation and SSC are inversely related along ripening. Thus, chlorophyll content is a proxy for SSC but not a direct measure of it. However, the 4ν(C–H) and 4ν (CH_2) bands are direct sources of information, since they relate directly with the concentration of organic molecules and may reflect changes in the sugar content. An interesting detail is that the peak associated with the band 4ν (O–H) is below the level VIP= 1, but still is recognized by the model as locally relevant.

SSC models are the most frequent in the literature and therefore their discussion covers most of the relevant comments for comparison between published results and associated methods (Table 4.2).

Table 4.2: Kiwifruit SSC models' prediction. Valid. = Validation; IV = Internal validation; EV = External validation.

R^2	RMSEP (%)	SDR	Range	Kiwifruit	Valid.	Reference
0.80	1.24	2.2	675-895	'Jintao'	IV	This chapter
0.44-0.54	0.66-0.89	-	800-2500	'Hayward'	-	Arazuri et al. (2005)
0.85-0.94	0.73-1.10	-	424-1000	'Hayward'	IV	Benelli et al. (2022)
0.94	0.66	-	800-2500	'Qinmei'	IV	Chen &

						Han (2012)
0.99	0.40	11.5	800-2500	‘Hayward’ + ‘Boerica’	IV	Ciccoritti et al. (2019)
0.82-0.94	0.76-0.92	-	800-1000	‘Hort16A’	IV	Clark et al. (2004)
0.69	1.43	-	800-1000	‘Hort16A’	EV	Clark et al. (2004)
0.77	0.97	-	865-1711	‘Xixuan’	IV	Guo et al. (2016)
0.97	0.59	-	865-1711	‘Huayou’	IV	Guo et al. (2016)
-	0.9	-	865-1711	‘Xuxiang’	IV	Guo et al. (2019)
0.97-0.98	0.46-0.55	-	408-2492	‘Hayward’	IV	Lee et al. (2012)
0.80-0.84	1.38-1.58	2.2-2.5	730-1200	‘Autumn Sense’ + ‘Daesung’	IV	Lee et al. (2019)
0.58-0.83	0.66-1.02	1.5-2.3	400-2450	‘Hayward’	IV	Li et al. (2017)
0.77	0.76	1.9	740-1070	‘Zesy002’	EV	Li et al. (2018)
0.74	0.7	-	1002–2300	*Actinidia chinensis*	IV	Ma et al. (2021)
0.88-0.90	0.36-0.39	2.7-3.5	800-1100	‘Hayward’	IV	McGlone & Kawano (1998)
0.76-0.85	0.47-0.96	1.4-2.2	800-1100	‘Hayward’	EV	McGlone & Kawano (1998)
0.94	0.32	-	800-1100	‘Hayward’	IV	McGlone et al.

						(2002)
0.89-0.93	0.31-0.71	-	800-1100	‘Hort16A’	IV	McGlone et al. (2007)
0.93	0.26	-	400-1000	‘Hayward’	IV	Moghimi et al. (2010)
0.61-0.79	0.97-2.08	1.5-2.4	729–975	‘Autumn sense’ + ‘Chungsan’ + ‘Daesung’ + ‘Green ball’	IV	Sarkar et al. (2020)
0.93	0.80	-	300-1100	Actinidia chinensis	IV	Schaare & Fraser (2000)
0.97	0.36	-	400-2200	-	IV	Shibang (2021)
0.91	1.01	3.3	730-1147	‘Jintao’	IV	Vieira et al. (2017)
0.95	0.40	3.3	450-1000	‘Xuxiang’ + ‘Hongyang’ + ‘Cuixiang’	IV	Zhu et al. (2017)

There are not SSC models for ‘Jintao’ kiwifruit, except for that of Vieira et al. (2017). Although there is extensive experience with the Kiwi Meter (Rocchi et al., 2016), it does not provide directly SSC.

The results obtained in other kiwifruit cultivars are still relevant for the comparison. They showed that the results of SSC model developed in this work are inferior to most the results published in the literature. The global panorama of the published models may be understood by two main factors: *i)* the quality of the equipment, which translates in SNR values across some wavelength range; *ii)* the fruit variability covered in the dataset (different orchards or sources, harvesting periods, shelf-life and storage conditions). There is a third transversal factor to explain the performance parameters, which is the use of a proper external validation (EV).

In the following paragraphs these factors are discussed, together with other secondary features that may add additional insight into the results. Most of the published studies use internal validation (IV), which used a homogeneous splitting of the entire dataset as calibration and validation, while in EV, calibration and validation are heterogeneous datasets, obtained, for example, from different orchards or years. EV is more demanding than IV and therefore, a degradation of the results is expected when going from IV to EV. Examples of that difficulty may be found in McGlone & Kawano (1998) [RMSEP ~ 0.4 % in IV vs. RMSEP ~ 0.5 – 1 % in EV]; in Clark et al. (2004) [RMSEP ~ 0.8 – 0.9 % in IV vs. RMSEP ~ 1.4 % in EV] and Li et al. (2018) [RMSEP ~ 0.8%]. Considering that the present work used IV, the SSC model performance (RMSEP = 1.24 %) resembles more that of EV results. The 4 × 5-fold double cross-validation method used here increased RMSEP only by 0.1 % relatively to the standard IV (results not shown), so that other factors should explain the large RMSEP obtained. There is a clear trend in the published reports: the more homogeneous the dataset, the better the predictions for SSC. For example, Moghimi et al. (2010) [RMSEP = 0.32 %], Zhu et al. (2017) [RMSEP = 0.4 %] or Shibang (2021) [RMSEP = 0.36 %] use only one source/orchard and limited size datasets. Adding more variability by measuring fruit in different conditions, either by allowing some delay between the measurements or by using different storage and/or shelf-life conditions, usually tends to increase RMSEP. For example, Arazuri et al. (2005) included five different conditions in shelf-life and obtained RMSEP ~ 0.7 % (average of results in that paper). Guo et al. (2016) acquired two lots separated two weeks and measured the fruit in several days, along ripening, obtaining RMSEP ~ 0.6 – 1.0 %.

Models with several orchards tend to deliver the higher (and more realistic) RMSEP values. For example, Clark et al. (2004), with 20 orchards obtained RMSEP ~ 0.8 – 0.9 % (in IV); Li et al. (2017), with 50 orchards obtained RMSEP ~ 0.7 – 1.0 %; Lee et al. (2019), with 3 orchards obtained RMSEP ~ 1.4 – 1.6 % and Sarkar et al. (2020), with 10 orchards obtained RMSEP ~ 1.0 – 2.1 %.

The present work adds a new source of variability to the data. For the first time, the data includes measurements from the early pre-harvest. In the previous studies the variability is obtained by collecting the fruit some weeks before or after the harvest (commercial season) or by changing postharvest conditions. In this work, the variability is obtained from the very ripening process, along a period of 12 (orchard 2) or 13 weeks (orchard 1). Therefore, the datasets were very heterogeneous, including fruit in very different developmental stages. This means very different chemical and structural compositions MIXed in the same dataset. For example, the proportion of starch and sugars is very different at harvest and 10 weeks before, which represents an additional difficulty for retrieving information from the C–H bands. The cellular structure also changes considerably in that period, introducing more variability in the scattering effects. These factors necessarily sum up to degrade the calibration models' performance obtained in this work when compared to others developed more homogeneous samples. The spectrometer used in this work is noise limited above 950 nm, due to very poor SNR (Figure 4.1C). For this reason, important bands might be not included in the models, as the water band at 960 nm, 3ν(O–H), that should have an indirect, but important role in the SSC model (since more solubilized solids means less absolute quantity of water per juice unit volume). However, the best model for SSC did not include it, probably because of low SNR in that band. Therefore, low SNR in the water band may degrade the model predictions and this applies to all the models developed in this chapter.

4.3.2 Colorimetric parameters

The Hue pulp calibration model also delivers good performance (Figure 4.4A). There is an agglomeration of points in the upper part of the plot because most of the fruit had Hue above 110 º, as can also be seen in Figure 4.5. However, a good linearity was maintained for the lower values of Hue.

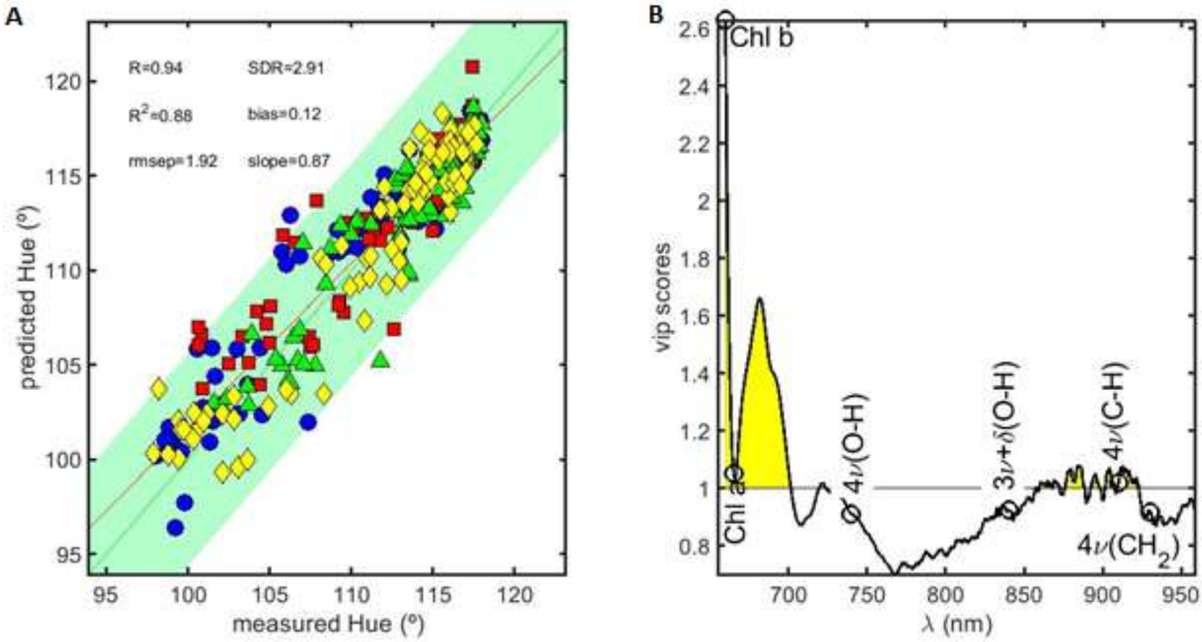

Figure 4.4: A) measured versus predicted values for ‘Jintao’ kiwifruit Hue. Each symbol corresponds to one test set. The green shadowed band has a half-width equal to the standard deviation of Hue. B) average VIP scores of the four models. The shadowed area corresponds to VIP > 1 and the white circles to the nominal position of the spectroscopic bands indicated.

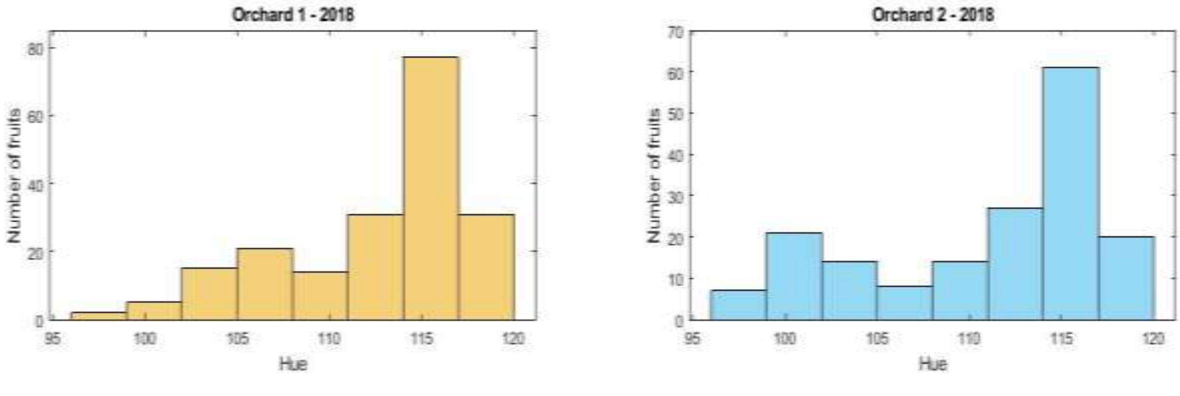

Figure 4.5: Histogram of Hue for ‘Jintao’ kiwifruit orchard 1 and orchard 2 in 2018.

The VIP scores plot has a prominent peak at about 660 nm, which may be assigned to the red peak of chlorophyll *b* (Figure 4.4B). Generally, there is a preponderance of the chlorophylls, a and b, in the model. Their importance is twofold: on one side there is an indirect correlation, since the chlorophyll content decreases simultaneously with Hue along ripening; on the other side, there is a direct correlation with the red colour and thus with Hue. As in the SSC model, there are two more bands with VIP > 1, and they are the same: 4v (O–H) and 4v (C–H). These cannot be a direct source of colour information, since they are out of the visible. So, they are conveying indirect information of water and organic molecules content changes along ripening.

Hue is a colorimetric parameter that changes approximately from around 120º (light green) to 100 º (yellow - green) along the ripening process (McGuire, 1992). Therefore, it would be expectable to have the best calibration model defined in the visible range or, at least, including green and yellow. However, this was not observed. In fact, including the wavelength range below 660 nm (red) degraded the model. Part of the explanation is that the spectral range below 500 nm is in the higher noise regime (Figure 4.1C). Thus, the spectral band 400 – 500 nm is not included in the model (Table 4.1). However, this does not explain why the band 500 – 660 nm is also rejected. This is probably because absorption in that range is largely determined by carotenoid content, which changes much less than chlorophyll along ripening. Therefore, the later relates much better than the former with changes in pulp colour. Skin colour necessarily interferes with the pulp colour measurement, since light must cross the skin twice, along the path between the light injection fiber and the light collection fibers. Furthermore, in the reflectance mode there are additional photons scattered by the skin, which are devoid of information from the pulp. As mentioned above, the interactance probe used in this work may have collected such photons with corresponding degradation of the results. On the other side, the near infrared part of the spectrum is less contaminated by the skin absorption because its pigments absorb essentially in the visible, and this explains why the calibration model includes the infrared.

There are not many reports on the prediction of Hue (Table 4.3). Clark et al. (2004) obtained RMSEP = 0.85–1.37 º in IV and 1.11 º in EV, McGlone et al. (2007) obtained RMSEP = 0.98–1.05 º and Schaare & Fraser (2000) obtained RMSEP =

1.63 º. Again, the present results are inferior to the published ones, although similar to last one. A possible reason for this situation is a best SNR provided by the spectrometer employed by these authors, which allowed them to use lower wavelengths.

Table 4.3: Kiwifruit Hue models' prediction. Valid. = Validation; IV = Internal validation; EV = External validation.

R^2	RMSEP(º)	SDR	Range	Kiwifruit	Valid.	Reference
0.88	1.92	2.9	660-959	'Jintao'	IV	This chapter
0.68-0.86	0.85-1.37	-	500-750	'Hort16A'	IV	Clark et al. (2004)
0.63	1.11	-	500-750	'Hort16A'	EV	Clark et al. (2004)
0.81-0.88	0.98-1.05	-	500-750	'Hort16A'	IV	McGlone et al. (2007)
0.82	1.63	-	300-1100	*Actinidia chinensis*	IV	Schaare & Fraser (2000)

Relatively to the other colorimetric parameters models, a*, L*, b* and chroma, only a* delivers good performance (Figure 4.6A). Its VIP scores plot reveal that the fundamental source of information is the chlorophyll band, with a minor contribution from the 4v (C–H) band (Figure 4.6B). This agrees with the fact that the a* measures the green to red transition and is intimately related with the chlorophyll content.

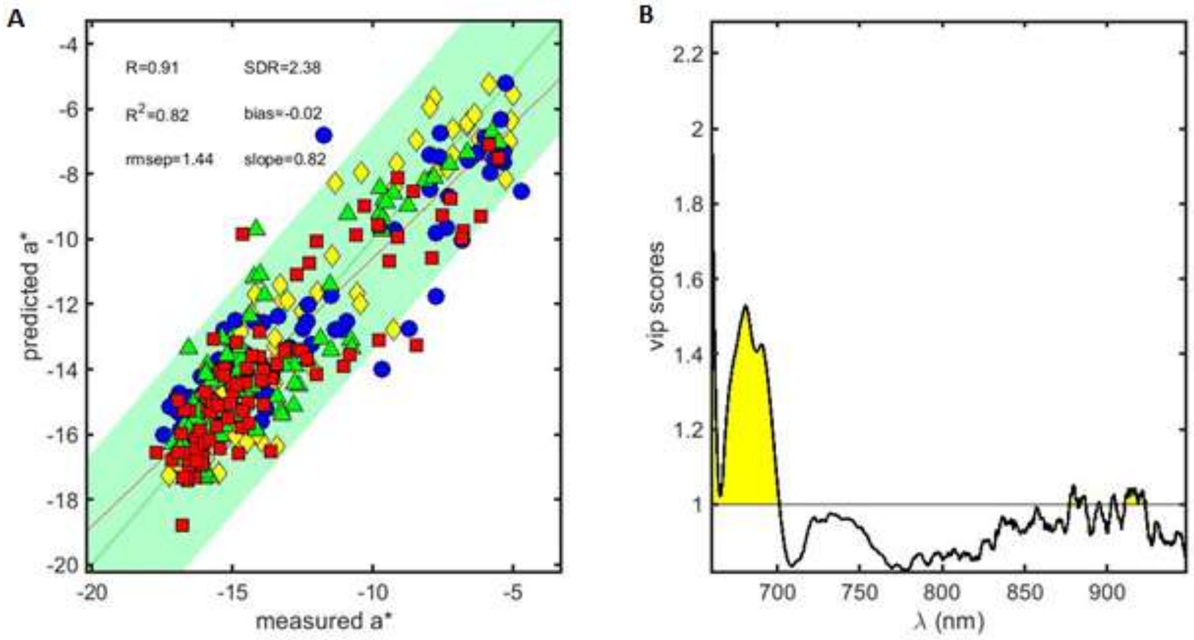

Figure 4.6: A) measured versus predicted values for 'Jintao' kiwifruit a*. Each symbol corresponds to one test set. The green shadowed band has a half-width equal to the standard deviation of a*. B) average VIP scores of the four models. The shadowed area corresponds to VIP > 1.

.

The performance of the remaining colorimetric parameters L*, b* and chroma are all poor, with SDR < 1.4 for all the three cases (Figure 4.7A, Figure 4.**8**A and Figure 4.**9**A).

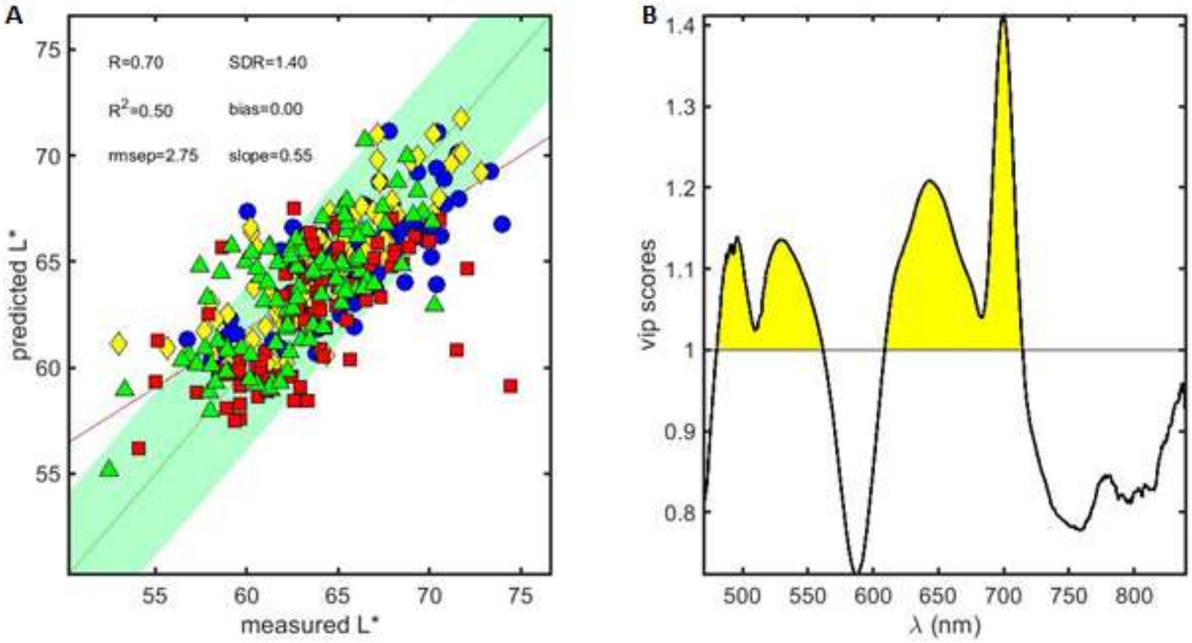

Figure 4.7: A) measured versus predicted values for ‘Jintao’ kiwifruit L*. Each symbol corresponds to one test set. The green shadowed band has a half-width equal to the standard deviation of L*. B) average VIP scores of the four models. The shadowed area corresponds to VIP > 1.

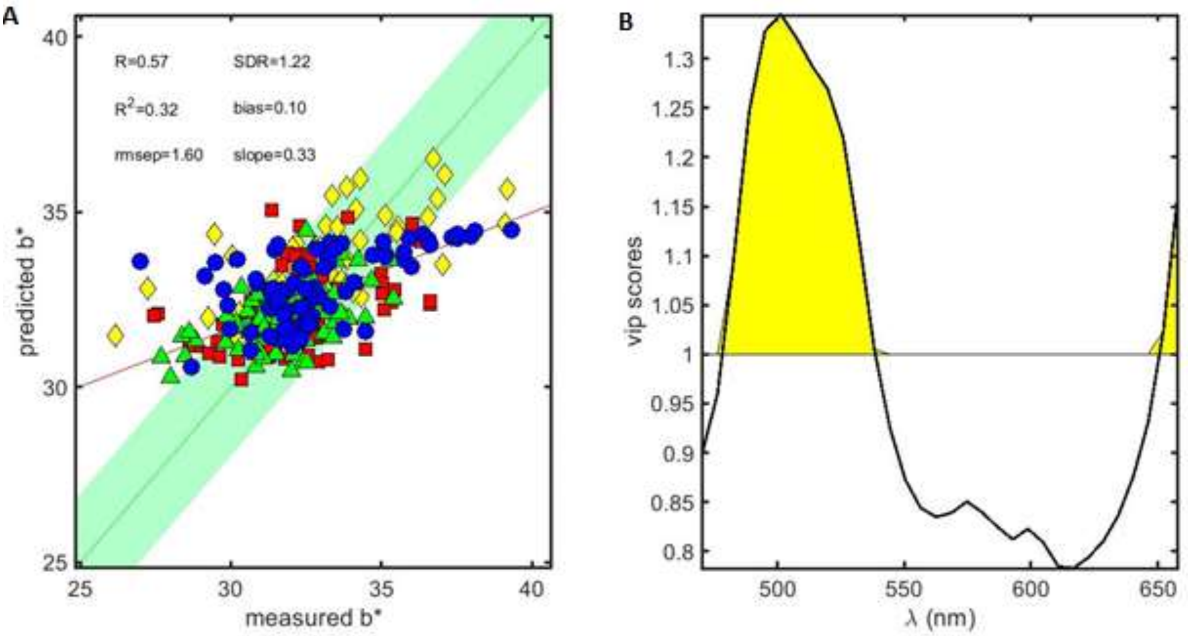

Figure 4.8: A) measured versus predicted values for ‘Jintao’ kiwifruit b*. Each symbol corresponds to one test set. The green shadowed band has a half-width equal to the standard deviation of b*. B) average VIP scores of the four models. The shadowed area corresponds to VIP > 1.

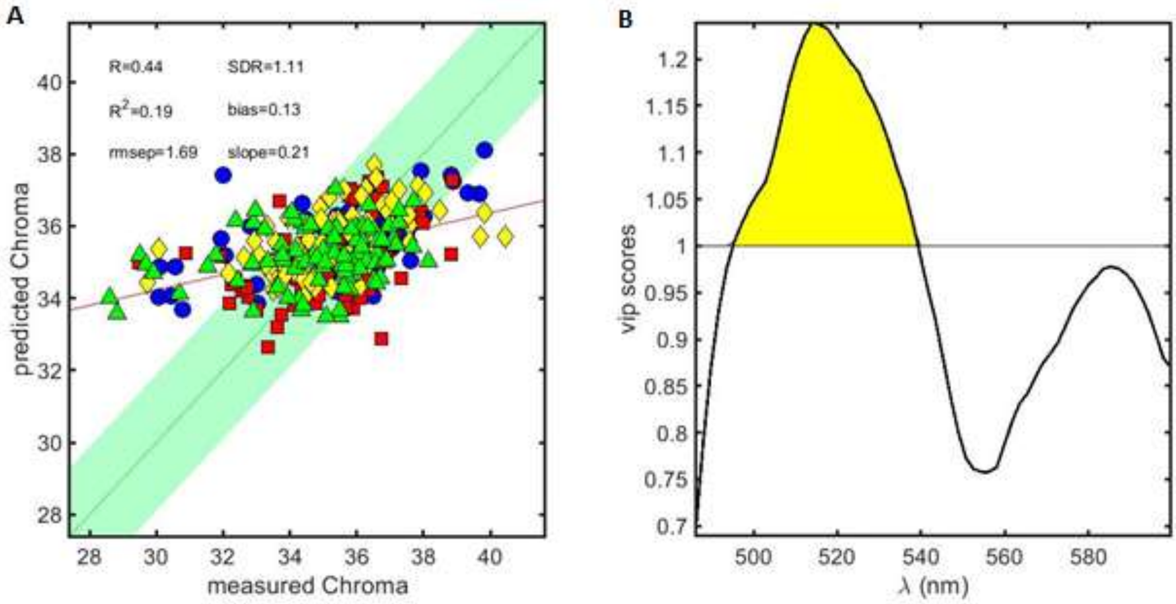

Figure 4.9: A) measured versus predicted values for ‘Jintao’ kiwifruit chroma. Each symbol corresponds to one test set. The green shadowed band has a half-width equal to the standard deviation of chroma. B) average VIP scores of the four models. The shadowed area corresponds to VIP > 1.

The poor performance of the b* model results from the difficulty in retrieving reliable information on the blue, as mentioned above (Figure 4.8). The average reflectance in the blue, although low, seems enough for the purpose of building models (Figure 4.1A and 4.1B). However, SNR is very low in the blue (Figure 4.1C), yielding a poor-quality signal in that range and, consequently, perform a poor model.

These finding highlights, again, the crucial role of SNR for obtaining good models. The difficulties found in the L* and chroma models result from the original problems in the determination of b*, since the correct calculation of L* and chroma depends on the correct estimate of b*.

Other reports about kiwifruit L*, b*, a* and chroma were not found.

4.3.3 Dry matter

The performance of the DM model is fair (Figure 4.10A). This means that coarse separation of fruit is possible, in high and low values.

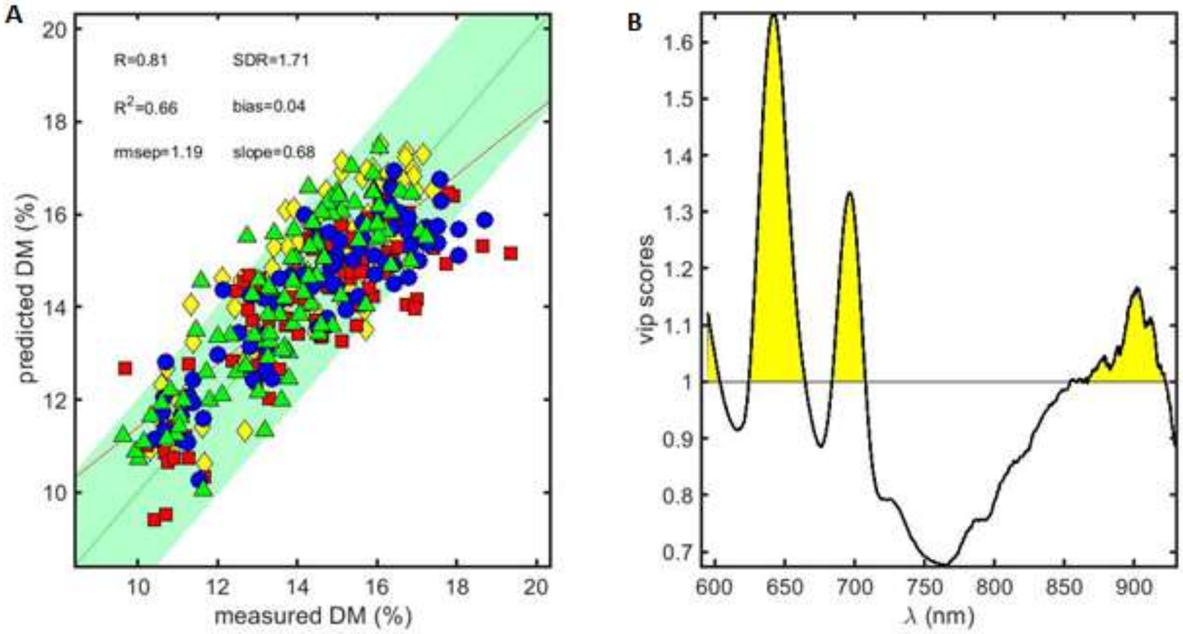

Figure 4.10: A) measured versus predicted values for ‘Jintao’ kiwifruit DM. Each symbol corresponds to one test set. The green shadowed band has a half-width equal to the standard deviation of DM. B) average VIP scores of the four models. The shadowed area corresponds to VIP > 1.

In the case of dry matter, the larger deviations from the measured values are observed mainly in the squares, since for the test set #1 (squares) the maximum DM value of 19.4 % in validation exceeds by more than 1 % the maximum value in calibration (18.7 %), affecting the models’ performance (Table 4.4).

Table 4.4: Statistics of the four dataset pairs calibration/test used for the prediction of ‘Jintao’ kiwifruit SSC, Hue, DM and firmness.

Validation set	Calibration set	IQA	Calibration				Validation			
			mean	std	max	min	mean	std	max	min
1 (squares)	234	SSC (%)	6.7	2.7	14.5	3.7	6.7	2.8	14.3	3.5
		Hue (º)	112	6	118	98	113	5	118	101
		DM (%)	14.2	1.98	18.7	9.6	14.4	2.2	19.4	9.7
		Firmness (N)	57.5	13.5	91.9	11.4	55.4	12.7	83.6	18.2
2 (triangles)	134	SSC (%)	6.8	2.8	14.5	3.5	6.4	2.7	13.0	4.0
		Hue (º)	112	6	118	98	113	4	118	102
		DM (%)	14.5	2.1	19.4	9.7	13.8	1.8	17.2	9.6
		Firmness (N)	58.0	13.2	91.9	11.4	54.3	13.3	84.3	18.3
3 (circles)	124	SSC (%)	6.6	2.7	14.5	3.5	6.9	2.9	14.3	3.7
		Hue (º)	112	5	118	98	111	6	118	98
		DM (%)	14.2	2.0	19.4	9.6	14.7	2.2	18.7	10.4
		Firmness (N)	56.2	13.0	91.1	18.2	59.5	14.3	91.9	11.4
4 (diamonds)	123	SSC (%)	6.7	2.8	14.3	3.5	6.7	2.7	14.5	4.1
		Hue (º)	112	5	118	98	111	6	118	98
		DM (%)	14.3	2.1	19.4	9.6	14.3	1.9	17.4	10.3
		Firmness (N)	56.2	13.6	91.9	11.4	59.3	12.4	91.1	27.5

For DM, the upper wavelength range is 931 nm, which excludes the main water peak. However, the result displayed in Figure 4.10B shows another, sub-optimal model, that includes the water band. The reason to illustrate two different models is to discuss the role of the 3v (O–H) absorption band, located near 960 nm. This is the main feature related to water content and yet the best model for DM did not include it (Table 4.1). On the other side, the sub-optimal model of Figure 4.10B includes the water band, which takes the prominent role, as observed in the VIP scores plot. Spectrometer noise is again the most likely explanation for the absence of the water peak in the best model, since the band at 960 – 980 nm is already in the higher noise regime (Figure 4.1C). Since the changes in DM content are of the order of few percent, a level of SNR below 200 (observed in the water band) makes a real difference in terms of numerical reliability. This is an extreme example of the importance of SNR, since the most important source of information was excluded due to the noise affecting it.

The comparison with the literature results is the most unfavourable of all the IQA (Table 4.5). Published results for DM include RMSEP= 0.33 % (Ciccoritti et al., 2019), 0.44 – 0.50 % in IV and 0.54 % in EV (Clark et al., 2004), 0.77% (Kim et al., 2018), 0.36 – 0.44 % in IV and 0.47 – 0.69 % in EV (McGlone and Kawano, 1998), 0.29 % (McGlone et al., 2002), 0.24 – 0.40 % (McGlone et al., 2007), 0.53 – 0.59 % (Qiang et al., 2010), 0.41 – 0.57 % (Tang et al., 2010) and 0.73 % (Vieira et al., 2017).

Table 4.5: Kiwifruit dry matter models' prediction. Valid. = Validation; IV = Internal validation; EV = External validation.

R^2	RMSEP(%)	SDR	Range	Kiwifruit	Valid.	Reference
0.66	1.19	1.7	595-931	'Jintao'	IV	This chapter
0.98	0.33	7.8	850-2500	'Hayward' + 'Boerica'	IV	Ciccoritti et al. (2019)
0.90-0.93	0.44-0.50	-	800-1000	'Hort16A'	IV	Clark et al. (2004)
0.91	0.54	-	800-1000	'Hort16A'	EV	Clark et al. (2004)
0.74	0.77	3.4	729-975	'Saehan'	IV	Kim et al. (2018)
0.86-0.92	0.36-0.44	2.7-3.6.	800-1100	'Hayward'	IV	McGlone & Kawano (1998)
0.85-0.86	0.47-0.69	0.9-2.5	800-1100	'Hayward'	EV	McGlone & Kawano (1998)
0.94	0.29	-	800-1000	'Hayward'	IV	McGlone et al. (2002)
0.91-0.97	0.24-0.40	-	800-1000	'Hort16A'	IV	McGlone et al. (2007)
0.88-0.90	0.53-0.59	-	1000-2500	'Zhonghua'	IV	Quiang et al. (2010)
0.86-0.94	0.41-0.57	-	1000-2500	'Zhonghua'	IV	Tang et al. (2010)
0.47	0.73	1.4	730-1147	'Jintao'	IV	Vieira et al. (2017)

4.3.4 Firmness

The calibration model of firmness has R^2 = 0.61, RMSEP= 8.39 N and SDR= 1.59, which means that it captures some information (Figure 4.11A). Inspection of VIP scores reveals, again, a preponderance of the chlorophyll band and some weight attributed to a new band centred around 785 nm (Figure 4.11B). The relation with chlorophyll is indirect, as its content decreases together with firmness along ripening. On the other side, the 785 nm region is interesting because it lacks relevant chemical absorption bands. However, this may be appropriate for modelling firmness, since the changes induced by the scattering effects of the tissue structure are less obscured by absorption effects in this spectral region.

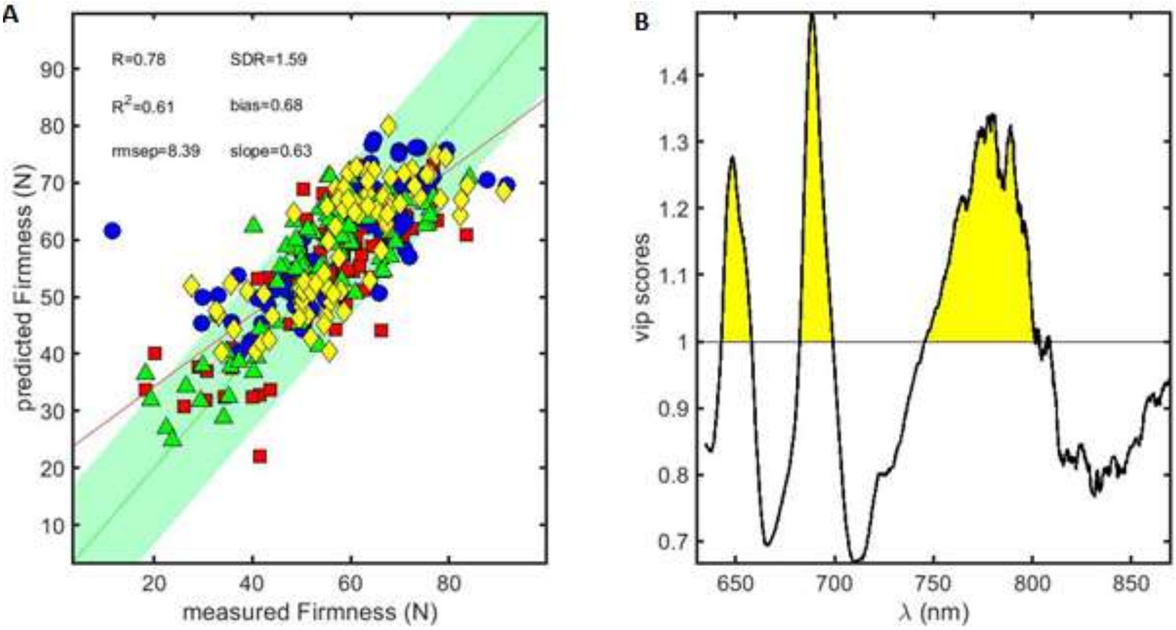

Figure 4.11: A) measured versus predicted values for ‘Jintao’ kiwifruit firmness. Each symbol corresponds to one test set. The green shadowed band has a half-width equal to the standard deviation of firmness. B) average VIP scores of the four models. The shadowed area corresponds to VIP > 1.

Despite the moderate/poor result, the firmness model is the one that compares better with the literature (Table 4.6), being approximately equal to those obtained by Benelli et al. (2022) [RMSEP= 9.9 – 14.5 N], Fu et al. (2007) [6.3 – 7.0 N], Li et al. (2018) [11.9 N], McGlone & Kawano (1998) [4.5 – 7.8 N in IV], Vieira et al. (2017) [11.6 N], although inferior to the results obtained by Lee et al. (2012) [2.8 –

4.0 N] and Li et al. (2017) [2.7 – 4.3 N]. The latter were obtained in the approximate range 400 – 2500 nm, which may point to some advantage of using longer wavelengths. Wang et al (2022a) obtained the best RMSEP = 0.37 N, however the spectra was acquired from kiwifruit slices, with no interference of skin signal as in the other reports.

Table 4.6: Kiwifruit firmness models' prediction. Valid. = Validation; IV = Internal validation; EV = External validation.

R^2	RMSEP(N)	SDR	Range	Kiwifruit	Valid.	Reference
0.61	8.4	1.6	635-870	'Jintao'	IV	This chapter
0.82-0.92	9.9-14.5	-	424-1000	'Hayward	IV	Benelli et al. (2022)
0.49-0.57	6.3-7.0	-	800-2500	'Qinmei'	IV	Fu et al. (2007)
0.88-0.94	2.8-4.0	-	408-2492	'Hayward'	IV	Lee et al. (2012)
0.30-0.60	2.7-4.3	1.4-1.7	400-2450	'Hayward'	IV	Li et al. (2017)
0.56	11.9	1.4	740-1070	'Zesy002'	EV	Li et al. (2018)
0.52-0.76	4.5-7.8	1.6-2	800-1100	'Hayward'	IV	McGlone & Kawano (1998)
0-0.42	12-85	< 1	800-1100	'Hayward'	EV	McGlone & Kawano (1998)
0.81	11.6	2.3	730-1147	'Jintao'	IV	Vieira et al. (2017)
0.90	0.37	2.89	833-2500	'Qinmei'	IV	Wang et al. (2022a)
0.98	36.3	5.2	450-1000	'Xuxiang'	IV	Zhu et al. (2017)

4.3.5 Titrable acidity

The model for TA has poor to zero performance with R^2 = 0.12, RMSEP= 0.12 % and SDR= 1.04 it has an almost null predictive power (Figure 4.12A).

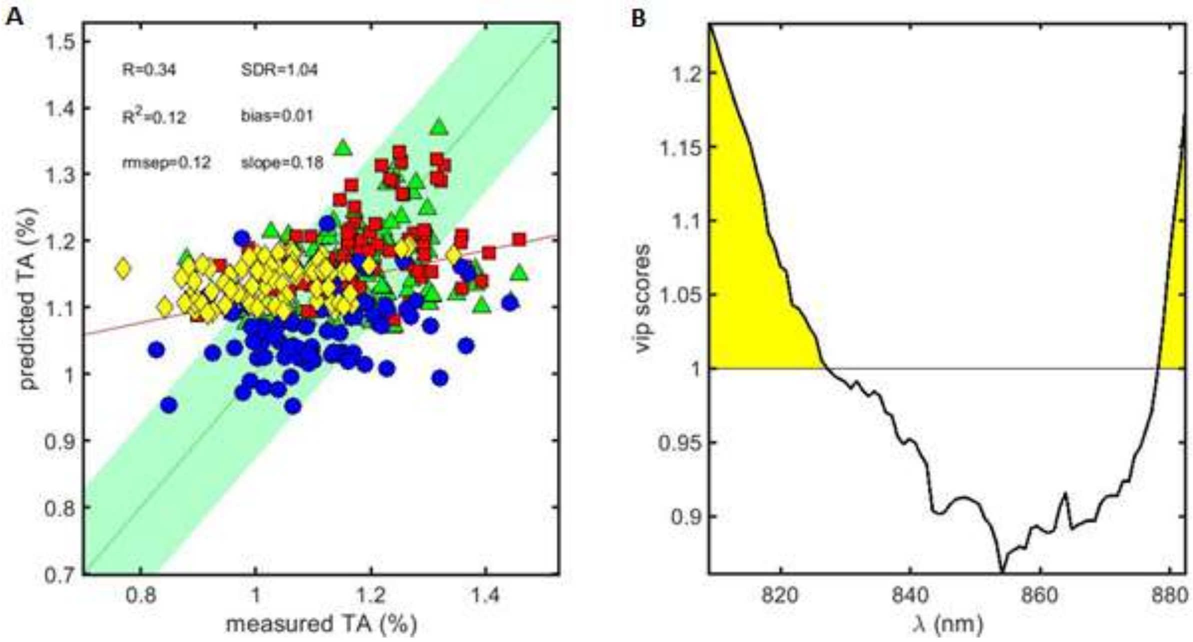

Figure 4.12: A) measured versus predicted values for ‘Jintao’ kiwifruit TA. Each symbol corresponds to one test set. The green shadowed band has a half-width equal to the standard deviation of TA. B) average VIP scores of the four models. The shadowed area corresponds to VIP > 1.

It is interesting that the model of Vieira et al. (2017) predicted slightly better (R^2 = 0.52, RMSEP= 0.25 % and SDR = 1.4), probably because it included wavelengths up to 1147 nm (Table 4.7). The spectral range seems decisive here. Using an upper range of 2500 nm, Ciccoritti et al. (2019) and Lee et al. (2012) obtained R^2 > 0.9.

Table 4.7: Kiwifruit titrable acidity models' predictions. Valid. = Validation; IV = Internal validation; EV = External validation.

R^2	RMSEP (%)	SDR	Range	Kiwifruit	Valid.	Reference
0.12	0.12	1.0	809-883	'Jintao'	IV	This chapter
0.93	0.19	3.9	850-2500	'Hayward' + 'Boerica'	IV	Ciccoritti et al. (2019)
0.90-0.95	0.21-0.39%	-	408-2492	'Hayward'	IV	Lee et al. (2012)
0.52	0.25%	1.4	730-1147	'Jintao'	IV	Vieira et al. (2017)

4.3.6 pH

The same comments of TA apply to pH, although the pH results are slightly better (R^2 = 0.43, RMSEP= 0.12 and SDR= 1.32) (Figure 4.13A).

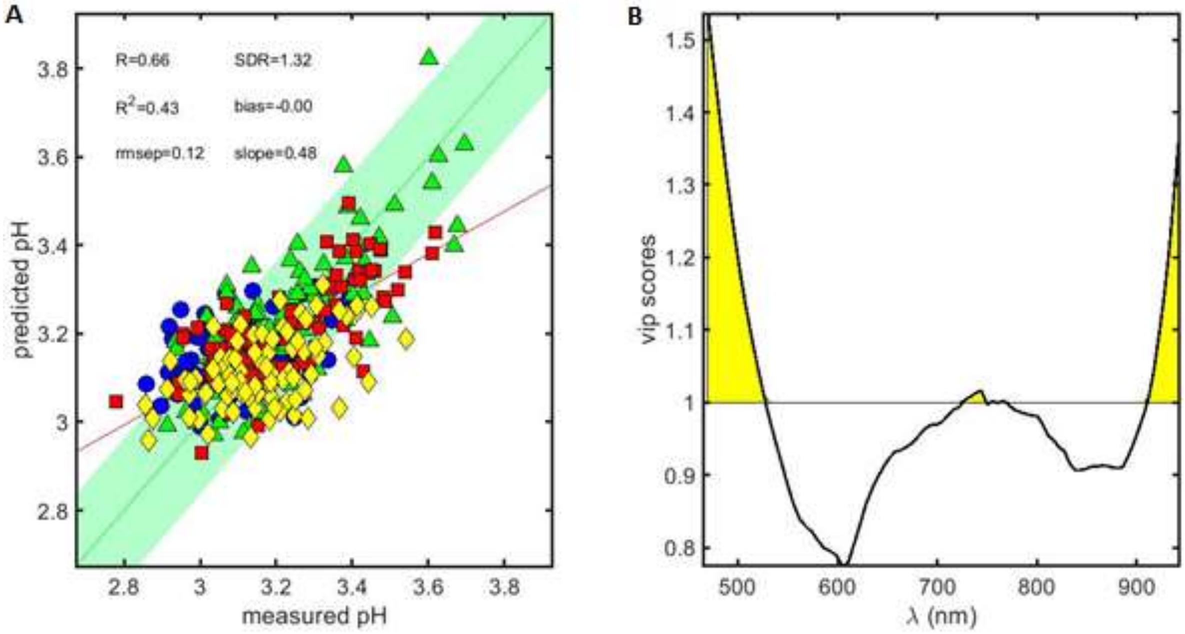

Figure 4.13: A) measured versus predicted values for 'Jintao' kiwifruit pH. Each symbol corresponds to one test set. The green shadowed band has a half-width equal to the standard deviation of pH. B) average VIP scores of the four models. The shadowed area corresponds to VIP > 1.

These results are clearly worse than the references available (Table 4.8). Moghimi et al. (2010), in which a high-quality benchtop spectrometer was used, and Wang et al. (2022c) with a similar range ~ 400 - 1100 nm obtained the same RMSEP= 0.076, despite the latter used hyperspectral fluorescence.

Zhu et al. (2017) [R^2 = 0.91, RMSEP= 0.015 and SDR= 2.6] and Ma et al. (2021) [R^2 = 0.68 and RMSEP= 0.13] may have benefited from a more adequate wavelength range. Although Ma et al. (2021) used hyperspectral imaging, also studied *Actinidia chinensis* and is the report that compares better with the work of this chapter [R^2 = 0.43 and RMSEP= 0.12].

Table 4.8: Kiwifruit pH models' prediction. Valid. = Validation; IV = Internal validation; EV = External validation.

R^2	RMSEP	SDR	Range	Kiwifruit	Valid.	Reference
0.43	0.12	1.3	470-948	'Jintao'	IV	This chapter
0.68	0.13	-	1002–2300	*Actinidia chinensis*	IV	Ma et al. (2021)
0.94	0.076	2.6	400-1000	'Hayward'	IV	Moghimi et al. (2010)
0.85	0.076	2.7	376.80–1011.05	'Red Sun'	IV	Wang et al. (2022c)
0.91	0.015	2.6	951-1670	'Xuxiang' + 'Hongyang'+ 'Cuixiang'	IV	Zhu et al. (2017)

4.4 Average 'Jintao' kiwifruit calibration model's predictions

Since the decision of harvesting is, usually, done by taking into account the average values of an orchard instead of individual fruit values, it was tested if average predictions could be an improvement over individual ones.

This approach was applied to predict all 'Jintao' kiwifruit IQA and the results showed that the average daily measurements are, in general, very close to the average daily predictions (Figure 4.14 to Figure 4.23), which is confirmed by the low number of asterisks in figures A and B, meaning that there are only a few statistically different means ($p < 0.05$).

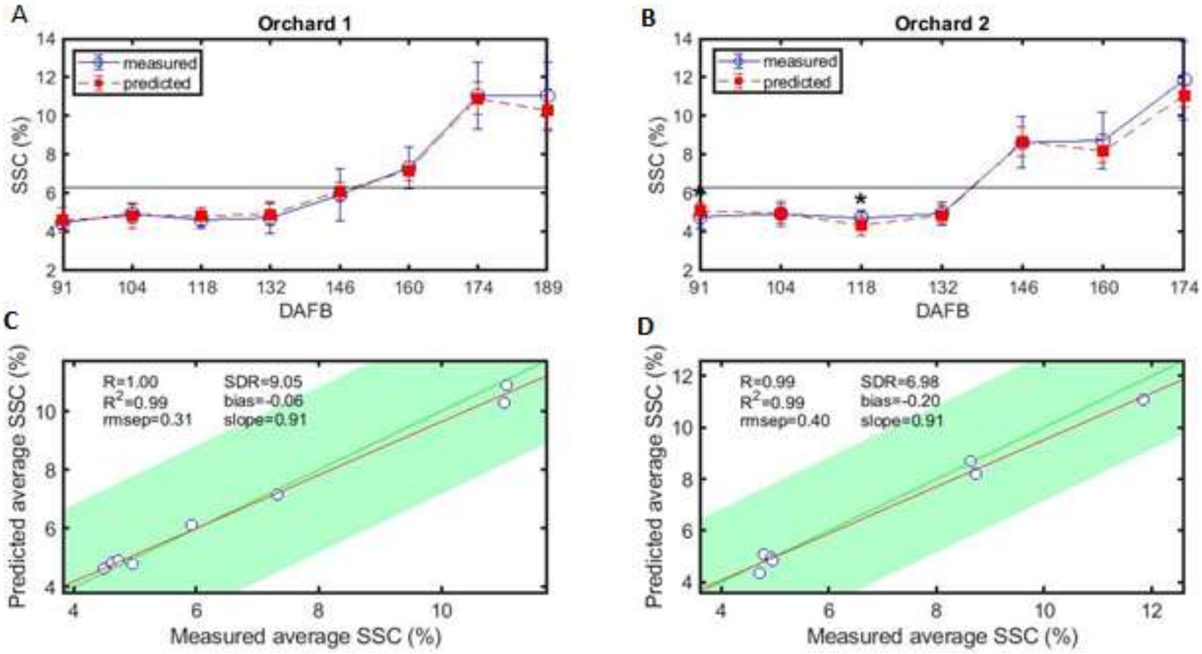

Figure 4.14: Average measured (open squares / solid line) and predicted (closed squares / dashed line) 'Jintao' kiwifruit SSC values for each date in: A) orchard 1; B) orchard 2. Each point represents the mean of the values in each DAFB (Days After Full Bloom) and the error bars represent their standard deviation. Statistically different means ($p < 0.05$) are signalled with an asterisk. Plot of average measured vs. average predicted Hue values and associated prediction statistics for: C) orchard 1; D) orchard 2.

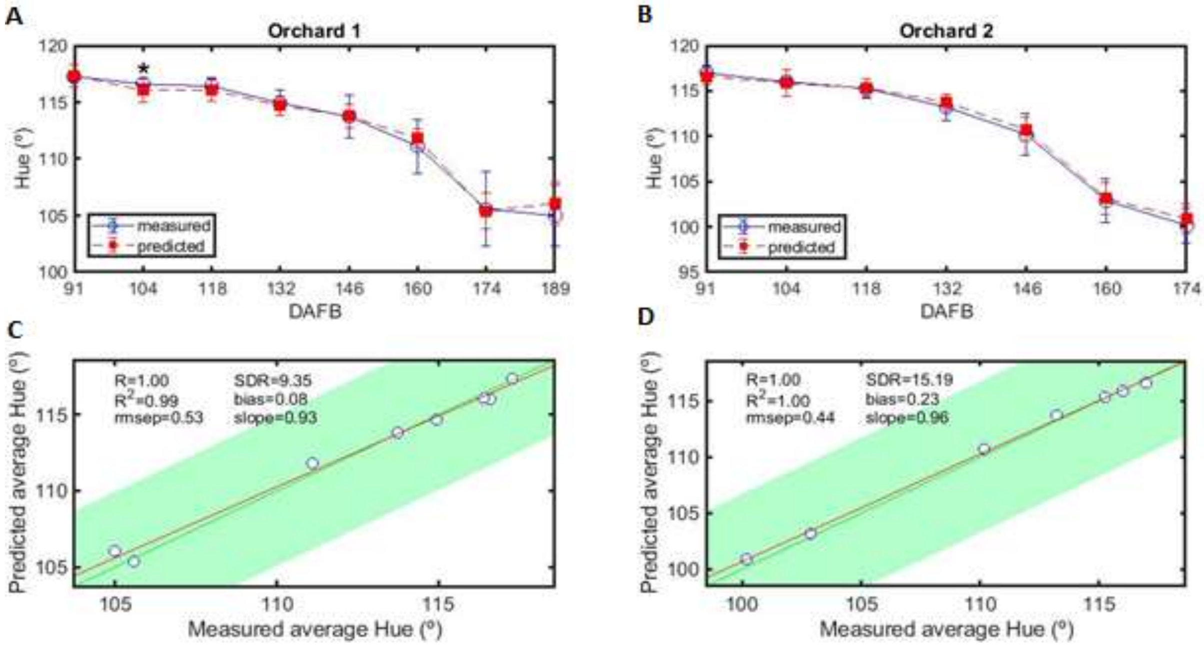

Figure 4.15: Average measured (open squares / solid line) and predicted (closed squares / dashed line) 'Jintao' kiwifruit Hue values for each date in: A) orchard 1; B) orchard 2. Each point represents the mean of the values in each DAFB (Days After Full Bloom) and the error bars represent their standard deviation. Statistically different means ($p < 0.05$) are signalled with an asterisk. Plot of average measured vs. average predicted Hue values and associated prediction statistics for: C) orchard 1; D) orchard 2.

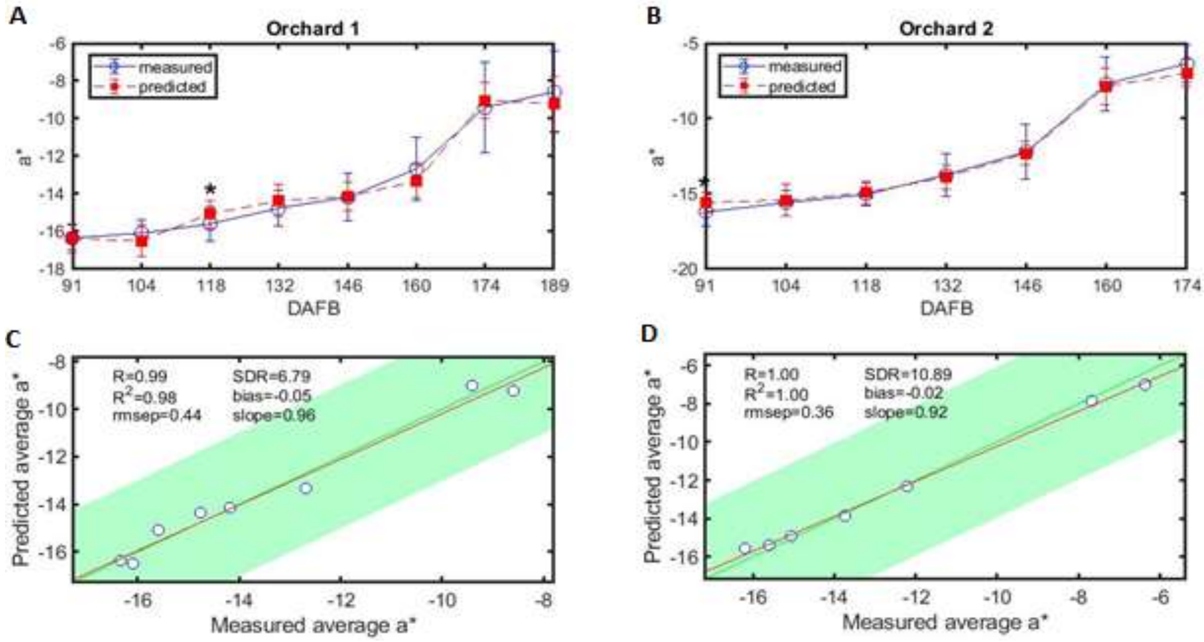

Figure 4.16: Average measured (open squares / solid line) and predicted (closed squares / dashed line) 'Jintao' kiwifruit a* values for each date in: A) orchard 1; B) orchard 2. Each point represents the mean of the values in each DAFB (Days After Full Bloom) and the error bars represent their standard deviation. Statistically different means ($p < 0.05$) are signalled with an asterisk. Plot of average measured vs. average predicted Hue values and associated prediction statistics for: C) orchard 1; D) orchard 2.

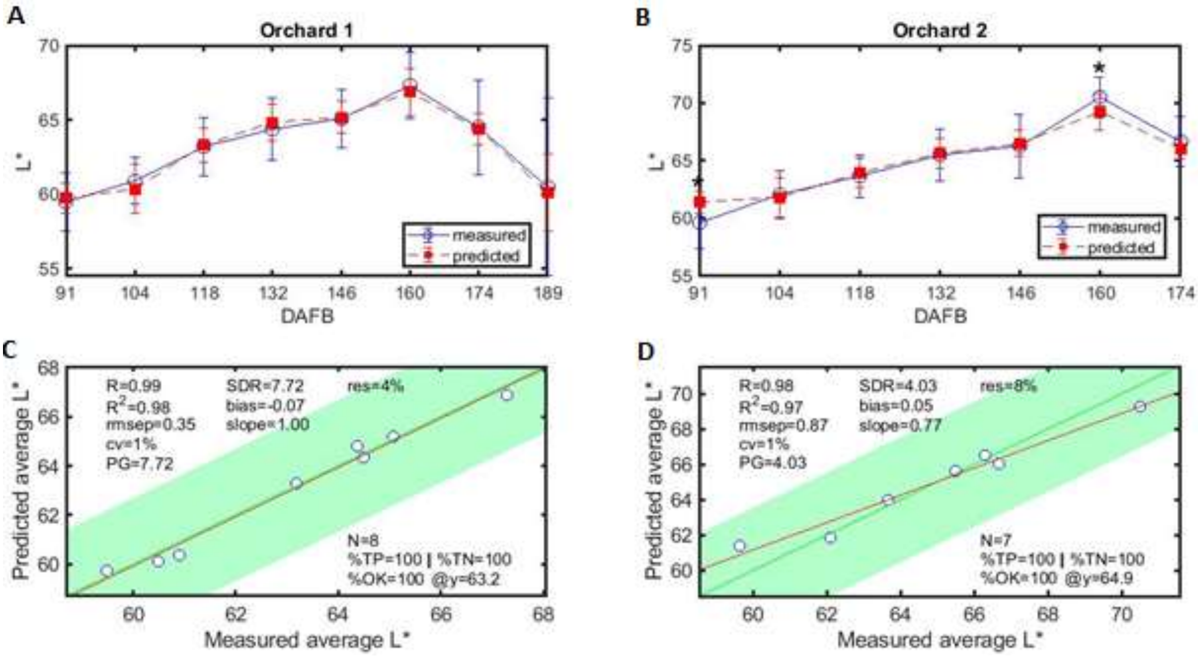

Figure 4.17: Average measured (open squares / solid line) and predicted (closed squares / dashed line) 'Jintao' kiwifruit L* values for each date in: A) orchard 1; B) orchard 2. Each point represents the mean of the values in each DAFB (Days After Full Bloom) and the error bars represent their standard deviation. Statistically different means ($p < 0.05$) are signalled with an asterisk. Plot of average measured vs. average predicted Hue values and associated prediction statistics for: C) orchard 1; D) orchard 2.

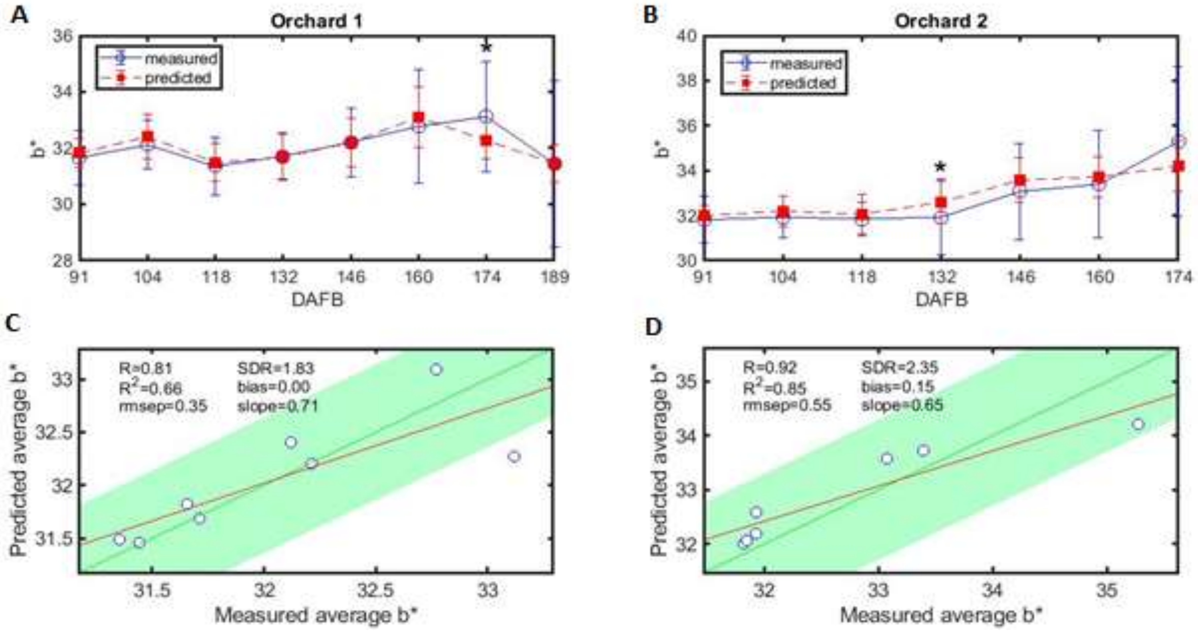

Figure 4.18: Average measured (open squares / solid line) and predicted (closed squares / dashed line) 'Jintao' kiwifruit b* values for each date in: A) orchard 1; B) orchard 2. Each point represents the mean of the values in each DAFB (Days After Full Bloom) and the error bars represent their standard deviation. Statistically different means ($p < 0.05$) are signalled with an asterisk. Plot of average measured vs. average predicted Hue values and associated prediction statistics for: C) orchard 1; D) orchard 2.

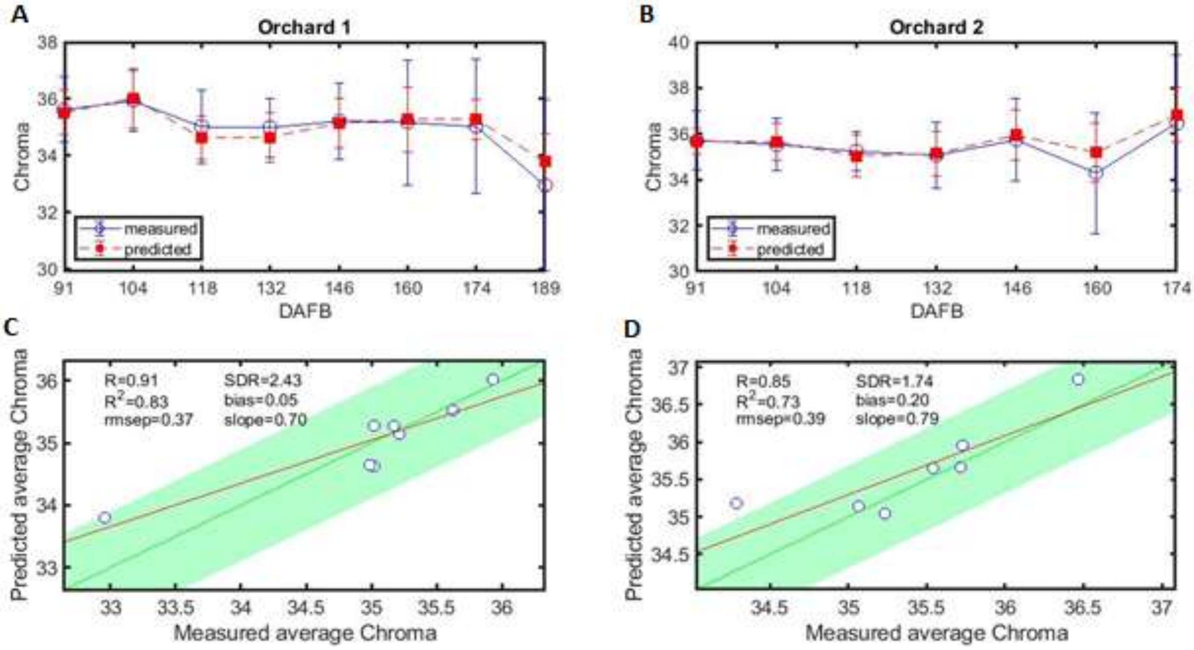

Figure 4.19: Average measured (open squares / solid line) and predicted (closed squares / dashed line) 'Jintao' kiwifruit chroma values for each date in: A) orchard 1; B) orchard 2. Each point represents the mean of the values in each DAFB (Days After Full Bloom) and the error bars represent their standard deviation. Statistically different means ($p < 0.05$) are signalled with an asterisk. Plot of average measured vs. average predicted Hue values and associated prediction statistics for: C) orchard 1; D) orchard 2.

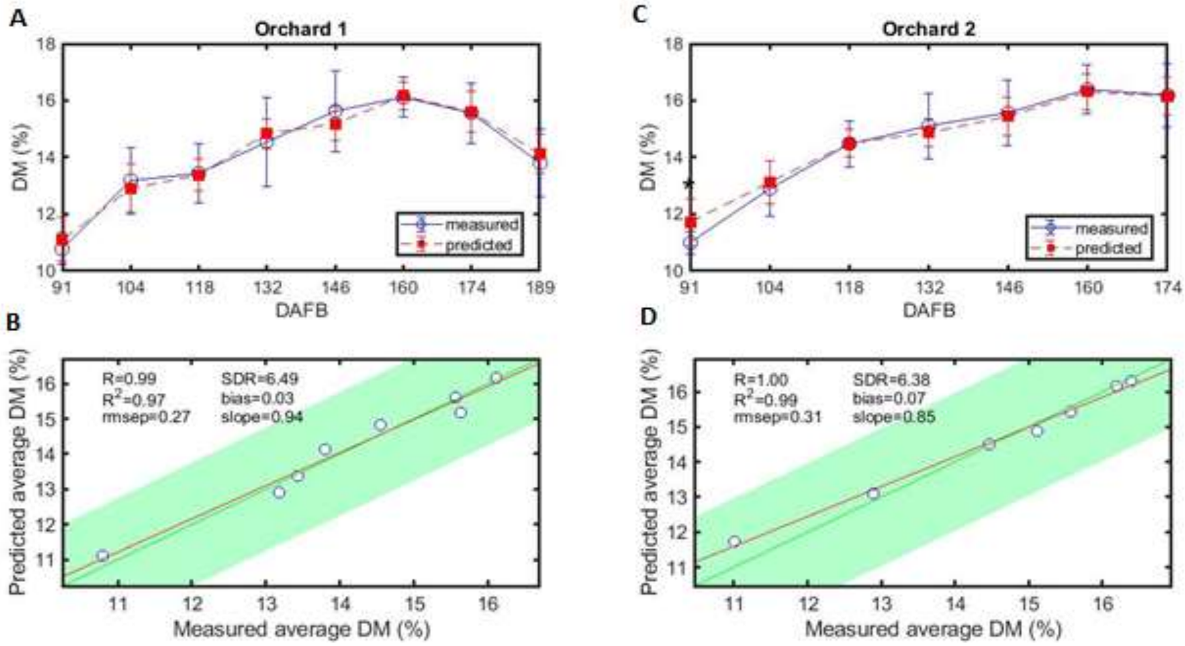

Figure 4.20: Average measured (open squares / solid line) and predicted (closed squares / dashed line) 'Jintao' kiwifruit dry matter values for each date in: A) orchard 1; B) orchard 2. Each point represents the mean of the values in each DAFB (Days After Full Bloom) and the error bars represent their standard deviation. Statistically different means ($p < 0.05$) are signalled with an asterisk. Plot of average measured vs. average predicted Hue values and associated prediction statistics for: C) orchard 1; D) orchard 2.

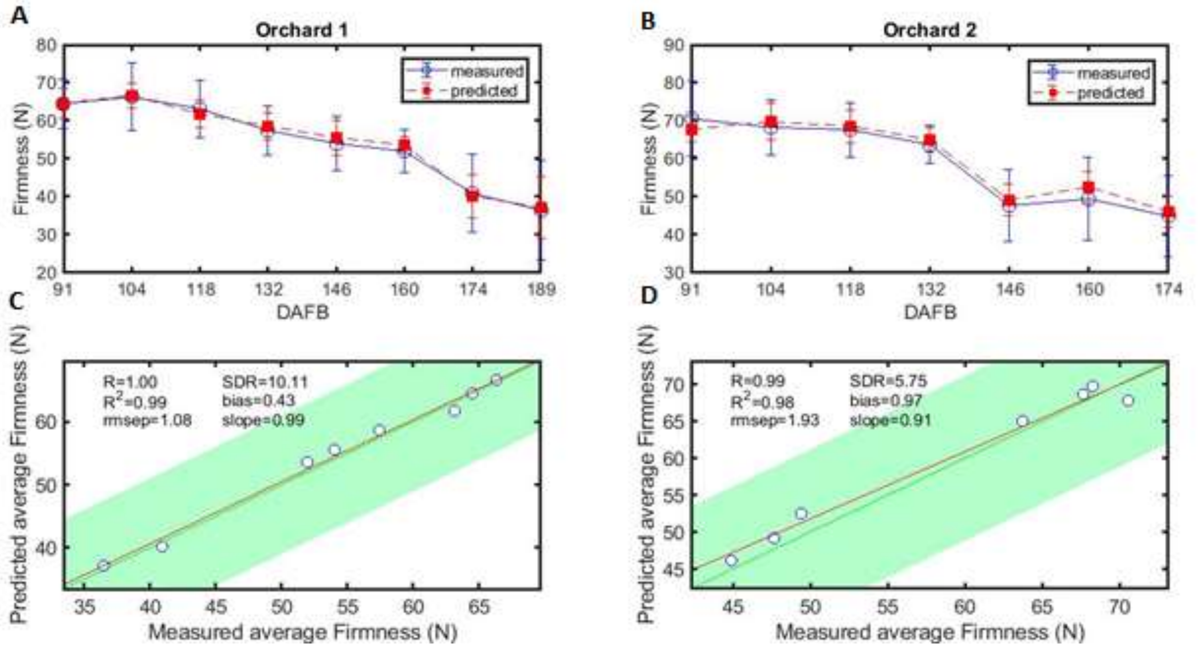

Figure 4.21: Average measured (open squares / solid line) and predicted (closed squares / dashed line) 'Jintao' kiwifruit firmness values for each date in: A) orchard 1; B) orchard 2. Each point represents the mean of the values in each DAFB (Days After Full Bloom) and the error bars represent their standard deviation. Statistically different means ($p < 0.05$) are signalled with an asterisk. Plot of average measured vs. average predicted Hue values and associated prediction statistics for: C) orchard 1; D) orchard 2.

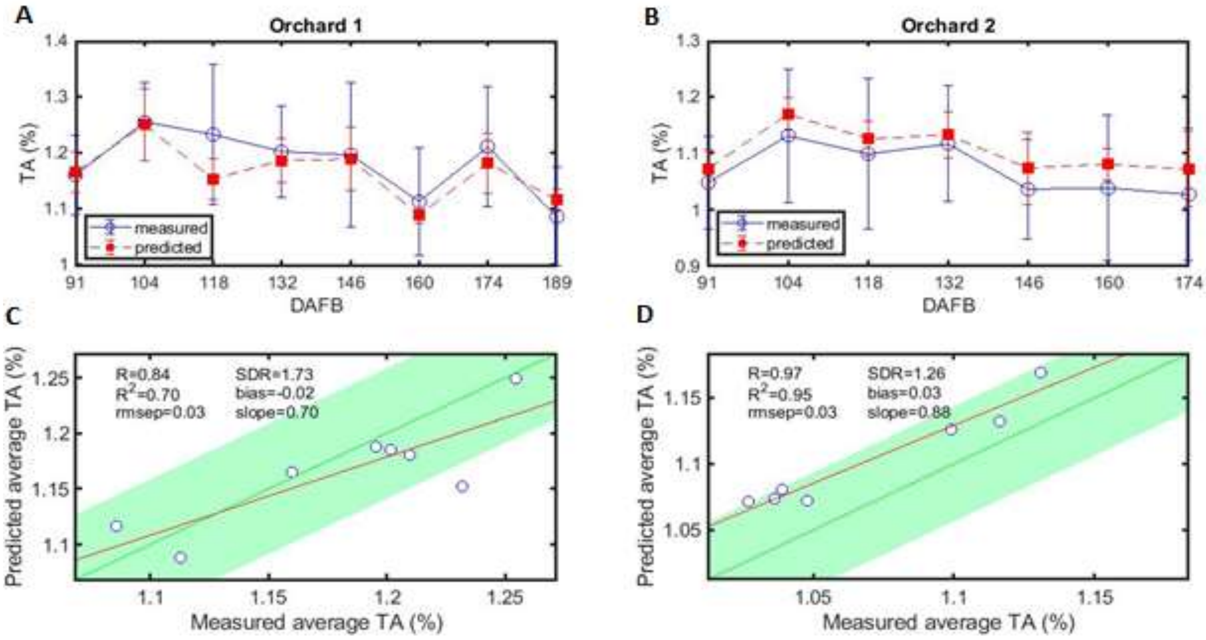

Figure 4.22: Average measured (open squares / solid line) and predicted (closed squares / dashed line) 'Jintao' kiwifruit titrable acidity (TA) values for each date in: A) orchard 1; B) orchard 2. Each point represents the mean of the values in each DAFB (Days After Full Bloom) and the error bars represent their standard deviation. Statistically different means ($p < 0.05$) are signalled with an asterisk. Plot of average measured vs. average predicted Hue values and associated prediction statistics for: C) orchard 1; D) orchard 2.

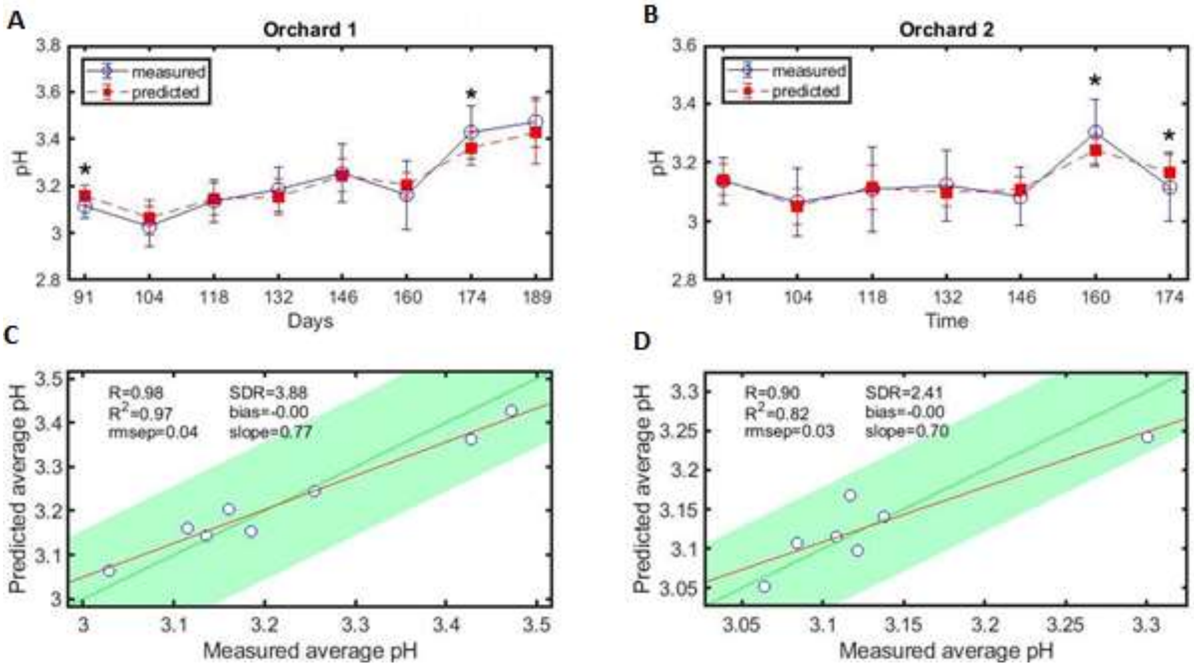

Figure 4.23: Average measured (open squares / solid line) and predicted (closed squares / dashed line) ‘Jintao’ kiwifruit pH values for each date in: A) orchard 1; B) orchard 2. Each point represents the mean of the values in each DAFB (Days After Full Bloom) and the error bars represent their standard deviation. Statistically different means ($p < 0.05$) are signalled with an asterisk. Plot of average measured vs. average predicted Hue values and associated prediction statistics for: C) orchard 1; D) orchard 2.

Indeed, from a total of 150 mean values observed [(8 +7) days x 2 orchards x 10 IQA] and their corresponding predicted mean values, only 13 (8.7 %) are statistically significant different (Table 4.9). The percentage is lower considering orchard 1 only (6.3 % or 5 in 80), but it is higher in orchard 2 (11.4 % or in 8 in 70).

This translates into R^2 values equal or above 0.97, except for b*, chroma, pH (only orchard 2) and TA (only orchard 1), six SDR values above 9 (both orchards Hue, orchard 1 SSC, orchard 1firmness and orchard 2 a*) and two of them are above 10 (orchard 1 firmness and orchard 2 a*) and one above 15 (orchard 2 Hue) (Table 4.10). Comparing Table 4.10 and Table 4.1, RMSEP values are around 3 – 5 times lower than those obtained for individual predictions and for firmness prediction the difference is even bigger with values, approximately, 9 times lower in orchard 1. These are excellent results, especially taking into account that the performance of some models, obtained in the chapter before, using the individual values is poor.

Table 4.9: Significant differences between average measured and average predicted ‘Jintao’ kiwifruit IQA values for each DAFB (Days After Full Bloom) (1 means difference; 0 no difference).

	Orchard 1								Orchard 2						
DAFB	91	104	118	132	146	160	174	189	91	104	118	132	146	160	174
SSC	0	0	0	0	0	0	0	0	1	0	1	0	0	0	0
Firmness	0	0	0	0	0	0	0	0	0	0	0	0	0	0	0
DM	0	0	0	0	0	0	0	0	1	0	0	0	0	0	0
TA	0	0	0	0	0	0	0	0	0	0	0	0	0	0	0
pH	1	0	0	0	0	0	1	0	0	0	0	0	0	1	1
L*	0	0	0	0	0	0	0	0	1	0	0	0	0	1	0
a*	0	0	1	0	0	0	0	0	1	0	0	0	0	0	0
b*	0	0	0	0	0	0	1	0	0	0	0	1	0	0	0
Hue	0	1	0	0	0	0	0	0	0	0	0	0	0	0	0
Chroma	0	0	0	0	0	0	0	0	0	0	0	0	0	0	0

Table 4.10: Results obtained in the PLS models for ‘Jintao’ kiwifruit quality attributes using average values.

	Orchard 1					Orchard 2				
IQA	RMSEP	R^2	SDR	Bias	Slope	RMSEP	R^2	SDR	Bias	Slope
SSC (%)	0.31	0.99	9.05	-0.06	0.91	0.40	0.99	6.98	-0.20	0.91
Firmness (N)	1.08	0.99	10.11	0.43	0.99	1.93	0.98	5.75	0.97	0.91
Dry matter (%)	0.27	0.97	6.49	0.03	0.94	0.31	0.99	6.38	0.07	0.85
TA (%)	0.03	0.70	1.73	-0.02	0.70	0.03	0.95	1.26	0.03	0.88
pH	0.04	0.97	3.88	0.00	0.77	0.03	0.82	2.41	0.00	0.70
L*	0.35	0.98	7.72	-0.07	1.00	0.87	0.97	4.03	0.05	0.77
a*	0.44	0.98	6.79	-0.05	0.96	0.36	1.00	10.89	-0.02	0.92
b*	0.35	0.66	1.83	0.00	0.71	0.56	0.85	2.35	0.15	0.65
Hue (˚)	0.53	0.99	9.35	0.08	0.93	0.44	1.00	15.19	0.23	0.96
Chroma	0.37	0.83	2.43	0.05	0.70	0.39	0.73	1.74	0.20	0.79

The conclusion is that the prediction of the average IQA for an orchard, or part of an orchard, is much more reliable than the prediction of individual IQA values. This was expected, due to the averaging effect. Therefore, good calibration models allow to achieve excellent average models, which in turn allow for an efficient follow-up of ripening in the orchard.

Average predictions provide a very reliable way of monitoring ripening and predict the harvest date. For example, in orchard 2, the average prediction of SSC at 146 DAFB signals perfectly the onset of harvesting (Figure 4.14B). For orchard 1, the average prediction at 160 DAFB is slightly delayed (Figure 4.14A).

In practice, more frequent assessments will allow to identify the IQA evolution patterns and to predict the optimal harvest date with some days/weeks in advance, what is very important for producers trading.

4.5 Best IQA for monitoring ‘Jintao’ kiwifruit ripening

The results of previous section lead to a question: why are poor models able to deliver good average predictions? Because the average values of some IQA vary very little from day to day. In other words, the averages to predict are approximately constant along ripening. This also implies that those IQA are useless for monitoring purposes.

A specific IQA is potentially useful for monitoring ripening if it varies significantly over time. Of course, practical application requires that selected IQAs meet the two conditions: robust models and significant variation over time.

The variability of the average daily values, in 2018, is shown in Table 4.11 in the column named “Season Change” and it is quantified as % change:

$$\text{Season Change} = \frac{\max(y_{av}) - \min(y_{av})}{mean\ (y_{av})}, \qquad (4.1)$$

where y_{av} represents the average daily measurements of a generic IQA.

Table 4.11: Season change, global change and % change of 'Jintao' kiwifruit IQA variation, using the data from 2018.

IQA	Orchard 1			Orchard 2			
	Season Change (%)	Global change (%)	% Season	Season Change (%)	Global change (%)	% Season	Good for follow-up?
SSC	101	203	50	104	181	57	Y
Firmness	57	121	47	52	146	36	N
Dry matter	38	69	55	37	58	64	Y
TA	14	66	21	10	63	16	N
pH	12	29	41	8	22	36	N
L*	13	38	34	17	32	53	N/Y
a*	-61	-103	59	-79	-102	77	Y
b*	8	46	17	11	42	26	N
Hue	12	19	63	15	18	83	Y
Chroma	11	44	25	5	36	14	N

All the colorimetric parameters change very little, except a*. The latter changes between 61 % (orchard 1) and 79 % (orchard 2), while b*, for example, only changes between 8 % and 11 % for the same orchards.

Table 4.11 contains two more columns for each orchard, which are the global change and the % of season change.

Global change is calculated in the same way as Season Change (6),

$$\text{Global change} = \frac{\max(y) - \min(y)}{mean\ (y)}\ x\ 100\ , \qquad (4.2)$$

but now y represents the measurements for a given IQA and not the daily average, as in Season Change (6). As the name suggests, it represents the global change on the data. The global change considers all the data variability (inter-days and intra-day variability), while the seasonal change only considers the inter-days variability associated with ripening. The column named % season is the ratio of the two preceding columns:

$$\%\ \text{season} = \frac{season\ change}{global\ change}\ x\ 100 \qquad (4.3)$$

It is a simple way to quantify the percentage of global variability that may be assigned to the seasonal changes.

Taking parameter b* as example. Its seasonal variability is only 17% of the global variability in orchard 1 and 26% in orchard 2. Thus, most of the variability is not explained by ripening but by intra-day variations). This means that each day shows approximately the same variability, centred on the same average value.

An opposite behaviour is shown, for example, by a*. Its seasonal variability is 59% of the global variability in orchard 1 and 77% in orchard 2. This means that the ripening changes are the main source of variability.

Only the IQA with dominant seasonal change should be used for ripening follow-up. It was considered “good for follow-up”, accordingly a threshold of 50% in % Season.

In practice, it is necessary that the selected IQAs satisfy the two conditions:

1. Be associated with robust models;
2. Be useful for follow-up.

The conclusion is that a*, Hue and SSC meet both criteria and are good follow-up IQA and the others have limited interest. The borderline IQAs are firmness, DM and L*. However, from these only DM is a potential candidate to the list of IQAs to be monitored, since firmness is not suitable for follow-up and L* does not have a robust model.

Chapter 5

Validation of prediction models

Afonso, Andreia M.; Antunes, Maria Dulce: Cavaco, Ana M.; Guerra, Rui. (2023). A simple calibration transfer method for temporal evaluation of kiwifruit ripening by Vis-NIR spectroscopy. (in preparation to be submitted)

5.1 Preliminary data exploration from two years

The raw data from the four datasets, two years and two orchards, is depicted in Figure 5.1.

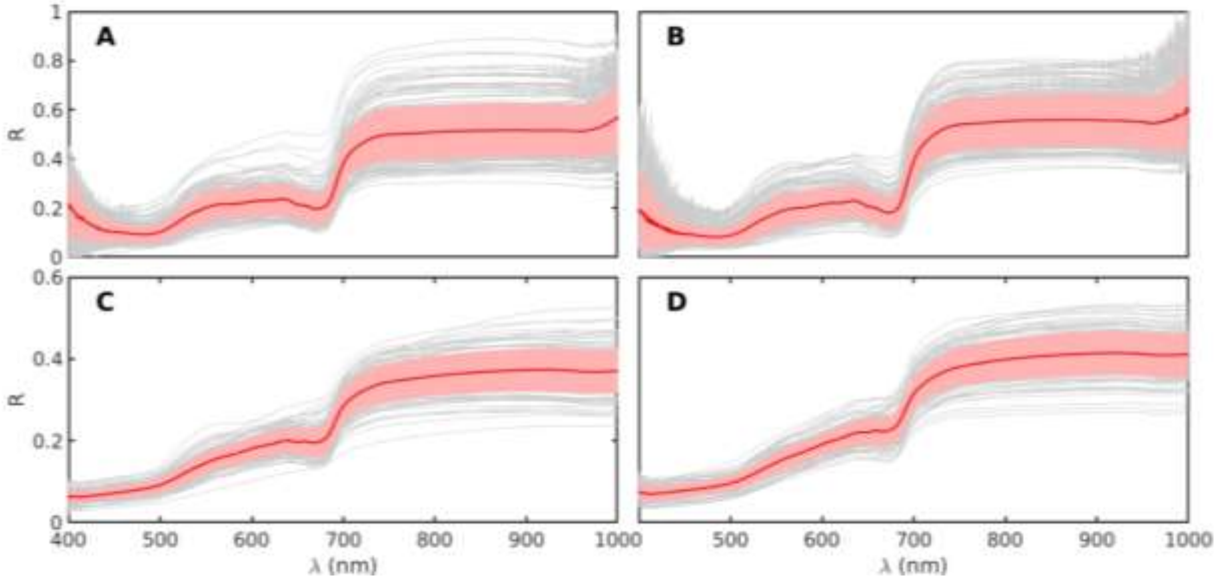

Figure 5.1: 'Jintao' kiwifruit reflectance data of the four datasets. The red line represents the average spectrum of the dataset and the pink band represents one standard deviation above and below the average. Behind the band, individual spectra are represented in gray. A) Orchard 1, 2018; B) Orchard 2, 2018; C) Orchard 1, 2019; D) Orchard 2, 2019.

It is clear from the plots that the spectral patterns are clearly distinct between the two years. The most distinctive features are:

1) A plateau in the region 500 - 600 nm, observed in 2018, which is replaced by a slope in 2019;
2) More pronounced dips at the chlorophyll absorption peak (680 nm) in 2018;
3) Excess noise in the 2018 spectra wings;
4) Highest reflectance values at the 2018 NIR plateau.

It was not possible to perform a proper calibration transfer. Apart from the feature 3, which is obviously caused by the different spectrometer sensors, it is not possible to tell whether the other discrepant features were caused by a different kiwifruit structure or by the hardware itself. Although the most probable scenario is a MIX of the two effects, it is very plausible that the hardware plays a dominant role in the production of such dissimilar spectra. This represents a serious complication for validation of the data, since the data is split in two blocks with different spectral characteristics and no calibration transfer is possible. The exploration of this problem and its partial solution is explained in the next sections.

The evolution of the spectra along time, for each orchard, is depicted in Figure 5.2. In this plot, each curve is the average of data for each day. A colour code was used to help in the interpretation of the plots. The colour map changes from green to red as DAFB increase. The colour map is absolute, i.e., it is the same for the four orchards. Therefore, only the 2018 plots have purely green curves, since they start much earlier (91 DAFB) than the 2019 plots, which start only at 148 DAFB. This is why the 2019 plots show only brown and red curves.

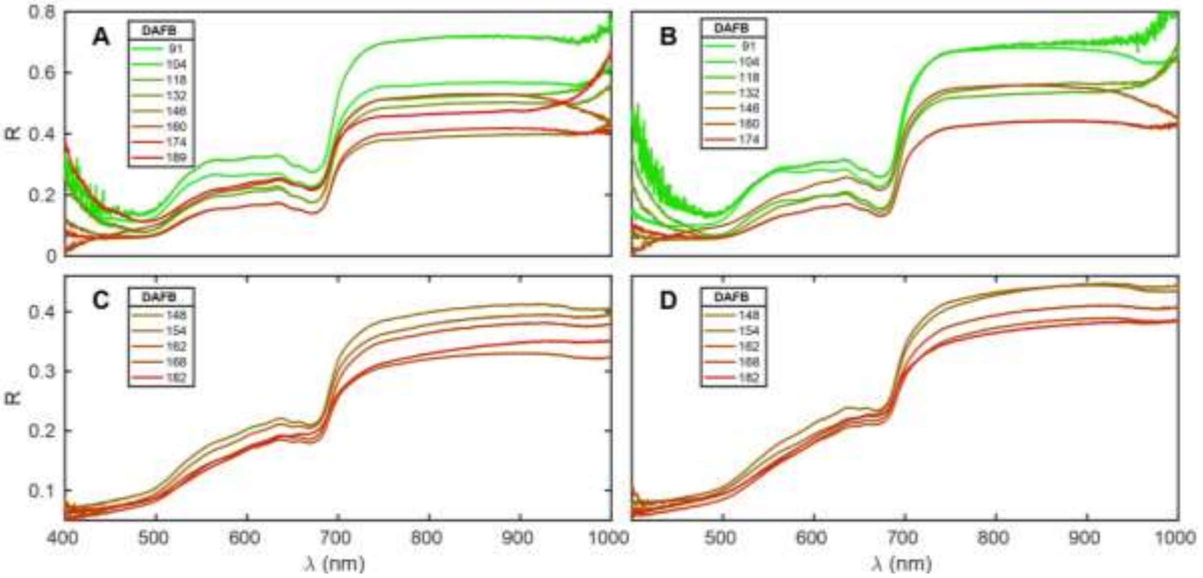

Figure 5.2: 'Jintao' kiwifruit average reflectance of the four datasets along time. Each curve is the average of data for each day. The curves are coloured from less ripe (green) to riper (red). DAFB = Days after full bloom. A) Orchard 1, 2018; B) Orchard 2, 2018; C) Orchard 1, 2019; D) Orchard 2, 2019.

The most obvious feature in all the four plots is that the main differences between the curves arise from relative vertical shifts. The shapes of all the curves are similar, but they are displaced in the vertical relatively to each other. This is due to structural changes in the tissue, which affect the backscattering level. It is a transverse effect to all wavelengths, since the vertical displacement is observed uniformly across the whole spectral range. In the last chapter it was already observed a coarse correlation between firmness and the reflectance at the NIR plateau (Figure 4.1). It is now possible to observe what happens to the plateau's reflectance in the four datasets.

The inclusion of a second year provides insight into the relation between reflection and physiological changes. This is done in Figure 5.3, which shows the average reflectance along time, at 850 nm, a wavelength located in the NIR plateau. There is a global trend for the reflectance to decrease with DAFB. This corresponds to the intuitive idea that less ripe fruit scatter more due higher firmness. However, there are fluctuations superimposed on the global pattern. The important point to retain here is that those fluctuations are approximately the same for the 2018 data and, approximately, the same for the 2019 data, although the fluctuation patterns of the two years is clearly different. The best explanation for this fact is that the reflectance level may be influenced by the climatic conditions. There are, indeed, relevant differences between the two years regarding precipitation. In Braga district, in 2018 during 146 – 176 DAFB, the total precipitation was 117.8 mm (IPMA, 2018c), while, in 2019, in 151-170 DAFB, a shorter period than the previous, the total was 194.1 mm (IPMA, 2019).

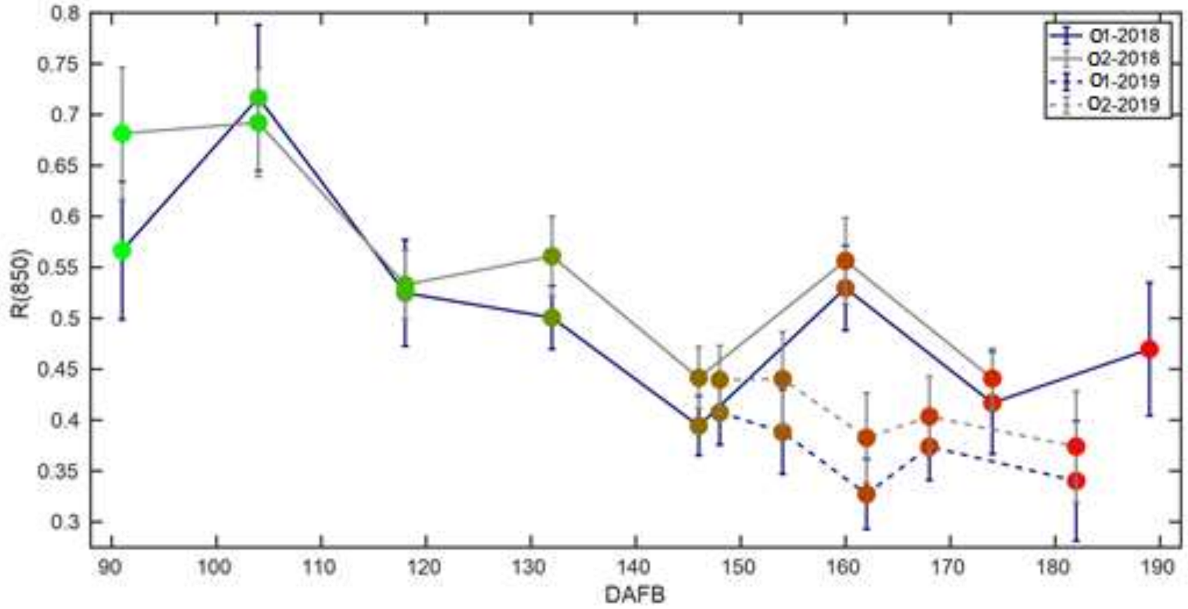

Figure 5.3: 'Jintao' kiwifruit average reflectance (for each day and orchard) along time, at 850 nm. The points retain the DAFB colour code, from less ripe (green) to riper (red). DAFB = Days after full bloom. The Orchard 1 data is plotted in blue, the Orchard 2 data is plotted in gray. The 2018 data is plotted with continuous line and the 2019 data is plotted with a dashed line.

Figure 5.4 shows the 'Jintao' kiwifruit average firmness, for each day and orchard, versus the corresponding average reflectance at 850 nm. Again, there is a global trend: reflectance at 850 nm and firmness are loosely proportional, with a plateau in the high firmness regime. However, there are large variations in reflectance at 850 nm that are not explained by firmness variations.

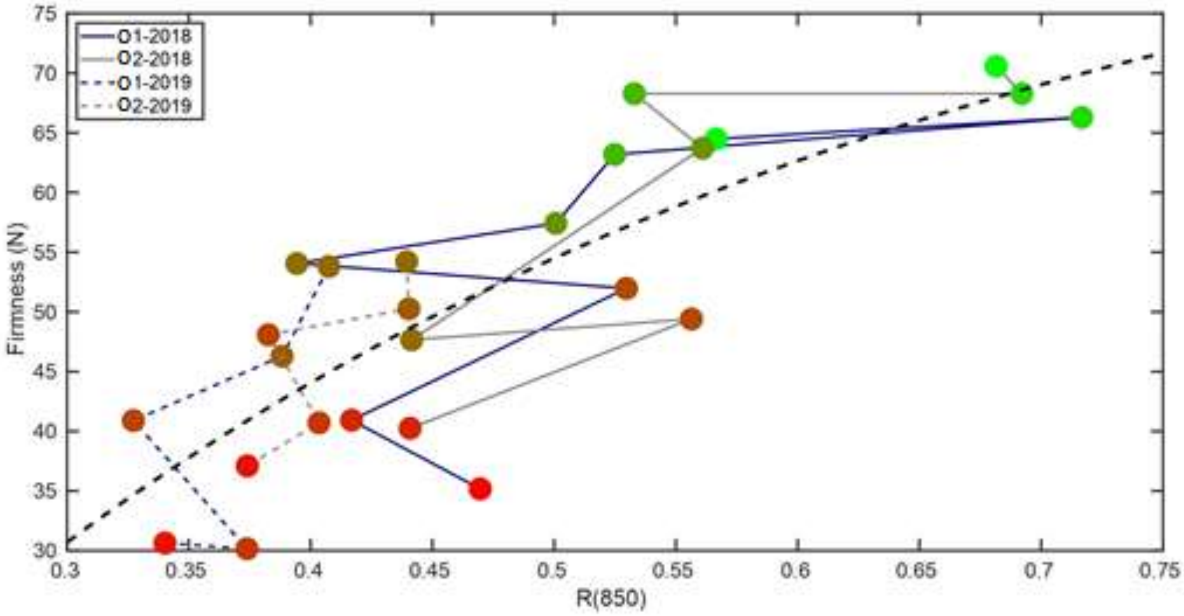

Figure 5.4: ‘Jintao’ kiwifruit average firmness (for each orchard and day) vs. the corresponding average reflectance at 850 nm. The points retain the DAFB colour code, from less ripe (green) to riper (red). The Orchard 1 data is plotted in blue, the Orchard 2 data is plotted in gray. The 2018 data is plotted with continuous line and the 2019 data is plotted with a dashed line.

Taken together, Figure 5.2, Figure 5.3 and Figure 5.4 suggest the following conclusions:

1) The main source of variation in the fruit's spectra comes from vertical shifts on reflectance, which is linked to the scattering properties of the tissues;
2) The climatic conditions influence the structure and physiology of the fruit, which, in turn, affect the scattering properties of the tissues;
3) Changes in the scattering properties have a loose relation with changes in firmness.

The Standard Normal Variate (SNV) transform is a classical pre-processing technique that removes a large part of the scattering effects. Figure 5.5 shows the results of applying the SNV transform to the curves of Figure 5.2.

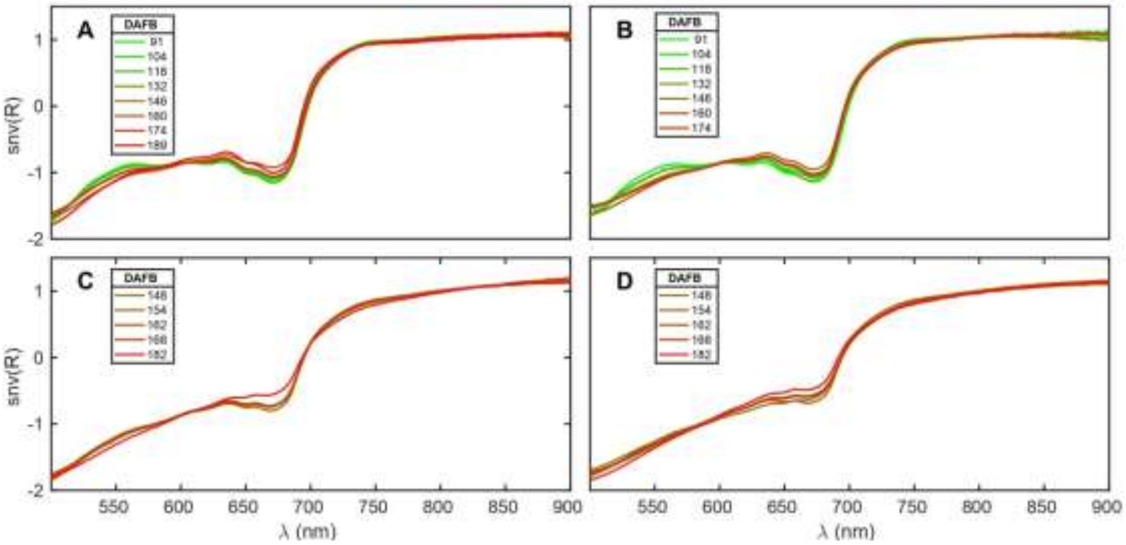

Figure 5.5: SNV applied to average reflectance of the four datasets along time (SNV applied to the curves of Figure 5.2). Each curve is the SNV transform of the average of data for each day. The curves are coloured from less ripe (green) to riper (red). DAFB = Days after full bloom. A) Orchard 1, 2018; B) Orchard 2, 2018; C) Orchard 1, 2019; D) Orchard 2, 2019.

Clearly, all the curves are now very similar in each orchard. The vertical shift has been removed and the spectra now appear closely packed. There are still some variations in shape (not in height), especially in the pigments region. The calibration models will infer information from these small variations. The difference in shape between the 2018 and 2019 data remains. This will be the main cause of the difficulties found in building robust calibration models for the internal quality parameters.

Since average curves mask the true variability in the data, even after SNV transformation, in Figure 5.6 all the individual spectra after SNV transformation are showed. Comparison with Figure 5.1 show a clear reduction of variability, although not so spectacular as in the transformation from Figure 5.2 to Figure 5.5.

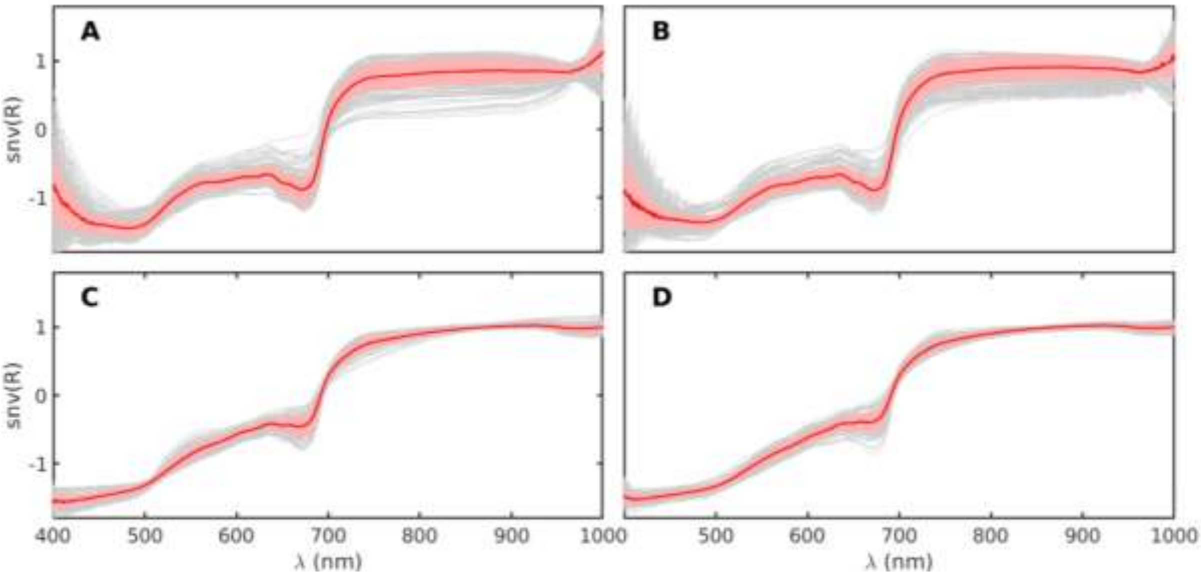

Figure 5.6: Reflectance data of the four datasets transformed by SNV (SNV applied to the curves of Figure 5.1). The red line represents the average (SNV) spectrum of the dataset and the pink band represents one standard deviation above and below the average. Behind the band, individual spectra are represented in gray. A) Orchard 1, 2018; B) Orchard 2, 2018; C) Orchard 1, 2019; D) Orchard 2, 2019.

Summarizing this section, the motivations and challenges to build robust calibration models are now clearer:

1) The spectra differ in shape between 2018 and 2019;
2) The weather conditions superimposed different fluctuation patterns on the spectra;
3) The 2019 data does not include data with DAFB < 148, while the 2018 data starts at DAFB = 91.

In the previous chapter internal double cross-validation was performed. This seemed to be the best option for only two datasets. In the next sections of this chapter, with data from two years and two orchards, will be described the successive attempts to build calibration models robust to true external validation.

5.2 Pre-processing selection

In this chapter, one more criterion was introduced to improve the choice of the best pre-processing, as explained in Figure 2.9.

The relation between RMSECV, RMSEP and RMSET is shown in Figure 5.7. The data for this plot has been obtained from the selection of best pre-processing for SSC from a collection of 84 candidates (review Section 2.7.4.2). It is important to stress that the data shown here was not used for the pre-processing choice. This is just a posteriori analysis to check the meaning of the Algorithm 1 (see Table 2.13). Figure 5.7A shows RMSEP as a function of RMSECV. There is linearity between them and that lower RMSECV generally yields lower RMSEP. There are, however, exceptions and sometimes the result may be very bad. For example, the point in the upper left had RMSECV ~ 1.2 % but RMSEP ~ 5.2 %. This was obtained with smooth + gradient with a very large width and should not be tried under normal conditions. The red points represent the pre-processing that satisfy simultaneously (2.6) and (2.7). These conditions reduce the available choices to a narrower band around the (dotted) tendency line. Particularly, the most problematic points are avoided.

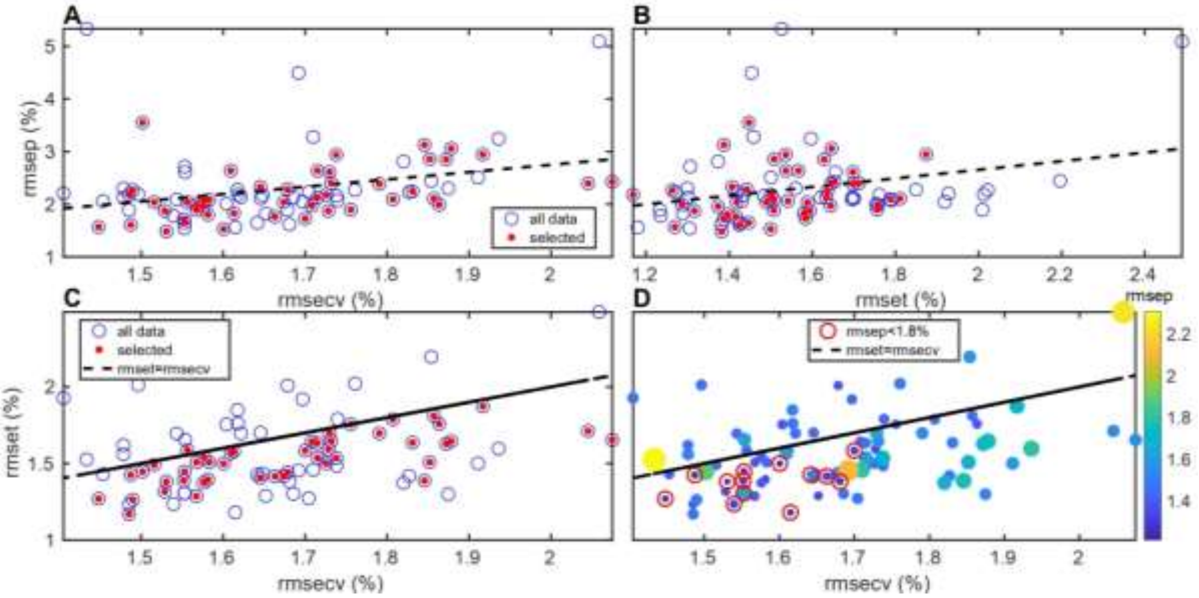

Figure 5.7: Relation between RMSECV, RMSEP and RMSET, obtained from a pre-processing optimization procedure based on Algorithm 1. A) RMSEP vs. RMSECV; B) RMSEP vs. RMSET; C) RMSET vs. RMSECV; D) RMSET vs. RMSECV, with the colour and size of the points being given by RMSEP. The red dots in A, B and C represent the pre-processing that satisfy conditions (2.6) and (2.7). The dotted lines in A and B represent a linear fit, while in C and D represent RMSET = RMSECV. The red circles in D represent RMSEP < 1.8%.

Plot B is similar to plot A, but with RMSET in the abscissa. The trend is similar, but RMSECV seems more robust to predict RMSEP. And this was to expect, since the train is done in the CV set. Plot C shows RMSET vs. RMSECV. The black dotted line represents RMSET = RMSECV. It shows that RMSET tend to be lower than RMSECV, which is also to expect, since the tuning dataset is homogeneous with the CV dataset and much smaller, which means less probability to find spectra out of the model. The selected pre-processing (red dots) corresponds to the central core of the cloud of points, which is also in agreement with the meaning of (2.6) and (2.7).

Finally, plot D shows RMSET vs. RMSECV, with the colour and size of the points being given by RMSEP. Lower RMSEP values correspond to smaller blue points and the higher ones to larger yellow dots. The best RMSEP values obtained (< 1.8 %) are encircled in red. They were found in the lower left corner of the plot, precisely for the lower values of RMSET and RMSECV. They are also found below the line RMSET = RMSECV, consistent with the selected points in plot C.

5.2.1 Internal validation for ‘Jintao’ kiwifruit SSC

As described in the previous section, the process started with pre-processing optimization.

Table 5.1 shows the best 10 results of pre-processing optimization in the MIX Mode (review Section 2.7.4.3). They are the best considering they yield the lowest 10 values of RMSECV. However, not all pass the criterion expressed by equations (2.6) and (2.7). The column named “Q” displays 1 for the transformations that satisfy the condition. The lowest RMSECV with Q=1 is the simple transformation abs + SNV (see abbreviations in Table 2.14). The first line illustrates the potential problems of the pre-processing optimizations. The best RMSECV is obtained through a local SNV transformation of (λ range)/4 = (560 nm)/4 = 140 nm. However, RMSET is clearly above RMSECV, signalling possible inconsistency of the calibration model. For this reason, Q=0 and the transformation are rejected. The value of RMSEP confirms that, indeed, this transformation would lead to poor predictions. Therefore, it was the third transformation, abs + SNV, to be selected.

Table 5.1: The ten best results of pre-processing optimization in the MIX Mode, for SSC. SDR, RMSE and R^2 have the usual meanings of standard deviation ratio, root mean square of error and squared correlation coefficient. To these symbols, the subscripts p, cv and t are added, meaning prediction, cross-validation and tuning, respectively. The table is ordered by ascending RMSECV. Q=1 if conditions (2.6) and (2.7) are satisfied (Q=0 imply rejecting the transformation). The abbreviations for the transformations are the following: hsg = abs + smoothing + Savitzky Golay; lnsv = local SNV; norm01 = abs + normalization between 0 and 1; sg = abs + Savitzky-Golay. The fractions n/m after the abbreviations represent a derivative order n and a filter width of size (λ range)/m = (560 nm)/m.

SDRp	**RMSEP**	**R^2p**	**SDRcv**	**RMSECV**	**R^2cv**	**SDRt**	**RMSET**	**R^2t**	**Q**	**Transformation**
1.350	2.204	0.504	2.218	1.405	0.796	1.547	1.928	0.618	0	lnsv 1/4
0.442	5.333	0.101	2.367	1.433	0.821	1.972	1.526	0.745	0	hsg2 1/2
1.978	**1.568**	**0.749**	**2.164**	**1.448**	**0.786**	**2.262**	**1.269**	**0.807**	**1**	**abs+snv**
1.457	2.060	0.604	2.215	1.453	0.796	1.925	1.431	0.760	1	hsg 2/32
1.399	2.124	0.596	2.181	1.478	0.789	1.674	1.620	0.701	0	sg 2/64
1.334	2.299	0.540	2.139	1.478	0.781	2.054	1.560	0.764	0	hsg 1/8 snv
1.557	1.886	0.615	2.129	1.485	0.779	2.344	1.234	0.822	1	norm01+hsg 1/32
1.407	2.179	0.571	2.172	1.485	0.788	2.290	1.169	0.816	1	hsg 2/64
1.834	1.609	0.722	2.124	1.487	0.778	2.166	1.424	0.785	1	norm01+hsg 1/8
1.379	2.265	0.540	2.100	1.490	0.773	2.239	1.263	0.813	1	hsg 1/8

The prediction results for the abs + SNV transformation are shown Figure 5.8. The statistical performance parameters differ slightly from those obtained in Table 5.1 because in the optimization process the models are built only from the CV dataset, while in the final validation step, the model is built directly from the calibration dataset = CV + tuning datasets. Figure 5.8A is the classical plot of predicted vs. measured SSC. With RMSEP = 1.63%, which is still a large value when compared with those of the literature, it is still possible to achieve a SDR close to 2 (SDR = 1.91) due to the large dispersion of the SSC values.

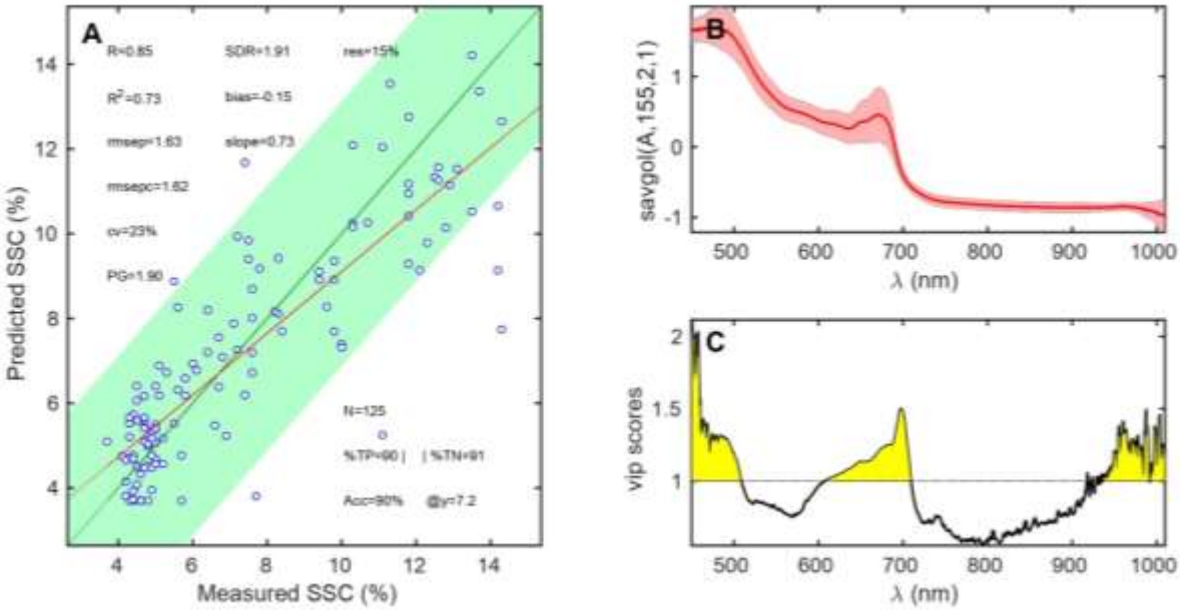

Figure 5.8: Best results for the prediction of SSC, based on the pre-processing optimization in the MIX Mode, which selected the transformation abs + SNV. A) predicted vs. measured SSC values; B) average transformed spectrum (red line) and one standard deviation bands (pink area); C) VIP scores.

Figure 5.8B shows the average transformed spectra, with large absorption in the pigments' region (below 700 nm) and a large low-absorption plateau above 750 nm. Finally, Figure 5.8C shows the VIP scores, with the areas VIP > 1 highlighted in yellow. There are 3 main spectral zones that contribute more to the model; i) 450 – 500 nm is related with carotenoids and blue absorption by chlorophyll; ii) 600 – 700 nm is related with red absorption by chlorophyll; and iii) 920 — 1000 nm is probably related with the second overtone of O–H stretching and the third overtones of C–H and C–H_2 stretching. As mentioned above, the KS method was used to split the calibration and validation sets. It is, therefore, interesting to observe if the resulting SSC values are well distributed. The SSC statistics for the calibration and validations sets is shown in Table 5.2.

Table 5.2: Basic statistics for the SSC values in the calibration and validation sets obtained by applying the KS algorithm to the reflectance spectra transformed by abs + SNV, leading to the results shown in Figure 5.8.

	Mean	Std. Deviation	Max	Min
Calibration set	8.3	3.1	17.3	3.5
Validation set	7.2	3.1	14.3	3.7

The distributions have a mismatch of 1.1 % SSC, but the same standard deviation is three times larger. On the other side, the range of SSC variation in the validation set is contained within that of the calibration set. The histograms of SSC distribution in both sets are shown in Figure 5.9.

Figure 5.9A shows that all the SSC classes (corresponding to the bins of the histogram) are well represented in both sets, except for the larger values of SSC, above 14.5, that are only present in calibration (which is not a problem for validation). Figure 5.9B shows that the class proportions are not exactly the same, with the validation set more balanced towards the lower SSC.

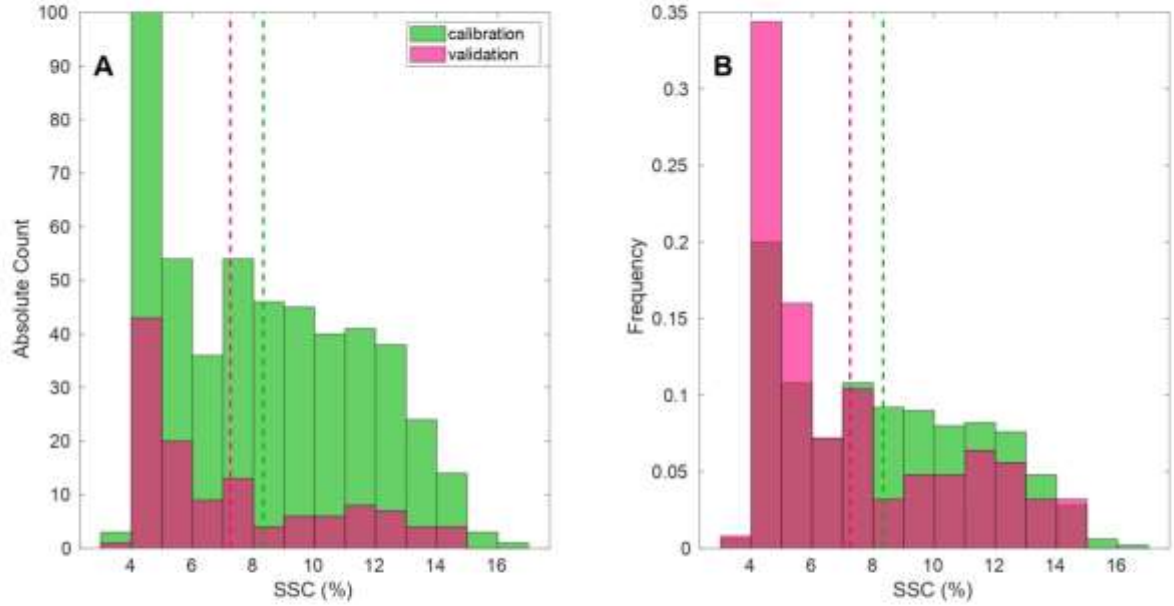

Figure 5.9: Histograms for the distribution of SSC in the calibration and validation sets, relative to the model shown in Figure 5.8. A) Absolute counts. B) Relative frequency counts. The green dashed line represents the calibration average and the magenta dashed line represents the validation average.

Table 5.3 shows the results of pre-processing optimization in the SNV Mode. The lower wavelength limit has been scanned from 380 nm to 720 nm in 20 nm steps, while the upper limit has been scanned from 880 nm to 1020 nm, also in 20 nm steps. The scanning of the wavelength range limits is a basic form of variable selection.

Table 5.3: The ten best results of pre-processing optimization in the SNV Mode. The common symbols to Table 5.1 have the same meaning. The new symbols λ_i and λ_f represent the lower and upper limits of the wavelength range selected.

SDRp	**RMSEP**	**R^2p**	**SDRcv**	**RMSECV**	**R^2cv**	**SDRt**	**RMSET**	**R^2t**	**Q**	**λ_i**	**λ_f**
1.850	1.620	0.717	2.210	1.403	0.795	2.149	1.595	0.793	0	480	1000
1.802	**1.783**	**0.695**	**2.212**	**1.413**	**0.795**	**2.194**	**1.449**	**0.793**	**1**	**600**	**960**
1.420	2.017	0.574	2.213	1.426	0.796	2.354	1.464	0.822	1	380	980
1.918	1.527	0.741	2.261	1.429	0.804	2.147	1.427	0.788	1	640	1000
1.874	1.659	0.717	2.159	1.435	0.785	2.494	1.319	0.841	0	440	1000
1.779	1.669	0.695	2.203	1.439	0.794	2.262	1.440	0.804	1	640	1020
1.777	1.757	0.701	2.185	1.441	0.790	2.398	1.328	0.824	0	620	1020
1.832	1.735	0.701	2.167	1.444	0.787	2.401	1.332	0.827	0	620	980
1.865	1.633	0.728	2.199	1.445	0.793	2.432	1.291	0.833	0	600	1020
2.024	1.535	0.758	2.111	1.463	0.775	2.113	1.575	0.776	0	440	980

The performance of the best SNV model is shown Figure 5.10. The results are very similar to those obtained in MIX mode, especially because the MIX mode also selected abs + SNV transform. The most interesting point to note relatively to the previous figure is that the VIP scores show two peaks in the region 600 – 700 nm, where the previous model showed only a peak. It is probable that these two peaks, located at 650 nm and 690 nm, correspond roughly to the absorption peaks of chlorophyll a and b.

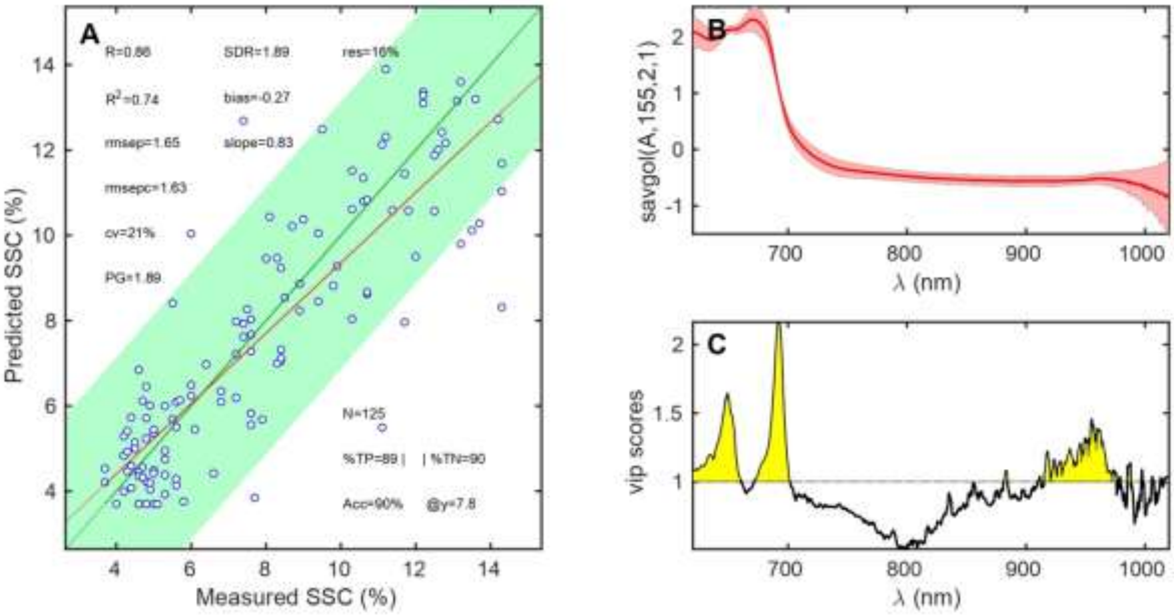

Figure 5.10: Best results for the prediction of SSC, based on the pre-processing optimization in the SNV Mode (abs + SNV), which selected the wavelength range 600 – 960 nm. A) predicted vs. measured SSC values; B) average transformed spectrum (red line) and one standard deviation bands (pink area); C) VIP scores.

Finally, the pre-process selection was applied to Savitzky-Golay derivation (SG Mode). This was the most complex optimization, involving a three-dimensional grid search on lower wavelength range, upper wavelength range and filter width. Besides, it was run for first and second derivative. Adding SNV before or after the derivative was also tested, but without any obvious advantage.

Table 5.4 shows the results of pre-processing optimization in this mode. The lower wavelength limit has been scanned from 460 nm to 680 nm in 10 nm steps, the upper limit has been scanned from 880 nm to 1020 nm, in 20 nm steps, and the filter width was scanned from 25 points to 175 points in steps of 10 (that is, approximately from 14 nm to 100 nm in steps of 6 nm). The first order derivative delivered slightly better results and the second order was discarded.

Table 5.4: The ten best results of pre-processing optimization in the SG Mode. The common symbols to Table 5.3 have the same meaning. The new symbol *w* represents the filter width selected.

SDRp	RMSEP	R^2p	SDRcv	RMSECV	R^2cv	SDRt	RMSET	R^2t	Q	λ_i	λ_f	w
1.716	**1.751**	**0.668**	**1.851**	**1.529**	**0.708**	**1.937**	**1.593**	**0.737**	**1**	**690**	**1020**	**155**
1.709	1.787	0.655	1.863	1.532	0.713	2.083	1.515	0.769	0	700	1000	145
1.426	2.113	0.521	1.832	1.585	0.703	1.799	1.757	0.693	1	640	1000	35
1.611	1.927	0.625	1.871	1.589	0.715	2.014	1.576	0.751	1	660	980	115
1.521	1.982	0.583	1.785	1.591	0.687	1.890	1.671	0.724	1	590	980	115
1.768	1.692	0.709	1.791	1.591	0.690	1.991	1.719	0.748	1	690	980	145
1.506	2.090	0.603	1.979	1.592	0.746	2.101	1.499	0.775	1	670	920	175
1.667	1.815	0.644	1.919	1.596	0.729	1.904	1.689	0.722	0	640	1020	105
1.632	1.827	0.638	1.852	1.596	0.709	2.001	1.484	0.761	1	610	980	115
1.711	1.752	0.671	1.821	1.600	0.700	2.082	1.454	0.774	0	600	960	165

The performance of the best SG model is shown in Figure 5.11. The results are slightly better than those obtained in MIX Mode and in SNV mode, reaching the threshold of SDR = 2. The selected model excludes almost all the pigments' information but still retains the 690 nm peak of chlorophyll a, where the VIP scores peak. It is also interesting to note that the SNV based models (Figure 5.10) target essentially the pigments range plus an wavelength range above 900 nm, related with O–H and C–H stretching bands, while the SG model retains only the upper end of the pigments region and the NIR plateau region, between 750 nm and 900 nm, where that main contributions might be the third overtone of O–H stretching (around 750 nm) and the band $3\nu + \delta(O-H)$, that is, the combination of the second overtone of O–H stretching with the fundamental bending vibration, which occurs around 840 nm. There is, however, another possibility. NIR plateau avoid most of important bands, making it sensitive to small changes in secondary bands and, for this reason, the model may eventually capture these small variations upon the plateau.

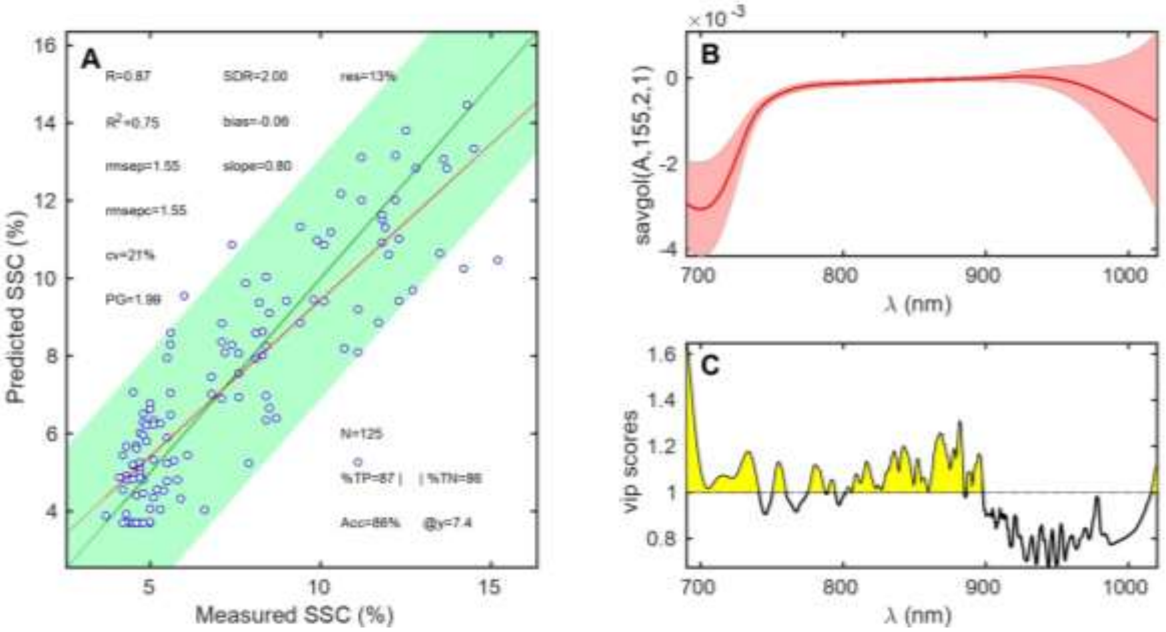

Figure 5.11: Best results for the prediction of SSC, based on the pre-processing optimization in the SG Mode (abs + SG), which selected the wavelength range 690 – 1020 nm, a filter width of 155 points (about 90 nm) and the first derivative. A) predicted vs. measured SSC values; B) average transformed spectrum (red line) and one standard deviation bands (pink area). C) VIP scores.

As a general conclusion, the three optimization procedures lead to similar results. This is a demonstration of the robustness of the analysis since equivalent results have been obtained through different approaches and pre-processing transformations. The statistical parameters SDR ~ 1.8 – 2.0 and RMSEP ~ 1.5 – 1.6 % correspond to the best figures extracted from this dataset, with internal validation being always the best case. As shown in the next section, external validation achieves worse results.

The summary of the results obtained in internal validation in the three optimization modes is displayed in Table 5.5.

Table 5.5: Summary of the results obtained in internal validation in the three optimization modes (TP = “True Positive”: TN = “True Negative”; Acc = Accuracy).

Mode	SDR	RMSEP (%)	R^2	bias (%)	slope	TP (%)	TN (%)	Acc (%)
MIX	1.91	1.63	0.73	-0.15	0.73	90	91	90
SNV	1.89	1.65	0.74	-0.27	0.83	89	90	90
SG	**2.00**	**1.55**	**0.75**	**-0.06**	**0.80**	**87**	**86**	**86**

5.2.2 External validation for ‘Jintao’ kiwifruit SSC

In the previous section was used the validation scheme depicted at the right of the Figure 2.8, while in this section the validation results were obtained through the process depicted in the left panel, that is, external validation.

The only difference between the two methods is the way calibration and validation sets are chosen. Then, the calibration process was the same and was explained in Figure 2.9. Therefore, the same list of transformations in Table 2.14, the same Algorithm 1 (Table 2.13) and the three optimization modes, MIX, SNV and SG, were used again.

The splitting of calibration and validation sets is just given by grouping the orchards and the KS algorithm does not apply here. This means that the heterogeneity between them may increase relatively to the standard validation. The statistical description of the SSC values for the calibration and validation datasets in external validation in given in Table 5.6.

Table 5.6: Statistical description of the SSC values for the calibration and validation datasets in external validation. The symbols refer to the to the orchards' assignments in the following plots.

Validation set			Calibration				Validation			
Nr.	Symbol	Orchard	mean	std	max	min	mean	std	max	min
4	Red square	O1/2018	7.7	3.2	17.3	3.5	9.6	2.3	15.2	5.5
3	Green triangle	O2/2018	7.6	3.0	17.3	3.5	10.3	2.7	15.4	5.3
2	Blue circle	O1/2019	8.6	3.1	17.3	3.5	7.0	2.9	16.2	3.7
1	Yellow diamond	O2/2019	8.7	3.0	16.2	3.7	6.8	3.0	17.3	3.5

The histograms for the SSC distributions in the four stages of external validation are depicted in Figure 5.12. The upper plots represent absolute counts, while the lower plots correspond to the SSC class frequency. Each orchard is represented as a vertical pair. For example, the data for validation in orchard 1/2019 is shown in subfigures A/B. When the validation set was from 2019, it was more balanced to the higher SSC values than the calibration set. When the validation set was from 2018, the opposite was observed, it was more balanced to the lower SSC values than the calibration set. Mismatches were obvious. However, they were not too far from those observed in Figure 5.9, especially when the validation is performed in the 2018 orchards (E/F and G/H).

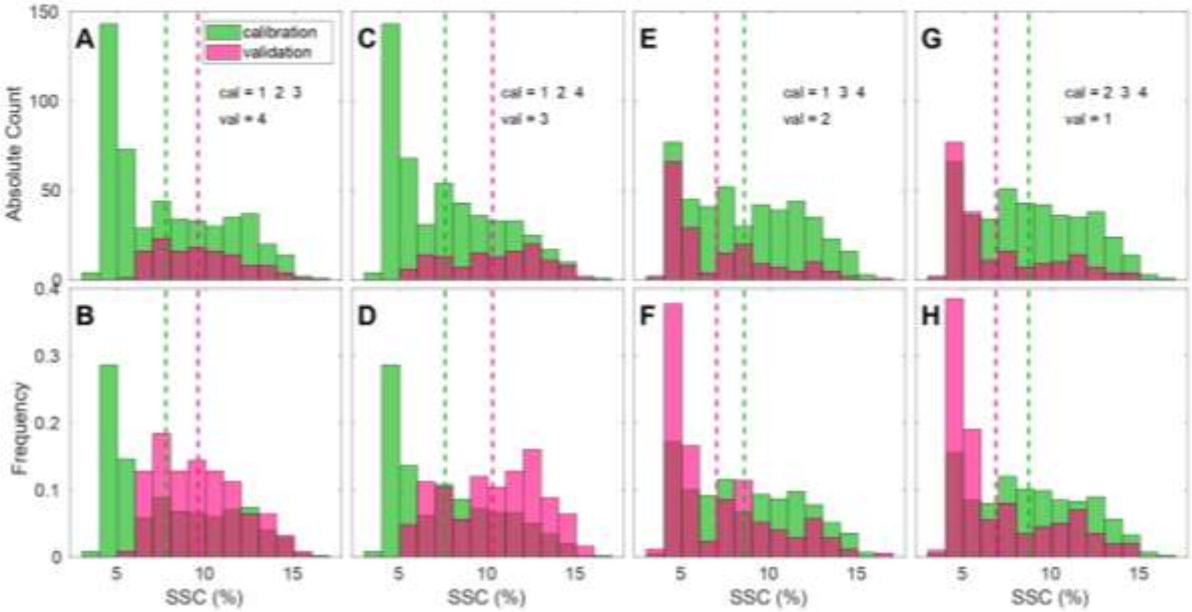

Figure 5.12: Histograms for the distribution of SSC in the calibration and validation sets, in external validation. A, C, E and G) absolute counts; B, D, F and H) Relative frequency counts. The green dashed line represents the calibration average and the magenta dashed line represents the validation average.

The results obtained for the MIX Mode, in external validation, are presented in Table 5.7. As explained above, these numbers correspond to the average over the four validations. For example, RMSECV is the average of RMSECV(1+2+3), RMSECV(1+2+4), RMSECV(1+3+4) and RMSECV(2+3+4), where the numbers in parenthesis represent the calibration set.

Table 5.7: The ten best results of pre-processing optimization in the MIX Mode and external validation, for SSC. SDR, RMSE and R2 have the usual meanings of standard deviation ratio, root mean square of error and squared correlation coefficient. To these symbols, the subscripts p, cv and t are added, meaning prediction, cross-validation and tuning, respectively. The table is ordered by ascending RMSCEV. Q=1 if conditions (2.6) and (2.7) were satisfied (Q=0 imply rejecting the transformation). The abbreviations for the transformations are the following: hsg = abs + smoothing + Savitzky Golay; lnsv = local SNV; norm01 = abs + normalization between 0 and 1; sg = abs + Savitzky-Golay. The fractions n/m after the abbreviations represent a derivative order n and a filter width of size (λ range)/m = (560 nm)/m.

SDRp	RSMEP	R^2p	SDRcv	RMSECV	R^2cv	SDRt	RMSET	R^2t	Q	Transformation
0.878	3.391	0.210	2.305	1.420	0.810	1.483	1.575	0.547	0	hsg2 1/64
0.851	3.305	0.204	2.265	1.442	0.804	1.553	1.514	0.596	0	hsg2 1/4
0.897	3.411	0.252	2.237	1.455	0.799	1.594	1.509	0.610	0	hsg2 1/32
0.774	3.681	0.185	2.226	1.462	0.796	1.850	1.342	0.691	0	hsg2 1/16
0.945	3.252	0.294	2.224	1.468	0.796	1.620	1.498	0.605	0	hsg2 1/8
1.082	**2.682**	**0.266**	**2.110**	**1.471**	**0.769**	**2.051**	**1.493**	**0.772**	**1**	**snv**
0.911	3.332	0.245	2.202	1.482	0.791	1.536	1.529	0.580	0	sg2 1/64
0.968	2.928	0.211	2.126	1.483	0.777	1.992	1.474	0.755	1	lnsv 1/32
1.030	2.703	0.280	2.128	1.486	0.778	1.751	1.619	0.685	0	abs
0.983	2.898	0.165	2.143	1.488	0.779	1.752	1.545	0.691	0	hsg1 1/8

The most striking result is the dramatic drop of the performance. In internal validation SDRp ~ 2, but in external validation, SDRp ~ 1.1, which means that the predictive ability of the model is almost null. Indeed, the results improve slightly when the statistical parameters are not calculated as an average but directly on the whole data. This is done in Figure 5.13.

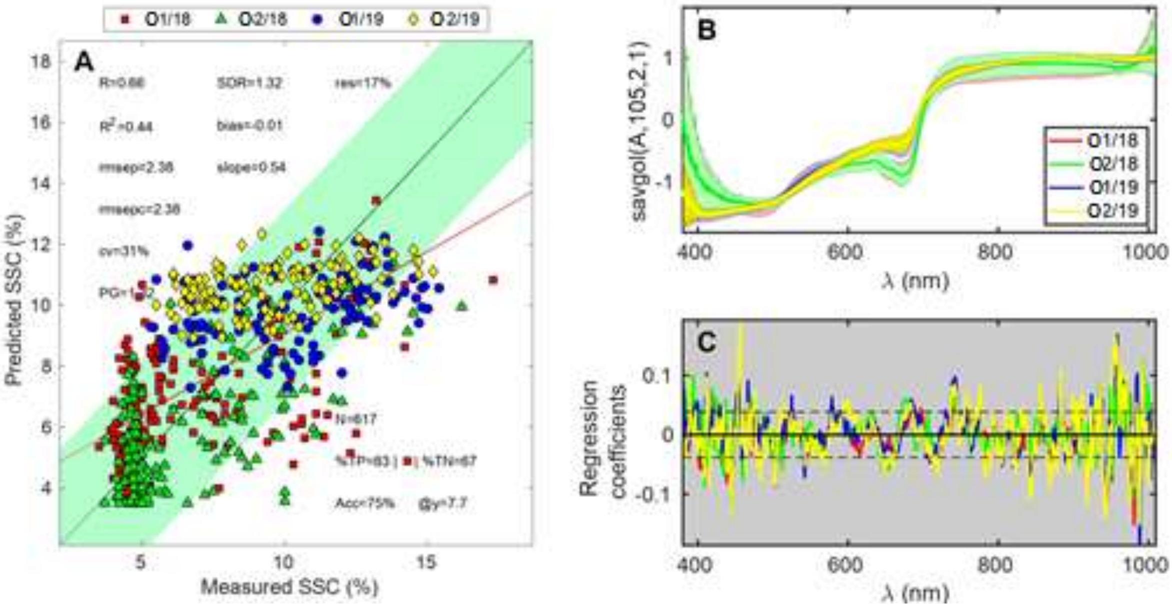

Figure 5.13: Best results for the prediction of SSC in external validation, based on the pre-processing optimization in the MIX Mode, which selected the transformation SNV. In the three sub plots, the colour convention is the same: red for the predictions of Orchard 1/2018 (having Orchard 2/2018, Orchard 1/2019 and Orchard 2/2019 as calibration); green for the predictions of Orchard 2/2018; blue for the predictions of Orchard 1/2019; and yellow for the predictions of Orchard 2/2019. A) predicted vs. measured SSC values; B) average transformed spectrum (central lines) and one standard deviation bands (coloured areas of a lighter colour, around the central line). C) Regression coefficients. The dashed lines represent one standard deviation calculated on the four regression vectors.

The four orchards are now clearly marked in Figure 5.13A with different colours. The difficulties in prediction are now very clear. For example, the predictions for Orchard 1/18 and Orchard 2/18 (red and green points, respectively) span approximately the interval 4 – 8 % when the real values are all around 5 %. This produces the vertical line of points at 5 %. On the other side, the predictions for the 2019 orchards are relatively flat, with values in the range 9 – 12%, for a true range of

5 – 15 %. This corresponds to the blue and yellow points arranged along a line with a small slope.

Figure 5.13B shows the average transformed spectrum, for each orchard (the central lines), surround by one standard deviation bands (coloured areas of a lighter colour, around the central line). Although SNV reduces the effects of scattering, it does not compensate for different shapes. Therefore, the differences between the two years are still very clear. The 2018 data is consistent, and this is why the red/pink band (Orchard 1/2018) is hardly noticed, since it is behind the green band (Orchard 2/2018), because they are very similar to each other. The same happens in the 2019 data as the blue/purple band (Orchard 1/2019) is hidden behind the yellow band (Orchard 2/2019). However, there is a clear difference between the 2018 and the 2019 curves, especially in the pigments range, 580 to 700 nm. This is the main source of the problems encountered in external validation.

Finally, Figure 5.13C shows the regression coefficients for the four models, with the same colour code. The general pattern is the same and the oscillations were essentially in the same positions for all the models. However, there were slight differences, especially, in the pigments range, 580 to 700 nm, in agreement with the differences observed in the spectra.

The results for SNV optimization are shown in Table 5.8. In the first ten best RMSECV results there was only one delivering Q = 1. For this reason, the table was extended to include the first twelve results. It is interesting to note that the two pre-processing with Q = 1 were two of the three that attained SDR>1. This is a clear indication that the selection criteria make sense and allow to choose the pre-processing with more probability of success in validation. On the other side, when compared with the corresponding Table 5.3, the number of transformations with Q = 1 are scarcer. This is a consequence of less homogeneity of the data in the calibration dataset. In the internal validation procedure, there is a balanced representation of the two years in the calibration set, while in external validation the years are distributed in the proportion 2:1. This heterogeneity is also reflected in the tuning dataset, which implies more difficulty to pass the consistency test between cross-validation and tuning results.

Table 5.8: The twelve best results of pre-processing optimization in the SNV Mode. The common symbols to Table 5.1 have the same meaning. $\lambda_i$and λ_f represent the lower and upper limits of the wavelength range selected.

SDRp	**RMSEP**	**R^2p**	**SDRcv**	**RMSECV**	**R^2cv**	**SDRt**	**RMSET**	**R^2t**	**Q**	λ_i	λ_f
0.942	3.041	0.195	2.189	1.415	0.788	2.011	1.571	0.756	0	620	1020
0.977	2.884	0.212	2.179	1.427	0.784	2.028	1.516	0.763	0	580	1020
0.948	2.984	0.206	2.174	1.437	0.783	1.988	1.524	0.752	0	600	1020
0.922	3.046	0.183	2.145	1.441	0.778	2.044	1.569	0.766	0	580	980
1.022	2.747	0.236	2.143	1.444	0.777	2.072	1.529	0.774	0	560	1000
0.971	2.928	0.191	2.158	1.445	0.783	1.991	1.518	0.746	0	660	1020
0.953	2.973	0.202	2.150	1.446	0.781	2.018	1.529	0.756	0	640	1020
1.068	**2.751**	**0.230**	**2.145**	**1.447**	**0.776**	**2.111**	**1.454**	**0.776**	**1**	**440**	**1000**
0.984	2.855	0.206	2.155	1.450	0.779	1.979	1.531	0.751	0	580	1000
0.877	3.299	0.159	2.135	1.458	0.776	1.983	1.621	0.743	0	640	980
0.998	2.848	0.223	2.146	1.460	0.777	2.007	1.514	0.757	0	640	1000
1.061	2.714	0.280	2.134	1.462	0.774	2.150	1.415	0.783	1	500	1020

The plots relative to the SNV mode are shown in Figure 5.14. The meaning of the plots is the same as in the previous figure. The results are slightly better than in the MIX mode. All the comments made to Figure 5.13 apply here.

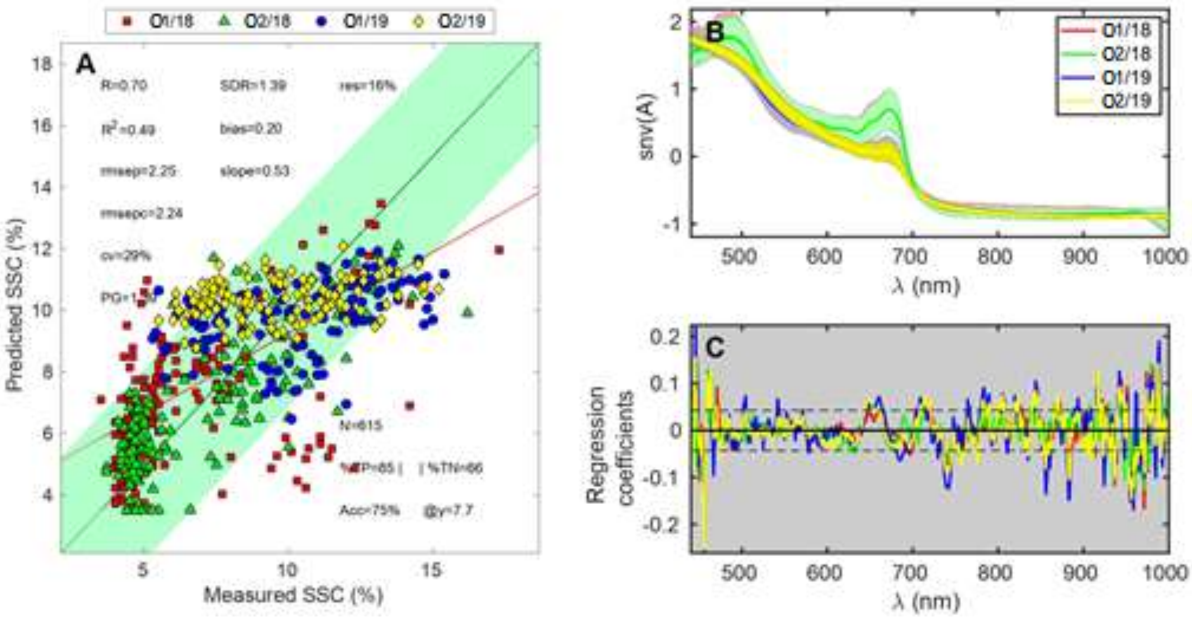

Figure 5.14: Best results for the prediction of SSC in external validation, based on the pre-processing optimization in the SNV Mode, which selected the spectral range 440 to 1000 nm. In the three sub plots, the colour convention is the same: red for the predictions of Orchard 1/2018 (having Orchard 2/2018, Orchard 1/2019 and Orchard 2/2019 as calibration); green for the predictions of Orchard 2/2018; blue for the predictions of Orchard 1/2019; and yellow for the predictions of Orchard 2/2019. A) predicted vs. measured SSC values; B) average transformed spectrum (central lines) and one standard deviation bands (coloured areas of a lighter colour, around the central line). C) Regression coefficients. The dashed lines represent one standard deviation calculated on the four regression vectors.

Finally, the results obtained in the SG mode are shown in Table 5.9 and in Figure 5.15. They are similar to those obtained in the MIX and SNV modes. Relatively to the internal validation, the selected model includes almost all of the chlorophyll peak, starting at 660 nm, but excludes the remaining pigments' information.

Table 5.9: The ten best results of pre-processing optimization in the SG Mode. The common symbols to Table 5.3 have the same meaning. The symbol w represents the filter width selected.

SDRp	RMSEP	R^2p	SDRcv	RMSECV	R^2cv	SDRt	RMSET	R^2t	Q	λ_i	λ_f	w
1.107	2.540	0.231	0.885	1.584	0.715	2.096	1.431	0.770	0	670	1000	175
1.151	**2.487**	**0.310**	**1.851**	**1.587**	**0.705**	**2.017**	**1.526**	**0.760**	**1**	**660**	**960**	**105**
1.134	2.469	0.267	1.888	1.587	0.715	2.000	1.505	0.750	1	680	1000	35
1.109	2.507	0.250	1.899	1.588	0.718	2.010	1.514	0.748	1	650	1020	175
1.082	2.580	0.244	1.949	1.589	0.733	2.027	1.460	0.760	1	680	1020	95
1.086	2.571	0.226	1.866	1.591	0.709	2.119	1.504	0.777	0	620	1000	25
1.136	2.531	0.280	1.904	1.591	0.722	1.992	1.572	0.752	1	680	960	115
1.047	2.627	0.201	1.881	1.591	0.712	1.883	1.616	0.735	1	570	1000	115
1.155	2.472	0.291	1.910	1.591	0.724	1.916	1.623	0.724	1	670	960	115
1.051	2.660	0.208	1.874	1.592	0.710	1.993	1.506	0.750	1	590	1020	65

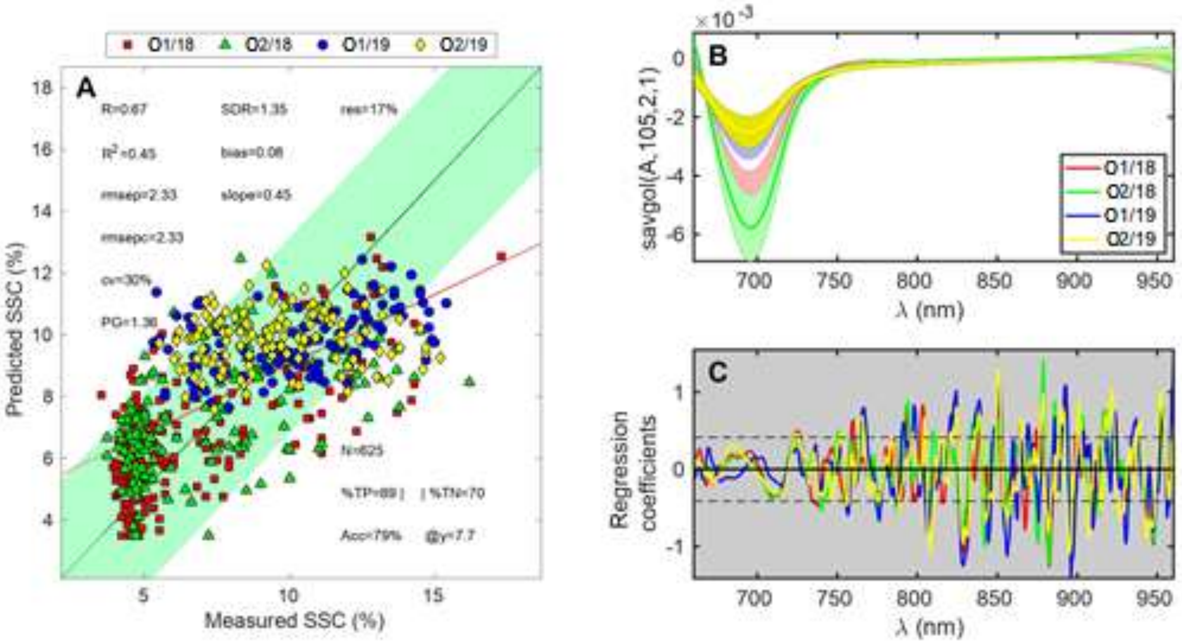

Figure 5.15: Best results for the prediction of SSC in external validation, based on the pre-processing optimization in the SG Mode, which selected the spectral range 660 to 960 nm and a filter width of 105 points (approximately 60 nm). In the three sub plots, the colour convention is the same: red for the predictions of Orchard 1/2018 (having Orchard 2/2018, Orchard 1/2019 and Orchard 2/2019 as calibration); green for the predictions of Orchard 2/2018; blue for the predictions of Orchard 1/2019; and yellow for the predictions of Orchard 2/2019. A) predicted vs. measured SSC values; B) average transformed spectrum (central lines) and one standard deviation bands (coloured areas of a lighter colour, around the central line); C) Regression coefficients. The dashed lines represent one standard deviation calculated on the four regression vectors.

The summary of the results obtained in external validation in the three optimization modes is displayed in Table 5.10.

Table 5.10: Summary of the results obtained in external validation in the three optimization modes (TP = “True Positive”: TN = “True Negative”; Acc = Accuracy).

Mode	SDR	RMSEP (%)	R^2	bias (%)	slope	TP (%)	TN (%)	Acc. (%)
MIX	1.32	2.38	0.44	-0.01	0.54	83	67	75
SNV	**1.39**	**2.25**	**0.49**	**0.20**	**0.53**	**85**	**66**	**75**
SG	1.35	2.33	0.45	0.08	0.45	89	70	79

The performances of the three modes, MIX, SNV and SG, are approximately equal in external validation. In the previous section it was found that they were also approximately equal in internal validation. Therefore, the relative evaluation of the pre-processing transformations seems insensitive to the type of validation, external or internal. Having this in mind, the next sections drop the optimization step and directly use the best transformations already found. However, another type of optimization will be performed, specifically in what concern variable selection.

5.3 Variable selection

The next step to improve the models' performance is to apply variable selection. The basic idea is that uninformative variables may represent noise and lower the models' prediction capacity. On the other side, a model purged from noisy variables could, in principle, withstand more robustly the validation against a new set, since the information is reduced to the essential. The problem, of course, is that the core variables in one dataset may not be core in another. For example, if one dataset corresponds to fruit grown in a dry season, while other corresponds to fruit grown in a wet season, it is plausible that the spectral information is encoded in different forms in the two datasets. Under these conditions, performing variable selection in the first dataset may worsen the predictions in the second, relatively to the case where all variables are considered. This is because variable selection may enhance the difference between the datasets. From this discussion, variable selection may be a good strategy when calibration and validation sets are homogeneous, but probably not recommended when the sets are heterogeneous. This is investigated in this section.

Ideally, it would be possible to run again all the pre-processing transformations, together with variable selection, to optimize the complete procedure, i.e., to find the transformations delivering the best RMSECV (or RMSET) after variable selection. These would be the best candidates to yield optimal results in validation. Probably, the new choices for pre-processing transformations would not match exactly the ones found in the previous section. However, the process would require too much time and, probably, would not deliver results significantly better than the ones obtained with the already adopted transformations. Therefore, the option taken was to keep the pre-processing transformations found in last section and apply variable selection on them.

5.3.1 Internal validation for ‘Jintao’ kiwifruit SSC

In this section, to keep the presentation more compact, only the best result in internal validation is illustrated in a plot, although the results of the three modes (MIX, SNV and SG) are still described in Table 5.11.

Table 5.11: Results of variable selection in internal validation. Mode: each one of the three modes of pre-processing optimization, as described in Section 2.9 (the optimization was not performed again). nLV: number of latent variables (median of the 30 runs). $n\lambda_i$: the number of wavelengths in the full spectra; $n\lambda_f$: the number of wavelengths remaining in the spectra after variable selection; f: the fraction of wavelengths selected; $nIter$: number of iterations in variable selection; $\overline{SDR}$: average value of SDR in the 30 model runs; σ(SDR): standard deviation of SDR in those 30 runs. $\overline{RMSEP}$: average value of RMSEP in the 30 model runs; σ(RMSEP): standard deviation of RMSEP in those 30 runs. $\overline{R2}$: average value of R^2 in the 30 model runs; σ(R^2): standard deviation of R^2 in those 30 runs.

Mode	nLV	$n\lambda_i$	$n\lambda_f$	f	$Iter$	SDR	σ(SDR)	RMSEP	σ(RMSEP)	R^2	$\sigma(R^2)$
MIX	14	959	356	37	2	2.12	0.15	1.48	0.11	0.78	0.03
SNV	**11**	**620**	**299**	**48**	**3**	**2.31**	**0.19**	**1.36**	**0.13**	**0.81**	**0.03**
SG	20	572	199	35	4	2.16	0.19	1.49	0.14	0.78	0.04

The best result was obtained in the SNV mode, which has previously selected as optimal the spectral range 600 to 960 nm. Figure 5.16 shows the results obtained in this mode. Note that, according to the Algorithm 2, the selection of calibration and validation sets is random and repeated N times, to build a statistic for the VIP scores and the regression vectors. In this work N = 30. Therefore, 30 models have been kept at the end of the process.

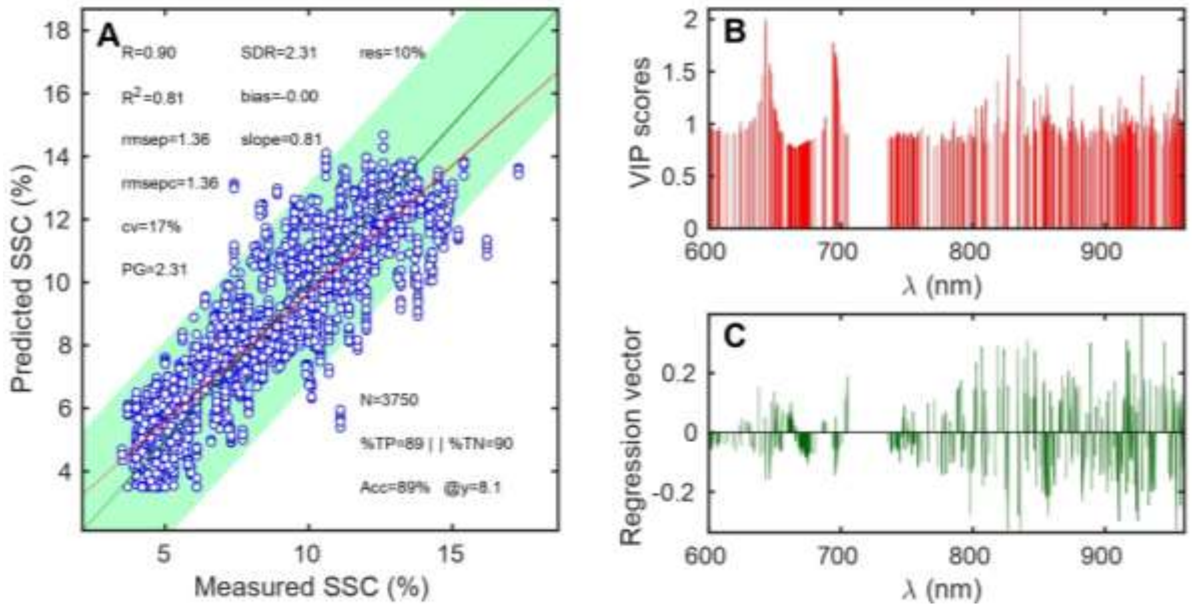

Figure 5.16: Best results for the prediction of SSC in internal validation, with variable selection. The transformation used was SNV in the range 440 to 1000 nm. A) Predicted SSC vs. measured SSC; B) The VIP scores of the selected wavelengths (0 in the eliminated wavelengths); C) the regression vector coefficients (0 in the eliminated wavelengths).

All the models' predictions are plotted together, and these results in a cloud of points represented in Figure 5.16A. The total number of samples is 200+175+125+125 = 625. At each run, 20% of the samples = 125 fruit, are left for validation, so, in the 30 runs, the total number of validation samples is 125 × 30 = 3750. It should be stressed, however, that this representation shows the results of 30 models, not the result of one model only. Therefore, it shows the typical performance of SNV in the range 600 – 960 nm, with variable selection. Although the values in Table 5.11 and Figure 5.16 agree, they could have slight differences due to the way they were calculated, different in the two cases. In the plot, it is calculated only once, for all the 3750 points. Table 5.11 presents the average and standard deviation of

RMSEP for each of the 30 models. This allows to give a confidence interval for the performance parameters:

$$\text{RMSEP} = 1.36 \pm 0.13\%\ \text{SSC} \tag{5.1}$$

$$\text{SDR} = 2.31 \pm 0.19 \tag{5.2}$$

$$R^2 = 0.81 \pm 0.03 \tag{5.3}$$

Figure 5.16B shows the VIP scores of the selected wavelengths, being zero at those rejected. There was one wavelength range that was globally rejected, between 700 and 740 nm approximately, which is the beginning of the NIR plateau. The VIP scores plot can be analysed by either searching for local peaks or by searching denser areas. The peaks are located around 650, 700 and 840 nm, which correspond broadly to chlorophyll (the first two) and to the combination band $3\nu + \delta(\text{O-H})$, already mentioned above. The more compact areas (denser) are located around the ranges 650 - 700nm, which corresponds again to chlorophyll; 740 - 760 nm, corresponding to $4\nu(\text{O-H})$, the third overtone of O-H; and to the range 910 - 930nm, corresponding to $4\nu(\text{C-H})$, the third overtones of C-H and C-H2 stretching. A final dense area is found close to the spectral limit at 960 nm. This is probably the beginning of the influence of the $3\nu(\text{O-H})$ peak, between 960 and 980 nm.

Figure 5.16C shows the regression vector, where rejected wavelengths have a null coefficient. Again, the more consistent bands are those which are denser and more constant, either positively or negatively. These areas coincide largely with the dense areas in the VIP scores plot. The range 650 - 700 nm contains a consistent set of negative coefficients. This is agreement with the expected inverse dependency between chlorophyll and SSC. There is another consistent negative coefficient range in 740 - 760 nm, related with $4\nu(\text{O-H})$. The negative signal is also according to the expected inverse relation between water content and SSC, along ripening. The rest of the regression coefficients is more difficult to interpret.

5.3.2 External validation for 'Jintao' kiwifruit SSC

The summary of the results obtained in external validation is displayed in Table 5.12, which discriminates each one of the four validations.

Table 5.12: Results of variable selection in external validation. Mode: one of the three modes of pre-processing optimization, as described in Section 2.9 (the optimization was not performed again). nLV: number of latent variables. $n\lambda_i$: the number of wavelengths in the full spectra; $n\lambda_f$: the number of wavelengths remaining in the spectra after variable selection; f: the fraction of wavelengths selected; $nIter$: number of iterations in variable selection; SDR, RMSEP and R^2 have the usual meaning.

Mode	valset	nLV	$n\lambda_i$	$n\lambda_f$	f	$nIter$	SDR	RMSEP	R^2
	4	14	1075	544	51	1	0.99	2.36	0.10
	3	12	1075	354	33	4	1.07	2.48	0.18
MIX	2	13	1075	423	39	1	1.29	2.25	0.52
	1	12	1075	347	32	5	1.10	2.72	0.24
Average							1.11	2.45	0.29
	4	11	958	399	42	4	1.01	2.30	0.16
	3	12	958	339	35	3	1.15	2.33	0.30
SNV	2	11	958	367	38	2	1.56	1.86	0.64
	1	11	958	380	40	5	1.31	2.27	0.43
Average							**1.26**	**2.19**	**0.38**
	4	16	518	154	30	4	0.95	2.46	0.01
	3	18	518	213	41	3	1.19	2.24	0.33
SG	2	16	518	156	30	6	1.22	2.37	0.36
	1	15	518	213	41	4	1.37	2.19	0.48
Average							1.18	2.31	0.33

As in Section 5.2, the values of SDR increase when calculated over all the four sets of predictions, relatively to those obtained by averaging the same sets. This may be observed in Figure 5.17A, which shows the best results obtained in the SNV mode. SDR = 1.44 in the figure, against an average SDR of 1.26 in the table. This is mainly an effect of scale, the SSC range is obviously larger in the aggregate set than in the individual ones, since the RMSEP values are essentially the same (2.18 in figure and 2.19 in the table).

Figures 5.17B to 5.17E report the VIP scores for each one of the four validations. In all models there is agreement in the position of the most important bands, with VIP > 1. These are centred around 500 nm, 700 nm (chlorophyll) and 930 nm (4v(C-H)). Apart from this common trend, the rejected bands differ considerably between the four calibrations. For example, the range 560 - 610 nm is rejected only in the fourth calibration, that is, for calset = {2,3,4}, which suggest that its importance in the other calibrations stems from the inclusion of dataset 1.

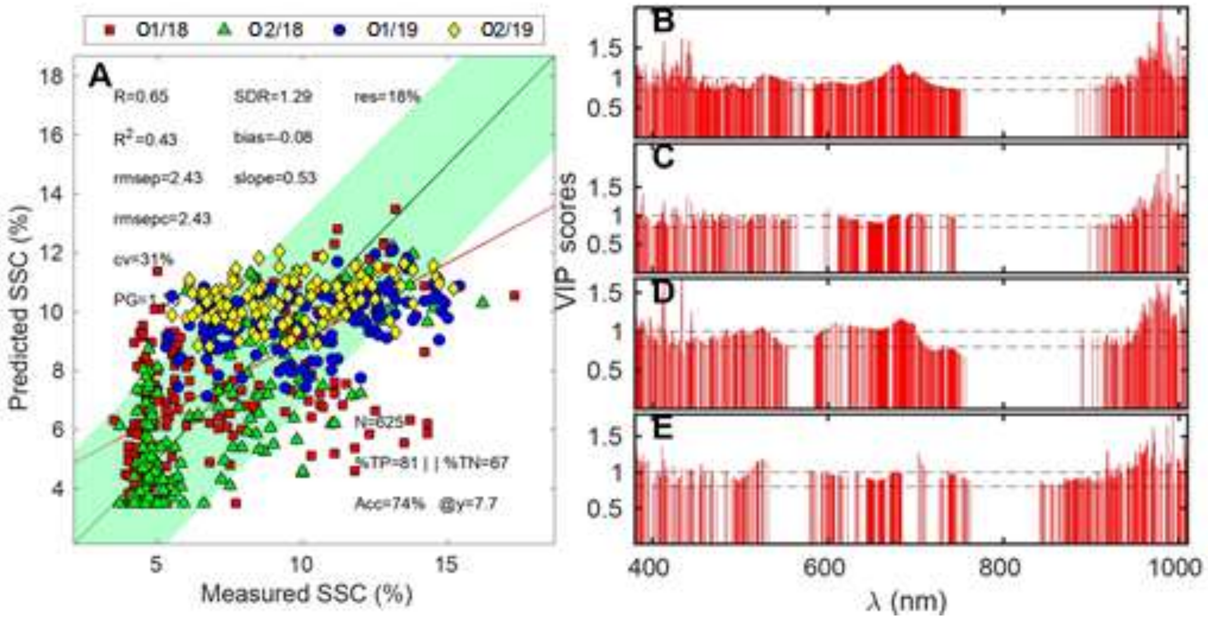

Figure 5.17: Best results for the prediction of 'Jintao' kiwifruit SSC in external validation, with variable selection. The transformation used was SNV in the range 440 to 1000 nm. A) Predicted SSC vs. measured SSC; B to E) The VIP scores of the selected wavelengths (0 in the eliminated wavelengths) for each one of the calibration runs [plot B refers to predictions to dataset 4 (Orchard 2/19) based on calibration on dataset 1+2+3].

The summary of the results obtained from the statistics on all the predictions is shown in Table 5.13.

Table 5.13: Summary of the results obtained in external validation in the three optimization modes with variable selection (TP = "True Positive": TN = "True Negative"; Acc = Accuracy).

Mode	SDR	RMSEP (%)	R^2	bias (%)	slope	TP (%)	TN (%)	Acc. (%)
MIX	1.29	2.43	0.43	-0.08	0.53	81	67	74
SNV	**1.44**	**2.18**	**0.52**	**0.19**	**0.49**	**89**	**64**	**76**
SG	1.37	2.30	0.47	-0.03	0.49	87	68	77

Comparing the results with the application (or not) of variable selection either when performed an external validation either an internal validation, the results showed that variable selection procedure improved the latter.

The best result in internal validation with the Kennard-Stone algorithm was SDR = 2.00, RMSEP = 1.55 % and R^2 = 0.75 (Table 5.5), obtained for the SG mode. With variable selection, the best result was SDR = 2.31 ± 0.19, RMSEP = 1.36 - 0.13 % and R^2 = 0.81 - 0.03. The SDR value is almost two standard deviations above the Kennard-Stone results, which represents a significant difference. The percentage change of SDR was of about 15%.

On the other side, the initial EV results were SDR = 1.39, RMSEP = 2.25 % and R^2 = 0.49, while with variable selection, SDR = 1.44, RMSEP = 2.18 % and R^2 = 0.52. The percentage change of SDR was less than 4 %, which may be simply caused by random fluctuations. It makes sense that variable selection does not improve EV. The process, applied to the aggregate of data from three orchards (calibration set), may lead to a data compression inconsistent with the spectral structure of the fourth orchard (validation), because the four datasets have different structures, i.e., relations between the wavelengths and SSC. On the contrary, in IV all the spectral variations are represented in the calibration dataset, and the spectral compression obtained by variable selection is very likely to be consistent with the validation dataset.

5.4 Orthogonal Signal Correction

5.4.1 Internal validation for 'Jintao' kiwifurit SSC

Following the approach in last section, only the best result in internal validation is illustrated in a plot, but the results of the three modes (MIX, SNV and SG) are described in Table 5.14. As in the process of variable selection, there were 30 calibration/validation rounds with datasets chosen randomly. These originated 30 values of SDR, RSMEP and R^2, which are summarized in the table, through the respective means and standard deviations.

Table 5.14: Results obtained with OSC in internal validation. The averages and standard deviations are obtained over 30 calibration/validation rounds with datasets chosen randomly.

Mode	**nLV**	**SDR**	**σ(SDR)**	$\overline{RMSEP}$	**σ(RMSEP)**	$\overline{R2}$	**σ(R^2)**
MIX	**11**	**2.17**	**0.19**	**1.48**	**0.12**	**0.79**	**0.04**
SNV	8	2.15	0.20	1.48	0.13	0.78	0.04
SG	19	1.99	0.15	1.59	0.12	0.75	0.04

The best result was obtained in the MIX mode and is represented in Figure 5.18 Figure 5.18A shows the standard predicted vs. measured plot, which shows results intermediate between Variable Selection and Kennard-Stone results. Figure 5.18B shows the VIP scores, which may be compared with those of Figure 5.18C. The importance of the NIR part of the spectrum increased, not only the larger yellow area above 620 nm, but also the appearance of a peak around 840 nm, the combination band of O-H. This makes sense, since the true information on SSC should be found on the NIR part of the spectrum, while the pigments' band information is only indirectly correlated. It seems, thus, that OSC has redirected the model towards the true source of information. The regression coefficients' plot, however, still presents the picture of well-defined lobes in the pigments' region, while the NIR region has a more oscillatory pattern.

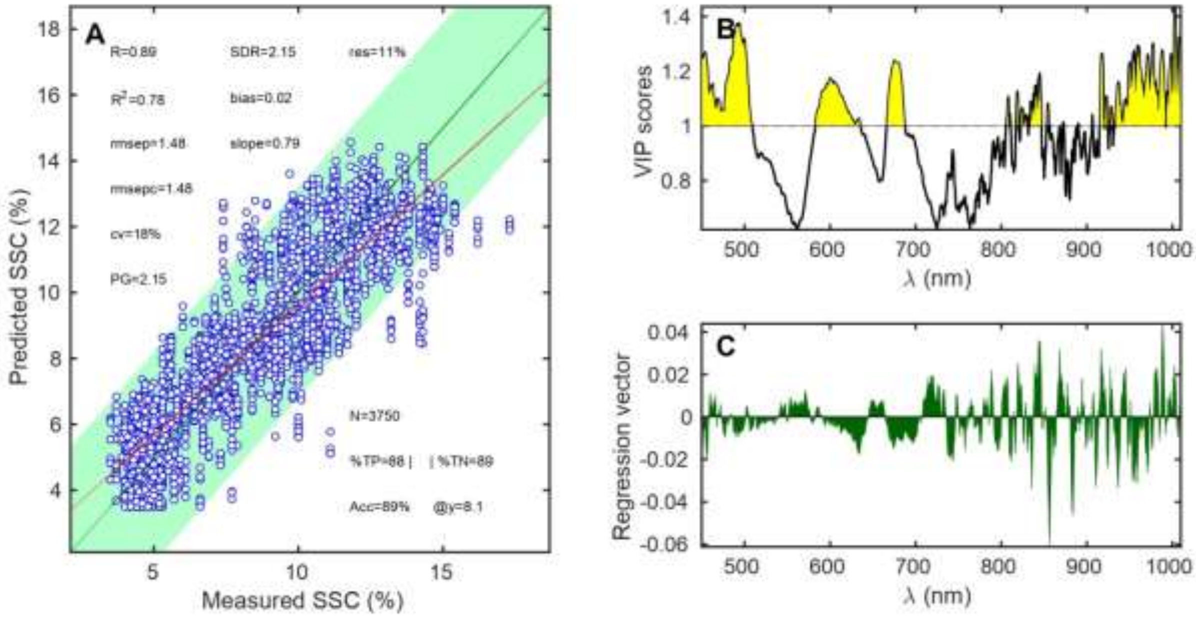

Figure 5.18: Best results for the prediction of SSC in internal validation, with OSC. The transformation used was SNV in the range 440 to 1000 nm. A) Predicted SSC vs. measured SSC; B) The VIP scores; C) The regression vector coefficients.

5.4.2 External validation of 'Jintao' kiwifruit SSC

The summary of the results obtained in external validation is displayed in Table 5.15, which discriminates each one of the four validations.

Table 5.15: Results of OSC in external validation of ‘Jintao’ kiwifruit SSC.

Mode	valset	nLV	SDR	RMSEP	R^2
	4	11	1.03	2.27	0.06
MIX	3	11	1.10	2.42	0.22
	2	9	1.53	1.89	0.59
	1	9	1.14	2.62	0.25
Average			**1.20**	**2.30**	**0.28**
	4	6	1.02	2.29	0.06
SNV	3	7	1.01	2.64	0.35
	2	8	1.22	2.38	0.35
	1	7	0.84	3.55	0.00
Average			1.02	2.71	0.19
	4	19	0.94	2.49	0.01
SG	3	19	1.16	2.30	0.37
	2	18	1.01	2.87	0.25
	1	17	1.07	2.80	0.19
Average			1.04	2.61	0.20

Note again that the values of SDR increase when calculated over all the four sets of predictions, relatively to those obtained by averaging the same sets. This may be observed in Figure 5.19A, which shows the best results, obtained in the MIX mode. SDR = 1.36 in the figure, against an average SDR of 1.20 in the table. Figure 5.19B shows the VIP scores obtained for each one of the calibrations. This picture explains why OSC fails in external validation. The orthogonalization process led to different weights of the spectral components in each set. This is very clear up to 750 nm. There is no consistency of OSC across the different orchards, and thus it fails to improve the results. The differences are not so obvious in the regression coefficients, Figure 5.19C.

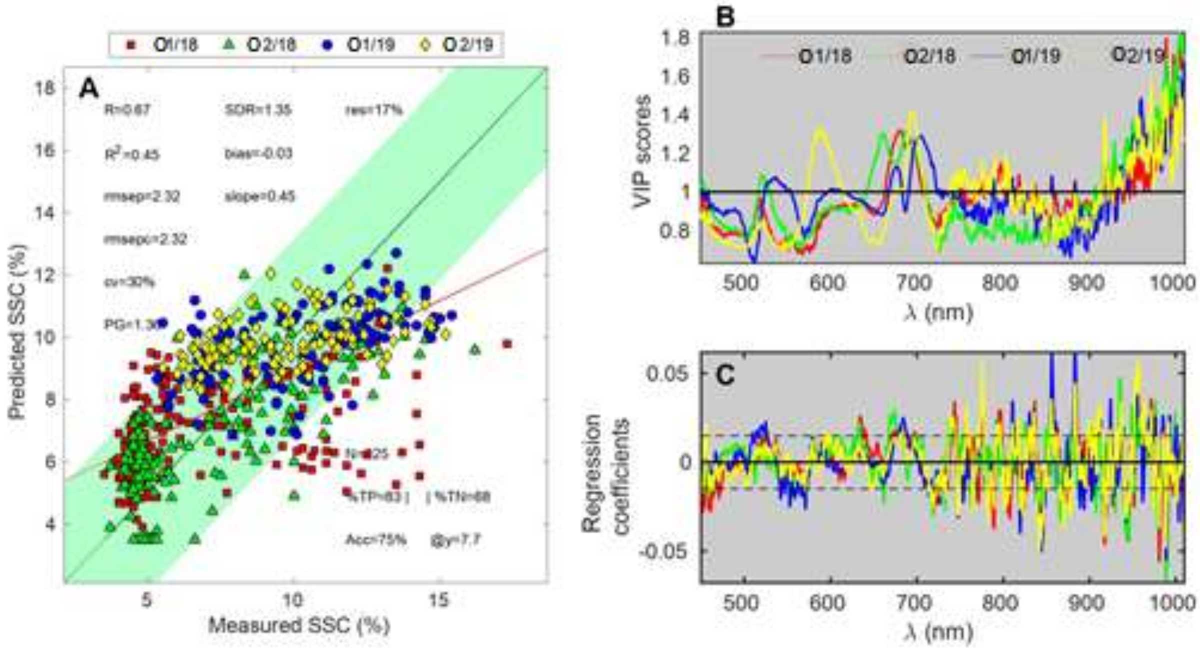

Figure 5.19: Best results for the prediction of SSC in external validation, with OSC. The transformation used was SNV in the range 450 to 1010 nm. A) Predicted SSC vs. measured SSC; B) The VIP scores; C) the regression vector coefficients. The curves/points relative to G1/18 (red) correspond to validation in that dataset, which means that the calibration set is constituted by the other sets; and in the same way, for the other curves.

The global results obtained from the three modes in the predicted/measured plot are **shown in Table 5.16.**

Table 5.16: OSC in external validation of 'Jintao' kiwifruit SSC with OSC. Results obtained from the predicted/measured plots.

Mode	SDR	RMSEP	R^2
MIX	**1.35**	**2.32**	**0.45**
SNV	1.30	2.43	0.42
SG	1.28	2.46	0.39

The results showed that OSC procedure improved slightly the internal validation. The best result in internal validation with the Kennard-Stone algorithm was SDR = 2.00, RMSEP = 1.55 % and R^2 = 0.75 (see Table 5.5), obtained for the SG mode. With OSC selection, the best result was SDR = 2.17 ± 0.19, RMSEP = 1.48 ± 0.12 % and R^2 = 0.79 ± 0.04. The SDR value is almost one standard deviation above the Kennard-Stone result. The percentage change of SDR was of about 9 %.

On the other side, the initial EV results were SDR = 1.39, RMSEP = 2.25 % and R2 = 0.49, while with OSC, SDR = 1.35, RMSEP = 2.32 % and R^2 = 0.45. The results were worse with OSC.

Again, it makes sense that OSC does not improve EV: the process, applied in the calibration set (three of the four orchards), may lead to a rotation of the loadings inconsistent with the spectral structure of the fourth orchard (validation), because the four datasets have different structures, i.e., relations between the wavelengths and SSC. On the contrary, in IV all the spectral variations are represented in the calibration dataset, and the transformation obtained by OSC is very likely to be consistent with the validation dataset.

Comparing Table 5.11 and Table 5.**14**, OSC seems to be less efficient than Variable Selection to improve the internal validation results. However, the difference is not very clear and more datasets should be analysed in order to extract any conclusion.

5.5 Calibration transfer

The problem of calibration transfer is a classic one in chemometrics.

In a typical application it is necessary to transfer a model built in one instrument to another one, with a different spectral response (and even within the same brand and model, the response is never the same).

There are two broad classes of methods for solving calibration transfer problem: 1) techniques that attempt to predict the response of the slave instrument based on the response of the master instrument, i.e., map the response of one instrument into another and 2) techniques that eliminate the differences between instruments, leaving only the parts they have in common. The most well-known method for the first type of methods is The Piece-wise Direct Standardization (PDS) method (Wang et al., 1991), while Orthogonal Signal Correction (OSC) (Wold et al. 1998), already used in the previous section, may also be applied to solve the calibration transfer problem, by removing the variations in one instrument that are orthogonal to variations in the other.

Tests were carried out with PDS, applied to average spectra from both spectrometers. In the absence of common samples, it was initially thought to use average spectra of fruits under similar conditions in 2018 and 2019. For example, averages of spectra from fruits with equal or close DAFB in 2018 and 2019, or with similar SSC. However, the results were quite unstable, in the sense that they were highly dependent on the chosen averages and even generated spectral artefacts. As such, these tests are not presented in this thesis.

A simpler approach was then considered, based on a normalization to daily averages, as described in Section 2.7.4.6.

Figure 5.20 illustrates the process of calibration transfer. This is done for the specific case of the 5th day (i = 5) in the Orchard 22/2019 dataset (third slave, k = 3). Therefore, the expressions above particularize here to i = 5 and k = 3.

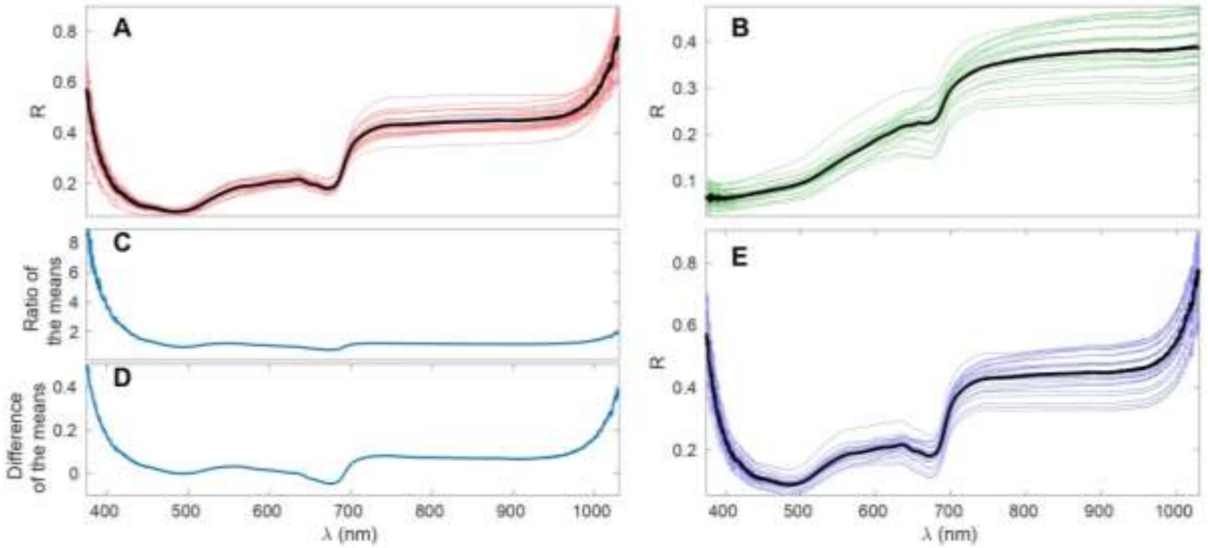

Figure 5.20: Illustration of the calibration transfer procedure. A: the synthetic master for the 5th day (i = 5) of Orchard 2/2019 (third slave, k = 3). In red, the individual synthetic master spectra $M_{5j}^{(3)}(\lambda)$, and in black the average, $\overline{M_5^{(3)}}(\lambda)$; B) The slave spectra, that is, the spectra from the 5th day (i = 5) of Orchard 2/2019 (third slave, k = 3). In green, the individual slave spectra $S_{5j}^{(3)}(\lambda)$, and in black the average $\overline{S_5^{(3)}}(\lambda)$; C) the ratio of averages, $R_5^{(3)}(\lambda)$; D) The difference of the averages, $D_5^{(3)}(\lambda)$; E) The transformed spectra. In blue, the individual transformed spectra $T_{5j}^{(3)}(\lambda)$, and in black the average, $\overline{T_5^{(3)}}(\lambda)$.

The spectra shown in Figure 5.20A correspond already to the synthetic master. In red, the individual spectra $M_{5j}^{(3)}(\lambda)$, and in black the average, $\overline{\overline{M_5^{(3)}}}(\lambda)$. Figure 5.20B shows the slave spectra. The difference between the two is very clear, and this has already pointed out in Figure 5.1 and Figure 5.**2** and subsequent discussion. In green, the individual slave spectra $S_{5j}^{(3)}(\lambda)$, and in black the average, $\overline{S_5^{(3)}}(\lambda)$. Figure 5.20C shows the ratio of averages, $R_5^{(3)}(\lambda)$ and Figure 5.20D shows their difference, $D_5^{(3)}(\lambda)$. Finally, in Figure 5.20E, the result of the transformation (5.19), having in blue, the individual transformed spectra $T_{5j}^{(3)}(\lambda)$, and in black the average, $\overline{T_5^{(3)}}(\lambda)$.

The transformed spectra resemble now the master spectra. Furthermore, the dispersion of the spectra has been kept. The slave spectra in B have more dispersion that the master spectra in A, especially in the NIR plateau. That dispersion is still apparent in E, after the transformation.

5.5.1 Internal validation for 'Jintao' kiwifruit SSC

This section is basically a repetition of all the previous sections, simply exchanging the set of initial spectra for the set of spectra transformed by the calibration transfer procedure. Thus, there is no point in repeating all the steps taken before, and the information will be displayed in a more compact form. Only graphs that contribute to give some new insight into the structure of the data will be presented. The three modes (MIX, SNV and SG) are still used, i.e., each calibration/validation process is performed with three different pre-processing transformations. The complete list of model types is shown in Table 5.17. This has been done before for the raw data and will be repeated for the calibration-transferred data.

Table 5.17: The 18 types of models developed for the raw and calibration-transferred data. Kennard-Stone applies to internal validation, while 3to1 means "3 orchards in calibration and 1 in validation" and is applied in external validation.

Model Type	Internal Validation	External Validation
Kennard-Stone or 3to1	MIX	MIX
	SNV	SNV
	SG	SG
Variable Selection	MIX	MIX
	SNV	SNV
	SG	SG
OSC	MIX	MIX
	SNV	SNV
	SG	SG

Given that the data changed, the initial pre-processing optimization, as described in Section 2.7.4.2, was repeated. The result is shown in Table 5.18.

Table 5.18: Pre-processing transformations chosen by the optimization process described in Section 2.9 applied to internal validation.

Mode	Transformation	λ_i	λ_f
MIX	snv	450	1010
SNV	abs+snv	380	1020
SG	sg(w=155,o=2,d=1)	650	1020

The global summary of the results obtained in internal validation is shown in Table 5.19. The main conclusion is that there is no significant improvement relatively to the raw data. Comparing this table with Table 5.11 and Table 5.14, there is no observable improvement. On the contrary, the results shown here are, on average, worse than those obtained without calibration transfer. This will be discussed again in the end of the section. A minor detail is the failure of the KS model for the SNV mode (SDR = 0.99). This is a consequence of the realistic, but blind choice of best pre-processing. It is not common, but it may happen that the best pre-processing chosen by Algorithm 1 fails in validation. This happened indeed in this case.

Table 5.19: Summary of the results obtained in internal validation with calibration-transferred data. KS =Kennard-Stone, VarSel = Variable selection, OSC = Orthogonal Signal Correction.

Model	**Mode**	**SDR**	**RMSEP(%)**	**R^2**
KS	MIX	1.82	1.64	0.73
	SNV	0.99	2.44	0.36
	SG	1.69	1.86	0.67
VarSel	MIX	2.04±0.16	1.55±0.13	0.76±0.04
	SNV	**2.26±0.18**	**1.41±0.13**	**0.8±0.03**
	SG	1.93±0.14	1.62±0.11	0.73±0.04
OSC	MIX	2.06±0.16	1.57±0.12	0.76±0.04
	SNV	2.08±0.17	1.52±0.12	0.77±0.03
	SG	1.83±0.15	1.73±0.13	0.71±0.04

It is interesting to note that higher uniformity of the calibration transferred dataset allows to shift the main directions of the model towards the true source of SSC information, as OSC as already done. This may be observed by comparing Figure 5.21 with the corresponding Figure 5.10. The main region of the VIP scores is now located in the NIR, close to the 3v(O-H) peak.

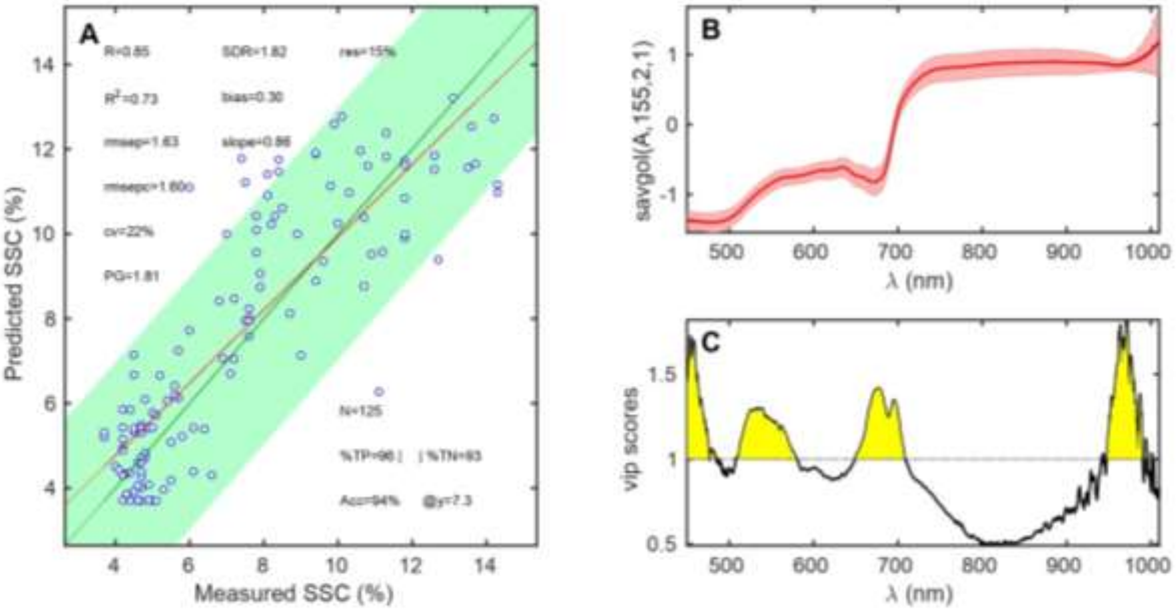

Figure 5.21: Best results for the prediction of SSC, based on the pre-processing optimization in the MIX Mode and on the calibration-transferred dataset. A) predicted vs. measured SSC values; B) average transformed spectrum (red line) and one standard deviation bands (pink area); C) VIP scores.

.

Another interesting aspect is that variable selection tends to be much more effective in the calibration transferred dataset. This is very clear, when comparing the best, Figure 5.16, with the new best result, in the transformed dataset, Figure 5.22. The VIP plot in Figure 5.16B is much denser, rejecting clearly only one band, in the approximate range 700 - 730 nm. In the transformed dataset, the VIP scores is less dense, and there are four rejected bands: 500 - 520 nm, 570 - 630 nm, 650 - 700 nm and 750 - 850 nm. The retained bands have more chemical meaning, including the pigments, the 4v(O-H) band at 740 nm and the region 900 - 1000 nm, with C-H and O-H bands. It is possible that the Variable Selection (VarSel) process is exhausted in the process of cancelling the differences between the two spectrometers, while in the calibration-transferred data, the effort goes directly into the selection of the appropriate bands. However, the initial results (without calibration transfer) are better than the current ones.

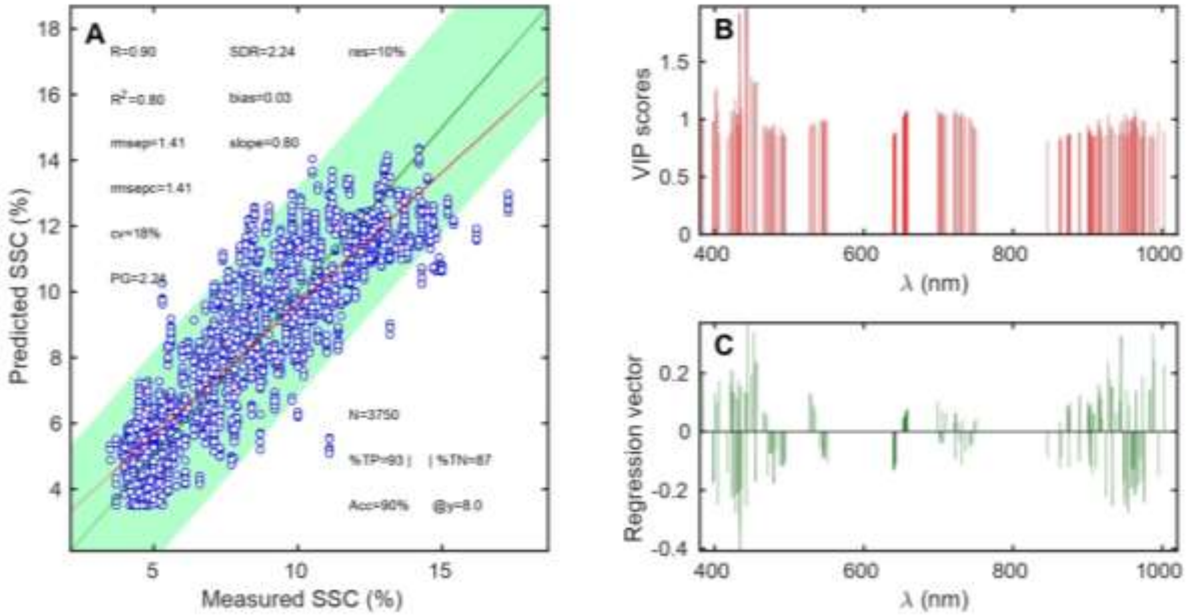

Figure 5.22: Best results for the prediction of SSC in internal validation, with variable selection and the calibration transferred dataset. The transformation used was SNV in the range 380 to 1020 nm. A) Predicted SSC vs. measured SSC; B) The VIP scores of the selected wavelengths (0 in the eliminated wavelengths); C) the regression vector coefficients (0 in the eliminated wavelengths).

5.5.2 External validation for ‘Jintao’ kiwifruit SSC

Given that the data changed, the initial pre-processing optimization, as described in Section 2.7.4.2, was repeated. The result is shown in Table 5.20.

Table 5.20: Pre-processing transformations chosen by the optimization process described in Section 2.9 applied to external validation.

Mode	Transformation	λ_i	λ_f
MIX	lsnv(w=529)	380	1010
SNV	abs+snv	400	1020
SG	sg(w=155,o=2,d=1)	650	1020

The global summary of the results obtained in internal validation is shown in **Table 5.21**. The main conclusion here is opposite to that of the internal validation. The calibration-transferred data yields significantly better results. In the raw data, the SDR values are all of the order of 1.3 - 1.4, in the best case. Here, SDR is always about 1.7 - 1.8. In terms of predictive power, it makes a big difference, especially for daily average predictions, as shown below. While SDR ~ 1.3 does not even allow for reasonable daily average predictions, a value of SDR ~ 1.8 is already enough to get robust average predictions.

Table 5.21: Summary of the results obtained in internal validation with calibration-transferred data. 3to1 = calibration with 3 orchards and validation with the other, VarSel = Variable selection, OSC = Orthogonal Signal Correction.

Model	Mode	SDR	RMSEP (%)	R^2
3to1	MIX	1.71	1.82	0.67
	SNV	1.77	1.77	0.69
	SG	1.67	1.89	0.65
VarSel	MIX	1.73	1.81	0.68
	SNV	1.75	1.80	0.68
	SG	1.62	1.95	0.62
OSC	MIX	1.77	1.78	0.68
	SNV	**1.81**	**1.73**	**0.7**
	SG	1.71	1.84	0.66

The differences of VIP scores between the raw and calibration-transferred data are also very noticeable. For the variable selection procedure, the finding is similar to that of internal validation: the selected variables are sparser and clear rejection bands appear. Comparing Figure 5.23 with Figure 5.17, this is very clear. While in the latter there are no rejection bands common to the four calibrations (sub plots B - E), in the former there are two bands consistently rejected: 550 - 650 nm and 750 - 850 nm (expect in subplot C, where this band is depleted, although not entirely rejected). They are also consistent with the results found in internal validation. Altogether, this seems to indicate that data uniformity allows the variable selection method to concentrate on the true information, while in heterogeneous data it concentrates in finding common features to the spectra obtained in two different spectrometers.

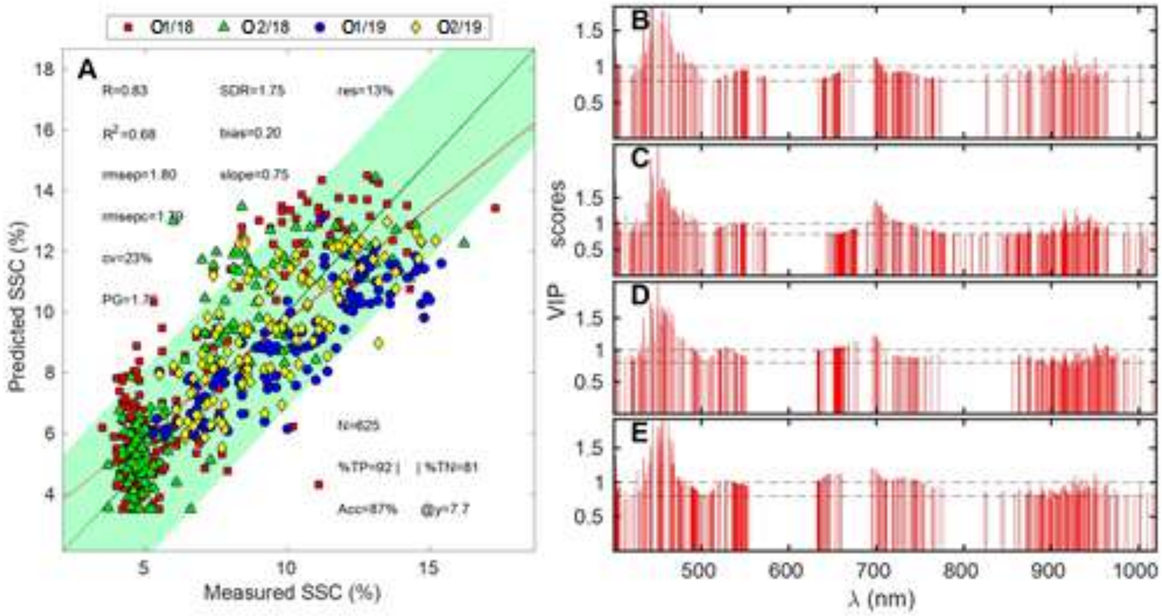

Figure 5.23: Best results for the prediction of SSC in external validation, with variable selection and the calibration transferred dataset. The transformation used was SNV in the range 400 to 1020 nm. A) Predicted SSC vs. measured SSC; B) The VIP scores of the selected wavelengths (0 in the eliminated wavelengths); C) the regression vector coefficients (0 in the eliminated wavelengths).

Lastly, it is important to note the difference in the regression slopes (0.75 in **Figure 5.23** vs. 0.49 in **Figure 5.17**). The linearity is much improved and the data is now mostly contained within the plot green band, of one standard deviation around the slope 1 straight line.

The OSC VIP scores contain another demonstration of consistence of the transformed data. Figure 5.24 shows the results of OSC in external validation. It should be compared with Figure 5.19, obtained with the original datasets. The main difference between the VIP scores in both figures is that they are relevant and consistent in the NIR, in Figure 5.24, while they are noisy and inconsistent for the original data, Figure 5.19. Even the pigments' region has a higher degree of consistency in transformed data. The same is true concerning the regression coefficients in the range 550 - 700 nm. Overall, the structure of the four models is more similar to each other when using the transformed datasets, resulting in a superior performance.

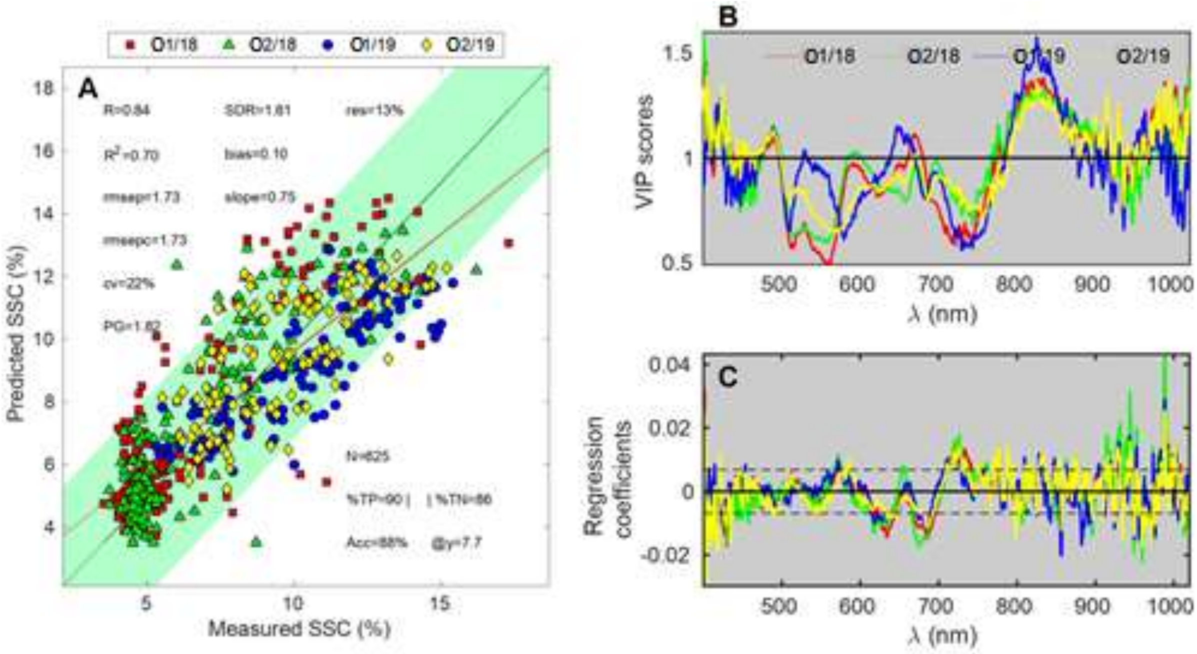

Figure 5.24: Best results for the prediction of SSC in external validation, with OSC and on the calibration-transferred dataset. The transformation used was ABS + SNV in the range 400 to 1020 nm. A) Predicted SSC vs. measured SSC; B) The VIP scores; C) the regression vector coefficients. The curves/points relative to Orchard 1/18 (red) correspond to validation in that dataset, which means that the calibration set is constituted by the other sets, and in the same way, for the other curves.

5.5.2.1 Daily average predictions

The advantage of the calibration transfer adopted is yet clearer if the daily orchard average is the only relevant parameter (as it is in most of the field applications). The results below follow strict external validation.

The prediction of the daily averages for orchard D is based on a model built only from data of the orchards A, B and C. The calibration transfer is performed, but this needs only the knowledge of DAFB and of the spectra, not the SSC values.

The models used in the next figures are the simple 3-to-1 versions.

Figure 5.25 shows the daily average predictions on the basis of the 3to1 models built from the original data. It is clear that the predictions miss the target many times. In Figures 5.25A and 5.25B, the predictions are mainly flat. The predictions in Figure 5.25C are the best, although with large fluctuations in the first days. Finally, the predictions in D show a “false alarm" in the second day (prediction above 8%, when the real value was below 5%) and a huge drop in the last day.

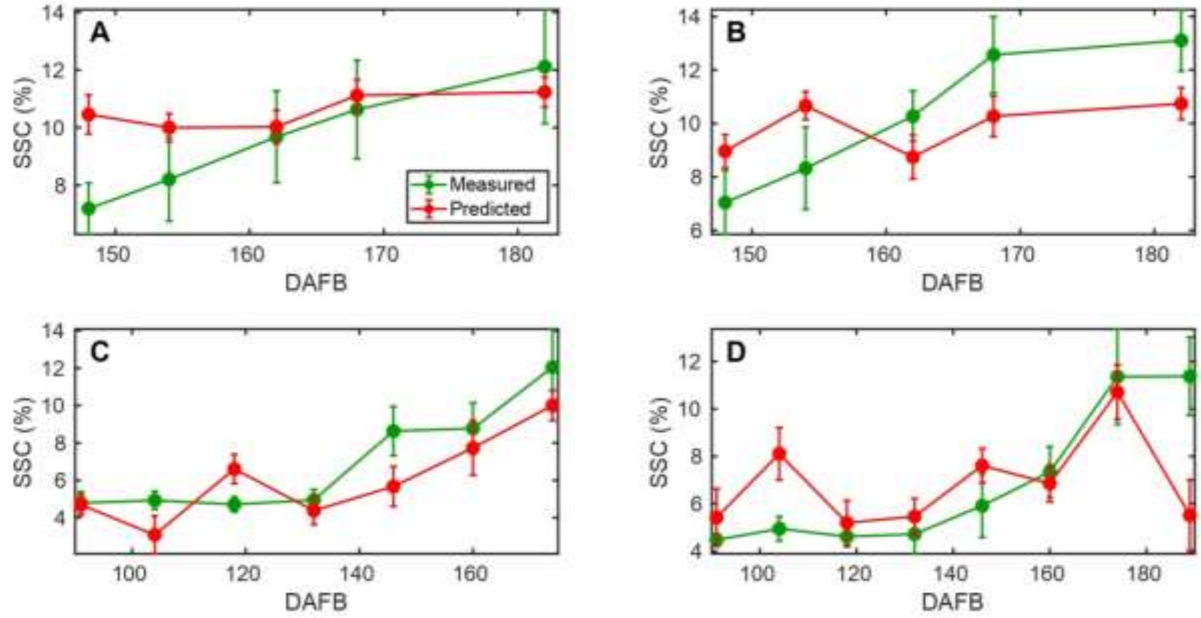

Figure 5.25: Daily average predictions based on the 3to1 models built from the original data. DAFB = days after full bloom. A) predictions for orchard D (Orchard 2/2019), based on the calibration on the other orchards; B) predictions for orchard C (Orchard 1/2019); C) predictions for orchard B (Orchard 2/2018); D) predictions for orchard A (Orchard 1/2018). The points represent the daily average and the errors bars represent the standard deviation.

Figure 5.26 shows the daily average predictions based on the 3to1 models built from the calibration transferred data. The predictions are much better, particularly, the predictions in sub-Figures 5.26A and 5.26B are no longer flat and follow the increasing trend of SSC. However, in Figure 5.26B there is still a significant bias, with the daily averages being consistently underestimated. Fortunately, this is the case that may be corrected with bias recalibration (Pires et al., 2022). Since this requires information from the new Y-block, it will not be considered here. The predictions in Figure 5.26C are still the best and much improved relatively to the previous figure. Finally, the predictions in D are also much improved, only with the first day out of the pattern.

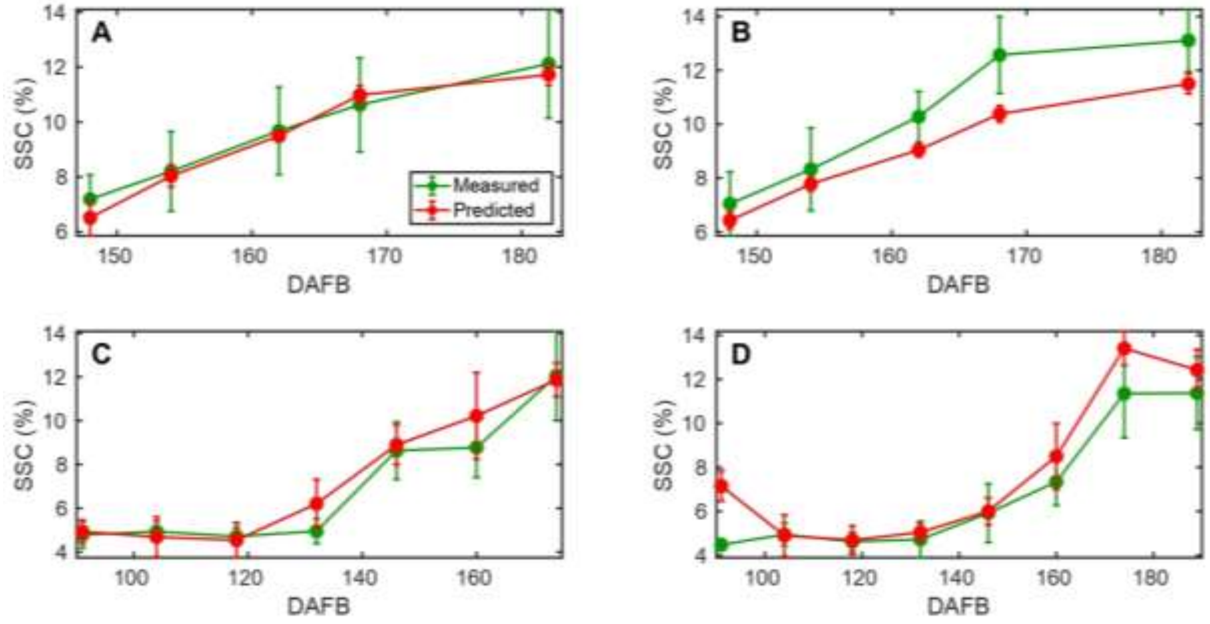

Figure 5.26: Daily average predictions based on the 3to1 models built from the calibration-transferred data. DAFB = days after full bloom. A) predictions for orchard 4 (Orchard 2/2019), based on the calibration on the other orchards; B) predictions for orchard 3 (Orchard 1/2019); C) predictions for orchard 2 (Orchard 2/2018); D) predictions for orchard 1 (Orchard 1/2018). The points represent the daily average and the errors bars represent the standard deviation.

5.6 Global comparison

All the results obtained in this chapter are summarized in Figure 5.27, in terms of the dimensionless parameter SDR. The internal validation results are depicted in the left half, in tones of blue, while the external validation results are in the right half, in tones of red. These two main regions are, in turn, divided in two others, one for the results obtained with the original data (no calibration transfer), and the other for the results obtained with calibration-transferred data (identified in the plot by “CalTransfer data"). These four sections (quarters) are still divided in more three, corresponding to the three types of models developed: Direct (KS validation in the case of Internal Validation, 3to1 - 3 orchards in calibration, 1 in validation - for external validation); VarSel and OSC. Each one of these sections is finally divided in the three modes of pre-processing, “MIX", “snv" and “sg". In total, 36 models were calculated for SSC and which allows to have a statistical perspective of the global behaviour of the models.

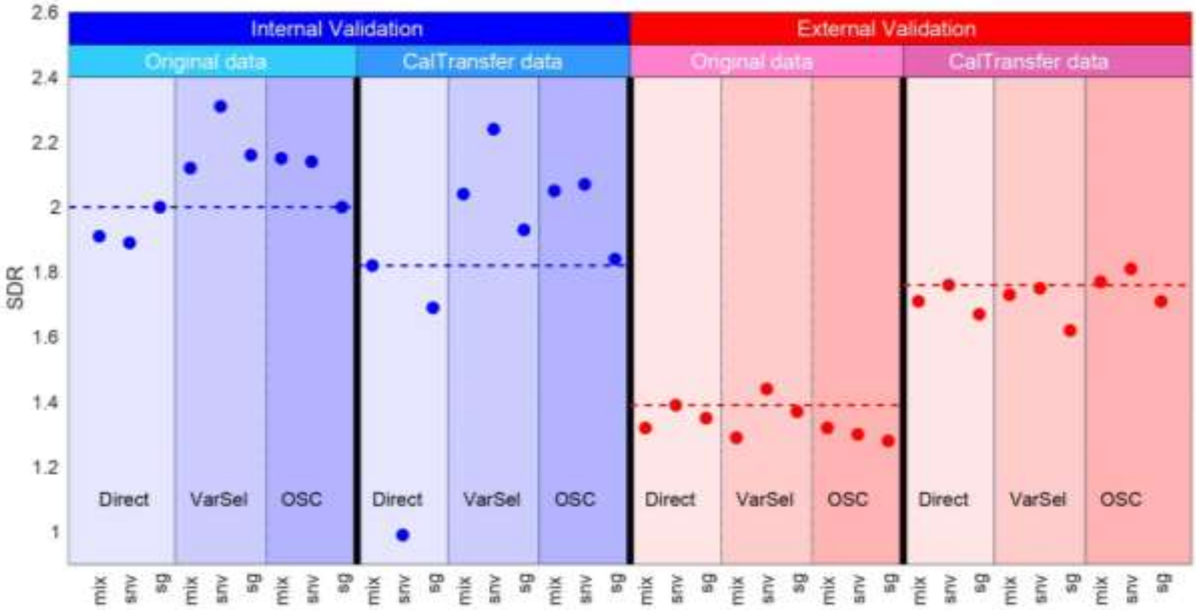

Figure 5.27: Summary of all the results based on the dimensionless parameter SDR. The internal validation results are depicted in the left half, in tones of blue, while the external validation results are in the right half, in tones of red. These two main regions are, in turn, divided in two others, one for the results obtained with the original data (no calibration transfer), and the other for the results obtained with calibration-transferred data (“CalTransfer data"). These four sections (quarters) are still divided in more three, corresponding to the three types of models developed: Direct (Kennard-Stone validation in the case of Internal Validation, 3to1 in external validation); Variable Selection (VarSel) and Orthogonal Signal Correction (OSC). Each one of these sections is finally divided in the three modes of pre-processing, “MIX", “snv" and “sg".

The best result obtained in the Direct Model (KS or 3to1) is the dashed reference line in each quarter. It allows to check visually if VarSel and/or OSC offer better results over the direct validation. Put shortly, the most striking conclusions of the study are:

1. External validation benefits significantly from calibration transfer (CT), but not from VarSel or OSC;

2. Internal Validation has the opposite behaviour, since it does not benefit from CT (actually worsens), but receives meaningful improvement by the implementation of VarSel or OSC;

These conclusions are, on one hand, easy to understand, and, on the other, difficult.

It is easy to understand that:

a) External validation benefits from CT. Indeed, the heterogeneity of the datasets difficult the application of a model built in three of the orchards to the fourth. CT reduces that heterogeneity and improves the predictions;

b) Internal validation benefits from VarSel or OSC, since calibration and validation datasets are very homogeneous, and any spectral transformation performed in the calibration dataset, that improves the relation between the X and Y blocks, is very likely to behave similarly in the validation dataset;

c) External validation in the original datasets does not benefit from VarSel or OSC, because, due data heterogeneity, the calibration dataset is not replicate in the validation dataset.

It is not easy to understand that:

a) External Validation does not benefit from VarSel or OSC, even in the calibration-transferred data. This probably means that the CT is only partly successful in removing data heterogeneity;
b) Internal Validation does not benefit from CT. This probably means that the CT procedure adopted destroys some of the information used by the original data model.

Overall, the procedure seems to work well for real life situations, when the models are tested in new data.

The global performance of daily average predictions may be also observed in a predicted vs. measured plot, and this is done in **Figure 5.28**. In Figure 5.28A the predictions come from the models built with the original data (corresponding to Figure 5.25). In Figure 5.28B the predictions come from the models built with the calibration transferred data (corresponding to Figure 5.26). The latter allow to predict the daily averages with very good precision, with SDR = 2.78 and RMSEP = 1.06 % and R^2 = 0.87.

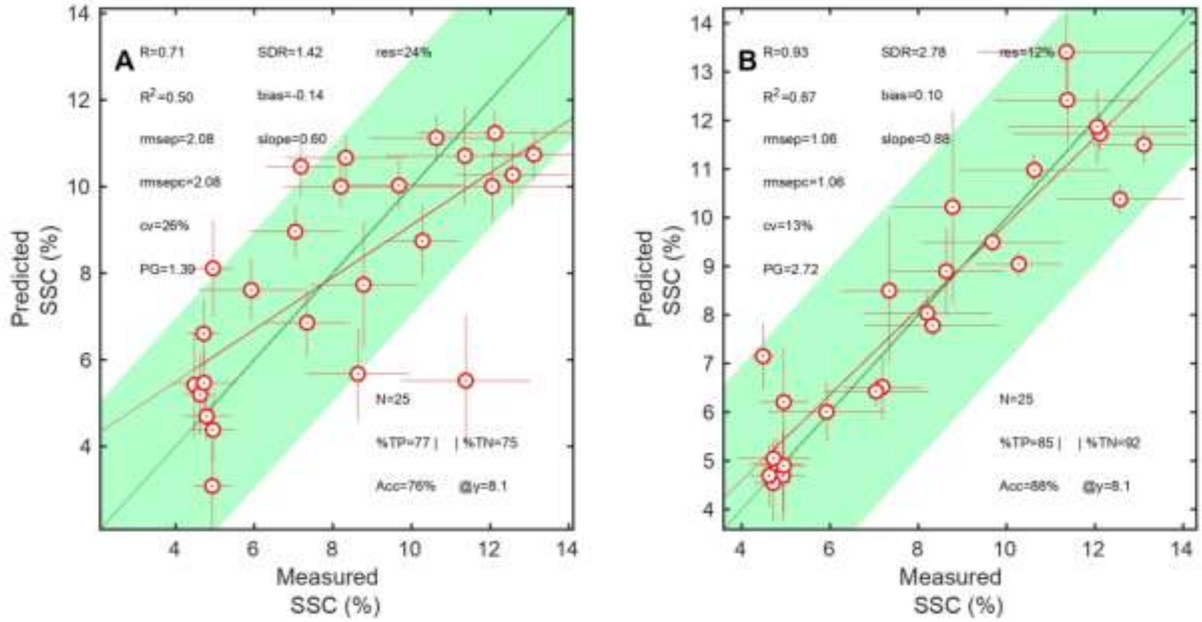

Figure 5.28: Predicted vs. measured daily average SSC, with predictions obtained through external validation 3-to-1 models. A) the models were built from the original data; B) the models were built from calibration-transferred data. The points represent the daily averages, the vertical error bars represent the standard deviation of the predictions and the horizontal error bars represent the standard deviation of the measured value.

Chapter 6

Kiwifruit storage ripening follow-up

Afonso, Andreia M.; Guerra, Rui; Cruz, Sandra; Antunes, Maria Dulce. (2023). Sensory evaluation and spectra evolution of two kiwifruit cultivars during cold storage. (submitted)

6.1 Ripening evolution of ‘Jintao’ kiwifruit during storage

6.1.1 Colorimetric parameters

The initial averages of L* for ‘Jintao’ kiwifruit, in 2018 to 2020, were 58.25, 61.85 and 66.70, respectively (Figure 6.1). The corresponding values at the end of cold storage were 53.27, 56.34 and 52.47, being very similar for the three years, independently of the initial storage value.

In 2019/2020 and 2020/2021, L* decreased in the first sampling dates and then stabilized, without significant differences along time, since 89 and 44 days of storage, respectively (Figures 6.1B and 6.1C). In 2018/2019 values also decreased till 89 storage days, however there is an increase at 103 and at 146 storage days (Figure 6.1A).

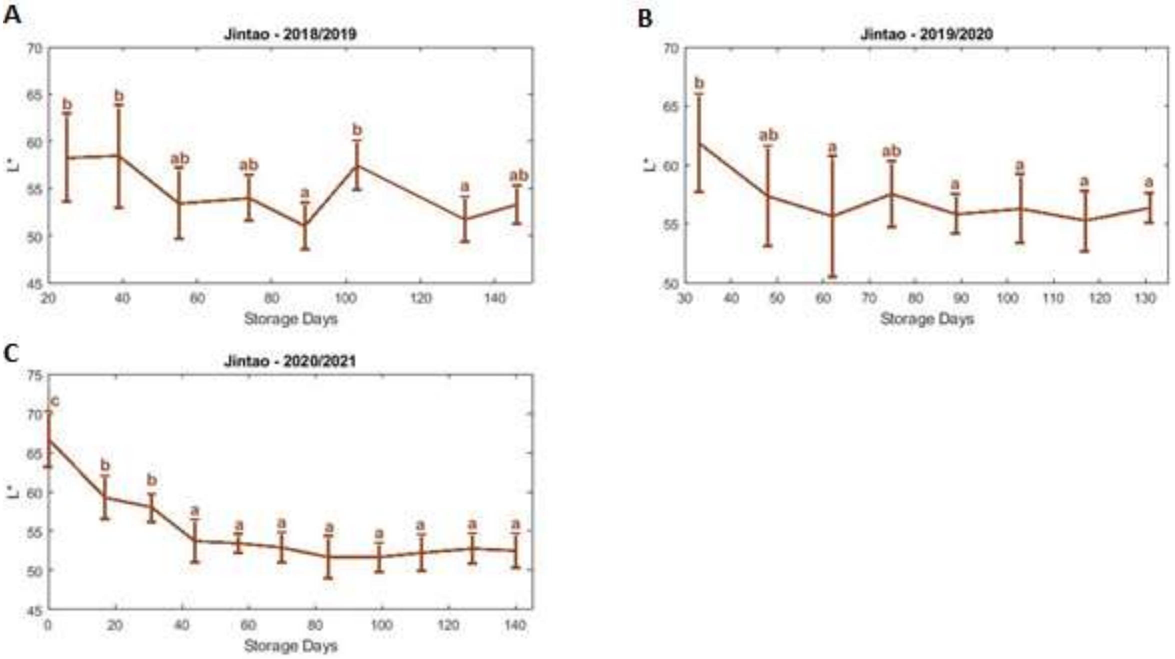

Figure 6.1: ‘Jintao’ kiwifruit temporal evolution of L* during storage along: A) 2018/2019; B) 2019/2020; C) 2020/2021. Data depicted is the Mean ± SE of 8 kiwifruit. Statistically different means ($p < 0.05$) between sampling dates are signalled with different letters.

The initial averages of b* for ‘Jintao’ kiwifruit, in 2018 to 2020, were 23.48, 27.78 and 34.04, respectively (Figure 6.2). The corresponding values at the end of storage were 26.50, 27.00 and 26.26, again very similar for the three years, independently of the initial storage b* value.

In 2018/2019, b* revealed an irregular evolution since increased till 103 storage days, except at 89th day, and then decreased, while in 2019/2020 there are not significant differences along storage (Figures 6.2A and 6.2B). In 2020/2021, b* showed a different pattern with values decreasing till 84 days of storage, increasing a little next and stabilizing at the end (Figure 6.2C).

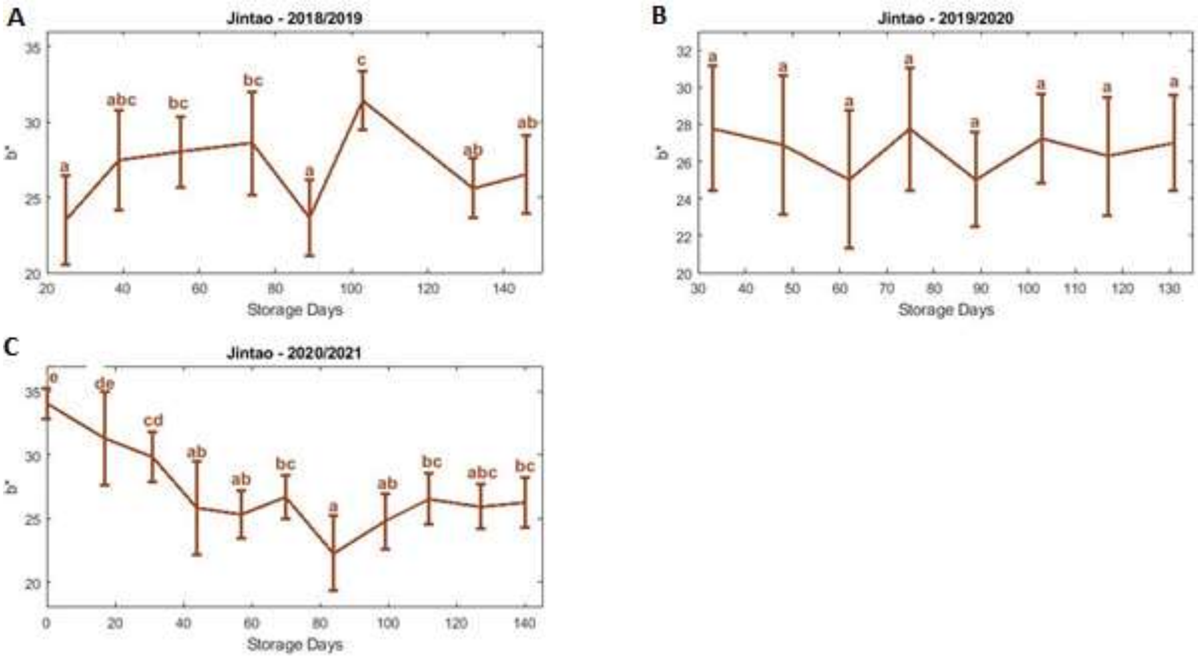

Figure 6.2: ‘Jintao’ kiwifruit temporal evolution of b* during storage along: A) 2018/2019; B) 2019/2020; C) 2020/2021. Data depicted is the Mean ± SE of 8 kiwifruit. Statistically different means ($p < 0.05$) between sampling dates are signalled with different letters.

The initial averages of chroma, in 2018 to 2020, were 24.04, 28.29 and 34.92, respectively (Figure 6.3). The corresponding values at the end of storage were 27.08, 27.36 and 26.44.

Chroma exhibited an evolution pattern similar to b*. In 2019/2020, there are no significant differences for chroma values along time (Figure 6.3B). In the other two years, the evolution pattern was more irregular with an increase on the first days in 2018/2019 and a decrease in 2020/2021, although the values stabilized at the end of the storage period (Figures 6.3 and 6.3C).

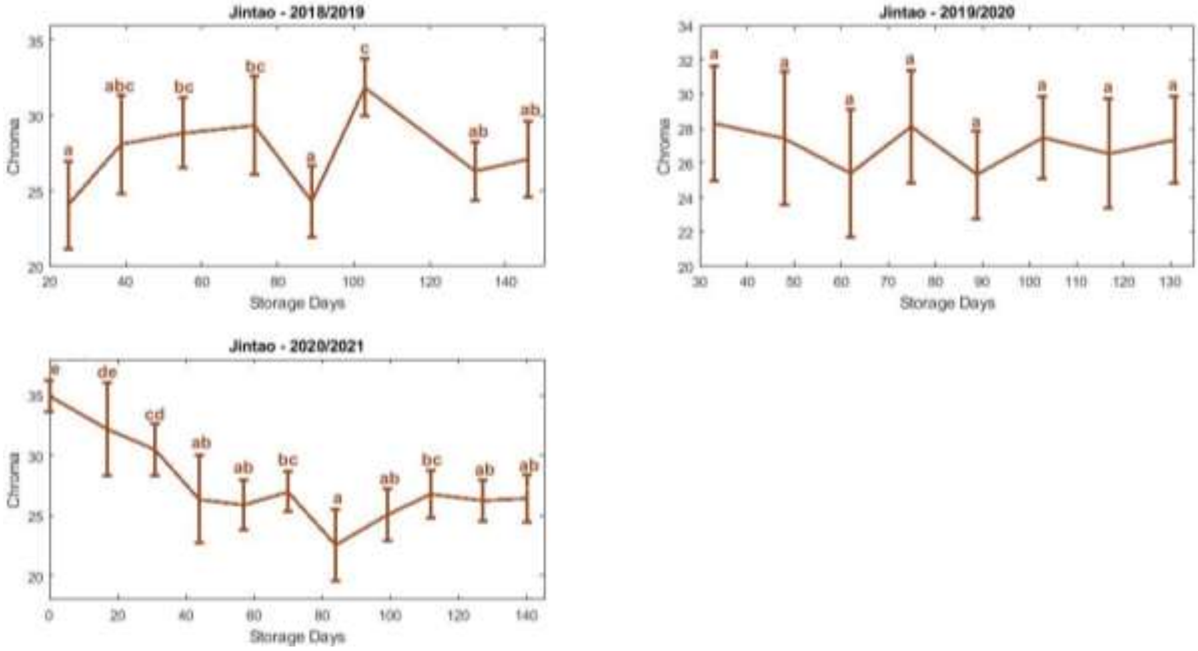

Figure 6.3: ‘Jintao’ kiwifruit temporal evolution of chroma during storage along: A) 2018/2019; B) 2019/2020; C) 2020/2021. Data depicted is the Mean ± SE of 8 kiwifruit. Statistically different means ($p < 0.05$) between sampling dates are signalled with different letters.

The initial averages of a*, in 2018 to 2020, were -4.92, -5.30 and -7.54, respectively (Figure 6.4). The corresponding values at the end of storage were -5.48, -4.39 and -3.04.

In 2018/2019, there are not significant differences along storage time for a* values (Figure 6.4A). In 2019/2020, a* values increased till 89 storage days, stabilize for the next sampling dates and decrease at 130th day (Figure 6.4B). In 2020/2021, a* showed an increased pattern during the storage (Figure 6.4C).

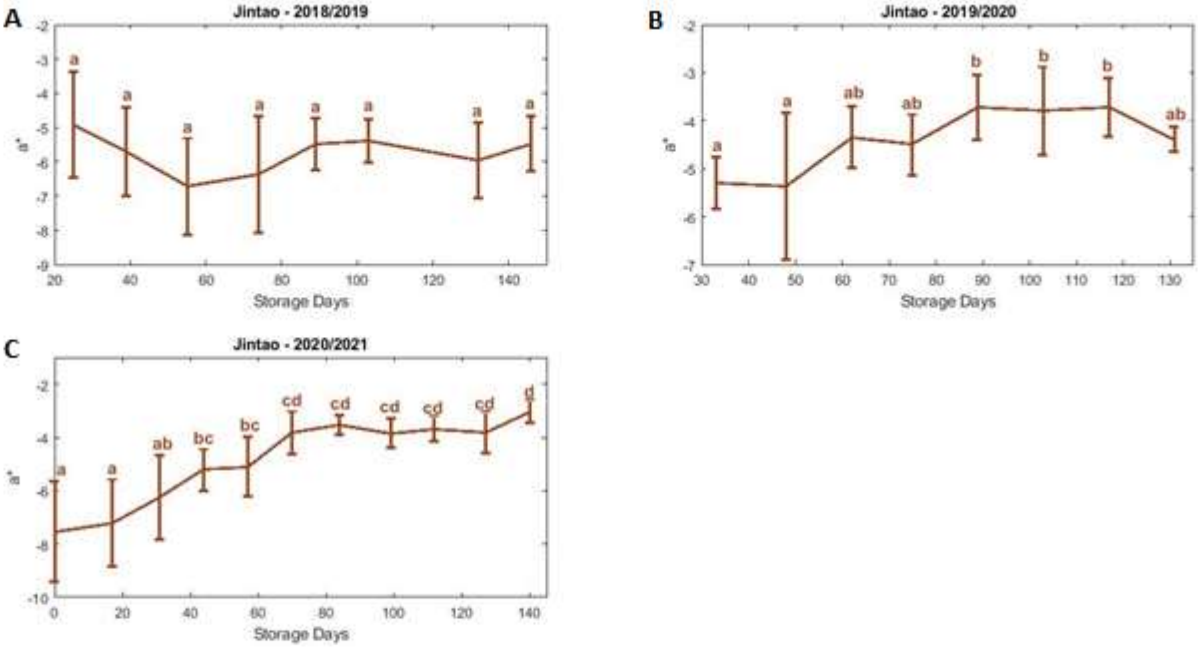

Figure 6.4: 'Jintao' kiwifruit temporal evolution of a* during storage along: A) 2018/2019; B) 2019/2020; C) 2020/2021. Data depicted is the Mean ± SE of 8 kiwifruit. Statistically different means ($p < 0.05$) between sampling dates are signalled with different letters.

The initial averages of Hue, in 2018 to 2020, were 101.9 º, 100.9 º and 102.4 º, respectively (Figure 6.5). The corresponding values at the end of storage were 101.8 º, 99.32 º and 96.68 º, meaning that, although the colour was similar at the beginning, in 2021, during storage, 'Jintao' kiwifruit became more yellow than in the previous years.

In 2018/2019, there were no significant differences among Hue values along storage time (Figure 6.5A). In both 2019/2020 and 2020/2021, hue angle decreased during time, however, in 2019/2020, at the last sampling date Hue slightly increased (Figures 6.5B and 6.5C).

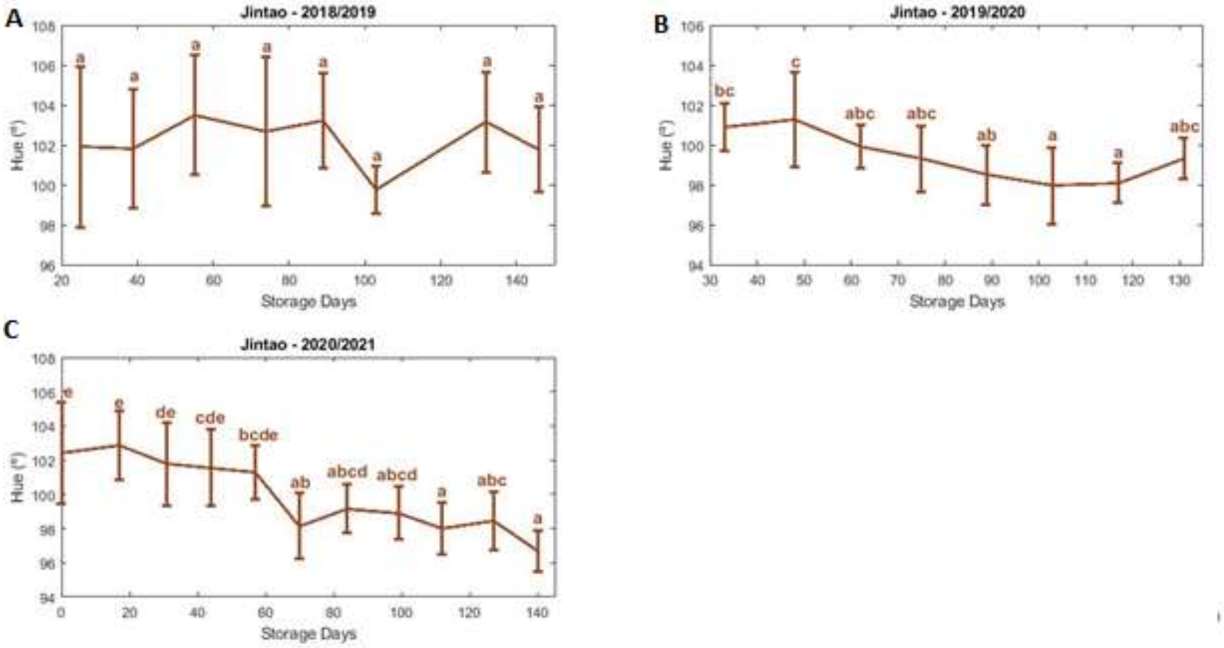

Figure 6.5: 'Jintao' kiwifruit temporal evolution of Hue during storage along: A) 2018/2019; B) 2019/2020; C) 2020/2021. Data depicted is the Mean ± SE of 8 kiwifruit. Statistically different means ($p < 0.05$) between sampling dates are signalled with different letters.

6.1.2 Firmness, SSC and DM

The initial averages of firmness for 'Jintao' kiwifruit, in 2018 to 2019, were 31.30 N, and 25.94 N, respectively (Figure 6.6). The corresponding final storage values were 3.20 N and 4.21 N. The firmness values in 2020/2021, due an equipment failure, were not considered.

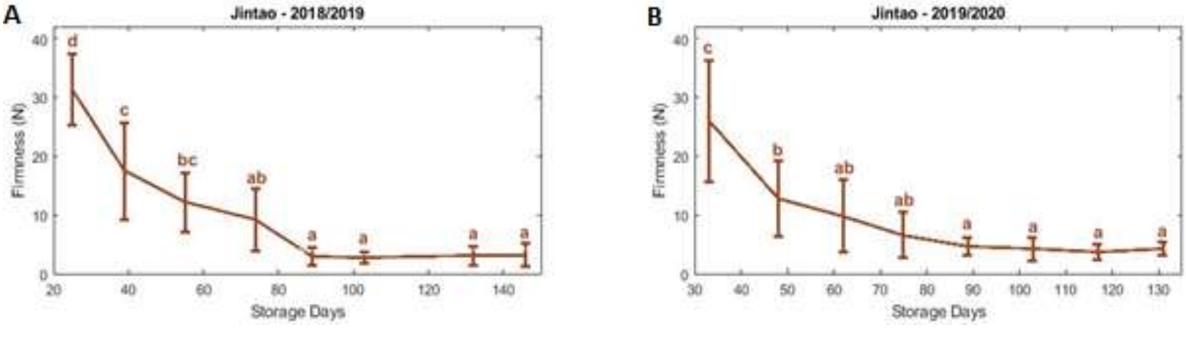

Figure 6.6: 'Jintao' kiwifruit temporal evolution of firmness during storage along: A) 2018/2019; B) 2019/2020. Data depicted is the Mean ± SE of 8 kiwifruit. Statistically different means ($p < 0.05$) between sampling dates are signalled with different letters.

In both seasons, firmness decreased fast in the first two months as described by Antunes & Sfakiotakis (2008) and then, from 89 days of storage, there were no more significant differences.

The initial averages of SSC for 'Jintao', in 2018 to 2020, were 12.1 %, 13.2 % and 11.4 %, respectively (Figure 6.7). The corresponding values at the end of storage were 13.7 %, 16.3 % and 14.8 %.

In 2019/2020 and 2020/2021, SSC values increased along storage (Figures 6.7B and 6.7C). In the latter, despite the kiwifruit SSC values when stored were higher than those reported by Huang et al. (2022), was also registered a rapidly increase, approximately, in the first two weeks. However, in 2018/2019, SSC values increased till 103 days of storage, but had a slight decrease after 132 days, then an increase at the end of storage (Figure 6.7A).

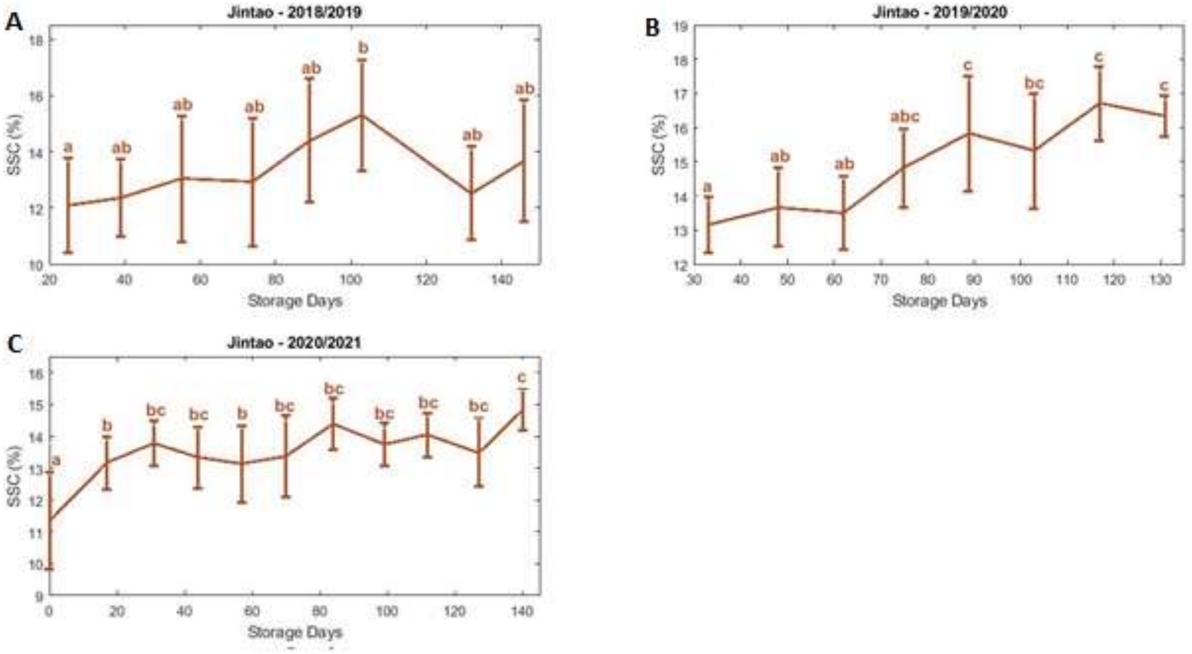

Figure 6.7: 'Jintao' kiwifruit temporal evolution of SSC during storage along: A) 2018/2019; B) 2019/2020; C) 2020/2021. Data depicted is the Mean ± SE of 8 kiwifruit. Statistically different means ($p < 0.05$) between sampling dates are signalled with different letters.

The initial averages of dry matter for ‘Jintao’ kiwifruit, in 2018 to 2020, were 14.01 %, 14.64 % and 15.67 %, respectively (Figure 6.8). The corresponding final storage values were 15.18 %, 16.89 % and 14.17 %.

Dry matter values evolved differently each year. In 2018/2019, there are not significant differences during storage, except at 39 and 103 days of storage (Figure 6.8A). In 2019/2020, dry matter values followed an increased pattern, while in 2020/2021 was the opposite, although at the last measurement day there was an increase of the values (Figures 6.8B and 6.8C).

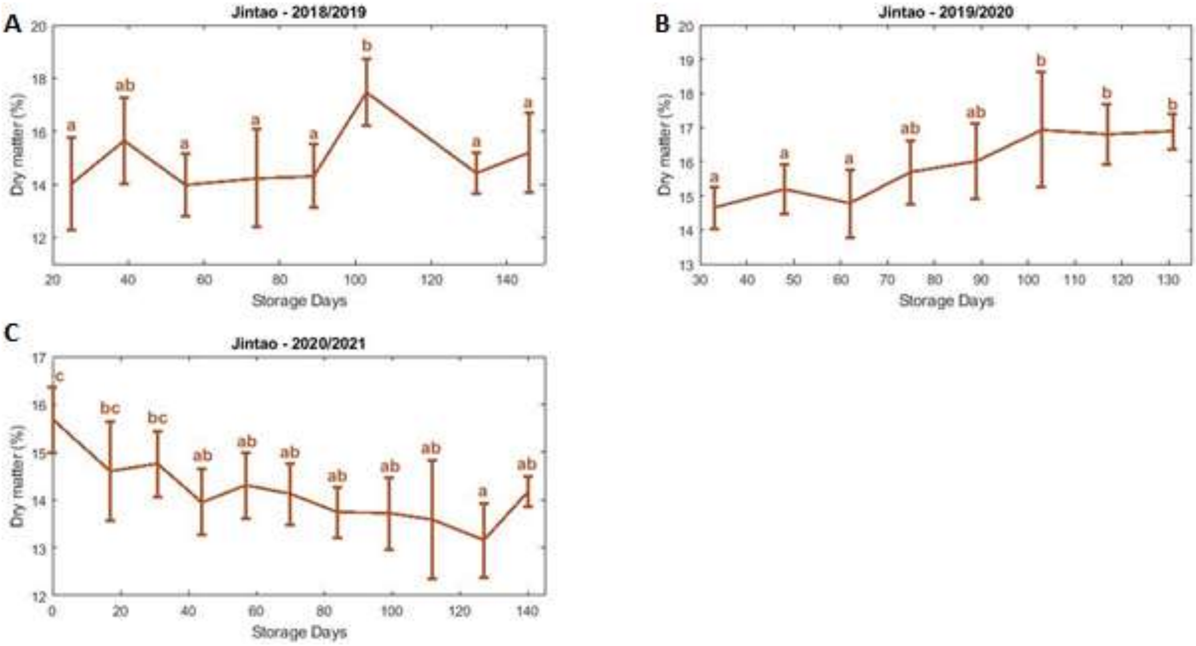

Figure 6.8: ‘Jintao’ kiwifruit temporal evolution of dry matter during storage along: A) 2018/2019; B) 2019/2020; C) 2020/2021. Data depicted is the Mean ± SE of 8 kiwifruit. Statistically different means ($p < 0.05$) between sampling dates are signalled with different letters.

6.1.3 pH and TA

The initial averages of pH for ‘Jintao’, in 2018 to 2020, were 3.37, 3.38 and 3.44, respectively (Figure 6.9). The corresponding final storage values were 3.72, 2.97 and 3.77.

Once more, the evolution occurred differently according to the year. In 2018/2019, from the 39 days of storage there are no significant differences, while in 2019/2020 the values decreased during storage, being the kiwifruit more acidic that those from the other years (Figures 6.9A and 6.9B). In 2020/2021, the pH values were very irregular with a significant increased at the end (Figure 6.9C).

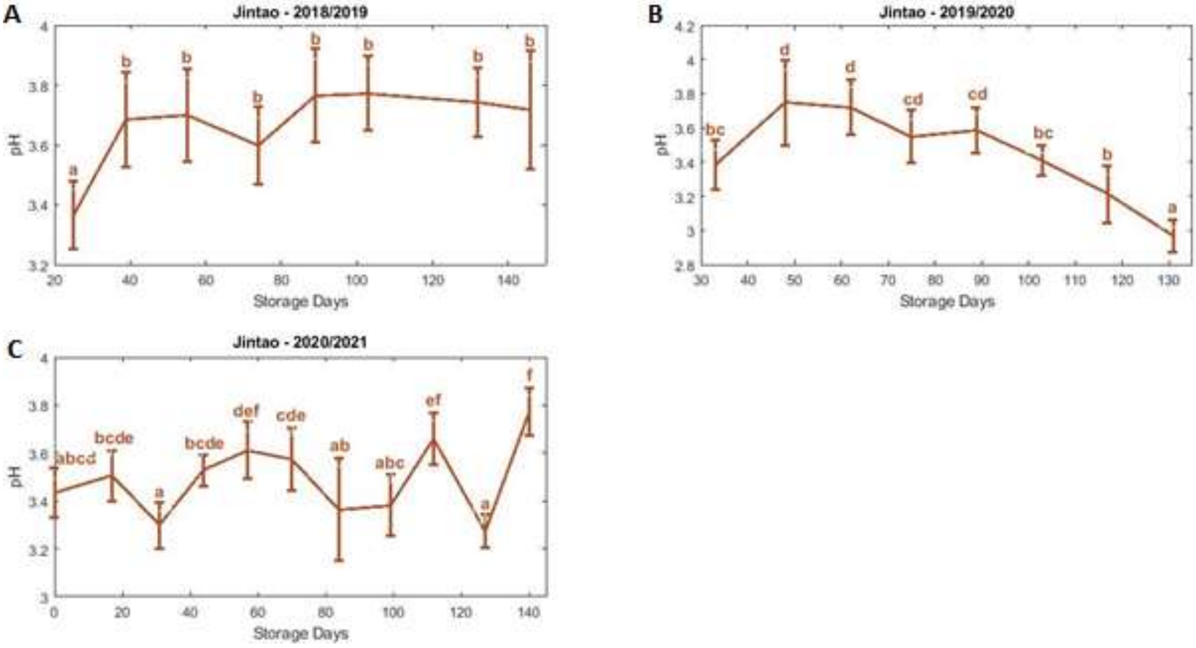

Figure 6.9: 'Jintao' kiwifruit temporal evolution of pH during storage along: A) 2018/2019; B) 2019/2020; C) 2020/2021. Data depicted is the Mean ± SE of 8 kiwifruit. Statistically different means ($p < 0.05$) between sampling dates are signalled with different letters.

The initial averages of TA for 'Jintao', in 2018 to 2020, were 1.14 %, 0.92 % and 1.35 %, respectively (Figure 6.10). The corresponding final storage values were 0.86 %, 1.15 % and 1.10 %.

In both 2018/2019 and 2020/2021, TA values, in general, decreased till 103 and 84 days of storage, respectively (Figures 6.10A and 6.10C). In the first year, values then increased, while in the last stabilized showing no significant differences in the last days, but, overall, considering only the initial and the final values, TA decreased during storage.

In other hand, in 2019/2020, kiwifruit titrable acidity slightly increased during storage (Figure 6.10B).

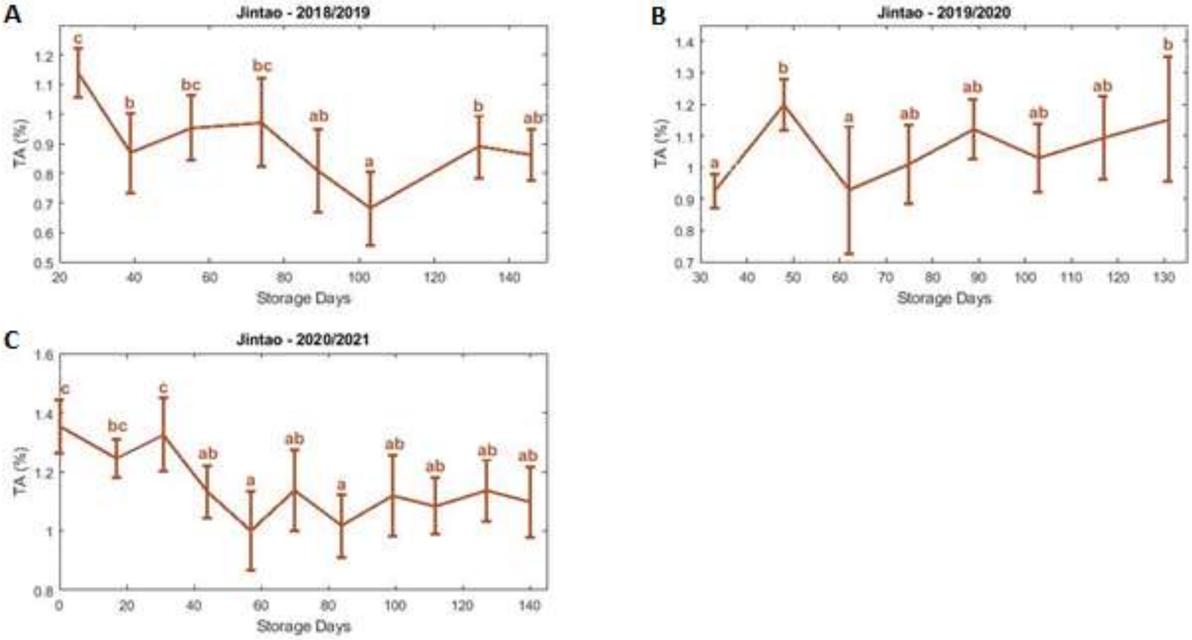

Figure 6.10: 'Jintao' kiwifruit temporal evolution of TA during storage along: A) 2018/2019; B) 2019/2020; C) 2020/2021. Data depicted is the Mean ± SE of 8 kiwifruit. Statistically different means ($p < 0.05$) between sampling dates are signalled with different letters.

6.2 Ripening evolution of 'Hayward' kiwifruit during storage

6.2.1 Colorimetric parameters

The initial averages of L* for 'Hayward' kiwifruit, in 2018 to 2020, were 54.39, 54.72 and 60.21, respectively (Figure 6.11). The corresponding final storage values were 52.68, 48.29 and 53.88.

In all years, L* values decreased in the first storage days. In 2019/2020 and in 2020/2021 there are no significant differences from 34 days of storage, except at 89th day, and from 27 days of storage, respectively (Figures 6.11B and 6.11C). In 2018/2019, L* values decreased till 74 days of storage and then slightly increased along time (Figure 6.11A). It is possible that this happened due to an over ripening since, in the first year, the kiwifruit stored were followed during more time till 172 storage days.

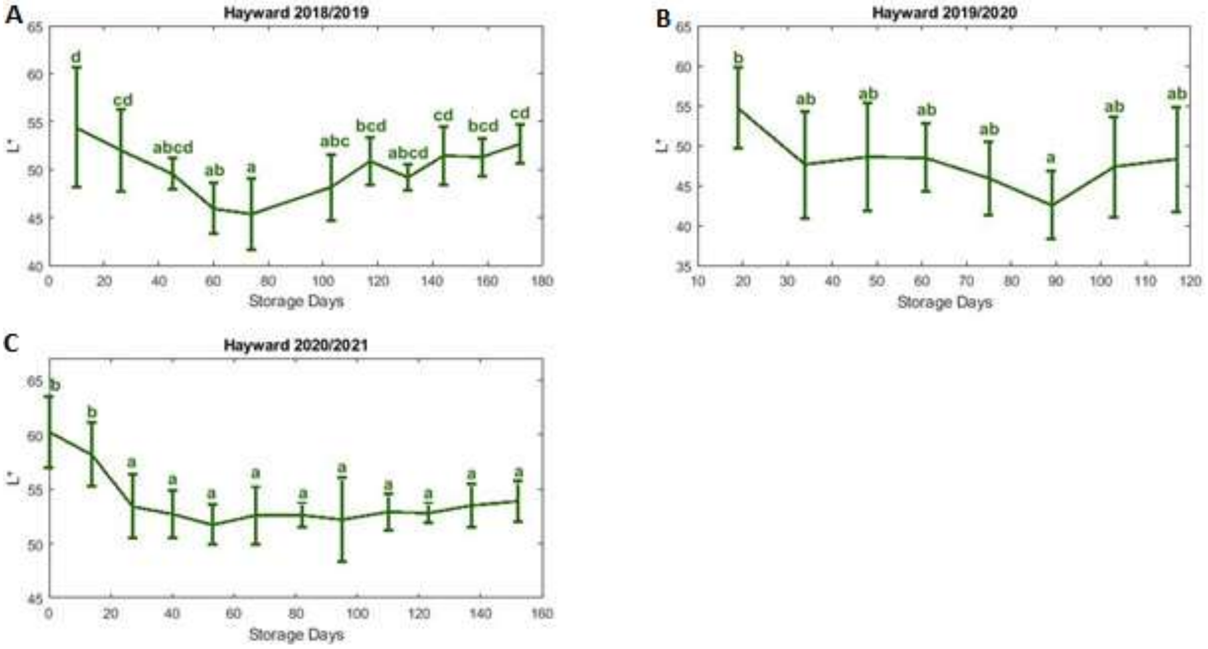

Figure 6.11: 'Hayward' kiwifruit temporal evolution of L* during storage along: A) 2018/2019; B) 2019/2020; C) 2020/2021. Data depicted is the Mean ± SE of 8 kiwifruit. Statistically different means ($p < 0.05$) between sampling dates are signalled with different letters.

The initial averages of b* for 'Hayward' kiwifruit, in 2018 to 2020, were 24.29, 29.91 and 31.77, respectively (Figure 6.12). The corresponding final storage values were 22.77, 20.21 and 23.36.

The initial averages of chroma, in 2018 to 2020, were 27.19, 33.33 and 34.88, respectively (Figure 6.13). The corresponding final values were 25.12, 22.82 and 25.27.

Chroma and b* values had a similar evolution. In the three years, values decrease till 74, 89 and 53 days of storage, respectively (Figures 6.12 and 6.13). Then, in 2020/2021, from that date, there were no more significant differences, except at 117 storage days, while in 2018/2019 and 2019/2022 the values begun to increase.

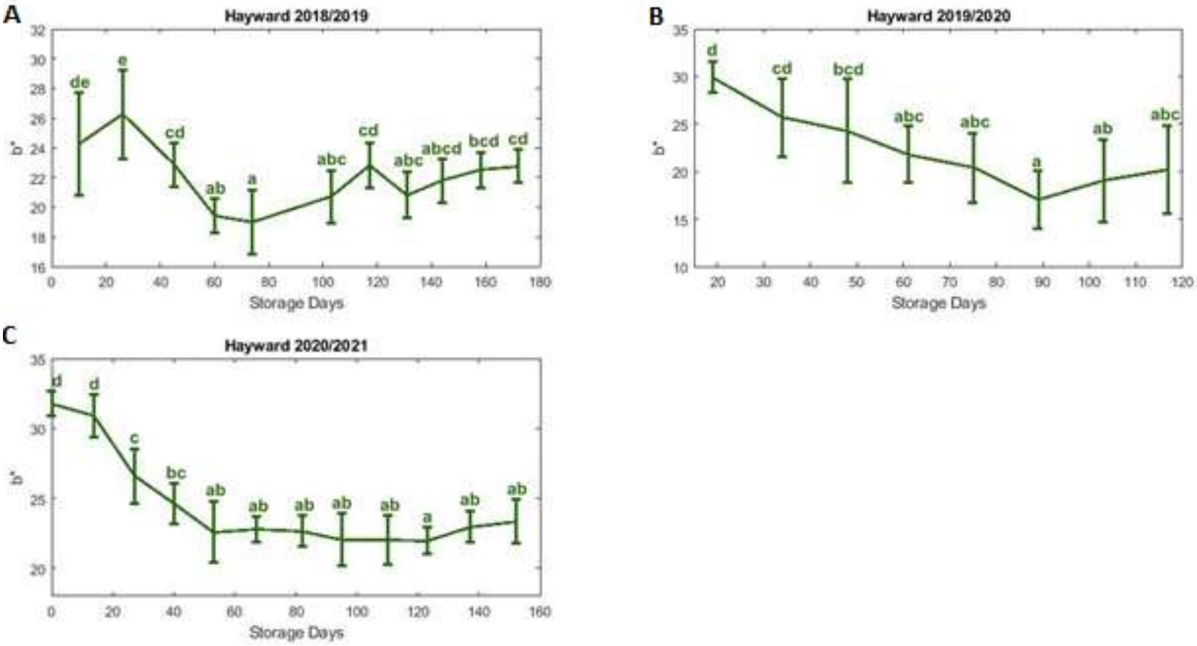

Figure 6.12: 'Hayward' kiwifruit temporal evolution of b* during storage along: A) 2018/2019; B) 2019/2020; C) 2020/2021. Data depicted is the Mean ± SE of 8 kiwifruit. Statistically different means ($p < 0.05$) between sampling dates are signalled with different letters.

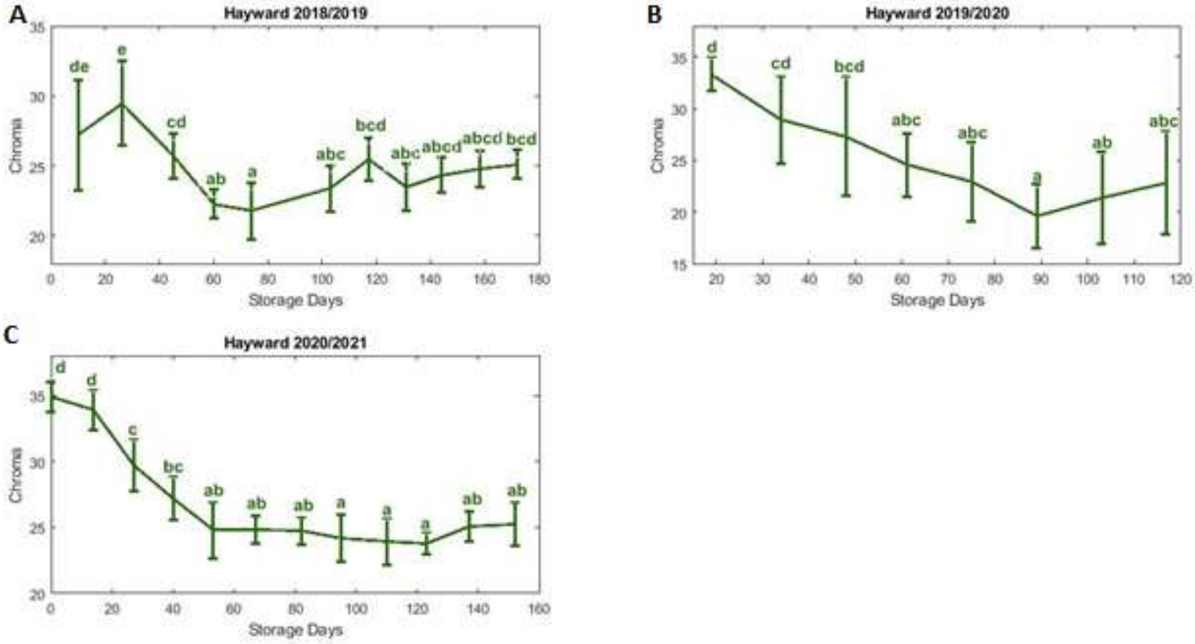

Figure 6.13: 'Hayward' kiwifruit temporal evolution of chroma during storage along: A) 2018/2019; B) 2019/2020; C) 2020/2021. Data depicted is the Mean ± SE of 8 kiwifruit. Statistically different means ($p < 0.05$) between sampling dates are signalled with different letters.

The initial averages of a* for ‘Hayward’, in 2018 to 2020, were -12.22, -14.68 and -14.38, respectively (Figure 6.14). The corresponding final storage values were -10.59, -10.58 and -9.59.

In 2018/2019 and 2020/2021, a* values during storage evolved at similar pattern, increasing till 74 and 67 days, respectively, and then, the tendency was to stabilize (Figure 6.14A and 6.14C). In 2019/2020, a* increased along time till 89 storage days, decreasing in the last day (Figure 6.14B).

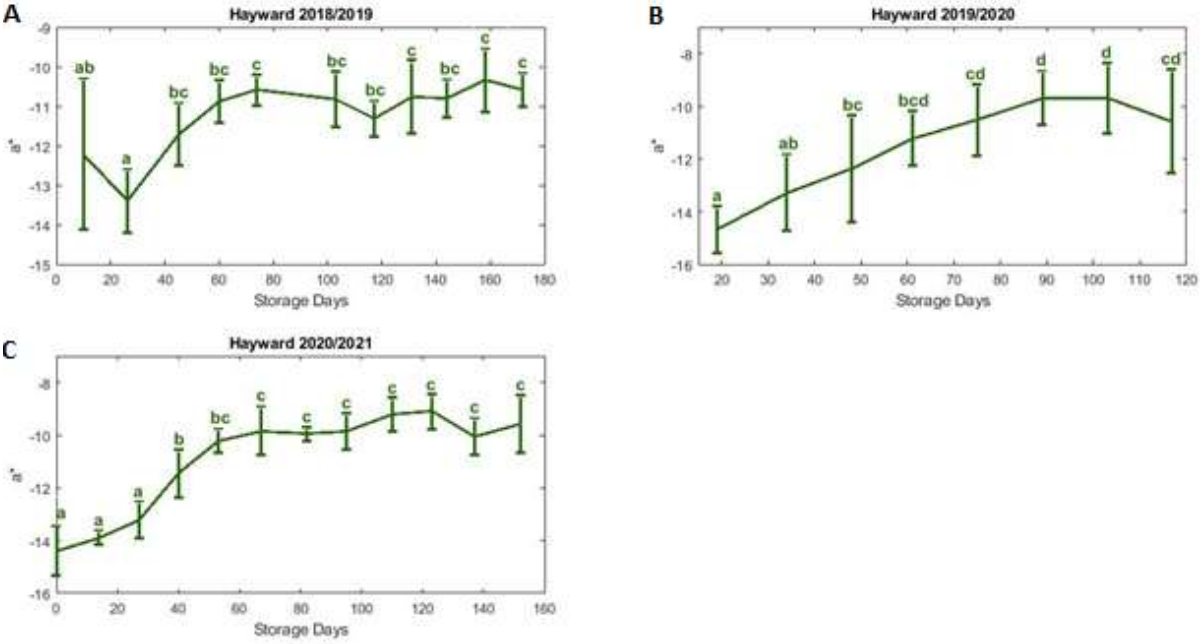

Figure 6.14: ‘Hayward’ kiwifruit temporal evolution of a* during storage along: A) 2018/2019; B) 2019/2020; C) 2020/2021. Data depicted is the Mean ± SE of 8 kiwifruit. Statistically different means ($p < 0.05$) between sampling dates are signalled with different letters.

The initial averages of Hue for ‘Hayward’ kiwifruit, in 2018 to 2020, were 116.7 º, 116.1 º and 114.3 º, respectively (Figure 6.15). The corresponding final storage values were 115.0 º, 118.0 º and 112.3 º.

In 2018/2019 and 2020/2021, Hue values decreased along storage, although in a more irregular way in the first year (Figures 6.15A and 6.15C). In 2019/2020 , there are no significant differences between 34 storage days and the final date, except at 89th day (Figure 6.15B).

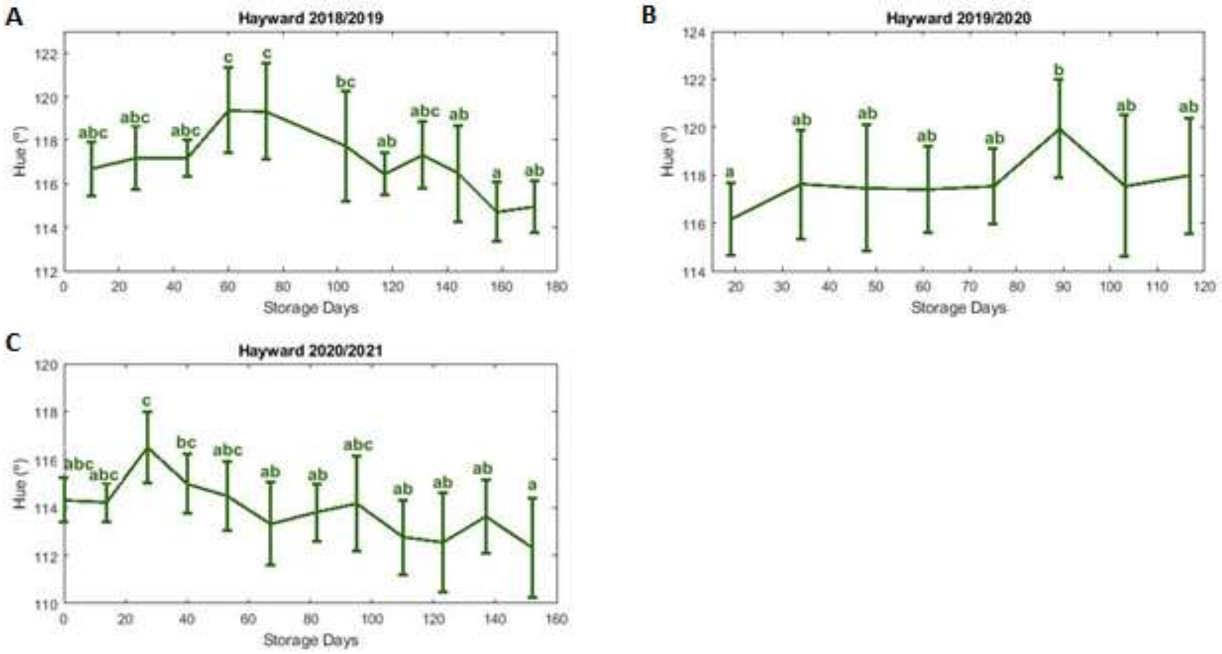

Figure 6.15: ‘Hayward’ kiwifruit temporal evolution of Hue during storage along: A) 2018/2019; B) 2019/2020; C) 2020/2021. Data depicted is the Mean ± SE of 8 kiwifruit. Statistically different means ($p < 0.05$) between sampling dates are signalled with different letters.

6.2.2 Firmness, SSC and DM

The initial averages of firmness for ‘Hayward’ kiwifruit, in 2018 to 2020, were 33.75 N, 39.69 N and 45.90 N, respectively (Figure 6.16). The corresponding final storage values were 5.24 N, 5.10 N and 4.74 N.

In 2018/2019, firmness values decreased in the first two months as described by Antunes & Sfakiotakis (2008); however, in 2019/2020 and in 2020/2021 the firmness declined especially in the first 40 days in storage, being more similar with the behaviour reported by Huang et al. (2022), in which over the first four weeks in storage, firmness decreased from ~54 N to ~10 N.

Furthermore, in all seasons, firmness values tend to be similar in the final slow phase of softening, independently of the values at harvest, as reported by Burdon et al. (2013).

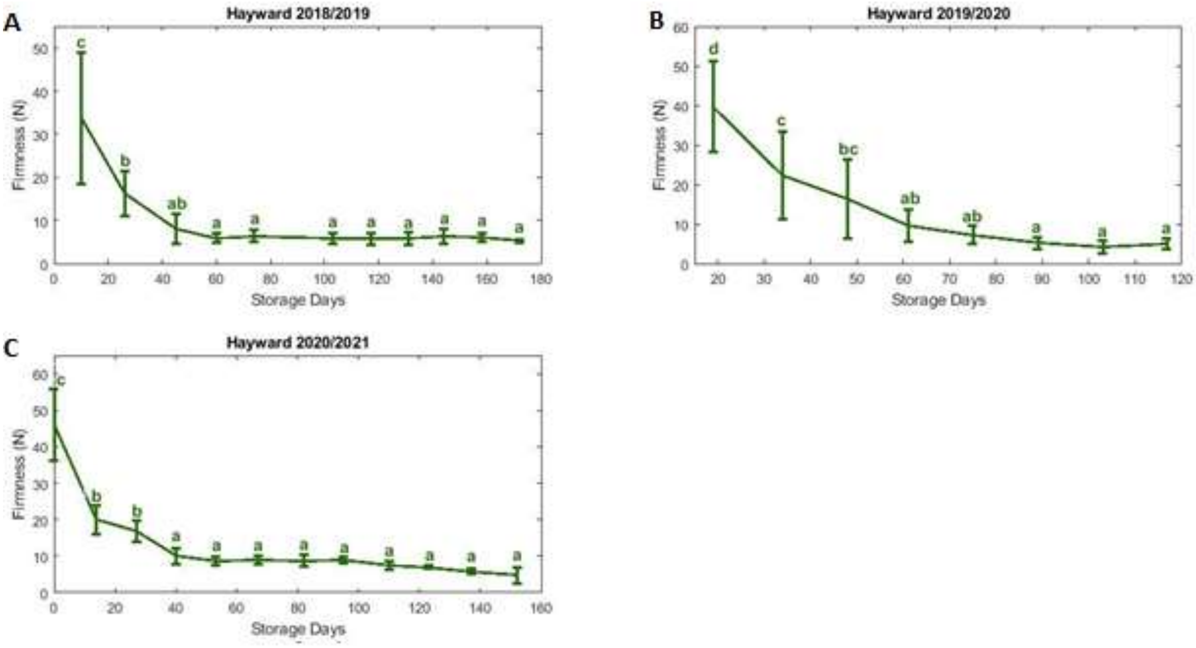

Figure 6.16: ‘Hayward’ kiwifruit temporal evolution of firmness during storage along: A) 2018/2019; B) 2019/2020; C) 2020/2021. Data depicted is the Mean ± SE of 8 kiwifruit. Statistically different means ($p < 0.05$) between sampling dates are signalled with different letters.

The initial averages of SSC for ‘Hayward’, in 2018 to 2020, were 7.1 %, 8.4 % and 8.9 %, respectively (Figure 6.17). The corresponding final storage values were 12.0 %, 11.8 % and 13.2 %.

In 2018/2019, SSC values increased till 117 days of storage, while in 2019/2020 increased till 61 storage days before stabilized (Figure 6.17A and 6.17B). In 2018/2019, SSC growth occurred throughout storage, reaching higher values than the previous years (Figure 6.17C).

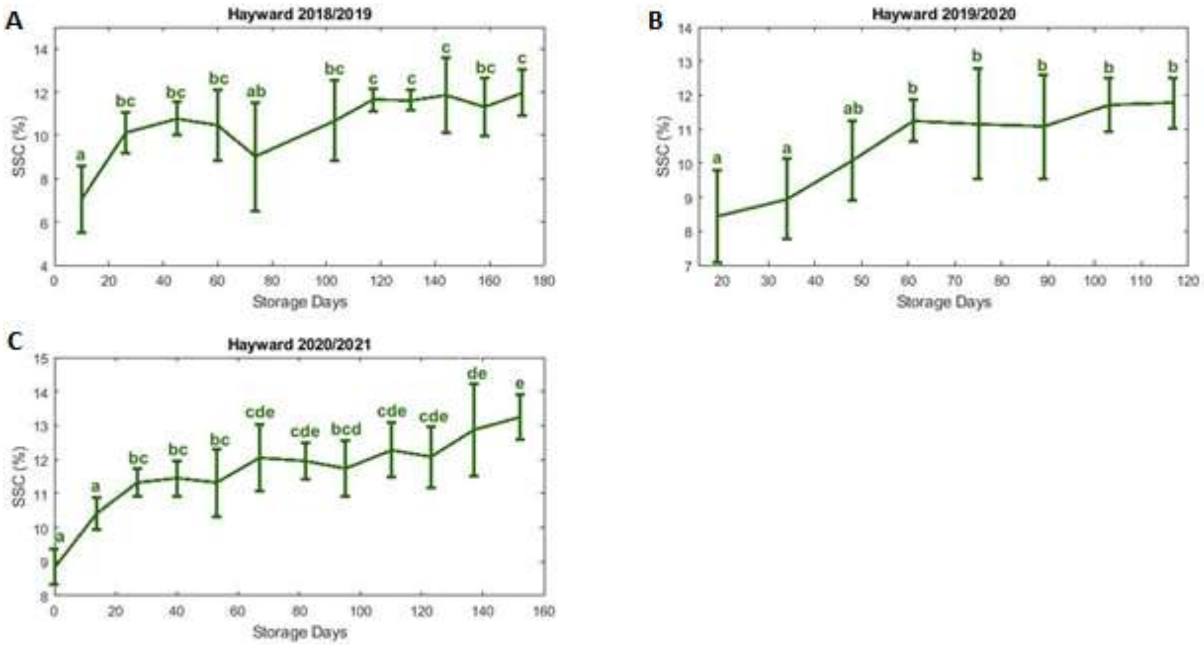

Figure 6.17: 'Hayward' kiwifruit temporal evolution of SSC during storage along: A) 2018/2019; B) 2019/2020; C) 2020/2021. Data depicted is the Mean ± SE of 8 kiwifruit. Statistically different means ($p < 0.05$) between sampling dates are signalled with different letters.

The initial averages of dry matter, in 2018 to 2020, were 11.60 %, 13.50 % and 14.38 %, respectively (Figure 6.18). The corresponding final storage values were 13.81 %, 14.48 % and 13.64 %

In 2018/2019 and 2019/2020, dry matter values tend to be stable in the first storage days before started to increase from 74 and from 75 storage days, respectively, stabilizing again in the case of the first year (Figures 6.18A and 6.18B). In 2020/2021, there are no significant differences, except at 0 and at 67 days of storage (Figure 6.18C). In this year there is not a growth phase, possibly due a higher initial value than the previous years.

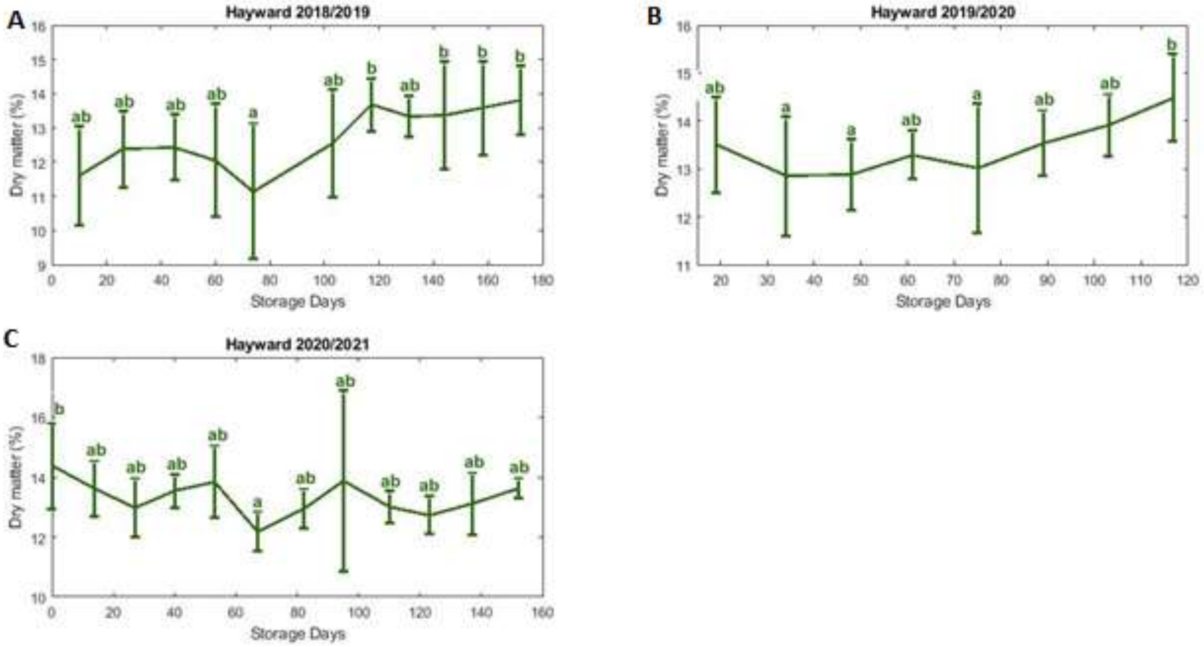

Figure 6.18: ‘Hayward’ kiwifruit temporal evolution of dry matter during storage along: A) 2018/2019; B) 2019/2020; C) 2020/2021. Data depicted is the Mean ± SE of 8 kiwifruit. Statistically different means ($p < 0.05$) between sampling dates are signalled with different letters.

6.2.3 pH and TA

The initial averages of pH for ‘Hayward’ kiwifruit, in 2018 to 2020, were 3.52, 3.06 and 3.25, while the final storage values were, respectively, 3.42, 2.76 and 3.30 (Figure 6.19).

In 2018/2019 and 2020/2021, the pH evolution during storage was very irregular, especially in the latter (Figures 6.19A and 6.19C). In 2019/2020, pH values increased till 48 storage days and then decreased till 120 days (Figure 6.19B).

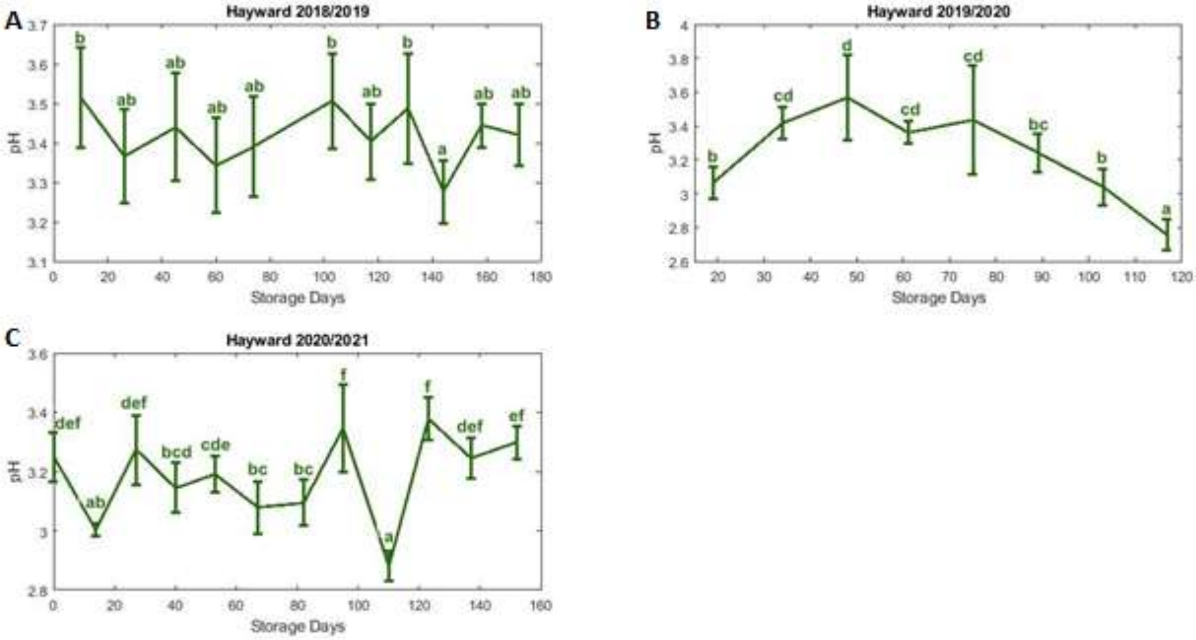

Figure 6.19: 'Hayward' kiwifruit temporal evolution of pH during storage along: A) 2018/2019; B) 2019/2020; C) 2020/2021. Data depicted is the Mean ± SE of 8 kiwifruit. Statistically different means ($p < 0.05$) between sampling dates are signalled with different letters.

The initial averages of TA for 'Hayward' kiwifruit, in 2018 to 2020, were 1.07 %, 1.36 % and 1.33 %, respectively (Figure 6.20). The corresponding values at the end of storage were 1.22 %, 1.42 % and 1.49 %.

In 2018/2019, TA values increased till 45 storage days, then decreased till 70 days before increase again (Figure 6.20A). In 2019/2020, TA decrease till 61 days of storage and then increased, with no significant differences in the sampling dates, while in 2020/2021, after the decreased, values were maintained stable till 123 days then increased (Figures 6.20B and 6.20C).

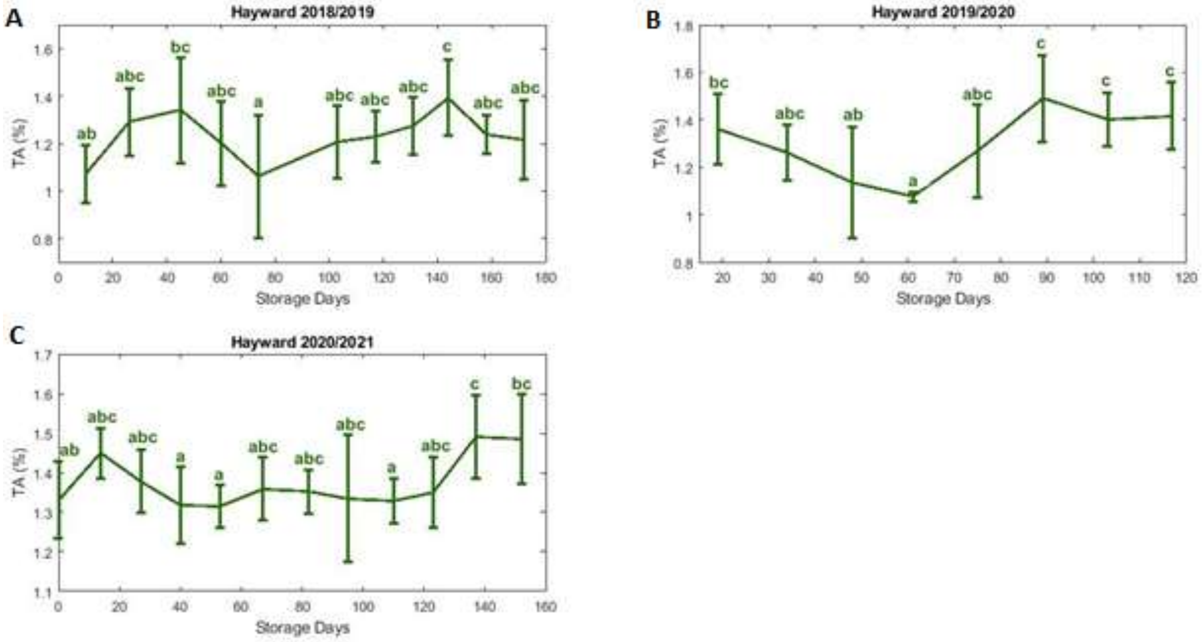

Figure 6.20: 'Hayward' kiwifruit temporal evolution of TA during storage along: A) 2018/2019; B) 2019/2020; C) 2020/2021. Data depicted is the Mean ± SE of 8 kiwifruit. Statistically different means ($p < 0.05$) between sampling dates are signalled with different letters.

6.3 Sensory evaluation

Sensory evaluation of kiwifruit was done through ripening as described in Section 2.6.

6.3.1 'Jintao' kiwifruit

The median for all sensory parameters evaluated in kiwifruit *Actinidia chinensis* 'Jintao' was around 6-point Likert scale for all sets and along the time, and the interquartile range, as a measure of dispersion, had low values as described in Table 6.1, between 0 and 3, for most cases. The maximum obtained was 7-point and the minimum value was 2.

In fact, for all the three years, independently of the month, all parameters evaluated where very consistent with a 6-point evaluation through time and through years, meaning that 'Jintao' kiwifruit was very appreciated by the panellists regardless kept in storage for 2.5 or 4.5 months at 0 ºC, despite for *Actinidia* *chinensis*, the storage period, at low temperature, is, usually, four months or less (Asiche et al., 2017).

Table 6.1: Descriptive statistics for *Actinidia chinensis* 'Jintao' kiwifruit according to panellist's evaluation. Hedonic scale was the 7-point, ranging from 1 = Dislike very much and 7 = Like very much.

Storage Days	Month and year	Parameter	Median	Minimum	Maximum	Range	Inter quartile range
74	January 2019	Fruit Appearance	6	4	7	3	1
		Pulp Appearance	6	3	7	4	1.25
		Aroma	5.5	3	7	4	1.25
		Texture	6	5	7	2	1.25
		Sweetness	6	2	7	5	1
		Acidity	6	2	7	5	3
		Global Taste	6	5	7	2	1.25
132	March 2019	Fruit Appearance	6	5	6	1	0
		Pulp Appearance	6	4	7	3	0
		Aroma	6	3	6	3	1
		Texture	5	2	7	5	2
		Sweetness	6	4	7	3	1
		Acidity	6	4	7	3	3
		Global Taste	6	2	7	5	1
75	January 2020	Fruit Appearance	6	4	7	3	1
		Pulp Appearance	6	4	7	3	2
		Aroma	6	4	7	3	1

		Texture	6	3	7	4	2
		Sweetness	6	3	7	4	2
		Acidity	6	2	7	5	3
		Global Taste	6	3	7	4	2
		Fruit Appearance	6	2	7	5	0.75
		Pulp Appearance	6	3	7	4	0.75
131	March 2020	Aroma	6	3	7	4	1
		Texture	6	2	7	5	0.75
		Sweetness	6	2	7	5	2
		Acidity	6	3	7	4	1.75
		Global Taste	6	2	7	5	1.75
70	January 2021	Fruit Appearance	7	3	7	4	1
		Pulp Appearance	6	3	7	4	2
		Aroma	6	4	7	3	2
		Texture	6	2	7	5	1
		Sweetness	6	5	7	2	1
		Acidity	6	4	7	3	1
		Global Taste	7	4	7	3	1
		Fruit Appearance	6	3	7	4	1
		Pulp Appearance	6	3	7	4	1
127	March 2021	Aroma	6	3	7	4	2
		Texture	6	5	7	2	1
		Sweetness	6	4	7	3	2
		Acidity	6	4	7	3	2
		General Taste	6	4	7	3	1

Pairwise comparisons for the same months in different years were performed revealing differences only for acidity between January 2020 and January 2021 (Figure 6.21), texture between March 2019 and March 2021, fruit appearance between March 2021 and March 2019, as well March 2021 and March 2020 (Figure 6.22).

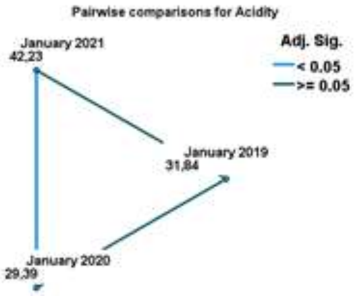

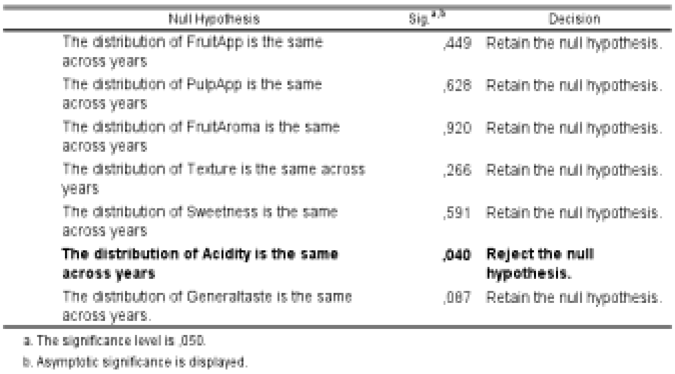

Null Hypothesis	Sig.[a,b]	Decision
The distribution of FruitApp is the same across years	,449	Retain the null hypothesis.
The distribution of PulpApp is the same across years	,628	Retain the null hypothesis.
The distribution of FruitAroma is the same across years	,920	Retain the null hypothesis.
The distribution of Texture is the same across years	,266	Retain the null hypothesis.
The distribution of Sweetness is the same across years	,591	Retain the null hypothesis.
The distribution of Acidity is the same across years	**,040**	**Reject the null hypothesis.**
The distribution of Generaltaste is the same across years.	,087	Retain the null hypothesis.

a. The significance level is ,050.

b. Asymptotic significance is displayed.

Figure 6.21: Pairwise Comparisons for acidity and table of Independent-Samples Kruskal-Wallis test results for ‘Jintao’ kiwifruit.

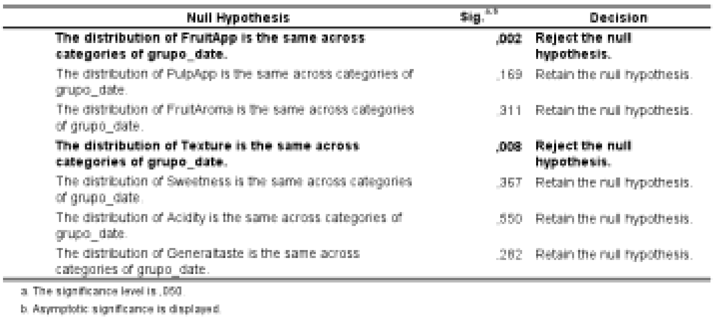

Null Hypothesis	Sig.[a,b]	Decision
The distribution of FruitApp is the same across categories of grupo_date.	**,002**	**Reject the null hypothesis.**
The distribution of PulpApp is the same across categories of grupo_date.	,169	Retain the null hypothesis.
The distribution of FruitAroma is the same across categories of grupo_date.	,311	Retain the null hypothesis.
The distribution of Texture is the same across categories of grupo_date.	**,008**	**Reject the null hypothesis.**
The distribution of Sweetness is the same across categories of grupo_date.	,367	Retain the null hypothesis.
The distribution of Acidity is the same across categories of grupo_date.	,550	Retain the null hypothesis.
The distribution of Generaltaste is the same across categories of grupo_date.	,282	Retain the null hypothesis.

a. The significance level is ,050.

b. Asymptotic significance is displayed.

Figure 6.22: Pairwise Comparisons for fruit appearance and texture, and table of Independent-Samples Kruskal-Wallis test results for ‘Jintao’ kiwifruit.

Further analysis was performed applying MDS by year and by month (Figure 6.23).

The results show that pulp appearance and fruit appearance are always linked, as well as general taste and sweetness, except in March 2020, meaning that, overall, the fruit appearance reflects on pulp appearance and sweetness has an impact on taste.

The degree of ability to explain the results of MDS were analysed through STRESS-I values (Table 6.2). Since STRESS-I value were below 25 %, the error rate is also still below the fair value. The value of 90 and upper percent in the RSQ value (R-Squared is a statistical measure of how close the data are to the fitted regression line), show that the results of MDS analysis on consumers' taste can be well explained.

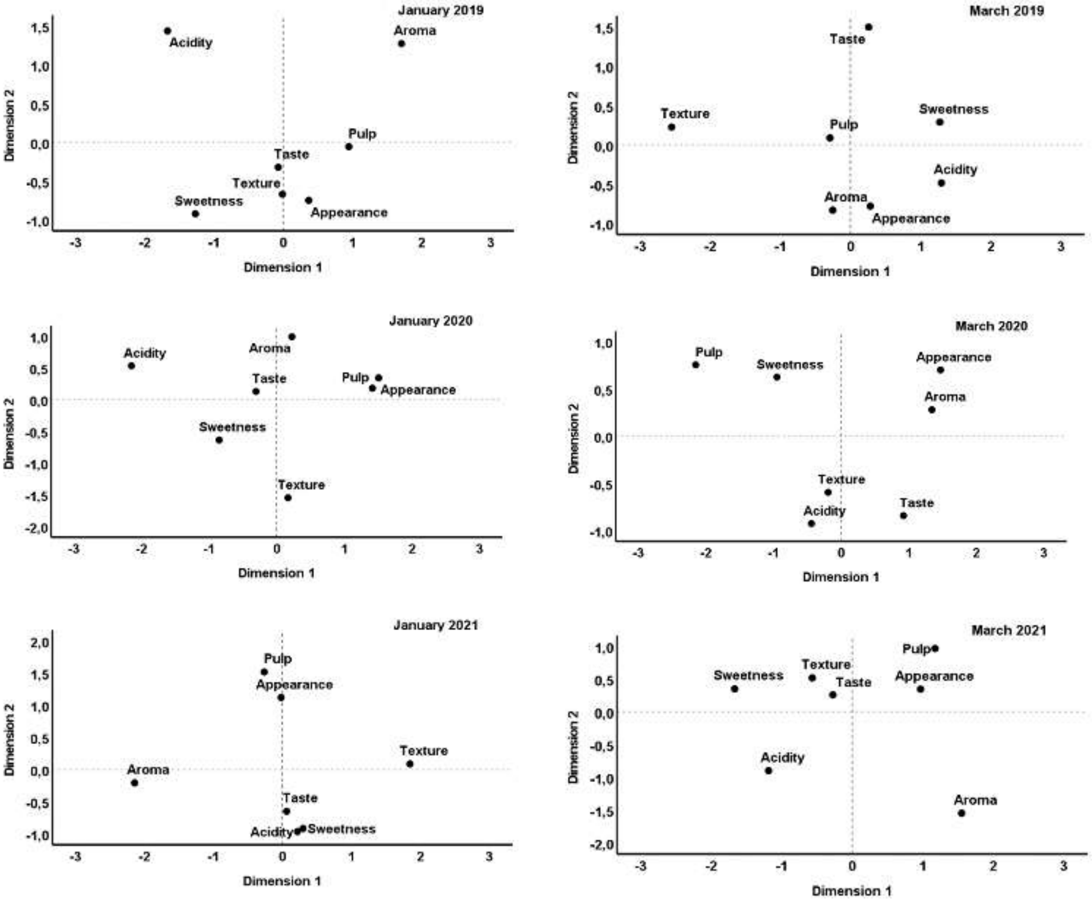

Figure 6.23: MDS (Multidimensional scaling) diagrams showing Euclidean distance method between the perceptions of consumer's taste in *Actinidia chinensis* 'Jintao' kiwifruit.

Table 6.2: Values of STRESS-I and RSQ for MDS ALSCAL methodology.

Storage Days	Month and year	STRESS-I value	RSQ value
74	January 2019	0.025	0.985
132	March 2019	0.060	0.994
75	January 2020	0.076	0.894
131	March 2020	0.135	0.961
70	January 2021	0.032	0.979
127	March 2021	0.047	0.997

6.3.2 ‘Hayward’ kiwifruit

For ‘Hayward’ kiwifruit the median was around 6-point Likert scale for all sets and along the time, and the interquartile range, as a measure of dispersion, had low values between 0 and 3 (Table 6.3), although a little more irregular than ‘Jintao’ possibly due a higher number of sensory evaluations and a longer storage time. The maximum obtained was 7-point and the minimum value was 1-point.

Table 6.3: Descriptive statistics for ‘Hayward’ kiwifruit according to panellists’ evaluation. Hedonic scale was the 7-point, ranging from 1 = Dislike very much and 7 = Like very much.

Storage Days	Month and year	Parameter	Median	Minimum	Maximum	Range	Inter quartile range
74	February 2019	Appearance	7	6	7	1	0.5
		Pulp	6	6	7	1	1
		Aroma	6	4	7	3	2
		Texture	6	2	7	5	0
		Sweetness	5	2	7	5	1
		Acidity	6	3	7	4	2
		Taste	6	3	7	4	1.5
131	April 2019	Appearance	7	5	7	2	1
		Pulp	6	5	7	2	1
		Aroma	5.5	3	7	4	1
		Texture	6	5	7	2	1
		Sweetness	5	2	7	5	1.75
		Acidity	5.5	2	7	5	2.5
		Taste	6	2	7	5	1
172	May 2019	Appearance	6.5	5	7	2	1
		Pulp	6	6	7	1	1
		Aroma	6	4	7	3	1
		Texture	6	4	7	3	1
		Sweetness	6	2	7	5	1.75
		Acidity	5.5	2	7	5	2.75
		Taste	6	3	7	4	1
61	January 2020	Appearance	6	5	7	2	1
		Pulp	7	4	7	3	1
		Aroma	6	3	7	4	1
		Texture	6	2	7	5	1
		Sweetness	5	2	7	5	3
		Acidity	5	2	7	5	3

		Taste	6	2	7	5	2
53	January 2021	Appearance	6.5	5	7	2	1
		Pulp	7	5	7	2	1
		Aroma	6	4	7	3	1.25
		Texture	6	4	7	3	0.5
		Sweetness	5	1	7	6	2
		Acidity	5	1	7	6	1.25
		Taste	6	1	7	6	1
123	March 2021	Appearance	6	5	7	2	1
		Pulp	6	5	7	2	1
		Aroma	6	4	7	3	1
		Texture	7	3	7	4	1
		Sweetness	6	1	7	6	1
		Acidity	6	1	7	6	2
		Taste	6	3	7	4	1
152	April 2021	Appearance	6	4	7	3	1
		Pulp	6	4	7	3	1
		Aroma	6	4	7	3	2
		Texture	7	5	7	2	1
		Sweetness	6	5	7	2	1
		Acidity	6	3	7	4	2
		Taste	6	5	7	2	1

Considering the homologous months of sampling, statistical differences were found, with the application of the Mann-Whitney nonparametric test for two independent samples, between April 2019 and April 2021 for sweetness and overall taste ($p<0.05$) (Table 6.4). Although the sensory evaluations mentioned were performed at the same month, in the last one the kiwifruit were in storage 20 days more than in 2019, what possibly was enough to cause the statistically difference.

Table 6.4: Mann-Whitney independent test applied in ‘Hayward’ kiwifruit sweetness and general taste evaluation.

Parameter	Group date	N	Mean Rank	Sum of Ranks	Probability
Sweetness	April 2019	17	13.82	235	<0.001
	April 2021	24	26.08	626	
	Total	41			
Taste	April 2019	17	14.88	253	0.003
	April 2021	24	25.33	608	
	Total	41			

The MDS analysis shows that for ‘Hayward’, as ‘Jintao’ kiwifruit, pulp appearance and fruit appearance, and also general taste and sweetness are always linked (Figure 6.24).

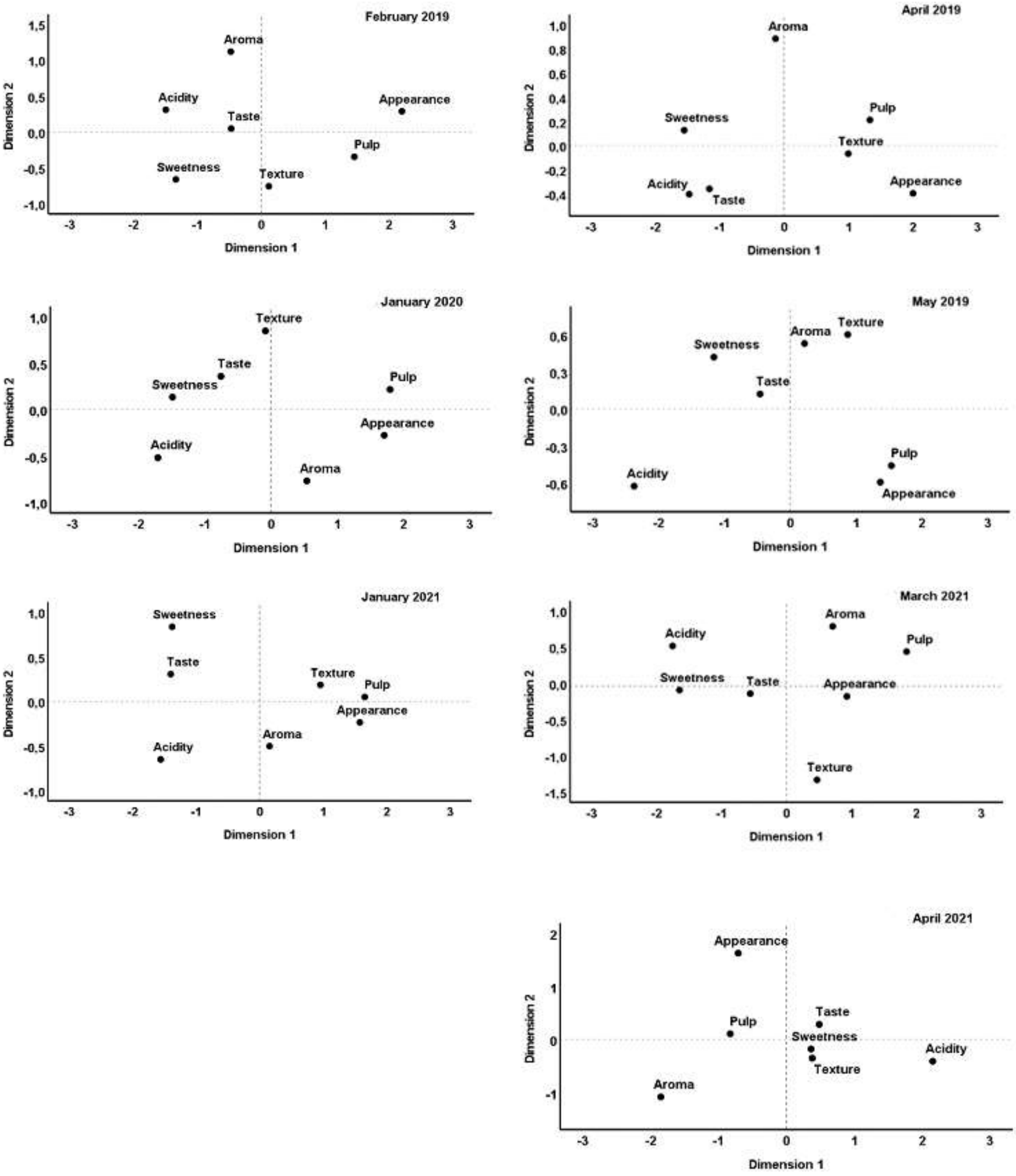

Figure 6.24: Multidimensional scaling (MDS) diagrams showing Euclidean distance method between the perceptions of consumer's taste in 'Hayward' kiwifruit.

6.3.3 ROC analysis

Performing a receiver operating characteristic (ROC) analysis along time by each sensory evaluation, showed that, for both cultivars, sweetness and acidity were the variables that respond with better scores for General taste (Figure 6.25), confirming that these two parameters are crucial factors for consumer acceptance (Marsh et al., 2006; Garcia et al., 2012). However, for ‘Jintao’ aroma seems to be important for global taste in January and March 2020, and also appearance in March 2020 and texture in March 2021. For ‘Hayward’ texture had also impact in May 2019 and pulp appearance in April 2021, perhaps due overripeness.

<table>
<tr><th>‘Jintao’</th><th>‘Hayward’</th></tr>
<tr><td>January 2019
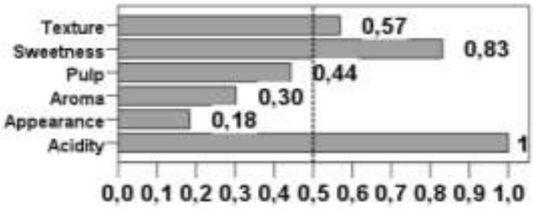
</td>
<td>February 2019
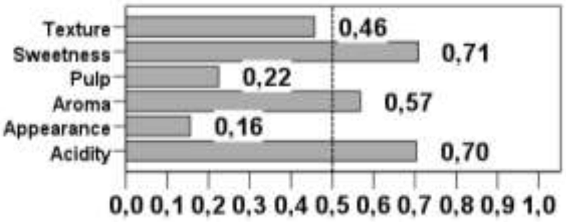
</td></tr>
<tr><td>March 2019
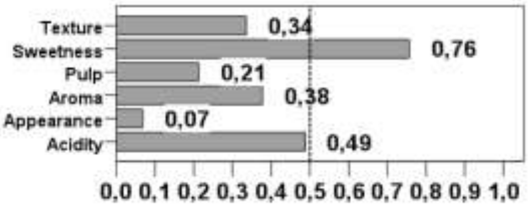
</td>
<td>April 2019
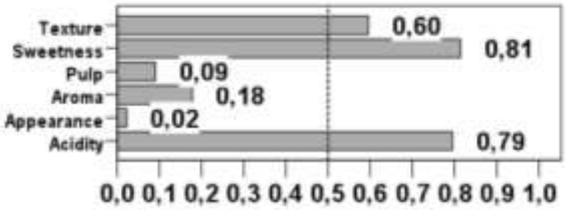
</td></tr>
<tr><td>January 2020
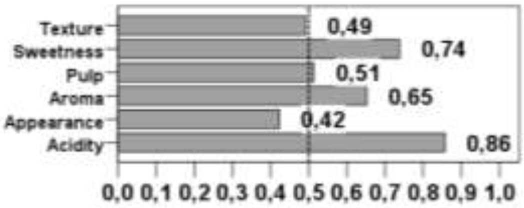
</td>
<td>May 2019
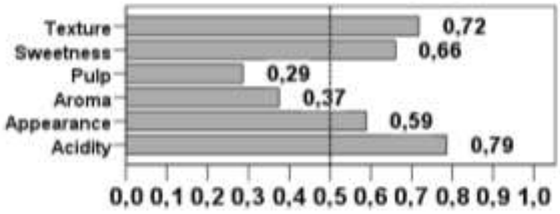
</td></tr>
<tr><td>March 2020</td><td>January 2020</td></tr>
</table>

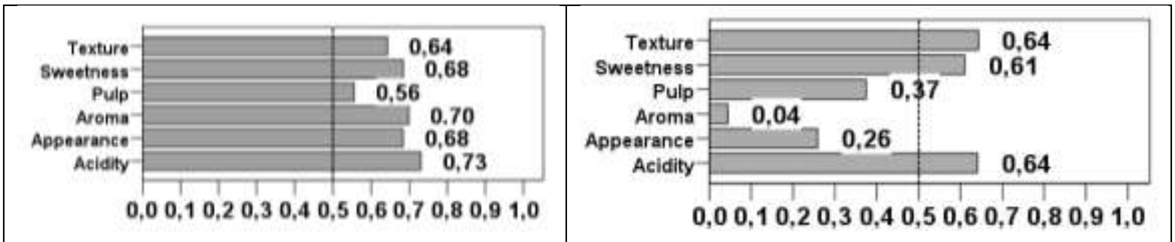

January 2021 | January 2021

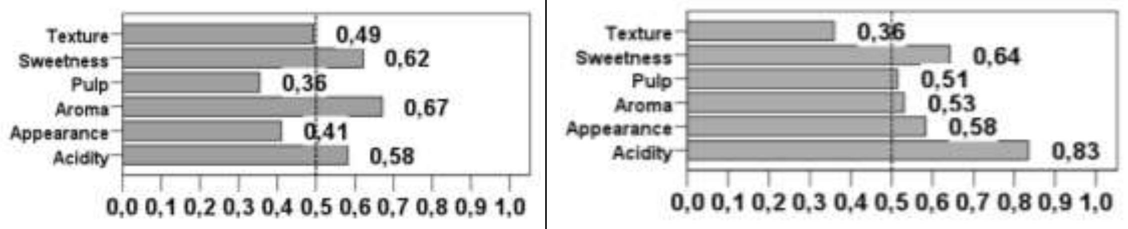

March 2021 | March 2021

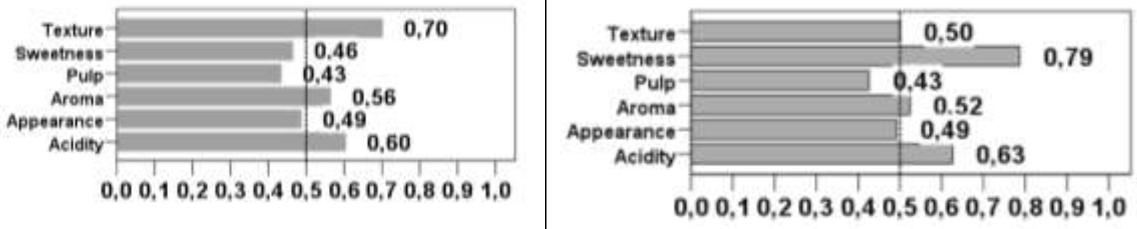

April 2021

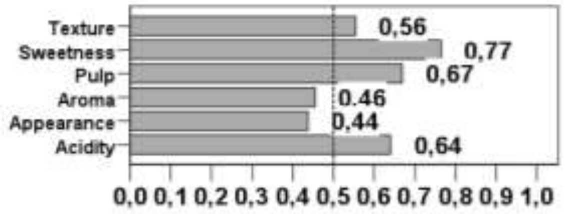

Figure 6.25: Model quality for ROC curve analysis with tasters' variables according to General taste maximum value given (7-point) and the perceptions of consumer's taste in kiwifruit ('Jintao' on the left and 'Hayward' kiwifruit on the right).

Instead of applying the ROC analysis for each month and year, ROC can be performed to obtain an overall model quality. This approach reveals that, for both cultivars, sweetness, acidity and texture were the variables that respond with better scores for General taste. Aroma has also importance for the General taste on 'Jintao' (Figure 6.26).

These results confirm, in first place, that, for each cultivar, sensory evaluation depends on different attributes. For example, for 'Golden Delicious' apples, values of firmness, SSC and TA are important, while for 'Elstar' apples consumer acceptance is more dependent on aroma and juiciness (Hoehn et al., 2003; Rizzolo et al., 2010); in second, that sweetness, acidity and aroma are critical to consumer acceptance of kiwifruit (Marsh et al., 2006; Garcia et al., 2012; Wang et al., 2021).

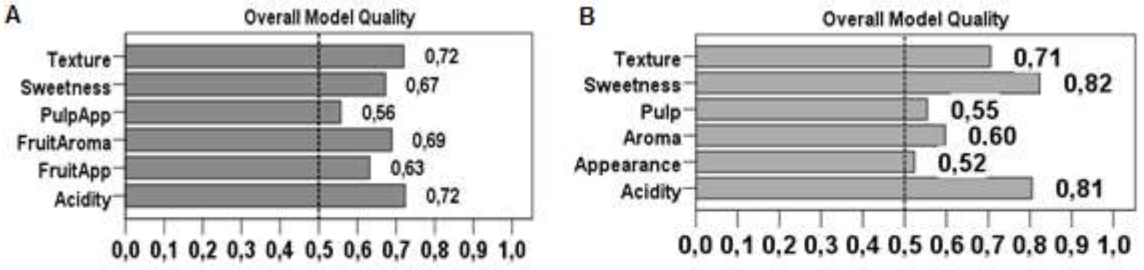

Figure 6.26: Global Model quality for ROC curve analysis with tasters' variables according to General taste maximum value given (7-point) at: A) 'Jintao' kiwifruit; B) 'Hayward' kiwifruit.

6.4 Average spectra temporal evolution of cold stored kiwifruit

Organoleptic evaluation is the most practical and cost-effective method to evaluate the freshness of agricultural products, however the sensory information is affected by personal preferences, experiences and subjective feelings (Wang et al., 2022) and in fruit that ripen rapidly there is the risk that its quality can deteriorated prior to sensory and consumer assessments (Jaeger et al., 2003).

The use of a low-cost, reliable (Nicolaï et al., 2007) and chemical-free method (Shah et al., 2020), that could provide useful information to predict the optimum eating-ripe phase would be a plus to fulfil consumers' preference. An obvious option is the use of the visible-near infrared (VisNIR-DRS) spectroscopy, since it is one of the most successful non-destructive methods for quality assessment of fruit (Afonso et al., 2022; Tian et al., 2022).

The averaged transformed spectra of VisNIR-DRS acquired during storage are represented in Figure 6.27 for 'Jintao' and in Figure 6.28 for 'Hayward' kiwifruit. There was not a consistent evolution pattern of the spectra in the three years.

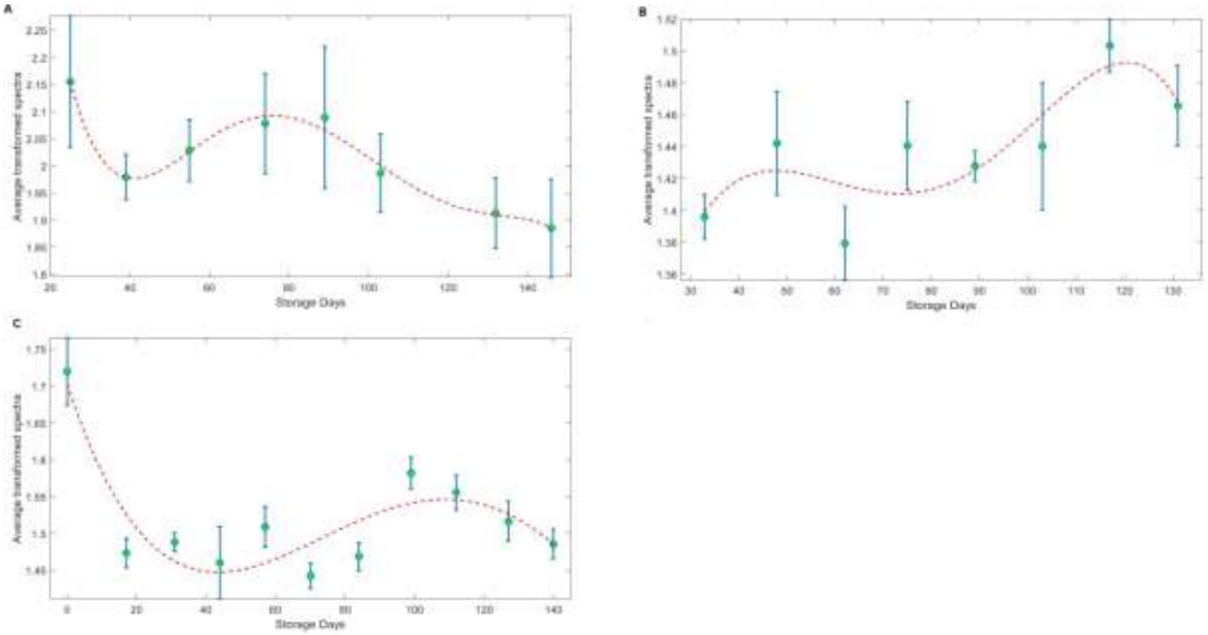

Figure 6.27: Averaged transformed reflectance spectra at 680 nm acquired along storage time for 'Jintao' kiwifruit during: A) 2018/2019; B) 2019/2020; C) 2020/2021. Data depicted is the Mean ± SE of 8 kiwifruit.

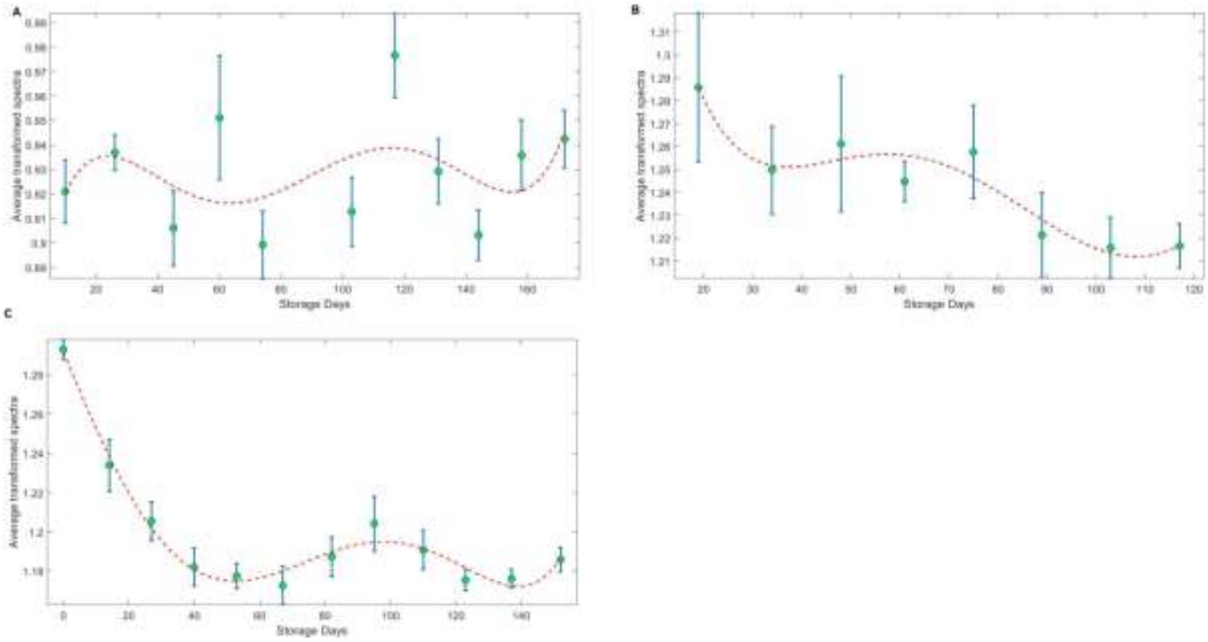

Figure 6.28: Averaged transformed reflectance spectra at 680 nm acquired along storage time for 'Jintao' kiwifruit during: A) 2018/2019; B) 2019/2020; C) 2020/2021. Data depicted is the Mean ± SE of 8 kiwifruit.

Being firmness an IQA that consistently decreases with storage time, it could be expected that with the loss of kiwifruit firmness, the reflectance will be lower since soft fruit has less scattering. However, as mentioned before (Section 4.1), the turbid biological material complicates the absorption and scattering processes (Quin & Lu, 2008) and the complexity and the heterogeneities of the fruit's tissue (Nicolaï et al., 2007; Saeys et al., 2019) affects the relationship between the reflectance spectra and the mechanical properties (Cen et al., 2013; Afonso et al., 2022). Furthermore, it was reported in apples that cell wall degradation reduces the scattering events (Bobelyn et al., 2010), but air filled pores caused by cells water loss leads to an increase of them (Schotsmans et al., 2004), which also complicates this relation (Rizzolo et al., 2010).

Moreover, since kiwifruit of each cultivar were from two different orchards and not from the same batch, an extra complexity might have been added.

Despite all these difficulties, the spectra collected show differences along the storage time, meaning that VisNIR-DRS spectroscopy is able to identify chemical and physical changes that occur during kiwifruit ripening in cold storage.

6.5 Spectra reflectance correlation with internal quality attributes

Sweetness and texture have a major impact in consumer acceptance, for both cultivars, according the sensory evaluation results. For this reason, was investigated if there is a good correlation between kiwifruit SSC and firmness and their reflectance spectra acquired during storage and at which wavelength (Figure 6.29 andFigure 6.**30**).

6.5.1 SSC

In the first place, correlation between kiwifruit SSC and their reflectance spectra showed to be very different in each year/season. Even to the point that, in one year (2018/2019) there is a good positive correlation and in the other two, although not so relevant, the correlation is negative for the same wavelength range (500 – 800 nm), while in 800 – 950 nm, the correlation inverted in all seasons (Figure

6.29A). Although very irregular through years, for 'Jintao' kiwifruit the higher correlation was obtained in the range 650 – 710 nm (≥0.8), followed by the range 820 – 950, in 2018/2019. The latter range revealed to have a negative correlation with 'Hayward' SSC also for kiwifruit from 2018/2019 (Figure 6.29B). There was also a good correlation, but positive, in the range 730 - 780 nm for the previous season, and a negative one between 635 – 690 nm in 2020/2021.

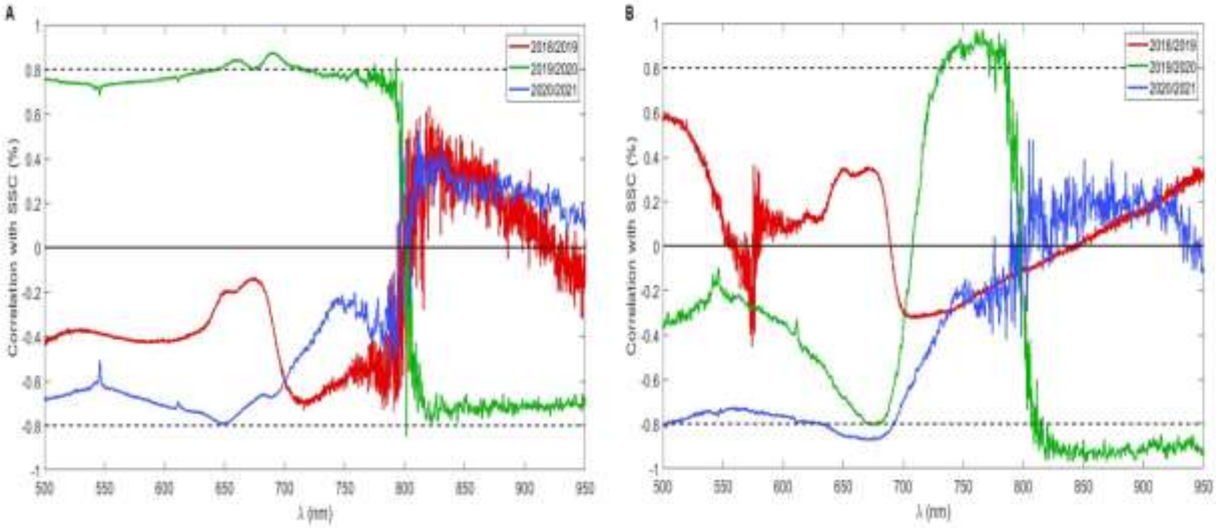

Figure 6.29: Correlation between soluble solids content (SSC) and VisNIR-DRS reflectance spectra of: A) 'Jintao' kiwifruit; B) 'Hayward' kiwifruit. Each colour line represents a different year/season (red = 2018/2019; green = 2019/2020; blue = 2020/2021).

Results showed a very irregular correlation between soluble solids content and reflectance spectra, but there is, effectively, wavelength ranges with good correlation values, meaning that VisNIR-DRS spectroscopy can be used to predict SSC of kiwifruit during storage with special attention to 635 – 780 nm, and so the kiwifruit consumers' preference.

This range (635 – 780 nm), when compared with the one used in the models to predict SSC 'Jintao' kiwifruit (Table 4.1), is integrated in the latter (675 – 895 nm), confirming that these wavelengths have a good correlation with SSC kiwifruit either while on-tree either during storage.

6.5.2 Firmness

Correlation values between reflectance spectra and ‘Jintao’ firmness are totally opposite in the two years showed (Figure 6.30A). The only relevant correlation was found at 695 – 720 nm in 2018/2019, which is also part of the range used in the firmness models prediction in Chapter 4 (Table 4.1). In the case of ‘Hayward’ kiwifruit, correlation between firmness and reflectance spectra is even more irregular, not only between seasons, but also along the wavelengths in the same year (Figure 6.30B). There is a good positive correlation in the range 500 - 705 nm in 2020/2021 and at 810 - 950 nm in 2019/2020. A negative correlation was found at 740 - 785 nm in 2019/2020.

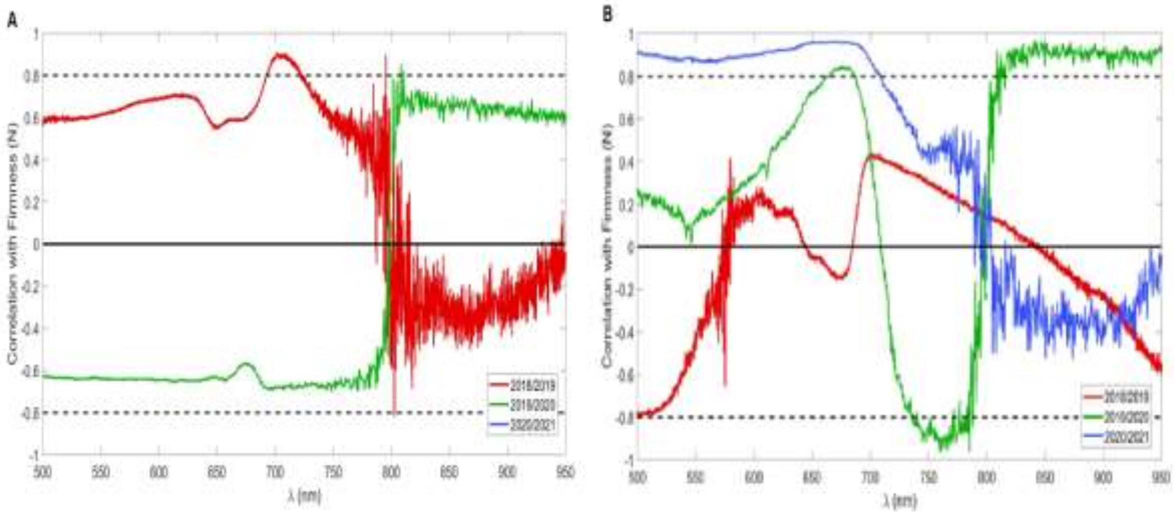

Figure 6.30: Correlation between firmness and VisNIR-DRS reflectance spectra of: A) ‘Jintao’ kiwifruit; B) ‘Hayward’ kiwifruit. Each colour line represents a different year/season (red = 2018/2019; green = 2019/2020; blue = 2020/2021).

6.5.3 Other IQA

Considering the results above, further investigation was performed to analyse other internal quality attributes and a good correlation with reflectance spectra was found for ‘Jintao’ kiwifruit dry matter (Figure 6.31A) and, not so good but still relevant, for titrable acidity (Figure 6.31B).

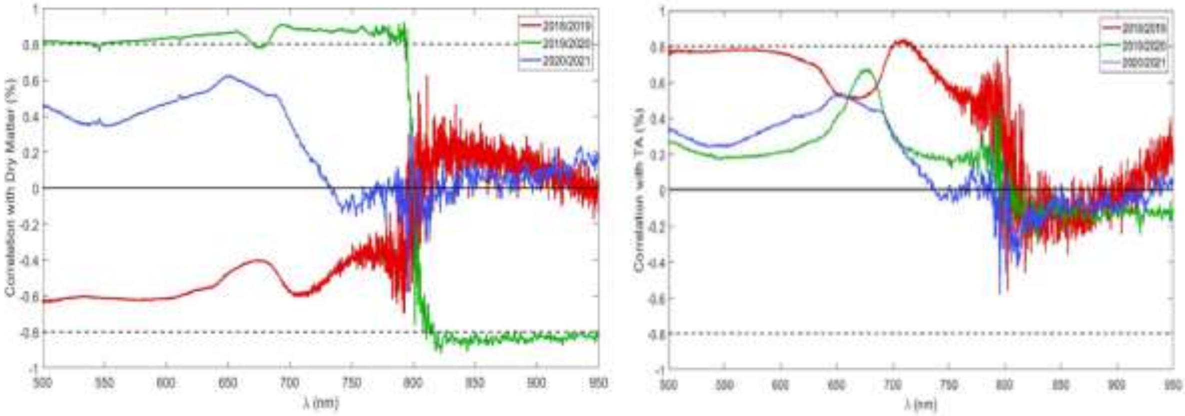

Figure 6.31: Correlation between VisNIR-DRS reflectance spectra of ‘Jintao’ kiwifruit and: A) Dry matter; B) Titrable acidity. Each colour line represents a different year/season (red = 2018/2019; green = 2019/2020; blue = 2020/2021).

Correlation between dry matter of ‘Jintao’ kiwifruit and reflectance spectra acquired during storage is, in fact, very similar with the correlation showed in Figure 6.20A for SSC in 2019/2020, highlighting the high correlation (≥ 0.8) at almost all spectrum of this year, which was positive at 550 - 665 nm and 685 - 790 nm, and negative at 820 – 950 nm.

On the other hand, although titrable acidity showed only a high positive correlation at 700 - 715 nm, correlation between 500-595 nm is very close to 0.8 in 2018/2019.

In this work, applying the receiver operating characteristic (ROC) analysis to sensory evaluation performed during cold storage of two kiwifruit cultivars, through three years, reveal that for ‘Jintao’ and ‘Hayward’ kiwifruit sweetness, acidity and texture were the variables, for panellists, with better impact scores in kiwifruit General taste through cold storage.

Since the VisNIR-DRS spectroscopy showed to be able to distinguish the chemical and physical changes that occur during kiwifruit ripening in cold storage and there are good correlation values between soluble solids content and reflectance spectra in the 635 – 780 nm wavelength range, this technology could be an objective alternative to determine optimum eating-ripe phase since is not affected by sensorial consumer’ preferences, among others.

Chapter 7

General conclusions and future perspectives

7.1 General conclusions

This thesis aimed to monitor the complete ripening process of two distinct cultivars of kiwifruit, namely the green-fleshed 'Hayward' and the yellow-fleshed 'Jintao', from the initial stage on the tree to the eating-ripe phase, using visible near infrared spectroscopy (VisNIR). The goal was to explore the potential of VisNIR-DRS as a dependable tool for non-destructive monitoring of fruit quality.

First and foremost, it is worth noting that a 'hard mode' approach was adopted in this study:

- The calibration models created in this research for predicting the internal quality parameters of 'Jintao' kiwifruit were based on a highly heterogeneous dataset that included fruit in various developmental stages.
- In addition to using data from two different orchards collected over two years, an unexpected challenge arose when the spectrometer was lost and had to be replaced by a second one.
- By utilizing four distinct datasets (one for each year and orchard), rigorous external validations could be conducted.

However, the innovation of this study lies precisely in the challenges described above. While there are numerous reports on the use of spectroscopy to predict kiwifruit internal quality attributes (IQA), these reports typically focus on only a few IQA and are limited to post-harvest analysis. Pre-harvest monitoring, on the other hand, enables better orchard management and can aid in determining the ideal harvest date, which is critical for increasing producers' revenue and ensuring high-quality fruit. In these reports, the data usually originate from the same batch and are divided in a proportion of 75% calibration and 25% validation, indicating that only internal validation is performed, with minimal heterogeneity. This is why the performance models found in literature are overoptimistic. In contrast, this study utilized a highly diverse dataset that covered kiwifruit ripening on the tree until one week after their commercial harvest season. Moreover, the heterogeneity arose from different orchards and years. External validations were also conducted with the four independent datasets, with three of them being used for calibration and the remaining one for validation. External validation is crucial for evaluating how calibration models will perform with new data. Finally, special attention was given to the 'Jintao' kiwifruit, as little information was available about this cultivar that is rapidly expanding commercially.

Despite all these difficulties, this study yielded promising results. After testing several combinations of pre-processing treatments and wavelengths using data from the first year, robust models were obtained for Hue (RMSEP = 1.92; R^2 = 0.88; Range = 660 – 959 nm), SSC (RMSEP = 1.24%; R2 = 0.80; Range = 675 – 895 nm), and a* (RMSEP = 1.44; R2 = 0.82; Range = 660 – 948 nm) by applying only SNV to spectra.

The experimental design enabled testing of the accuracy of average predictions from these calibration models, specifically for predicting the average IQA for each sampling day and each of the four data subsets considered. The prediction of IQA averages on these specific dates resulted in excellent outcomes, with R^2 values equal to or greater than 0.97, six SDR values exceeding 9 and RMSEP values that were at least 3-5 times lower than those obtained for individual predictions. As orchard management is based on averages rather than individual values, this result reinforces the practicality of Vis-NIR technology in the field.

The quality of the calibration models and the relative changes of the monitored IQA along ripening suggest that a*, Hue, and SSC are useful IQA for monitoring the ripening of 'Jintao' kiwifruit. These parameters exhibit good performance models and significant variations over time.

The results obtained for the data of the first year must be viewed with care, since they were not obtained through strict external validation, but rather through independent datasets built from the trees of the two orchards. While this approach does provide some indication of model performance, it is not as rigorous as external validation with completely independent data sets. Additionally, the analysis of the two-year data set revealed that the results from the first year may have been overly optimistic, which further underscores the importance of external validation in developing and accessing calibration models.

Regarding the analysis of the complete two-year dataset, the focus of the models developed in this study was solely on the SSC of 'Jintao' kiwifruit due to the complexity of the procedure. The performance of external validation was compared with the standard internal validation. Good performance models were achieved with internal validation (SDR = 2), although, the same did not apply to external validation. In both cases, a pre-processing optimization step was included, which consisted of three modes of operation: MIX (a MIXture of different types of pre-processing tested), SNV (tested on different spectral ranges), and SG (Savitzky-Golay tested on different ranges, filter width, and derivative order), which ultimately delivered approximately equivalent performance.

In an attempt to improve the performance of the models, variable selection and orthogonal signal correction were employed. However, it was found that only the internal validation performance was improved, while the external validation results remained largely unaffected. This suggests that these techniques may have limited value in the context of stringent external validation.

As it was not possible to perform the usual calibration transfer due to the lack of common samples, an alternative approach was used based on a normalization procedure between the daily average spectra. This led to an improvement in the external validation model performance, achieving an SDR value of 1.8.

The final step of the study attempted to combine variable selection, orthogonal signal correction and calibration transfer in order to improve the model's performance. However, no improvement was observed, which suggests that both variable selection and orthogonal signal correction are local improvements that may not be transferable to independent datasets.

It is interesting to note that the simple form of calibration transfer used in this study was successful, whereas other approaches were not. The normalization procedure used in this approach removes part of the variability related to the differences between the spectrometers by normalizing the "slave" spectra average to the "master" average on each day. It is also possible that large spectral feature differences associated with pulp structure changes are partially cancelled out. This simple but powerful technique could be an effective way to improve the prediction of new data in orchard monitoring applications. However, further tests need to be conducted using different datasets.

It is worth noting that in some cases, the differences among orchards or instruments may be incorporated into the models. Therefore, removing these differences may lower the quality of the predictions.

In the post-harvest phase, a novel approach using ROC (Receiver Operating Characteristic) was employed to obtain an overall assessment of the model quality. Results revealed that sweetness, acidity, and texture were the variables that showed the best scores for General taste in both cultivars studied. For ‘Jintao’ kiwifruit, aroma also had a significant impact on General taste. Furthermore, considering the IQAs that influence consumers' acceptance, a strong correlation between SSC and reflectance was found for both cultivars, with the 635 – 780 nm range being the most important. Regarding firmness, a good correlation with reflectance spectra was observed, particularly in ‘Hayward’ kiwifruit. For ‘Jintao’ kiwifruit, reflectance spectra also showed a strong correlation with dry matter, and a moderate but still relevant correlation with titrable acidity.

There are some common thoughts that apply to all the sections of this study.

Firstly, the study duration of two years is relatively limited, and a three-year study would improve the variability covered by the model and reduce prediction errors in the validation dataset. Therefore, long-term datasets are essential in developing the field of VisNIR-DRS in fruit quality monitoring.

Secondly, the hardware used in the study is critical. The signal-to-noise ratio determines the useful wavelength range, and it was necessary to eliminate wavelengths above 950 nm, even though the spectrometer could detect up to 1020 nm. Reproducibility of measurements and a stable contact between probe and fruit are also crucial, and it is essential to probe deep into the pulp. The optical probes used in the study had a small separation between injection and collection fibers and mostly probed superficial tissue, possibly contaminated by light reflected at the fruit skin, as seen in the spectra. With a good hardware setup, almost any basic model will work, while a poor hardware setup makes it difficult to achieve good results, even with sophisticated machine learning models. Therefore, the hardware setup is crucial in obtaining accurate VisNIR-DRS measurements in fruit quality monitoring.

The third point to consider is the significant spectral variations in fruit. This is evident in the correlations between SSC and the spectra of cold-stored fruit, as shown in section 6. The correlations differ each year, indicating that various factors contribute to the shape of the reflectance spectra. The correlation between SSC and the spectra is just a by-product of how other factors shape the overall reflectance. There are two approaches to tackle this issue. The first approach, which is commonly used, is to eliminate unwanted variation as much as possible through pre-processing techniques such as SNV or OSC. The second approach, although more challenging, is to comprehend and model the major factors that define the spectra shapes.

7.2 Future perspectives

Looking ahead to the future, it is clear that scientific and technological advancements are interconnected. From a scientific standpoint, it is vital to expand the database of spectra by including data on a range of factors, such as different years, producers, soil types and production methods. Additionally, it is essential to conduct further research into the effectiveness of the proposed average normalization procedure for calibration transfer, which may facilitate data transfer between instruments or orchards. Moreover, exploring methods that can better extract the relevant information from the data and gaining a better understanding of the reasons for variability in the reflectance spectra are crucial.

On the technological front, the primary objective is to develop a portable device that uses VisNIR-DRS spectroscopy and has integrated robust models capable of accurately predicting the main IQA of kiwifruit while still on the tree and estimating their optimal harvest date with good performance. To achieve this goal, it is necessary to develop reliable and reproducible sampling methods in pure interactance mode, optimize the spectral device to ensure a good signal-to-noise ratio across a broad wavelength range, perform field tests with producers to assess the economic impact of VisNIR-DRS in orchard management, and create a user-friendly interface, display, and software to provide real-time information.

Chapter 8

References

Abbott, J. A. (1999). Quality measurement of fruits and vegetables. *Postharvest biology and technology*, *15*(3), 207-225. https://doi.org/10.1016/S0925-5214(98)00086-6

Aernouts, B., Erkinbaev, C., Watté, R., Van Beers, R., Do Trong, N. N., Nicolaï, B., & Saeys, W. (2015). Estimation of bulk optical properties of turbid media from hyperspectral scatter imaging measurements: metamodeling approach. *Optics Express*, *23*(20), 26049-26063. https://doi.org/10.1364/OE.23.026049

Afonso, A. M., Antunes, M. D., Cruz, S., Cavaco, A. M., & Guerra, R. (2022). Non-destructive follow-up of 'Jintao' kiwifruit ripening through VISNIR-DRS spectroscopy–individual vs. average calibration model's predictions. *Postharvest Biology and Technology*, *188*, 111895. https://doi.org/10.1016/j.postharvbio.2022.111895

Alexandrakis, G., Farrell, T. J., & Patterson, M. S. (1998). Accuracy of the diffusion approximation in determining the optical properties of a two-layer turbid medium. *Applied optics*, *37*(31), 7401-7409. https://doi.org/10.1364/AO.37.007401

Ampomah-Dwamena, C., McGhie, T., Wibisono, R., Montefiori, M., Hellens, R. P., & Allan, A. C. (2009). The kiwifruit lycopene beta-cyclase plays a significant role in carotenoid accumulation in fruit. *Journal of Experimental Botany*, *60*(13), 3765-3779. https://doi.org/10.1093/jxb/erp218

Anderson, N. T., Walsh, K. B., Subedi, P. P., & Hayes, C. H. (2020). Achieving robustness across season, location and cultivar for a NIRS model for intact mango fruit dry matter content. *Postharvest Biology and Technology*, *168*, 111202. https://doi.org/10.1016/j.postharvbio.2020.111202

Anderson, N. T., Walsh, K. B., Flynn, J. R., & Walsh, J. P. (2021). Achieving robustness across season, location and cultivar for a NIRS model for intact mango fruit dry matter content. II. Local PLS and nonlinear models. *Postharvest Biology and Technology*, *171*, 111358. https://doi.org/10.1016/j.postharvbio.2020.111358

Anderson, N. T., & Walsh, K. B. (2022). The evolution of chemometrics coupled with near infrared spectroscopy for fruit quality evaluation. *Journal of Near Infrared Spectroscopy*, *30*(1), 3-17. https://doi.org/10.1364/JNIRS.30.000003

Andersson, M. (2009). A comparison of nine PLS1 algorithms. *Journal of Chemometrics: A Journal of the Chemometrics Society*, *23*(10), 518-529. https://doi.org/10.1002/cem.1248

Antunes, M. D. C., Pateraki, I., Kanellis, A. K., & Sfakiotakis, E. M. (2000). Differential effects of low-temperature inhibition on the propylene induced autocatalysis of ethylene production, respiration and ripening of 'Hayward' kiwifruit. *The Journal of Horticultural Science and Biotechnology*, *75*(5), 575-580. https://doi.org/10.1080/14620316.2000.11511288

Antunes, M. D. C., & Sfakiotakis, E. M. (2002). Ethylene biosynthesis and ripening behaviour of 'Hayward' kiwifruit subjected to some controlled atmospheres. *Postharvest Biology and Technology*, *26*(2), 167-179. https://doi.org/10.1016/S0925-5214(02)00040-6

Antunes, M. D. (2007). The role of ethylene in kiwifruit ripening and senescence. *Stewart Postharvest Review*, *3*(2), 1. https://dx.doi.org/10.2212/spr.2007.2.9

Antunes, M. D. C., & Sfakiotakis, E. M. (2008). Changes in fatty acid composition and electrolyte leakage of 'Hayward' kiwifruit during storage at different temperatures. *Food chemistry*, *110*(4), 891-896. https://doi.org/10.1016/j.foodchem.2008.02.089

Arazuri, S., Jarén, C., & Arana, J. I. (2005). Selection of the temperature in the sugar content determination of kiwi fruit. *International journal of infrared and millimeter waves*, *26*(4), 607-616. https://doi.org/10.1007/s10762-005-4076-8

Asiche, W. O., Mitalo, O. W., Kasahara, Y., Tosa, Y., Mworia, E. G., Ushijima, K., Nakano, R., & Kubo, Y. (2017). Effect of storage temperature on fruit ripening in three kiwifruit cultivars. *The Horticulture Journal*, OKD-028. https://doi.org/10.2503/hortj.OKD-028

Barnes, R. J., Dhanoa, M. S., & Lister, S. J. (1989). Standard normal variate transformation and de-trending of near-infrared diffuse reflectance spectra. *Applied spectroscopy*, *43*(5), 772-777. https://doi.org/10.1366/0003702894202201

Beers, R. V., Aernouts, B., Watté, R., Schenk, A., Nicolaï, B., & Saeys, W. (2017). Effect of maturation on the bulk optical properties of apple skin and cortex in the 500–1850 nm wavelength range. *Journal of food engineering*, *214*, 79-89. https://doi.org/10.1016/j.jfoodeng.2017.06.013

Beever, D.J., & Hopkirk, G. (1990). Fruit development and fruit physiology. In: I.J. Warrington and G.C. Weston (Editors). Kiwifruit Science and Management. Ray Richards Publisher, Auckland. pp. 97-126.

Benelli, A., Cevoli, C., Fabbri, A., & Ragni, L. (2022). Ripeness evaluation of kiwifruit by hyperspectral imaging. *Biosystems Engineering*, *223*, 42-52. https://doi.org/10.1016/j.biosystemseng.2021.08.009

Benítez, S., Achaerandio, I., Sepulcre, F., & Pujolà, M. (2013). Aloe vera based edible coatings improve the quality of minimally processed 'Hayward'kiwifruit. *Postharvest Biology and Technology*, *81*, 29-36. https://doi.org/10.1016/j.postharvbio.2013.02.009

Berardinelli, A., Benelli, A., Tartagni, M., & Ragni, L. (2019). Kiwifruit flesh firmness determination by a NIR sensitive device and image multivariate data analyses. *Sensors and Actuators A: Physical*, *296*, 265-271. https://doi.org/10.1016/j.sna.2019.07.027

Bertone, E., Venturello, A., Leardi, R., & Geobaldo, F. (2012). Prediction of the optimum harvest time of ‘Scarlet’ apples using DR-UV–Vis and NIR spectroscopy. *Postharvest Biology and Technology*, *69*, 15-23. https://doi.org/10.1016/j.postharvbio.2012.02.009

Blanke, M. M. (2013). Non-invasive assessment of firmness and NIR sugar (TSS) measurement in apple, pear and kiwi fruit. *Erwerbs-obstbau*, *55*(1), 19-24. https://doi.org/10.1007/s10341-013-0181-3

Bobelyn, E., Serban, A. S., Nicu, M., Lammertyn, J., Nicolaï, B. M., & Saeys, W. (2010). Postharvest quality of apple predicted by NIR-spectroscopy: Study of the effect of biological variability on spectra and model performance. *Postharvest biology and technology*, *55*(3), 133-143. https://doi.org/10.1016/j.postharvbio.2009.09.006

Boquete, E. J., Trinchero, G. D., Fraschina, A. A., Vilella, F., & Sozzi, G. O. (2004). Ripening of ‘Hayward’ kiwifruit treated with 1-methylcyclopropene after cold storage. *Postharvest Biology and Technology*, *32*(1), 57-65. https://doi.org/10.1016/j.postharvbio.2003.09.013

Borovsky, Y., & Paran, I. (2008). Chlorophyll breakdown during pepper fruit ripening in the chlorophyll retainer mutation is impaired at the homolog of the senescence-inducible stay-green gene. *Theoretical and Applied Genetics*, *117*(2), 235-240. https://doi.org/10.1007/s00122-008-0768-5

Burdon, J., McLeod, D., Lallu, N., Gamble, J., Petley, M., & Gunson, A. (2004). Consumer evaluation of “Hayward” kiwifruit of different at-harvest dry matter contents. *Postharvest biology and technology*, *34*(3), 245-255. https://doi.org/10.1016/j.postharvbio.2004.04.009

Burdon, J., Lallu, N., Pidakala, P., & Barnett, A. (2013). Soluble solids accumulation and postharvest performance of ‘Hayward’ kiwifruit. *Postharvest biology and technology*, *80*, 1-8. https://doi.org/10.1016/j.postharvbio.2013.01.009

Burdon, J., Pidakala, P., Martin, P., McAtee, P. A., Boldingh, H. L., Hall, A., & Schaffer, R. J. (2014a). Postharvest performance of the yellow-fleshed ‘Hort16A’ kiwifruit in relation to fruit maturation. *Postharvest Biology and Technology*, *92*, 98-106. https://doi.org/10.1016/j.postharvbio.2014.01.004

Burdon, J., Punter, M., Billing, D., Pidakala, P., & Kerr, K. (2014b). Shrivel development in kiwifruit. *Postharvest biology and technology*, *87*, 1-5. https://doi.org/10.1016/j.postharvbio.2013.07.031

Burdon, J., Pidakala, P., Martin, P., Billing, D., & Boldingh, H. (2016). Fruit maturation and the soluble solids harvest index for ‘Hayward’ kiwifruit. *Scientia Horticulturae*, *213*, 193-198. https://doi.org/10.1016/j.scienta.2016.10.027

Burdon, J., Martin, P., Ireland, H., Schaffer, R., McAtee, P., Boldingh, H., & Nardozza, S. (2021). Transcriptomic analysis reveals differences in fruit maturation between two kiwifruit cultivars. *Scientia Horticulturae*, *286*, 110207. https://doi.org/10.1016/j.scienta.2021.110207

Castro, H., Siopa, C., Casais, V., Castro, M., Loureiro, J., Gaspar, H., & Castro, S. (2021). Pollination as a key management tool in crop production: Kiwifruit orchards as a study case. *Scientia Horticulturae*, *290*, 110533. https://doi.org/10.1016/j.scienta.2021.110533

Cavaco, A. M., Pires, R., Antunes, M. D., Panagopoulos, T., Brázio, A., Afonso, A. M., Silva, L., Lucas, M. R., Cadeiras, B., Cruz, Sandra P., & Guerra, R. (2018). Validation of short wave near infrared calibration models for the quality and ripening of 'Newhall' orange on tree across years and orchards. *Postharvest Biology and Technology*, *141*, 86-97. https://doi.org/10.1016/j.postharvbio.2018.03.013

Cavaco, A. M., Cruz, S. P., Antunes, M. D., Guerra, R., Pires, R., Afonso, A. M., Brázio, A., Silva, L., Lucas, M. R., Daniel, M., & Panagopoulos, T. (2021a). Spatiotemporal modelling of the quality and ripening of two cultivars of "Algarve Citrus" orchards at different edaphoclimatic conditions. *Postharvest Biology and Technology*, *172*, 111386. https://doi.org/10.1016/j.postharvbio.2020.111386

Cavaco, A. M., Passos, D., Pires, R. M., Antunes, M. D., & Guerra, R. (2021b). Nondestructive Assessment of Citrus Fruit Quality and Ripening by Visible–Near Infrared Reflectance Spectroscopy. In M. S. Khan & I. A. Khan (Eds.), *Citrus*. DOI: 10.5772/intechopen.95970

Cavaco, A. M., Utkin, A. B., Marques da Silva, J., & Guerra, R. (2022). Making Sense of Light: The Use of Optical Spectroscopy Techniques in Plant Sciences and Agriculture. *Applied Sciences*, *12*(3), 997. https://doi.org/10.3390/app12030997

Cen, H., Lu, R., Mendoza, F., & Beaudry, R. M. (2013). Relationship of the optical absorption and scattering properties with mechanical and structural properties of apple tissue. *Postharvest Biology and Technology*, *85*, 30-38. https://doi.org/10.1016/j.postharvbio.2013.04.014

Chai, J., Wang, Y., Liu, Y., Yong, K., & Liu, Z. (2021). 1-MCP extends the shelf life of ready-to-eat 'Hayward' and 'Qihong' kiwifruit stored at room temperature. *Scientia Horticulturae*, *289*, 110437. https://doi.org/10.1016/j.scienta.2021.110437

Chai, J., Wang, Y., Liu, Y., Gu, Z., & Liu, Z. (2022). High O2/N2 controlled atmosphere accelerates postharvest ripening of 'Hayward' kiwifruit. *Scientia Horticulturae*, *300*, 111073. https://doi.org/10.1016/j.scienta.2022.111073

Chandrasekaran, I., Panigrahi, S. S., Ravikanth, L., & Singh, C. B. (2019). Potential of near-infrared (NIR) spectroscopy and hyperspectral imaging for quality and safety assessment of fruits: An overview. *Food Analytical Methods*, *12*(11), 2438-2458. https://doi.org/10.1007/s12161-019-01609-1

Chen, X., & Han, W. (2012). Spectroscopic determination of soluble solids content of 'Qinmei' kiwifruit using partial least squares. *African Journal of Biotechnology*, *11*(10), 2528. DOI:10.5897/AJB11.3177

Cheng, N. Y., Chen, C. C., Liang, B. J., & Tseng, S. H. (2019). Nondestructive evaluation of apple fruit quality by frequency-domain diffuse reflectance spectroscopy: variations in apple skin and flesh. *Applied Sciences*, *9*(11), 2355. https://doi.org/10.3390/app9112355

Cheng, J., Guo, W., Du, R., & Zhou, Y. (2022). Optical properties of different kiwifruit cultivars (Actinidia deliciosa and Actinidia chinensis) and their correlation with internal quality. *Infrared Physics & Technology*, *123*, 104113. https://doi.org/10.1016/j.infrared.2022.104113

Choi, H. R., Baek, M. W., Cheol, L. H., Jeong, C. S., & Tilahun, S. (2022). Changes in metabolites and antioxidant activities of green 'Hayward' and gold 'Haegeum' kiwifruits during ripening with ethylene treatment. *Food Chemistry*, *384*, 132490. https://doi.org/10.1016/j.foodchem.2022.132490

Ciccoritti, R., Paliotta, M., Amoriello, T., & Carbone, K. (2019). FT-NIR spectroscopy and multivariate classification strategies for the postharvest quality of green-fleshed kiwifruit varieties. *Scientia Horticulturae*, *257*, 108622. https://doi.org/10.1016/j.scienta.2019.108622

Clark, C. J., McGlone, V. A., De Silva, H. N., Manning, M. A., Burdon, J., & Mowat, A. D. (2004). Prediction of storage disorders of kiwifruit (Actinidia chinensis) based on visible-NIR spectral characteristics at harvest. *Postharvest biology and technology*, *32*(2), 147-158. https://doi.org/10.1016/j.postharvbio.2003.11.004

Cortés, V., Blasco, J., Aleixos, N., Cubero, S., & Talens, P. (2019). Monitoring strategies for quality control of agricultural products using visible and near-infrared spectroscopy: A review. *Trends in Food Science & Technology*, *85*, 138-148. https://doi.org/10.1016/j.tifs.2019.01.015

Costa, G., Bonora, E., Fiori, G., & Noferini, M. (2010). Innovative non-destructive device for fruit quality assessment. In *VII International Symposium on Kiwifruit 913* (pp. 575-581). https://doi.org/10.17660/ActaHortic.2011.913.78

Cozzolino, D., & Roberts, J. (2016). Applications and developments on the use of vibrational spectroscopy imaging for the analysis, monitoring and characterisation of crops and plants. *Molecules*, *21*(6), 755. https://doi.org/10.3390/molecules21060755

Crisosto, C. H., & Kader, A. A. (1999). Kiwifruit postharvest quality maintenance guidelines. *Central Valley Postharvest Newsletter*, *8*(3), 1-11. Retrieved from https://ucanr.edu/sites/kac/files/123823.pdf

Cruz, S., Guerra, R., Brazio, A., Cavaco, A. M., Antunes, D., & Passos, D. (2021). Nondestructive simultaneous prediction of internal browning disorder and quality attributes in 'Rocha' pear (*Pyrus communis L.*) using VISNIR-DRS spectroscopy. *Postharvest Biology and Technology*, *179*, 111562. https://doi.org/10.1016/j.postharvbio.2021.111562

Famiani, F., Baldicchi, A., Farinelli, D., Cruz-Castillo, J. G., Marocchi, F., Mastroleo, M., Moscatello, S., Proietti, S., & Battistelli, A. (2012). Yield affects qualitative kiwifruit characteristics and dry matter content may be an indicator of both quality and storability. *Scientia Horticulturae*, *146*, 124-130. https://doi.org/10.1016/j.scienta.2012.08.009

Farrés, M., Platikanov, S., Tsakovski, S., & Tauler, R. (2015). Comparison of the variable importance in projection (VIP) and of the selectivity ratio (SR) methods for variable selection and interpretation. *Journal of Chemometrics*, *29*(10), 528-536. https://doi.org/10.1002/cem.2736

Fazayeli, A., Kamgar, S., Nassiri, S. M., Fazayeli, H., & De la Guardia, M. (2019). Dielectric spectroscopy as a potential technique for prediction of kiwifruit quality indices during storage. *Information Processing in Agriculture*, *6*(4), 479-486. https://doi.org/10.1016/j.inpa.2019.02.002

Feng, J., Maguire, K. M., & MacKay, B. R. (2002). Factors affecting ethylene production of Hayward kiwifruit. In *V International Symposium on Kiwifruit 610* (pp. 203-209). https://doi.org/10.17660/ActaHortic.2003.610.27

Ferguson, I. B. (1980). Movement of mineral nutrients into the developing fruit of the kiwifruit (Actinidia chinensis Planch). *New Zealand journal of agricultural research*, *23*(3), 349-353. https://doi.org/10.1080/00288233.1980.10425366

Filzmoser, P., Liebmann, B., & Varmuza, K. (2009). Repeated double cross-validation. *Journal of Chemometrics: A Journal of the Chemometrics Society*, *23*(4), 160-171. https://doi.org/10.1002/cem.1225

Fu, X., Ying, Y., Lu, H., Xu, H., & Yu, H. (2007). FT-NIR diffuse reflectance spectroscopy for kiwifruit firmness detection. *Sensing and Instrumentation for Food Quality and Safety*, *1*(1), 29-35. https://doi.org/10.1007/s11694-007-9004-2

Gambi, F., Pilkington, S. M., McAtee, P. A., Donati, I., Schaffer, R. J., Montefiori, M., Spinelli, F., & Burdon, J. (2018). Fruit of three kiwifruit (Actinidia chinensis) cultivars differ in their degreening response to temperature after harvest. *Postharvest Biology and Technology*, *141*, 16-23. https://doi.org/10.1016/j.postharvbio.2018.03.009

Gao, M., Guo, W., Huang, X., Du, R., & Zhu, X. (2021). Effect of pressing and impacting bruises on optical properties of kiwifruit flesh. *Postharvest Biology and Technology*, *172*, 111385. https://doi.org/10.1016/j.postharvbio.2020.111385

Garcia, C. V., Quek, S. Y., Stevenson, R. J., & Winz, R. A. (2012). Kiwifruit flavour: a review. *Trends in Food Science & Technology*, *24*(2), 82-91. https://doi.org/10.1016/j.tifs.2011.08.012

Gardner, J. W., & Bartlett, P. N. (1994). A brief history of electronic noses. *Sensors and Actuators B: Chemical*, *18*(1-3), 210-211. https://doi.org/10.1016/0925-4005(94)87085-3

Gerasopoulos, D., Chlioumis, G., & Sfakiotakis, E. (2006). Non-freezing points below zero induce low-temperature breakdown of kiwifruit at harvest. *Journal of the Science of Food and Agriculture*, *86*(6), 886-890. https://doi.org/10.1002/jsfa.2429

Gol, N. B., Patel, P. R., & Rao, T. R. (2013). Improvement of quality and shelf-life of strawberries with edible coatings enriched with chitosan. *Postharvest Biology and Technology*, *85*, 185-195. https://doi.org/10.1016/j.postharvbio.2013.06.008

Goldberg, T., Agra, H., & Ben-Arie, R. (2019). Non-destructive measurement of fruit firmness to predict the shelf-life of 'Hayward' kiwifruit. *Scientia Horticulturae*, *244*, 339-342. https://doi.org/10.1016/j.scienta.2018.09.057

Gowen, A. A., O'Donnell, C. P., Cullen, P. J., Downey, G., & Frias, J. M. (2007). Hyperspectral imaging–an emerging process analytical tool for food quality and safety control. *Trends in food science & technology*, *18*(12), 590-598. https://doi.org/10.1016/j.tifs.2007.06.001

Gowen, A. A., Tiwari, B. K., Cullen, P. J., McDonnell, K., & O'Donnell, C. P. (2010). Applications of thermal imaging in food quality and safety assessment. *Trends in food science & technology*, *21*(4), 190-200. https://doi.org/10.1016/j.tifs.2009.12.002

Gowen, A. A., Feng, Y., Gaston, E., & Valdramidis, V. (2015). Recent applications of hyperspectral imaging in microbiology. *Talanta*, *137*, 43-54. https://doi.org/10.1016/j.talanta.2015.01.012

Greer, D. H., & Weedon, M. M. (2013). The impact of high temperatures on Vitis vinifera cv. Semillon grapevine performance and berry ripening. *Frontiers in plant science*, *4*, 491. https://doi.org/10.3389/fpls.2013.00491

Guo, W., Zhao, F., & Dong, J. (2016). Nondestructive measurement of soluble solids content of kiwifruits using near-infrared hyperspectral imaging. *Food Analytical Methods*, *9*(1), 38-47. https://doi.org/10.1007/s12161-015-0165-z

Guo, J., Yuan, Y., Dou, P., & Yue, T. (2017). Multivariate statistical analysis of the polyphenolic constituents in kiwifruit juices to trace fruit varieties and geographical origins. *Food chemistry*, *232*, 552-559. https://doi.org/10.1016/j.foodchem.2017.04.037

Guo, W., Li, W., Yang, B., Zhu, Z., Liu, D., & Zhu, X. (2019). A novel noninvasive and cost-effective handheld detector on soluble solids content of fruits. *Journal of Food Engineering*, *257*, 1-9. https://doi.org/10.1016/j.jfoodeng.2019.03.022

Haff, R. P., & Toyofuku, N. (2008). X-ray detection of defects and contaminants in the food industry. *Sensing and Instrumentation for Food Quality and Safety*, *2*(4), 262-273. https://doi.org/10.1007/s11694-008-9059-8

Hallett, I. C., Macrae, E. A., & Wegrzyn, T. F. (1992). Changes in kiwifruit cell wall ultrastructure and cell packing during postharvest ripening. *International Journal of Plant Sciences*, *153*(1), 49-60. https://doi.org/10.1086/297006

Harker, F. R., & Hallett, I. C. (1994). Physiological and mechanical properties of kiwifruit tissue associated with texture change during cool storage. *Journal of the American Society for Horticultural Science*, *119*(5), 987-993. https://doi.org/10.21273/JASHS.119.5.987

Harman, J. E., & McDonald, B. (1982). Controlled atmosphere storage of kiwifruit: Effects on storage life and fruit quality. *Postharvest Physiology and Storage, XXI IHC 138*, 195-202. https://doi.org/10.17660/ActaHortic.1983.138.22

Hertog, M. L., Nicholson, S. E., & Jeffery, P. B. (2004). The effect of modified atmospheres on the rate of firmness change of ‘Hayward’ kiwifruit. *Postharvest Biology and Technology*, *31*(3), 251-261. https://doi.org/10.1016/j.postharvbio.2003.09.005

Hoehn, E., Gasser, F., Guggenbühl, B., & Künsch, U. (2003). Efficacy of instrumental measurements for determination of minimum requirements of firmness, soluble solids, and acidity of several apple varieties in comparison to consumer expectations. *Postharvest Biology and Technology*, *27*(1), 27-37. https://doi.org/10.1016/S0925-5214(02)00190-4

Hong, F. W., & Chia, K. S. (2021). A review on recent near infrared spectroscopic measurement setups and their challenges. *Measurement*, *171*, 108732. https://doi.org/10.1016/j.measurement.2020.108732

Hu, W., Sun, D. W., & Blasco, J. (2017). Rapid monitoring 1-MCP-induced modulation of sugars accumulation in ripening ‘Hayward’ kiwifruit by Vis/NIR hyperspectral imaging. *Postharvest Biology and Technology*, *125*, 168-180. https://doi.org/10.1016/j.postharvbio.2016.11.001

Hu, D., Lu, R., & Ying, Y. (2020). Spatial-frequency domain imaging coupled with frequency optimization for estimating optical properties of two-layered food and agricultural products. *Journal of Food Engineering*, *277*, 109909. https://doi.org/10.1016/j.jfoodeng.2020.109909

Huang, Y., Lu, R., Hu, D., & Chen, K. (2018). Quality assessment of tomato fruit by optical absorption and scattering properties. *Postharvest Biology and Technology*, *143*, 78-85. https://doi.org/10.1016/j.postharvbio.2018.04.016

Huang, W., Billing, D., Cooney, J., Wang, R., & Burdon, J. (2021). The role of ethylene and abscisic acid in kiwifruit ripening during postharvest dehydration. *Postharvest Biology and Technology*, *178*, 111559. https://doi.org/10.1016/j.postharvbio.2021.111559

Il'iasov, S. G., & Krasnikov, V. V. (1991). *Physical principles of infrared irradiation of foodstuffs*. Hemisphere Pub. Corp.

IPMA (2018a). Boletim Climatológico Agosto 2018 – Portugal Continental. Instituto Português do Mar e da Atmosfera. Retrieved from https://www.ipma.pt/pt/oclima/boletins/

IPMA (2018b). Boletim Climatológico Setembro 2018 – Portugal Continental. Instituto Português do Mar e da Atmosfera. Retrieved from https://www.ipma.pt/pt/oclima/boletins/

IPMA (2018c). Boletim Climatológico Outubro 2018 – Portugal Continental. Instituto Português do Mar e da Atmosfera. Retrieved from https://www.ipma.pt/pt/oclima/boletins/

IPMA (2019). Boletim Climatológico Outubro 2019 – Portugal Continental. Instituto Português do Mar e da Atmosfera. Retrieved from https://www.ipma.pt/pt/oclima/boletins/

Iwasawa, H., Morita, E., Yui, S., & Yamazaki, M. (2011). Anti-oxidant effects of kiwi fruit *in vitro* and *in vivo*. Biol. Pharm. Bull. 34 (1), 128–134. https://doi.org/10.1248/bpb.34.128

Jabbar, A., East, A. R., Jones, G., Tanner, D. J., & Heyes, J. A. (2014). Modelling batch variability in softening of 'Hayward' kiwifruit from at-harvest maturity measures. *Postharvest biology and technology*, *90*, 7-14. https://doi.org/10.1016/j.postharvbio.2013.11.008

Jabbar, A., & East, A. R. (2016). Quantifying the ethylene induced softening and low temperature breakdown of 'Hayward' kiwifruit in storage. *Postharvest Biology and Technology*, *113*, 87-94. https://doi.org/10.1016/j.postharvbio.2015.11.002

Jaeger, S. R., Rossiter, K. L., Wismer, W. V., & Harker, F. R. (2003). Consumer-driven product development in the kiwifruit industry. *Food quality and preference*, *14*(3), 187-198. https://doi.org/10.1016/S0950-3293(02)00053-8

Javadi, S., & Nassiri, S. M. (2014). Application of Acoustic Method for Estimation of Kiwifruit Firmness During Storage. *Tarım Makinaları Bilimi Dergisi, 10 (1)*, 13-17. Retrieved from https://dergipark.org.tr/en/pub/tarmak/issue/11569/137876

Ji, Y., Xu, M., & Wang, A. (2021). Recent advances in the regulation of climacteric fruit ripening: hormone, transcription factor and epigenetic modifications. *Frontiers of Agricultural Science and Engineering*, *8*(2), 314-334. https://doi.org/10.15302/J-FASE-2021386

Jordan, R. B., Walton, E. F., Klages, K. U., & Seelye, R. J. (2000). Postharvest fruit density as an indicator of dry matter and ripened soluble solids of kiwifruit. *Postharvest Biology and Technology*, *20*(2), 163-173. https://doi.org/10.1016/S0925-5214(00)00125-3

Kader, A. A. (2005). Increasing food availability by reducing postharvest losses of fresh produce. *Acta Horticulturae*. 682, 2169- 2176 https://doi.org/10.17660/ActaHortic.2005.682.296

Kader, A. A. (2008). Flavor quality of fruits and vegetables. *Journal of the Science of Food and Agriculture*, *88*(11), 1863-1868. https://doi.org/10.1002/jsfa.3293

Kamruzzaman, M., ElMasry, G., Sun, D. W., & Allen, P. (2011). Application of NIR hyperspectral imaging for discrimination of lamb muscles. *Journal of food engineering*, *104*(3), 332-340. https://doi.org/10.1016/j.jfoodeng.2010.12.024

Kaur, H., Künnemeyer, R., & McGlone, A. (2022). Correction of Temperature Variation with Independent Water Samples to Predict Soluble Solids Content of Kiwifruit Juice Using NIR Spectroscopy. *Molecules*, *27*(2), 504. https://doi.org/10.3390/molecules27020504

Kennard, R. W., & Stone, L. A. (1969). Computer aided design of experiments. Technometrics, 11(1), 137-148. DOI: 10.1080/00401706.1969.10490666

Kerr, A., Rafuse, H., Sparkes, G., Hinchey, J., & Sandeman, H. (2011). Visible/infrared spectroscopy (VIRS) as a research tool in economic geology: background and pilot studies from Newfoundland and Labrador. *Geological Survey, Report*, *11*, 145-166. Retrieved from https://www.gov.nl.ca/iet/files/mines-geoscience-publications-currentresearch-2011-kerrvirs-2011.pdf

Kim, M. S., Chen, Y. R., & Mehl, P. M. (2001). Hyperspectral reflectance and fluorescence imaging system for food quality and safety. *Transactions of the ASAE*, *44*(3), 721. DOI:10.13031/2013.6099

Kim, J. G., Park, Y., Shin, M. H., Muneer, S., Lerud, R., Michelson, C., Kang, D., Min, J. H., & Kumarihami, H. C. (2018). Application of NIR-Spectroscopy to predict the harvesting maturity, fruit ripening and storage ability of Ca-chitosan treated baby kiwifruit. *Journal of Stored Products and Postharvest Research*, *9*(4), 44-53. https://doi.org/10.5897/JSPPR2018.0257

Kruskal, J. B. (1964). Multidimensional scaling by optimizing goodness of fit to a nonmetric hypothesis. *Psychometrika*, *29*(1), 1-27. https://doi.org/10.1007/BF02289565

Kumarihami, H. P. C., Kim, Y. H., Kwack, Y. B., Kim, J., & Kim, J. G. (2022). Application of chitosan as edible coating to enhance storability and fruit quality of Kiwifruit: A Review. *Scientia Horticulturae*, *292*, 110647. https://doi.org/10.1016/j.scienta.2021.110647

Lakshmi, S., Pandey, A. K., Ravi, N., Chauhan, O. P., Gopalan, N., & Sharma, R. K. (2017). Non-destructive quality monitoring of fresh fruits and vegetables. *Defence Life Science Journal*, *2*(2), 103-110. DOI:10.14429/dlsj.2.11379

Lallu, N., Searle, A. N., & Macrae, E. A. (1989). An investigation of ripening and handling strategies for early season kiwifruit (Actinidia deliciosa cv Hayward). *Journal of the Science of Food and Agriculture*, *47*(4), 387-400. https://doi.org/10.1002/jsfa.2740470402

Lee, S. K., & Kader, A. A. (2000). Preharvest and postharvest factors influencing vitamin C content of horticultural crops. *Postharvest biology and technology*, *20*(3), 207-220. https://doi.org/10.1016/S0925-5214(00)00133-2

Lee, J. S., Kim, S. C., Seong, K. C., Kim, C. H., Um, Y. C., & Lee, S. K. (2012). Quality prediction of kiwifruit based on near infrared spectroscopy. *Horticultural Science & Technology*, *30*(6), 709-717. https://doi.org/10.7235/hort.2012.12139

Lee, S., Sarkar, S., Park, Y., Yang, J., & Kweon, G. (2019). Feasibility study for an optical sensing system for hardy kiwi (Actinidia arguta) sugar content estimation, *53*(3), 147-157. DOI:10.14397/jals.2019.53.3.147

Li, L., Lv, F. Y., Guo, Y. Y., & Wang, Z. Q. (2016). Respiratory pathway metabolism and energy metabolism associated with senescence in postharvest Broccoli (Brassica oleracea L. var. italica) florets in response to O2/CO2 controlled atmospheres. *Postharvest Biology and Technology*, *111*, 330-336. https://doi.org/10.1016/j.postharvbio.2015.09.032

Li, M., Pullanagari, R. R., Pranamornkith, T., Yule, I. J., & East, A. R. (2017). Quantitative prediction of post storage ‘Hayward’ kiwifruit attributes using at harvest VisNIR-DRS spectroscopy. *Journal of Food Engineering*, *202*, 46-55. https://doi.org/10.1016/j.jfoodeng.2017.01.002

Li, B., Lecourt, J., & Bishop, G. (2018). Advances in non-destructive early assessment of fruit ripeness towards defining optimal time of harvest and yield prediction — A review. *Plants*, *7*(1), 3. https://doi.org/10.3390/plants7010003

Li, M., Qian, Z., Shi, B., Medlicott, J., & East, A. (2018). Evaluating the performance of a consumer scale SCiO™ molecular sensor to predict quality of horticultural products. *Postharvest Biology and Technology*, *145*, 183-192. https://doi.org/10.1016/j.postharvbio.2018.07.009

Li, M., Pullanagari, R., Yule, I., & East, A. (2022a). Segregation of ‘Hayward’ kiwifruit for storage potential using VisNIR-DRS spectroscopy. *Postharvest Biology and Technology*, *189*, 111893. https://doi.org/10.1016/j.postharvbio.2022.111893

Li, D., Xie, X., Liu, X., Cheng, C., Guo, W., Zhong, C., & Atak, A. (2022b). Effects of Short-Term High Temperature on Gas Exchange in Kiwifruits (Actinidia spp.). *Biology*, *11*(11), 1686. https://doi.org/10.3390/biology11111686

Liang, J., Ren, Y., Wang, Y., Han, M., Yue, T., Wang, Z., & Gao, Z. (2021). Physicochemical, nutritional, and bioactive properties of pulp and peel from 15 kiwifruit cultivars. *Food Bioscience*, *42*, 101157. https://doi.org/10.1016/j.fbio.2021.101157

Liew, O. W., Chong, P. C. J., Li, B., & Asundi, A. K. (2008). Signature optical cues: emerging technologies for monitoring plant health. *Sensors*, *8*(5), 3205-3239. https://doi.org/10.3390/s8053205

Lin, J., Yu, L., Li, W., & Qin, H. (2018). Method for identifying maize haploid seeds by applying diffuse transmission near-infrared spectroscopy. *Applied Spectroscopy*, *72*(4), 611-617. DOI: 10.1177/0003702817742790

Liu, R., Lai, T., Xu, Y., & Tian, S. (2013). Changes in physiology and quality of Laiyang pear in long time storage. *Scientia Horticulturae*, *150*, 31-36. https://doi.org/10.1016/j.scienta.2012.10.017

Liu, D., Sun, D. W., & Zeng, X. A. (2014). Recent advances in wavelength selection techniques for hyperspectral image processing in the food industry. *Food and Bioprocess Technology*, *7*(2), 307-323. https://doi.org/10.1007/s11947-013-1193-6

Liu, D., Guo, W., Li, Q., & Xie, D. (2019). Relationship of the bulk optical properties in 950–1650 nm wavelength range with internal quality and microstructure of kiwifruit during maturation. *Biosystems Engineering*, *184*, 45-54. https://doi.org/10.1016/j.biosystemseng.2019.05.005

Liu, D., Xie, D., & Guo, W. (2020). Effect of CPPU on bulk optical properties of kiwifruit during storage in near-infrared range. *Journal of the Science of Food and Agriculture*, *100*(7), 3111-3119. https://doi.org/10.1002/jsfa.10345

Lorente, D., Escandell-Montero, P., Cubero, S., Gómez-Sanchís, J., & Blasco, J. (2015). Visible–NIR reflectance spectroscopy and manifold learning methods applied to the detection of fungal infections on citrus fruit. *Journal of Food Engineering*, *163*, 17-24. https://doi.org/10.1016/j.jfoodeng.2015.04.010

Lu, R. (2016). *Light scattering technology for food property, quality and safety assessment*. Crc Press: Boca Raton, FL, USA.

Lu, R., Van Beers, R., Saeys, W., Li, C., & Cen, H. (2020). Measurement of optical properties of fruits and vegetables: A review. *Postharvest Biology and Technology*, *159*, 111003. https://doi.org/10.1016/j.postharvbio.2019.111003

Luan, Y., Wang, S., Wang, R., & Xu, C. (2020). Accumulation of red apocarotenoid β-citraurin in peel of a spontaneous mutant of huyou (*Citrus changshanensis)* and the effects of storage temperature and ethylene application. *Food chemistry*, *309*, 125705. https://doi.org/10.1016/j.foodchem.2019.125705

Ma, T., Sun, X., Zhao, J., You, Y., Lei, Y., Gao, G., & Zhan, J. (2017). Nutrient compositions and antioxidant capacity of kiwifruit (Actinidia) and their relationship with flesh color and commercial value. *Food Chemistry*, *218*, 294-304. https://doi.org/10.1016/j.foodchem.2016.09.081

Ma, T., Xia, Y., Inagaki, T., & Tsuchikawa, S. (2021). Non-destructive and fast method of mapping the distribution of the soluble solids content and pH in kiwifruit using object rotation near-infrared hyperspectral imaging approach. *Postharvest Biology and Technology*, *174*, 111440. https://doi.org/10.1016/j.postharvbio.2020.111440

Ma, T., Zhao, J., Inagaki, T., Su, Y., & Tsuchikawa, S. (2022). Rapid and nondestructive prediction of firmness, soluble solids content, and pH in kiwifruit using Vis–NIR spatially resolved spectroscopy. *Postharvest Biology and Technology*, *186*, 111841. https://doi.org/10.1016/j.postharvbio.2022.111841

Magwaza, L. S., Opara, U. L., Cronje, P. J., Landahl, S., Nieuwoudt, H. H., Mouazen, A. M., Nicolaï, B., & Terry, L. A. (2014). Assessment of rind quality of 'Nules Clementine' mandarin fruit during postharvest storage: 2. Robust Vis/NIRS PLS models for prediction of physico-chemical attributes. *Scientia Horticulturae*, *165*, 421-432. https://doi.org/10.1016/j.scienta.2013.09.050

Magwaza, L. S., & Opara, U. L. (2015). Analytical methods for determination of sugars and sweetness of horticultural products—A review. *Scientia Horticulturae*, *184*, 179-192. https://doi.org/10.1016/j.scienta.2015.01.001

Manolopoulou, H., Lambrinos, G., & Assimaki, H. (1995). Modified atmosphere storage of Hayward kiwifruit. In *III International Symposium on Kiwifruit 444* (pp. 619-624). https://doi.org/10.17660/ActaHortic.1997.444.95

Marsh, K. B., Friel, E. N., Gunson, A., Lund, C., & MacRae, E. (2006). Perception of flavour in standardised fruit pulps with additions of acids or sugars. *Food Quality and Preference*, *17*(5), 376-386. https://doi.org/10.1016/j.foodqual.2005.04.011

Marsh, K. B., Boldingh, H. L., Shilton, R. S., & Laing, W. A. (2009). Changes in quinic acid metabolism during fruit development in three kiwifruit species. *Functional Plant Biology*, *36*(5), 463-470. https://doi.org/10.1071/FP08240

Martens, H., & Naes, T. (1987). Multivariate calibration by data compression. In P. Williams, K. Norris, & S. Paul (Eds.). *Near-infrared Technology in the Agricultural and Food Industries*. St. Paul, Minnesota: American Association of Cereal Chemists, pp.123-139

Martinsen, P., & Schaare, P. (1998). Measuring soluble solids distribution in kiwifruit using near-infrared imaging spectroscopy. *Postharvest Biology and Technology*, *14*(3), 271-281. https://doi.org/10.1016/S0925-5214(98)00051-9

McGhie, T. K., & Ainge, G. D. (2002). Color in fruit of the genus Actinidia: carotenoid and chlorophyll compositions. *Journal of Agricultural and Food Chemistry*, *50*(1), 117-121. https://doi.org/10.1021/jf010677l

McGlone, V. A., Abe, H., & Kawano, S. (1997). Kiwifruit firmness by near infrared light scattering. *Journal of Near Infrared Spectroscopy*, *5*(2), 83-89. https://doi.org/10.1255/jnirs.102

McGlone, V. A., & Kawano, S. (1998). Firmness, dry-matter and soluble-solids assessment of postharvest kiwifruit by NIR spectroscopy. *Postharvest Biology and Technology*, *13*(2), 131-141. https://doi.org/10.1016/S0925-5214(98)00007-6

McGlone, V. A., & Jordan, R. B. (2000). Kiwifruit and apricot firmness measurement by the non-contact laser air-puff method. *Postharvest Biology and Technology*, *19*(1), 47-54. https://doi.org/10.1016/S0925-5214(00)00068-5

McGlone, V. A., Jordan, R. B., & Martinsen, P. J. (2002a). Vis/NIR estimation at harvest of pre-and post-storage quality indices for ‘Royal Gala’ apple. *Postharvest Biology and Technology*, *25*(2), 135-144. https://doi.org/10.1016/S0925-5214(01)00180-6

McGlone, V. A., Jordan, R. B., Seelye, R., & Martinsen, P. J. (2002b). Comparing density and NIR methods for measurement of kiwifruit dry matter and soluble solids content. *Postharvest Biology and Technology*, *26*(2), 191-198. https://doi.org/10.1016/S0925-5214(02)00014-5

McGlone, V. A., Clark, C. J., & Jordan, R. B. (2007). Comparing density and VNIR methods for predicting quality parameters of yellow-fleshed kiwifruit (Actinidia chinensis). *Postharvest Biology and Technology*, *46*(1), 1-9. https://doi.org/10.1016/j.postharvbio.2007.04.003

McGuire, R. G. (1992). Reporting of objective color measurements. *HortScience*, *27*(12), 1254-1255. https://doi.org/10.21273/HORTSCI.27.12.1254

Milej, D., Abdalmalak, A., Janusek, D., Diop, M., Liebert, A., & Lawrence, K. S. (2016). Time-resolved subtraction method for measuring optical properties of turbid media. *Applied Optics*, *55*(7), 1507-1513. https://doi.org/10.1364/AO.55.001507

Minas, I. S., Tanou, G., Belghazi, M., Job, D., Manganaris, G. A., Molassiotis, A., & Vasilakakis, M. (2012). Physiological and proteomic approaches to address the active role of ozone in kiwifruit post-harvest ripening. *Journal of Experimental Botany*, *63*(7), 2449-2464. https://doi.org/10.1093/jxb/err418

Mishra, P., & Nikzad-Langerodi, R. (2020). Partial least square regression versus domain invariant partial least square regression with application to near-infrared spectroscopy of fresh fruit. *Infrared Physics & Technology*, *111*, 103547.

Mishra, P., Roger, J. M., Rutledge, D. N., & Woltering, E. (2020). Two standard-free approaches to correct for external influences on near-infrared spectra to make models widely applicable. *Postharvest Biology and Technology*, *170*, 111326. https://doi.org/10.1016/j.postharvbio.2020.111326

Mishra, P., & Woltering, E. (2021). Handling batch-to-batch variability in portable spectroscopy of fresh fruit with minimal parameter adjustment. *Analytica Chimica Acta*, *1177*, 338771. https://doi.org/10.1016/j.aca.2021.338771

Mitalo, O. W., Tokiwa, S., Kondo, Y., Otsuki, T., Galis, I., Suezawa, K., Kataoka, I., Doan, A. T., Nakano, R., Ushijima, K., & Kubo, Y. (2019). Low temperature storage stimulates fruit softening and sugar accumulation without ethylene and aroma volatile production in kiwifruit. *Frontiers in Plant Science*, *10*, 888. https://doi.org/10.3389/fpls.2019.00888

Moghimi, A., Aghkhani, M. H., Sazgarnia, A., & Sarmad, M. (2010). Vis/NIR spectroscopy and chemometrics for the prediction of soluble solids content and acidity (pH) of kiwifruit. *Biosystems engineering*, *106*(3), 295-302. https://doi.org/10.1016/j.biosystemseng.2010.04.002

Montefiori, M., McGhie, T. K., Hallett, I. C., & Costa, G. (2009). Changes in pigments and plastid ultrastructure during ripening of green-fleshed and yellow-fleshed kiwifruit. *Scientia Horticulturae*, *119*(4), 377-387. https://doi.org/10.1016/j.scienta.2008.08.022

Nicolaï, B. M., Beullens, K., Bobelyn, E., Peirs, A., Saeys, W., Theron, K. I., & Lammertyn, J. (2007). Nondestructive measurement of fruit and vegetable quality by means of NIR spectroscopy: A review. *Postharvest biology and technology*, *46*(2), 99-118. https://doi.org/10.1016/j.postharvbio.2007.06.024

Nicolaï, B. M., Defraeye, T., De Ketelaere, B., Herremans, E., Hertog, M. L., Saeys, W., Toricelli, A., Vandendriessche, T., & Verboven, P. (2014). Nondestructive measurement of fruit and vegetable quality. *Annu. Rev. Food Sci. Technol*, *5*(1), 285-312. DOI: 10.1146/annurev-food-030713-092410

Nie, S., Al Riza, D. F., Ogawa, Y., Suzuki, T., Kuramoto, M., Miyata, N., & Kondo, N. (2020). Potential of a double lighting imaging system for characterization of 'Hayward' kiwifruit harvest indices. *Postharvest Biology and Technology*, *162*, 111113. https://doi.org/10.1016/j.postharvbio.2019.111113

Oja, H. (2010). *Multivariate nonparametric methods with R: an approach based on spatial signs and ranks*. Springer Science & Business Media.

Ozturk, B., Uzun, S., & Karakaya, O. (2019). Combined effects of aminoethoxyvinylglycine and MAP on the fruit quality of kiwifruit during cold storage and shelf life. *Scientia Horticulturae*, *251*, 209-214. https://doi.org/10.1016/j.scienta.2019.03.034

Paterson, V. J., Macrae, E. A., & Young, H. (1991). Relationships between sensory properties and chemical composition of kiwifruit (Actinidia deliciosa). *Journal of the Science of Food and Agriculture*, *57*(2), 235-251. https://doi.org/10.1002/jsfa.2740570208

Paul, V., Pandey, R., & Srivastava, G. C. (2012). The fading distinctions between classical patterns of ripening in climacteric and non-climacteric fruit and the ubiquity of ethylene—an overview. *Journal of food science and technology*, *49*(1), 1-21. https://doi.org/10.1007/s13197-011-0293-4

Pilkington, S. M., Montefiori, M., Jameson, P. E., & Allan, A. C. (2012). The control of chlorophyll levels in maturing kiwifruit. *Planta*, *236*(5), 1615-1628. https://doi.org/10.1007/s00425-012-1723-x

Pires, R., Guerra, R., Cruz, S. P., Antunes, M. D., Brázio, A., Afonso, A. M., Daniel, M., Panagopoulos, T., Gonçalves, I. & Cavaco, A. M. (2022). Ripening assessment of ‘Ortanique’ (Citrus reticulata Blanco x Citrus sinensis (L) Osbeck) on tree by SW-NIR reflectance spectroscopy-based calibration models. *Postharvest Biology and Technology*, *183*, 111750. https://doi.org/10.1016/j.postharvbio.2021.111750

PLS_Toolbox 9.0 (2021). Eigenvector Research, Inc., Manson, WA USA 98831; software available at http://www.eigenvector.com.

Pourkhak, B., Mireei, S. A., Sadeghi, M., & Hemmat, A. (2017). Multi-sensor data fusion in the nondestructive measurement of kiwifruit texture. *Measurement*, *101*, 157-165. https://doi.org/10.1016/j.measurement.2017.01.024

Pu, H., Liu, D., Wang, L., & Sun, D. W. (2016). Soluble solids content and pH prediction and maturity discrimination of lychee fruits using visible and near infrared hyperspectral imaging. *Food Analytical Methods*, *9*(1), 235-244. https://doi.org/10.1007/s12161-015-0186-7

Qiang, L., Mingjie, T., Jianrong, C., Huazhu, L., & Chaitep, S. (2010). Selection of efficient wavelengths in NIR spectrum for determination of dry matter in kiwi fruit. *Maejo International Journal of Science and Technology*, *4*(1), 113-124.

Qin, J., & Lu, R. (2008). Measurement of the optical properties of fruits and vegetables using spatially resolved hyperspectral diffuse reflectance imaging technique. *Postharvest Biology and Technology*, *49*(3), 355-365. https://doi.org/10.1016/j.postharvbio.2008.03.010

Qin, J., & Lu, R. (2009). Monte Carlo simulation for quantification of light transport features in apples. *Computers and electronics in agriculture*, *68*(1), 44-51. https://doi.org/10.1016/j.compag.2009.04.002

Ragni, L., Berardinelli, A., & Guarnieri, A. (2010). Impact device for measuring the flesh firmness of kiwifruits. *Journal of Food Engineering*, *96*(4), 591-597. https://doi.org/10.1016/j.jfoodeng.2009.09.006

Ragni, L., Cevoli, C., Berardinelli, A., & Silaghi, F. A. (2012). Non-destructive internal quality assessment of “Hayward” kiwifruit by waveguide spectroscopy. *Journal of Food Engineering*, *109*(1), 32-37. https://doi.org/10.1016/j.jfoodeng.2011.10.002

Ramstad, K. M., Miller, H. C., & Kolle, G. (2016). Sixteen kiwi (Apteryx spp) transcriptomes provide a wealth of genetic markers and insight into sex chromosome evolution in birds. *BMC genomics*, *17*, 1-14. https://doi.org/10.1186/s12864-016-2714-2

Redgwell, R. J., Melton, L. D., & Brasch, D. J. (1990). Cell wall changes in kiwifruit following post harvest ethylene treatment. *Phytochemistry*, *29*(2), 399-407. https://doi.org/10.1016/0031-9422(90)85087-V

Richardson, A. C., Boldingh, H. L., McAtee, P. A., Gunaseelan, K., Luo, Z., Atkinson, R. G., David, K. M., Burdon, J. N., & Schaffer, R. J. (2011). Fruit development of the diploid kiwifruit, Actinidia chinensis' Hort16A'. *BMC Plant Biology*, *11*(1), 1-14. https://doi.org/10.1186/1471-2229-11-182

Rizzolo, A., Vanoli, M., Spinelli, L., & Torricelli, A. (2010). Sensory characteristics, quality and optical properties measured by time-resolved reflectance spectroscopy in stored apples. *Postharvest Biology and Technology*, *58*(1), 1-12. https://doi.org/10.1016/j.postharvbio.2010.05.003

Rizzolo, A., Vanoli, M., Bianchi, G., Zanella, A., Grassi, M., Torricelli, A., & Spinelli, L. (2014). Relationship between texture sensory profiles and optical properties measured by time-resolved reflectance spectroscopy during post-storage shelf life of 'Braeburn' apples. *J. Hortic. 22*, 113–121. https://doi.org/10.2478/johr-2014-0014

Rizzolo, A., & Vanoli, M. (2016). Time-resolved technique for measuring optical properties and quality of food. *Light Scattering Technology for Food Property, Quality and Safety Assessment; Lu, R.,* Ed.; CRC Press: Boca Raton, FL, USA, pp. 187–224

Roberts, W. G., & Gordon, M. H. (2003). Determination of the total antioxidant activity of fruits and vegetables by a liposome assay. *Journal of Agricultural and Food Chemistry, 51*, 1486–1493. https://doi.org/10.1021/jf025983t

Rocchi, L., Vidoni, S., Ceccarelli, A., Fiori, G., & Costa, G. (2016). Use of the DAindex TM for monitoring fruit ripening evolution in *A. chinensis* to precisely assess harvesting time “in planta”. *Journal of Berry Research*, *6*(4), 373-379. DOI:10.3233/JBR-160116

Rojas-Candelas, L. E., Chanona-Pérez, J. J., Méndez, J. M., Perea-Flores, M. J., Cervantes-Sodi, F., Hernández-Hernández, H. M., & Marin-Bustamante, M. Q. (2021). Physicochemical, structural and nanomechanical study elucidating the differences in firmness among four apple cultivars. *Postharvest Biology and Technology*, *171*, 111342. https://doi.org/10.1016/j.postharvbio.2020.111342

Ropodi, A. I., Panagou, E. Z., & Nychas, G. J. E. (2018). Rapid detection of frozen-then-thawed minced beef using multispectral imaging and Fourier transform infrared spectroscopy. *Meat science*, *135*, 142-147. https://doi.org/10.1016/j.meatsci.2017.09.016

Rowe, P. I., Künnemeyer, R., McGlone, A., Talele, S., Martinsen, P., & Seelye, R. (2014). Relationship between tissue firmness and optical properties of 'Royal Gala' apples from 400 to 1050 nm. *Postharvest Biology and Technology*, *94*, 89-96. https://doi.org/10.1016/j.postharvbio.2014.03.007

Saeys, W., Do Trong, N. N., Van Beers, R., & Nicolaï, B. M. (2019). Multivariate calibration of spectroscopic sensors for postharvest quality evaluation: A review. *Postharvest Biology and Technology*, *158*, 110981. https://doi.org/10.1016/j.postharvbio.2019.110981

Santagapita, P. R., Tylewicz, U., Panarese, V., Rocculi, P., & Dalla Rosa, M. (2016). Non-destructive assessment of kiwifruit physico-chemical parameters to optimise the osmotic dehydration process: A study on FT-NIR spectroscopy. *biosystems engineering*, *142*, 101-109. https://doi.org/10.1016/j.biosystemseng.2015.12.011

Sanz, V., López-Hortas, L., Torres, M. D., & Domínguez, H. (2021). Trends in kiwifruit and byproducts valorization. *Trends in Food Science & Technology*, *107*, 401-414. https://doi.org/10.1016/j.tifs.2020.11.010

Sarkar, S., Basak, J. K., Moon, B. E., & Kim, H. T. (2020). A comparative study of PLSR and SVM-R with various pre-processing techniques for the quantitative determination of soluble solids content of hardy kiwi fruit by a portable Vis/NIR spectrometer. *Foods*, *9*(8), 1078. https://doi.org/10.3390/foods9081078

Savitzky, A., & Golay, M. J. (1964). Smoothing and differentiation of data by simplified least squares procedures. *Analytical chemistry*, *36*(8), 1627-1639. https://doi.org/10.1021/ac60214a047

Schaare, P. N., & Fraser, D. G. (2000). Comparison of reflectance, interactance and transmission modes of visible-near infrared spectroscopy for measuring internal properties of kiwifruit (Actinidia chinensis). *Postharvest Biology and Technology*, *20*(2), 175-184. https://doi.org/10.1016/S0925-5214(00)00130-7

Schotsmans, W., Verlinden, B. E., Lammertyn, J., & Nicolaï, B. M. (2004). The relationship between gas transport properties and the histology of apple. *Journal of the Science of Food and Agriculture*, *84*(10), 1131-1140. https://doi.org/10.1002/jsfa.1768

Schroder, R., & Atkinson, R. G. (2006). Kiwifruit cell walls: towards an understanding of softening?. *New Zealand Journal of Forestry Science*, *36*(1), 112.

Retrieved from https://www.scionresearch.com/__data/assets/pdf_file/0011/59096/11Schroeder.pdf

Shah, S. S. A., Zeb, A., Qureshi, W. S., Arslan, M., Malik, A. U., Alasmary, W., & Alanazi, E. (2020). Towards fruit maturity estimation using NIR spectroscopy. *Infrared Physics & Technology*, *111*, 103479. https://doi.org/10.1016/j.infrared.2020.103479

Shafiee-Jood, M., & Cai, X. (2016). Reducing food loss and waste to enhance food security and environmental sustainability. *Environmental science & technology*, *50*(16), 8432-8443. https://doi.org/10.1021/acs.est.6b01993

Shah, S. S. A., Zeb, A., Qureshi, W. S., Arslan, M., Malik, A. U., Alasmary, W., & Alanazi, E. (2020). Towards fruit maturity estimation using NIR spectroscopy. *Infrared Physics & Technology*, *111*, 103479. https://doi.org/10.1016/j.infrared.2020.103479

Shao, Y., He, Y., Gómez, A. H., Pereir, A. G., Qiu, Z., & Zhang, Y. (2007). Visible/near infrared spectrometric technique for nondestructive assessment of tomato 'Heatwave' (Lycopersicum esculentum) quality characteristics. *Journal of Food Engineering*, *81*(4), 672-678. https://doi.org/10.1016/j.jfoodeng.2006.12.026

Shibang, M. (2021). Nondestructive determination of kiwifruit SSC using visible/near-infrared spectroscopy with genetic algorithm. *J. Eng. Sci. Technol*. Rev. 14. https:// doi.org/10.25103/jestr.141.11.

Shinzawa, H., Ritthiruangdej, P., & Ozaki, Y. (2011). Kernel analysis of partial least squares (PLS) regression models. *Applied spectroscopy*, *65*(5), 549-556. https://doi.org/10.1366/10-06187

Si, W., Xiong, J., Huang, Y., Jiang, X., & Hu, D. (2022). Quality Assessment of Fruits and Vegetables Based on Spatially Resolved Spectroscopy: A Review. *Foods*, *11*(9), 1198. https://doi.org/10.3390/foods11091198

Singh, H., Sridhar, A., & Saini, S. S. (2020). Ultra-low-cost self-referencing multispectral detector for non-destructive measurement of fruit quality. *Food Analytical Methods*, *13*(10), 1879-1893. https://doi.org/10.1007/s12161-020-01810-7

Sirisomboon, P., Tanaka, M., & Kojima, T. (2012). Evaluation of tomato textural mechanical properties. *Journal of Food Engineering*, *111*(4), 618-624. https://doi.org/10.1016/j.jfoodeng.2012.03.007

Slaughter, D.C., & Crisosto, C.H. (1998). Nondestructive internal quality assessment of kiwifruit using near-infrared spectroscopy. *Semin. Food Anal*. 3, 131–140.

Sneddon, T., Glowacz, M., Jeffery, P., & East, A. (2022). Severity of scuffing injury of 'Zesy002'kiwifruit as influenced by maturity. *New Zealand Journal of Crop and Horticultural Science*, 1-15. https://doi.org/10.1080/01140671.2022.2058025

Snelgar, W. P., Hall, A. J., Ferguson, A. R., & Blattmann, P. (2005). Temperature influences growth and maturation of fruit on ‘Hayward’kiwifruit vines. *Functional Plant Biology*, *32*(7), 631-642. https://doi.org/10.1071/FP05062

Song, J., & Bangerth, F. (1996). The effect of harvest date on aroma compound production from ‘Golden Delicious’ apple fruit and relationship to respiration and ethylene production. *Postharvest Biology and Technology*, *8*(4), 259-269. https://doi.org/10.1016/0925-5214(96)00020-8

Statista. (2022). Kiwi fruit: leading producers worldwide 2020. Available at: https://www.statista.com/statistics/812434/production-volume-of-leading-kiwi-producing-countries/ (accessed 15/11/2022)

Sugiyama, J., Al-Haq, M. I., & Tsuta, M. (2005). Application of portable acoustic firmness tester for fruits. *Information and technology for sustainable fruit and vegetable production. FRUTIC*, *5*, 12-16.

Suzuki, I., Ogawa, M., Seino, K., Nogawa, M., Naito, H., Yamakoshi, K. I., & Tanaka, S. (2018). Reagentless estimation of urea and creatinine concentrations using near-infrared spectroscopy for spot urine test of urea-to-creatinine ratio. *Advanced Biomedical Engineering*, *7*, 72-81. https://doi.org/10.14326/abe.7.72

Tang, M., Cai, J., & Lu, H. (2010). Long-term prediction of Zhonghua kiwifruit dry matter by near infrared spectroscopy. *Scienceasia*, *36*(3), 210-215. DOI:10.2306/scienceasia1513-1874.2010.36.210

Testolin, R., & Ferguson, A. R. (2009). Kiwifruit (Actinidia spp.) production and marketing in Italy. *New Zealand Journal of Crop and Horticultural Science*, *37*(1), 1-32. https://doi.org/10.1080/01140670909510246

Tian, S., Xu, Y., Jiang, A., & Gong, Q. (2002). Physiological and quality responses of longan fruit to high O2 or high CO2 atmospheres in storage. *Postharvest Biology and Technology*, *24*(3), 335-340. https://doi.org/10.1016/S0925-5214(01)00153-3

Tian, X., Li, J., Yi, S., Jin, G., Qiu, X., & Li, Y. (2020). Nondestructive determining the soluble solids content of citrus using near infrared transmittance technology combined with the variable selection algorithm. *Artificial Intelligence in Agriculture*, *4*, 48-57. https://doi.org/10.1016/j.aiia.2020.05.001

Tian, S., Tian, H., Yang, Q., & Xu, H. (2022). Internal quality assessment of kiwifruit by bulk optical properties and online transmission spectra. *Food Control*, *141*, 109191. https://doi.org/10.1016/j.foodcont.2022.109191

Tian, S., & Xu, H. (2022). Mechanical-based and Optical-based Methods for Nondestructive Evaluation of Fruit Firmness. *Food Reviews International*, 1-31. https://doi.org/10.1080/87559129.2021.2015376

Tian, S., Wang, J., & Xu, H. (2022a). Firmness measurement of kiwifruit using a self-designed device based on acoustic vibration technology. *Postharvest Biology and Technology*, *187*, 111851. https://doi.org/10.1016/j.postharvbio.2022.111851

Tian, S., Tian, H., Yang, Q., & Xu, H. (2022b). Internal quality assessment of kiwifruit by bulk optical properties and online transmission spectra. *Food Control*, *141*, 109191. https://doi.org/10.1016/j.foodcont.2022.109191

Tilahun, S., Choi, H. R., Lee, Y. M., Choi, J. H., Baek, M. W., Hyok, K., Parl, S. M., & Jeong, C. S. (2020). Ripening quality of kiwifruit cultivars is affected by harvest time. *Scientia Horticulturae*, *261*, 108936. https://doi.org/10.1016/j.scienta.2019.108936

Tirado-Kulieva, V. A., Hernández-Martínez, E., & Suomela, J. P. (2022). Non-destructive assessment of vitamin C in foods: a review of the main findings and limitations of vibrational spectroscopic techniques. *European Food Research and Technology*, 1-11. https://doi.org/10.1007/s00217-022-04023-w

Tombesi, A., Antognozzi, E., & Palliotti, A. (1993). Influence of light exposure on characteristics and storage life of kiwifruit. *New Zealand journal of crop and horticultural science*, *21*(1), 85-90. https://doi.org/10.1080/01140671.1993.9513750

Torkashvand, A. M., Rahpeik, M. E., Hashemabadi, D., & Sajjadi, S. A. (2016). Determining an appropriate fertilization planning to increase qualitative and quantitative characteristics of kiwifruit (Actinidia deliciosa L.) in Astaneh Ashrafieh, Gilan, Iran. *Air, Soil and Water Research*, *9*, ASWR-S38495. https://doi.org/10.4137/ASWR.S38495

Torkashvand, A. M., Ahmadi, A., & Nikravesh, N. L. (2017). Prediction of kiwifruit firmness using fruit mineral nutrient concentration by artificial neural network (ANN) and multiple linear regressions (MLR). *Journal of Integrative Agriculture*, *16*(7), 1634-1644. https://doi.org/10.1016/S2095-3119(16)61546-0

Torricelli, A., Contini, D., Dalla Mora, A., Martinenghi, E., Tamborini, D., Villa, F., Tosi, A., & Spinelli, L. (2015). Recent advances in time-resolved NIR spectroscopy for nondestructive assessment of fruit quality. *Chemical Engineering Transactions*, 43-48. DOI:10.3303/CET1544008

Tuchin, V. (2000). Tissue optics: light scattering methods and instruments for medical diagnosis. *SPIE Tutorial Texts in Optical Engineering*.

U.S. Department of Agriculture. (2019). FoodData Central. Available at: https://fdc.nal.usda.gov/index.html (accessed 15/11/2022).

Vanoli, M., Van Beers, R., Sadar, N., Rizzolo, A., Buccheri, M., Grassi, M., Lovati, F., Nicolaï, B., Aernouts, B., Watté, R., Torricelli, A., Spinelli, L., Saeys, W., & Zanella, A. (2020). Time-and spatially-resolved spectroscopy to determine the bulk optical properties of 'Braeburn'apples after ripening in shelf life. *Postharvest Biology and Technology*, *168*, 111233. https://doi.org/10.1016/j.postharvbio.2020.111233

Vieira, A. I., Guerreiro, A. C., Gago, C. L., Brázio, A., Guerra, R., Cavaco, A. M., Panagopoulos, T., Veloso, F., & Antunes, M. D. (2017). An attempt to find a non-destructive method to determine ripeness of kiwifruit (Actinidia chinensis Planch. 'Jintao'). In *IX International Symposium on Kiwifruit 1218* (pp. 489-496). https://doi.org/10.17660/ActaHortic.2018.1218.67

Walsh, K. B., Blasco, J., Zude-Sasse, M., & Sun, X. (2020a). Visible-NIR ‘point’ spectroscopy in postharvest fruit and vegetable assessment: The science behind three decades of commercial use. *Postharvest Biology and Technology*, *168*, 111246. https://doi.org/10.1016/j.postharvbio.2020.111246

Walsh, K. B., McGlone, V. A., & Han, D. H. (2020b). The uses of near infra-red spectroscopy in postharvest decision support: A review. *Postharvest Biology and Technology*, *163*, 111139. https://doi.org/10.1016/j.postharvbio.2020.111139

Wang, Y., Veltkamp, D. J., & Kowalski, B. R. (1991). Multivariate instrument standardization. *Analytical chemistry*, *63*(23), 2750-2756. https://doi.org/10.1021/ac00023a016

Wang, Y. S., Tian, S. P., & Xu, Y. (2005). Effects of high oxygen concentration on pro-and anti-oxidant enzymes in peach fruits during postharvest periods. *Food chemistry*, *91*(1), 99-104. https://doi.org/10.1016/j.foodchem.2004.05.053

Wang, Q., Lai, T., Qin, G., & Tian, S. (2009). Response of jujube fruits to exogenous oxalic acid treatment based on proteomic analysis. *Plant and cell physiology*, *50*(2), 230-242. https://doi.org/10.1093/pcp/pcn191

Wang, M. Y., MacRae, E., Wohlers, M., & Marsh, K. (2011). Changes in volatile production and sensory quality of kiwifruit during fruit maturation in Actinidia deliciosa ‘Hayward’ and A. chinensis ‘Hort16A’. *Postharvest Biology and Technology*, *59*(1), 16-24. https://doi.org/10.1016/j.postharvbio.2010.08.010

Wang, H., Peng, J., Xie, C., Bao, Y., & He, Y. (2015). Fruit quality evaluation using spectroscopy technology: a review. *Sensors*, *15*(5), 11889-11927. https://doi.org/10.3390/s150511889

Wang, H., Wang, J., Mujumdar, A. S., Jin, X., Liu, Z. L., Zhang, Y., & Xiao, H. W. (2021). Effects of postharvest ripening on physicochemical properties, microstructure, cell wall polysaccharides contents (pectin, hemicellulose, cellulose) and nanostructure of kiwifruit (*Actinidia deliciosa*). *Food Hydrocolloids*, *118*, 106808. https://doi.org/10.1016/j.foodhyd.2021.106808

Wang, S., Qiu, Y., & Zhu, F. (2021). Kiwifruit (Actinidia spp.): A review of chemical diversity and biological activities. *Food Chemistry*, *350*, 128469. https://doi.org/10.1016/j.foodchem.2020.128469

Wang, H., Wang, C., Peng, Z., & Sun, H. (2022a). Feasibility study on early identification of freshness decay of fresh-cut kiwifruit during cold chain storage by Fourier transform-near infrared spectroscopy combined with chemometrics. *Journal of Food Science*. https://doi.org/10.1111/1750-3841.16197

Wang, H., Li, X., Wang, J., Vidyarthi, S. K., Wang, H., Zhang, X. G., Gao, L., Yang, K.H., Zhang, J.S., & Xiao, H. W. (2022b). Effects of postharvest ripening on water status and distribution, drying characteristics, volatile profiles, phytochemical contents, antioxidant capacity and microstructure of kiwifruit (*Actinidia* *deliciosa*). *Food Control*, *139*, 109062. https://doi.org/10.1016/j.foodcont.2022.109062

Wang, X., Xu, L., Chen, H., Zou, Z., Huang, P., & Xin, B. (2022c). Non-Destructive Detection of pH Value of Kiwifruit Based on Hyperspectral Fluorescence Imaging Technology. *Agriculture*, *12*(2), 208. https://doi.org/10.3390/agriculture12020208

Wati, R. K., Pahlawan, M. F. R., & Masithoh, R. E. (2021). Development of calibration model for pH content of intact tomatoes using a low-cost Vis/NIR spectroscopy. In *IOP Conference Series: Earth and Environmental Science* (Vol. 686, No. 1, p. 012049). IOP Publishing. DOI:10.1088/1755-1315/686/1/012049

Welch, A., & Gemert, M. (2010). Overview of optical and thermal laser-tissue interaction and nomenclature. In *Optical - thermal response of laser-irradiated tissue*, 2nd ed.; Springer 3–12: Berlin.

Wold, S., Antti, H., Lindgren, F., & Ohman, J. (1998). Orthogonal signal correction of near-infrared spectra. Chemometrics and Intelligent laboratory systems, 44(1-2), 175-185. https://doi.org/10.1016/S0169-7439(98)00109-9

Wood, D. F., Imam, S. H., Orts, W. J., & Glenn, G. M. (2009, May). Fresh fruit: microstructure, texture, and quality. In *Scanning Microscopy 2009* (Vol. 7378, pp. 293-304). SPIE. https://doi.org/10.1117/12.821351

Wu, D., & Sun, D. W. (2013). Advanced applications of hyperspectral imaging technology for food quality and safety analysis and assessment: A review —Part I: Fundamentals. *Innovative Food Science & Emerging Technologies*, *19*, 1-14. https://doi.org/10.1016/j.ifset.2013.04.014

Yadav, J., Rani, A., Singh, V., & Murari, B. M. (2015). Comparative study of different measurement sites using NIR based non-invasive glucose measurement system. *Procedia Computer Science*, *70*, 469-475. https://doi.org/10.1016/j.procs.2015.10.082

Yang, H. Y., Inagaki, T., Ma, T., & Tsuchikawa, S. (2017). High-resolution and non-destructive evaluation of the spatial distribution of nitrate and its dynamics in spinach (Spinacia oleracea L.) leaves by near-infrared hyperspectral imaging. *Frontiers in plant science*, *8*, 1937. https://doi.org/10.3389/fpls.2017.01937

Yi, J., Kebede, B. T., Grauwet, T., Van Loey, A., Hu, X., & Hendrickx, M. (2016). A multivariate approach into physicochemical, biochemical and aromatic quality changes of purée based on Hayward kiwifruit during the final phase of ripening. *Postharvest Biology and Technology*, *117*, 206-216. https://doi.org/10.1016/j.postharvbio.2016.03.007

Xia, Y., Chen, T., Qin, G., Li, B., & Tian, S. (2016). Synergistic action of antioxidative systems contributes to the alleviation of senescence in kiwifruit. *Postharvest Biology and Technology*, *111*, 15-24. https://doi.org/10.1016/j.postharvbio.2015.07.026

Xia, H., Wang, X., Zhou, Y., Su, W., Jiang, L., Deng, H., Li, M., Zhuang, Q., Xie, Y., & Liang, D. (2021). Biochemical and molecular factors governing flesh-color development in two yellow-fleshed kiwifruit cultivars. *Scientia Horticulturae*, *280*, 109929. https://doi.org/10.1016/j.scienta.2021.109929

Xiao, X., & Li, M. (2022). Fusion of data-driven model and mechanistic model for kiwifruit flesh firmness prediction. *Computers and Electronics in Agriculture*, *193*, 106651. https://doi.org/10.1016/j.compag.2021.106651

Xie, Q., Zhang, H., Yan, F., Yan, C., Wei, S., Lai, J., Wang, Y., & Zhang, B. (2019). Morphology and molecular identification of twelve commercial varieties of kiwifruit. *Molecules*, *24*(5), 888. https://doi.org/10.3390/molecules24050888

Zeaiter, M., Roger, J. M., & Bellon-Maurel, V. (2005). Robustness of models developed by multivariate calibration. Part II: The influence of pre-processing methods. *TrAC Trends in Analytical Chemistry*, *24*(5), 437-445. https://doi.org/10.1016/j.trac.2004.11.023

Zerbini, P. E. (2006). Emerging technologies for non-destructive quality evaluation of fruit. *Journal of fruit and ornamental plant research*, *14*, 13. Retrieved from http://www.inhort.pl/files/journal_pdf/Suppl_2_2006/Suppl_2_full_1_2006.pdf

Zhang, W., Luo, Z., Wang, A., Gu, X., & Lv, Z. (2021). Kinetic models applied to quality change and shelf life prediction of kiwifruits. *LWT*, *138*, 110610. https://doi.org/10.1016/j.lwt.2020.110610

Zhu, Q., Guan, J., Huang, M., Lu, R., & Mendoza, F. (2016). Predicting bruise susceptibility of ‘Golden Delicious’ apples using hyperspectral scattering technique. *Postharvest Biology and Technology*, *114*, 86-94. https://doi.org/10.1016/j.postharvbio.2015.12.007

Zhu, H., Chu, B., Fan, Y., Tao, X., Yin, W., & He, Y. (2017). Hyperspectral imaging for predicting the internal quality of kiwifruits based on variable selection algorithms and chemometric models. *Scientific reports*, *7*(1), 1-13. https://doi.org/10.1038/s41598-017-08509-6

Zude, M. (2008). *Optical Monitoring of Fresh and Processed Agricultural Crops.* Group, CRC Press Taylor & Francis. https://doi.org/10.1201/9781420054033